University of Tennessee, Knoxville
Trace: Tennessee Research and Creative Exchange

Doctoral Dissertations Graduate School

12-2014

Elucidating Fundamental Mechanisms in Focused Electron- and Ion-Beam Induced Synthesis

Carlos M. Gonzalez
University of Tennessee - Knoxville, cgonzal6@vols.utk.edu

Recommended Citation
Gonzalez, Carlos M., "Elucidating Fundamental Mechanisms in Focused Electron- and Ion-Beam Induced Synthesis. " PhD diss., University of Tennessee, 2014.
https://trace.tennessee.edu/utk_graddiss/3129

This Dissertation is brought to you for free and open access by the Graduate School at Trace: Tennessee Research and Creative Exchange. It has been accepted for inclusion in Doctoral Dissertations by an authorized administrator of Trace: Tennessee Research and Creative Exchange. For more information, please contact trace@utk.edu.

To the Graduate Council:

I am submitting herewith a dissertation written by Carlos M. Gonzalez entitled "Elucidating Fundamental Mechanisms in Focused Electron- and Ion-Beam Induced Synthesis." I have examined the final electronic copy of this dissertation for form and content and recommend that it be accepted in partial fulfillment of the requirements for the degree of Doctor of Philosophy, with a major in Materials Science and Engineering.

Philip D. Rack, Major Professor

We have read this dissertation and recommend its acceptance:

Kurt E. Sickafus, Eric D. Lukosi, Gerd Duscher, Jason D. Fowlkes

Accepted for the Council:
Carolyn R. Hodges

Vice Provost and Dean of the Graduate School

(Original signatures are on file with official student records.)

Elucidating Fundamental Mechanisms in Focused Electron- and Ion-Beam Induced Synthesis

A Dissertation Presented for the

Doctor of Philosophy

Degree

The University of Tennessee, Knoxville

Carlos M. Gonzalez

December 2014

Copyright 2014 by

Carlos M. Gonzalez,

All rights reserved.

Dedication

For something deep that I hold utterly dear, something I am connected to which I humble before, and to which I owe everything I have. The one, who provides a most fascinating selection of raw materials that scientists can look into, mix, shape and transform into useful devices, all this while always abiding by a mutual, absolute, and never relative,

respect and harmony with Her Majesty, Mother Nature.

Acknowledgments

Ever grateful to Life, Luck, Fate, Health and my Maker for allowing me in this accidental modern life to end up at my age as a non-traditional student in the State of Tennessee to make possible the broadening of my knowledge base, especially regarding advanced materials and technologies. To Fate and Luck for allowing me despite my age, ethnicity and sexual orientation to make it to the finish line despite many societal hurdles and low expectations placed on the way.

To Mother (Linda Lee Titman) for having Faith in me and this noble mission of earning a graduate degree in UTK. For making it possible for me to move and drive from Omaha to Knoxville back in Jan 2010. To Aunt Susan (S. Brewster) for coming here with her husband Jim (J. Brewster) to visit me all the way from a small town in the Nebraska plains, and for helping me secure student loans when needed to finish my degree. To my dear Ana Celia (always Mami) and Manuel Rafael (always Dad) for cheering me up all the way from the Caribbean mountains in Utuado, Puerto Rico and for making monthly contributions to help with my college bills.

Ever grateful to Dr. Philip D. Rack (Advisor) for inviting me to work in UTK, for his guidance and generosity in dealing with a graduate student six years his senior. Most indebted to my Doctoral Committee for their support and selfless time commitment: Dr. Kurt E. Sickafus (MSE Department Head), Dr. Gerd Duscher, Dr. Eric D. Lukosi (NE) and Dr. Jason D. Fowlkes (ORNL-CNMS). Worth mentioning is Dr. Sickafus going out of his way to accommodate a defense date convenient to every committee member. Dr. Eric Lukosi for joining the committee only two months prior to defense on short notice. Dr. David C. Joy for having been part of the committee from the start (present at the 11/25/2013 proposal), but for personal reasons not been able to stay. I wish Dr. Joy utmost health and a speedy recovery.

My dearest and closest Friends while in Knoxville, Tennessee: Dr. Rajendra Timilsina, Chris Hartnett, Adam C. Lindsey, Dr. Nicholas A. Roberts and Dr. Jonathan D. Peak. Always indebted to a great proxy sister, Karen F. Rack, the best teacher in the world, and to her very bright and talented daughter, Kathryn M. Rack, both for being the kindest ladies I've ever met. Thank you to Dr. Rosario Gerhardt (MS Advisor, Georgia Tech), Dr. Jose L. Cruz-Rivera (CSU, Fullerton) and Andrew Ritter (AVX Corporation); all who believed in my potential four years ago when they submitted enthusiastic letters of recommendation to the Graduate School at UTK. My peers and colleagues in Dr. Rack's Group for their support since I arrived: Dr. Joo-Hyon Noh, Dr. Yueying Wu, Shaofang Fu, Anthony Wong, Dr. Matthew G. Lassiter, Dr. Seyeoul Kwon and Dr. Jiyong Noh. Special gratitude goes to people that have collaborated and supported the microscopy part of my research: Dr. Guoliang Li, Dr. Peizhi Liu, Winand Slingenbergh (Groningen University, NL) and Ondrej Dyck. Also, my deepest thanks goes to Dr. Huimeng M. Wu, Dr. Lewis A. Stern and Dr. Deying Xia for their unequaled support and hospitality during my visit to Carl Zeiss Microscopy (LLC) in Peabody, MA. I am truly indebted to Dr. John R. Dunlap for his unrelenting and patient help, always providing top-notch training and assistance regarding SEM, EDX, TEM and AFM.

My Undergraduate Research Assistants: Will McNabb, Joseph B. Ulrich, Adam M. Seal and Chase B. Joslin, who provided me with the grand satisfaction of mentorship. To those in UTK who day by day provided me with inspiration, support and friendship: Martha Gale, Carla Lawrence, Susan Seymour, Merry Koschan, Hua Wei, Sharon Sweetser Pound, William F. Holiway, Carol Winn, Dr. Roberto S. Benson, Dr. George M. Pharr and Dr. Chuck L. Melcher. And, my outstanding and favorite educators in the MSE Department: Dr. Veerle M. Keppens, Dr. James R. Morris, Dr. David J. Keffer and Dr. Ramki Kalyanaraman.

To Dr. Adam J. Rondinone who has been a close mentor of me in the Center for Nanophase Sciences (CNMS) in Oak Ridge National Labs (ORNL). Especially, for his dutiful hours training me in the Panalytical (Glancing XRD, XRR) and in the Orion Nanofab HIM. To Kevin Lester, Dale Hensley, Bernadetta Srijanto, Dayrl Briggs, and Rebecca Agapov for their support and camaraderie in the CNMS clean room team/facilities.

Lastly, to Centro Hispano of East TN for allowing me to teach and to collaborate with them. There is a higher purpose in life than ourselves, and they provided the means to reach out to local Latinos and Latinas that benefited and learned from my knowledge and passion for higher education and standards. My deepest appreciation goes to the UT-MRS and UT-SHPE Executive Boards for accepting me and allowing me to take the helm and lead the organizations for up to two years.

Abstract

A focused electron beam deposition process (FEBID) coupled with in-situ infrared pulsed laser assist (LA-EBID) has been implemented for higher purity tungsten nanowires using $W(CO)_6$ [tungsten hexacarbonyl] as parent precursor gas. Nanowires made of Co from $Co_2(CO)_8$ [dicobalt octacarbonyl] and Pt from $MeCpPtIVMe_3$ [trimethyl methylcyclopentadienyl platinum] have also been realized by using inert focused ion beams of helium and helium and neon, respectively. In all cases, higher electrical conductivities, higher purities and larger grain sizes have been obtained when compared with preceding traditional additive edit techniques. These new approaches will make possible successful nanoscale direct-write processes on complex structures of high technological relevance such as the Mo/Si EUV reflector mirror.

Etching of a nickel top absorber layer has been attained by using a neon focused ion beam (Ne-FIB), but not with a He-FIB. Subsurface or collateral damage due to defect generation and interactions still remains a side effect that needs to be minimized and corrected. Experiments made in a helium ion microscope (HIM) indicate that endpoint detection is possible for monitoring when a top film (Ni, Au, Cu, and SiO_2 [silicon dioxide]) in a multilayer structure has been milled through to an internal boundary by using a neon focused ion beam. In the case of helium ion irradiation, the electronic signature corresponding to the onset of nanobubbling (or swelling) has been captured, hence improving the detectability of this adverse effect. Models using an empirical 2-D Lambertian distribution have been deployed to predict how the secondary electron (SE) emissions vary as a function of the etch geometry and composition for one-, two- and three-component systems.

Table of Contents

Introduction 1

Chapter 1: Electrical Characterization of Laser Assisted Electron Beam Induced Deposition and Focused Ion Beam Induced Deposition of Nano-Wires 4

Summary 4

Literature Review 5

Experimental Methods 14

Results and Discussion 15

NW DC Electrical Measurements Review 15

LA-EBID Overview 19

W NWs Made Via LA-EBID 21

Pt NWs Made Via He- and Ne-IBID 29

Pt/C Considerations 32

Co NWs Made Via He-BID 39

NW Microstructural Considerations 42

Other Perspectives on Failure Modes 56

Conclusions 59

Chapter 2: Helium and Neon Focused Ion Beam Etching of the Mo/Si Extreme Ultra-Violet Mirror Mask Structure 60

Summary 60

Literature Review 61

General Background 61

Defect Generation and Interactions 65

Experimental Methods 78

Results and Discussion 79

Predictions Based on SRIM/TRIM 79

Focused Helium Beam Exposures 83

Helium Ion-Solid Modeling 92

Preliminary Experiments with Nickel Etching 94

Focused Neon Beam Exposures 96

Neon Ion-Solid Modeling 105

Ion Beam Energy Studies 109

Heating Considerations 113

Implanted Atoms, Recoils and Vacancy Concentrations 120

Defect Generation and Interactions in the Ni/Ru/40x(Mo/Si) Stack 126

Conclusions 137

Chapter 3: Helium and Neon Ion-Based Endpoint Detection 139

Summary 139

Literature Review 140

Experimental Methods 144

Results and Discussion 145

Secondary Electron Yields by Ion Irradiation 145

Endpoint Testing Considerations 147

Ni Endpoint Detection ……149

c-Si Endpoint Detection ……162

SiO_2/c-Si Endpoint Detection ……171

Au & Cu Endpoint Detection ……174

High-Contrast Endpoint Detection ……188

Conclusions ……190

Conclusions ……191

Future Work ……193

List of References ……194

Appendices……202

Vita……215

List of Tables

Table 1.1. Several properties of interest for materials involved in the dc electrical study ……...…13

Table 2.1. Reactions between defects ……………...…………..…………………………………………..77

Table 2.2. Summary of individual component's properties ………………..……...…………………83

Table 3.1. Comparison of SE yields of several materials when using a primary beam of electrons, helium ions and neon ions ……………………….……………………………………………………146

Table 3.2. Predictions by SRIM/TRIM, at 30 keV …………………………………..………..…..147

List of Figures

Figure 1.1. Energy losses for ions due to nuclear and electronic interactions …………………..….…6

Figure 1.2. Depiction of mass transfer mechanisms involved in a deposition process …........…....7

Figure 1.3. Deposition yield as a function of beam energy for the $MeC_pPt(IV)Me_3$ molecule …......9

Figure 1.4. Principle of FIB milling or etching ……………………………………………………...10

Figure 1.5. Molecular structures with ligands for $W(CO)_6$, $MeCpPtIVMe_3$ and $Co_2(CO)_8$ …………………………………………………..……………………………………………...15

Figure 1.6. 2-pt and 4-pt testing of nanowires on one representative test structure …………….....17

Figure 1.7. Microlens positioning on the Opto-probe assembly ……………………..……….……….20

Figure 1.8. Bar plot showing the relative resistivity calculations for the six W NW samples ......…23

Figure 1.9. Resistance data comparing a non-irradiated W NW versus a laser-treated W NW ….24

Figure 1.10. Plot showing the resistivity of an EBID and LA-EBID W NW …………………………25

Figure 1.11. Resistances measured for equal length segments of W NW. Resistances measured for increasing length segments of W NW at 10 μA …………………………………….……………..27

Figure 1.12. Data plotted to determine the contact resistance for a W NW ..…...………………..27

Figure 1.13. Resistivity data for a Pt NW deposited using He and Ne ………………...……………30

Figure 1.14. Comparison of nanostructures between He^+ and Ne^+ induced deposition of Pt …....32

Figure 1.15. Interaction volumes for 30 keV helium and for neon in the Pt/C structure ………..…34

Figure 1.16. Sputtering yields of Pt and C by Ne^+ at 20 keV from SRIM/TRIM simulations ………34

Figure 1.17. Temperatures computed from SRIM/TRIM's phonon energy for He and for Ne ion beams on SiO_2/Si (0 nm Pt/C) and on 300 nm thick Pt/C on SiO_2/Si …………………...……..……36

Figure 1.18. V-I sweep and calculated R-I curve for a Co NW made with a He ion beam ………..40

Figure 1.19. Calculated resistivity from the R-I curve for a Co NW made with a He ion beam …...41

Figure 1.20. TEM images for a Co NW at two different magnifications ……………………………41

Figure 1.21. Diagrams showing the microstructure in a tungsten nanowire ……………………..…44

Figure 1.22. I-V measured data for the W NW from 1 nA to 1 μA …………………………..………..47

Figure 1.23. Calculated Power from measured data versus current forthe W NW ……….………47

Figure 1.24. Several ρ versus T plots for bulk metals and for W NWs ……………………………...49

Figure 1.25. Calculated R from measured data versus current and fit ……………………..………54

Figure 1.26. Calculated ρ from measured data versus current and fit …………………...………..54

Figure 1.27. Estimated temperature as a function of the applied current ……………………..……55

Figure 1.28. Metallic region in the W NW ……………………………………………………….………55

Figure 1.29. Failure modes observed in nanowires during dc electrical characterization ……..…58

Figure 2.1. Bragg's law showing constructive interference in a Mo/Si multilayer stack mirror and the reflectance from a Mo/Si mirror at near normal incidence ……………………………...……62

Figure 2.2. Possible migration mechanisms for helium ……………………………………..………67

Figure 2.3. Interstitial diffusion, vacancy-assisted self-diffusion, diffusion of interstitial clusters and divacancy-assisted self-diffusion ……………………………………………………………...68

Figure 2.4. Electronic and nuclear energy losses for helium and for neon ……………………...81

Figure 2.5. TEM cross-sectional micrographs of nickel on top of a Mo/Si multilayer stack exposed to 16 and to 30 keV helium ion energies in doses ranging from $1x10^{16}$ to $1x10^{18}$ ions/cm^2 ……………………………………………………………………………………………..…84

Figure 2.6. Plot of AFM data at 16 and 30 keV at doses up to $1x10^{19}$ He^+/cm^2 ……….……………85

Figure 2.7. High magnification Z-contrast image of a 30 keV, $1x10^{17}$ He^+/cm^2 exposure ……..…86

Figure 2.8. Two comparable EELS spectra taken in the Mo/Si multilayers ……………….………88

Figure 2.9. Condition of a-Si layers in the stack closest to the beam irradiated region by He^+ 89

Figure 2.10. SAD analysis on the intermixed region ……………………………………………….………...90

Figure 2.11. Low loss EELS plot showing a peak for helium valence electron energy transition when exposed to the 200 keV electron irradiation beam ..…………………….………….…..……91

Figure 2.12. TEM adjusted image with modified contrast limits and brightness in order to carry out a particle size analysis as in the histogram shown …………………………………………...……91

Figure 2.13. Simulated electronic and the nuclear volumetric energy losses for helium ions at 30 keV at a dose of $1x10^{17}$ ions/cm^2 ……………………………………………...…….………...93

Figure 2.14. Simulated nuclear energy loss and the resultant helium implant concentrations compared to the experimental TEM micrograph …………………………………...….....……..94

Figure 2.15. A 1μm^2 etch box by neon on Ni(50 nm)/SiO2/Si and a 6x6 array of 200nm x 200nm etched nanoholes on a nickel top layer …………..……………………………….………….……95

Figure 2.16. Top NIM view of etched boxes and top SEM view for two etched boxes ………..….…97

Figure 2.17. Sequential TEM cross-sections illustrating the progression in etch depth and the formation of cavities below the surface ……………………………………….…………..…98

Figure 2.18. Via aspect ratios for 30 keV Ne^+ exposures of doses ranging up to 1.5 nC/μm^2........99

Figure 2.19. TEM images showing the poly-crystalline condition of the nickel top layer without implantation or exposure to neon, and the manifestation of small neon nanobubbles precipitating at grain boundaries ………………………………………………………………………...…..99

Figure 2.20. High magnification viewgraph while performing EDXS in the TEM around a large neon nanobubble located near the etch zone and directly under the beam trajectory for a dose of 0.7 nC/μm^2 ………………………………..……………………………………...…………102

Figure 2.21. Closer look at the condition of a-Si layer in the stack closest to the beam irradiated, or damaged, region by neon ………………………………….……………………..………103

Figure 2.22. Low loss EELS plot showing a peak for neon valence electron energy transition when exposed to the 200 keV electron irradiation beam …………………….……………………104

Figure 2.23. For 30 keV Ne^+ and $4x10^{17}$ ions/cm^2, showing the TEM adjusted image with different contrast limits (min, max) and brightness in order to do a particle size analysis ….....................…104

Figure 2.24. Experimental and simulated sputter yields of Ni under Ne^+ bombardment for energies up to 30 keV ……………………………………………………………...…………..……..105

Figure 2.25. 3- and 2-D sputter profiles (top) for Ne^+ in Ni at 30 keV and ~2x10^{17} ions/cm^2 106

Figure 2.26. Simulated nuclear energy loss and resultant neon implant concentrations compared to the experimental TEM micrograph exposed to 30 keV at a dose of 2x10^{17} Ne^+/cm^2 …………………………………………………………………………………………………......107

Figure 2.27. Comparison of the simulated volumetric nuclear energy losses of helium and of neon at 30 keV. EnvizION runs of 100k ions corresponded to a dose of ~1x10^{17} He^+/cm^2, and of 150k ions corresponded to a dose of ~2x10^{17} Ne^+/cm^2 …………………………………………………..108

Figure 2.28. Helium energy study ……………………………………….………………….…..110

Figure 2.29. Projected ranges and straggles for helium ion beam energies from 10 to 30 keV as predicted by SRIM/TRIM ……………………………………………………………………..…110

Figure 2.30. Energy study TEM images for neon ion beam etching at 5x10^{17} Ne^+/cm^2 and energies between 10 and 22.5 keV …………………………………….………….....…………………111

Figure 2.31. For a Ne^+ beam energy of 22.5 keV, exposures up to 1x10^{18} Ne^+/cm^2 …………….…112

Figure 2.32. Temperature profile versus time for thermal spike …………...……………………...114

Figure 2.33. Ion strikes for a 1 μs dwell time by a 1 pA ion beam ………………………….……115

Figure 2.34. Color maps for a neon ion beam incident on the mask with nickel top layer (50 nm) and at the beginning of the etching process, showing the temperatures at different positions, including depth …………………………………………………………………...……………116

Figure 2.35. Comparison between 30 and 10 keV neon on the mirror structure ………………...119

Figure 2.36. Implanted concentration profile for neon ion bombardment at 5x10^{16} Ne^+/cm^2 123

Figure 2.37. TRIM simulations showing the ion ranges for 30 keV He^+ and the number of vacancies created as functions of depth ……………………………………………………………126

Figure 2.38. Evolution of individual implanted helium and defects leading to the formation of nanobubbles preferentially located in the amorphous silicon layer ……………………………….128

Figure 2.39. Evolution of individual implanted neon and defects leading to the formation of nanobubbles and ultimately Ostwald ripening ……………………………………………………133

Figure 2.40. Etch profiles at 50 KX for $5x10^{17}$ and $1x10^{18}$ Ne^{+}/cm^{2} ,,,,,,,,,,,,,,,,,,,,,,,,,,,,,,..,,,,,,,,,,,135

Figure 2.41. Plots showing the change in width and its slope as a function of milling depth and the redeposition percentage as a function of aspect ratio (h/w) …..………………………………136

Figure 3.1. Effect of dwell times on the stage current signals ……………………………….……..148

Figure 3.2. Effect of pixel spacing on the stage current signals ……………………………………149

Figure 3.3. Detector voltage and the stage current for the profiling of the EUV mask …………...152

Figure 3.4. Comparison between the growth of a pillar and the etch of a via ……………....…153

Figure 3.5. Voltage signals from the E-T detector for w=250 nm boxes etched on the EUV mask with (Ni-Ru-Mo/Si) and another without (Ru-Mo/Si) the nickel top layer …………………..………153

Figure 3.6. A dependence on box size, or width, found during etching of the EUV mask ……….154

Figure 3.7. Experimental and smoothed data using a moving average filtering method ………155

Figure 3.8. Currents present in a specimen during ion irradiation and the dependence of SE counts at the E-T detector on depth ……………………………………….…………………………157

Figure 3.9. Experimental and fit data for the Ni EUV multilayer structure ……………..……….159

Figure 3.10. Signals collected from the E-T detector for 29 keV He^{+} in c-Si substrates …………163

Figure 3.11. Measured data from the stage current for four c-Si box widths ……….……………165

Figure 3.12. Measured data and fits for four silicon box widths …………….……………………..165

Figure 3.13. Etch depth dependencies on time and dose for a silicon substrate ……………….166

Figure 3.14. Aspect ratios plotted against the neon ion doses for silicon …………………………166

Figure 3.15. Fits from figure 3.12, all plotted together for widths from 100 to 500 nm …………...167

Figure 3.16. Three different neon beam currents …………………………...…….……………..168

Figure 3.17. Three different neon beam energies ………………………………………………..169

Figure 3.18. Neon in silicon for different box sizes, beam currents and beam energies …..……170

Figure 3.19. Data for 29 keV He^+ in SiO_2/Si at three different beam currents ………………….…172

Figure 3.20. Data for helium in SiO_2/Si at two different beam energies …………………………..173

Figure 3.21. Stage current data for helium in SiO_2/Si ………………………………………………173

Figure 3.22. HIM image showing a dose study of Au etching by He^+ ……………………………175

Figure 3.23. NIM image showing a dose study of Au etching by Ne^+ ……………………..……175

Figure 3.24. A dependence on box size, or width, found during Ne^+ etching of Au ……………...177

Figure 3.25. Extended line fits showing the voltage levels that the E-T detector would register at different times, and corresponding doses and depths, for each component: Au and Si ……..…177

Figure 3.26. Experimental and smoothed data using a moving average filtering method ……....178

Figure 3.27. Experimental and fit ISE vs. Dose data for Ne^+ on Au/Si ………………………….178

Figure 3.28. Signals for Au/SiO_2/c-Si undergoing helium etching ………………………………..…179

Figure 3.29. Comparison between helium and neon etching of Au/SiO_2/c-Si ……………………181

Figure 3.30. Extended line fits showing the voltage levels that the E-T detector would register at different times, and corresponding doses and depths, for each component: Au, SiO_2 and Si ….181

Figure 3.31. Experimental and fit ISE vs. Dose data for He^+ on $Au/SiO_2/Si$ …………………....182

Figure 3.32. Experimental and fit ISE vs. Dose data for the neon etch of $Au/SiO_2/c\text{-}Si$ ……....182

Figure 3.33. HIM image for a dose study of helium copper etching ($Cu/SiO_2/Si$) ……..………184

Figure 3.34. NIM image for a dose study of neon in a copper structure ($Cu/SiO_2/Si$) …….……184

Figure 3.35. Responses for two different Cu top layer thicknesses when etched by He^+ ….……185

Figure 3.36. Responses for two different Cu top layer thicknesses when etched by Ne^+ ……….186

Figure 3.37. Comparison between helium and neon etching of $Cu/SiO_2/c\text{-}Si$ …………………...186

Figure 3.38. Experimental and fit ISE vs. Dose data for the neon etch of $Cu/SiO_2/c\text{-}Si$ …………187

Figure 3.39. E-T voltage and stage current for Ne^+ etching of a high-contrast structure ………189

Figure 3.40. Comparison between He^+ and Ne^+ etching of C/Au/C and two stage biases …...189

Introduction

Scanning Electron Microscopes (SEM) have been around since the 1960s. Processes relying on electron beam induced processing (EBIP) have been explored basically for the last 20 years. It has not been until the most recent 10 years that intensive research has taken place utilizing this novel method dubbed focused electron beam induced processing (FEBIP). Intensive research is ongoing in order to unravel the full potential of electron beams, while minimizing and even eradicating its disadvantages. At this moment electron beam induced deposition (EBID) by focused beams has gained notoriety as a localized method for creating three-dimensional nanostructures. In some cases, EBIP is used as erase for removal of material from a target, but it requires the chemical assist of a reactive gas. This is a direct result of the low mass of the electrons. An electron beam can be used successfully in nanolithography by reacting with a sensitive polymeric resist. Direct deposition or write processing by interaction with an electron beam is viable when using chemical vapor deposition precursors injected from a reservoir. After exposure, a pattern can be developed in the sub-100 nm range. Milling, on the other hand, is a more challenging feat with an electron beam.

Ion beam processing has been around for quite some time. Its main application found in the semiconductor industry where dopant atoms such as P and B are implanted in silicon to form n- and p-regions, respectively. More recently, focused ion beams using gallium (Ga-FIBIP), from a liquid-metal ion source (LMIS), have been used for both, additive (deposition) and subtractive (etching) processes. Milling or physical etching is made viable using ions because of their significantly larger mass and kinetic energy that can be transferred to target atoms in a substrate. Ga^+ (~70 a.m.u.) has shown substantial advantages in milling, but it also has liabilities. In many cases, the “heavy” gallium atoms can introduce collateral damage into a sample. The prime

example is found in TEM sample preparation or thinning processes, where, if not enough care is observed, the final sample may easily be quite different from what was the original sample. Changes in the specimen can arise from implantation, extensive defect concentration, amorphization, heating and gallium-containing intermetallic compound formation. The natural progression in this technology has then been to move away from Ga^+ and towards chemical species that would not react with the specimen and that may introduce minimal damage and heat. This is when light unreactive gases such as helium and neon have come into the forefront by showing great promise for nanotechnology's full implementation.

A new kind of microscope was introduced by Zeiss Microscopy in recent years (2006). The Helium Ion Microscope (HIM) initially intended for superior imaging, has become the new crucible for deposition processes, by having a Gas Injection System (GIS) added to the apparatus. Helium (4 a.m.u.) is outstanding for imaging since its mass is greater than an electron where upon striking the sample it releases a barrage of useful secondary electrons. Nevertheless, helium has much smaller atomic mass than gallium, making any milling process impossible or very time consuming. Its principal benefit is that it does not chemically react with the specimen, although in many instances, nanobubble formation has been reported. Careful adjustment of parameters such as acceleration energy and beam current is mandatory. He^+ has already proven to be quite useful in implantations of materials where scientists seek unit cell expansion in order to study strain effects on a variety of properties such as electrical, optical or magnetic. At this point it would be trivial to recognize that the next logical step forward is the deployment of neon (10 a.m.u), since it has greater mass than the electron and helium, but less than gallium. Add to this the fact that it is also inert like helium. Therefore, neon presents itself as a prime candidate for ion beam nanoscale synthesis. Its benefits will reside somewhere in between what the very light helium and what the "heavier" argon (36 a.m.u.) have to offer.

Neon ion beam technology is currently under development and a wave of new possibilities are opening up as ion microscopes, employing a gas-field ion system (GFIS), are made capable of handling this gas. Ne^{+} offers the superb advantages of material modification without contamination, and of nanostructure deposition or removal in relatively short process times. As more is known and understood, trenches and holes can be patterned more precisely and deposits made purer. Predictive simulations such as SRIM/TRIM and EnvizION are playing an essential role in characterizing and understanding the many competing mechanisms present in neon-beam induced depositions or etching. Focused neon ion beam deposition can ultimately make possible an era of advances in extreme-ultraviolet (EUV) mask repair and editing by enabling very localized, nanoscale additions or subtractions of material in order to extend the useful service life of costly devices such as EUV masks used for IC manufacturing. In order to be implemented for this use, careful characterization of subsurface effects and damage must be undertaken. Heating considerations must also be taken into account. Additionally, recovery or healing strategies need to be developed in order to live up to the full promise of this method.

Chapter 1:

Electrical Characterization of Laser Assisted Electron Beam Induced Deposition and Focused Ion Beam Induced Deposition of Nano-Wires

Summary

Tungsten nanowires (NWs) 1.5 um long ~ 300nm wide and ~300nm thick synthesized via laser-assisted EBID (or LA-EBID) have been prepared in an FEI Novalab 600 dual beam electron and gallium ion microscope with a gas injection system (GIS) at the Center for Nanophase Sciences (CNMS) at Oak Ridge National Laboratory (ORNL). The precursor gas was tungsten hexacarbonyl, or $W(CO)_6$. NWs of platinum from trimethyl (methylcyclopentadienyl)platinum(IV) ($MeCpPtIVMe_3$) and from cobalt from $Co_2(CO)_8$ have been synthesized in an Orion HIM in the Zeiss Microscopy facilities. Electrical measurements by two- and four-point probe methods were undertaken in the Science & Engineering Research Facility (SERF) at The University of Tennessee-Knoxville. The results indicate that in all cases carbon, likely in the form of amorphous carbon, remains embedded in the structure. However, it has been possible, via laser assisted electron beam induced deposition (LA-EBID), to have the resistivity for W deposits be as low as 219 $\mu\Omega$-cm (40x bulk value). Pt deposits via He- and Ne-BID Pt had resistivities as low as 600 $\mu\Omega$-cm. Finally, cobalt deposited via He-BID resulted in the lowest resistivities of 50-100 $\mu\Omega$-cm (only 10x bulk). EDXS data from a Genesis x-ray microanalysis unit leads to the conclusion that LA-EBID has enhanced the metal contents to ~55 at % W. Similarly, Pt deposition via Ne-BID confirms its advantages when compared to He-BID, Ga-BID and EBID by improving purities, nanograin sizes and resistivities.

Literature Review

Electron and ion beam induced deposition is basically a highly localized chemical vapor deposition (CVD) process assisted by the electron or ion beams. In both, electron- and ion-beam processes, primary electrons and ions and the subsequent generation of secondary electrons (SEs) are responsible for ligand or bond rupturing in complex precursor gas molecules. SEs have energies ranging up to 50 eV. However, 90% of all SEs have energies below 10 eV (see figure 1.1a). Most bond dissociation energies lie within this range. For example, and to list a few: C-C (3.60 eV), C-H (4.25 eV), O-H (4.77 eV) and O=O (5.15 eV), Pt-C (6.0 eV), Ru-C (6.7 eV) and Ru-Ru (2.0 eV). Some gases of relevance to focused beam induced processing have the following enthalpies of formation: $W(CO)_6$, 1.47 eV; $Ru_3(CO)_{12}$, 1.38 eV, XeF_2, 1.12 eV. Again, all these remain within the range of energies for SEs. More specifically, only for ion beams, the stopping powers or energy losses to the target material will be both, electronic and nuclear, and not only electronic type interactions as in an electron beam. How these two apportion themselves will be governed mainly by the masses of the ions and target atoms, the ion energy and the density of the target atoms (see figure 1.1b).

(a) (b)

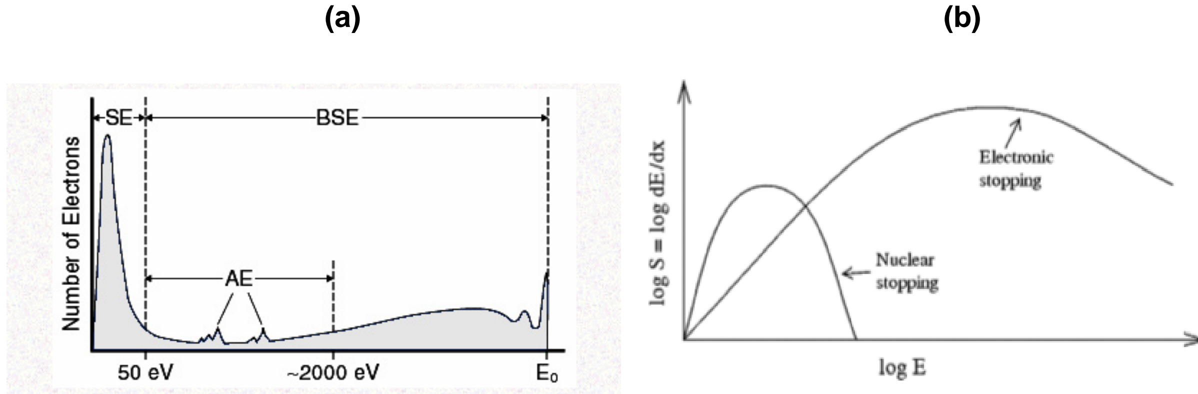

Figure 1.1. In a), the energy ranges for SE, AE and BSE electrons with respect to the primary beam energy [1], and in b), energy losses for ions due to nuclear and electronic interactions [2].

Several individual processes collaborate during the growth of a three-dimensional (3D) nanostructure. First, there is the molecule-solid interactions consisting mainly of surface diffusion, adsorption and desorption. Secondly, the electron (or ion)-solid interactions where the beam is focused on the substrate unravelling a series of elastic and inelastic collisions and energy transfer steps. Thirdly, electron (or ion)-molecule interactions where a charged particle with sufficient energy induces the scission of a bond in a precursor molecule. It takes only a few eV to produce this dissociation, but the probability is determined by the energy-dependent molecular cross-sections. The later can occur for instance by vibrational excitation, electronic excitation, dissociative electron attachment, neutral dissociation, dissociative ionization and bipolar dissociation [3]. The above interactions can lead to two important growth regimes: 1) where growth is electron or reaction rate limited, and 2) precursor-limited, where growth is limited by the arrival of molecules reaching the irradiated area. The following equation governs the above mechanisms present during a deposition assisted by an electron- or ion-beam:

$$\frac{\partial n}{\partial t} = s J \left(1 - \frac{n}{n_0}\right) + D \left(\frac{\partial^2 n}{\partial r^2} + \frac{1}{r}\frac{\partial n}{\partial r}\right) - \frac{n}{\tau} - \sigma f n,$$

where s is a sticking probability, J the precursor gas flux, n is the number of surface sites occupied by molecules (n_0 being the total number of sites on the surface), D is the diffusion coefficient, τ is the residence time and σ is the dissociation cross-section for the molecules [4]. The first (adsorption) and second (diffusion) terms are positive because these involve mass infusion, while the last two (desorption and dissociation) are negative since these involve mass extraction (refer to figure 1.2).

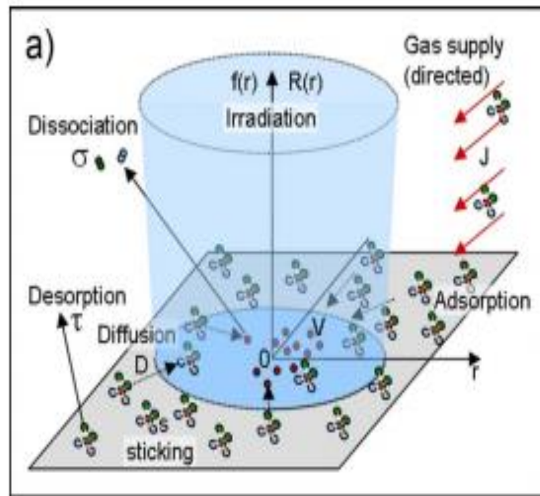

Figure 1.2. Depiction of mass transfer mechanisms involved in the deposition process [5].

There is a delicate interplay that must be maintained in order to get the best coverage possible. Each molecule shall be adsorbed onto the substrate surface and adhere to it for a short time. However, it is counterproductive for this molecule to leave the surface too soon so a maximum residence time is desired. While sticking on the surface the molecule will be subjected to electron strikes with energies sufficient to break the bonds in the molecule. If the cross-section is large enough for one of these energies there is a higher probability that the bond will be broken.

Typical dissociation cross-sections, $\sigma(E)$, are 10^{-3} to 10^{-2} nm^2 [3]. It has been reported that for $Ru_3(CO)_{12}$ at 40 keV, the cross-section is $2x10^{-17}$ cm^2 (or 0.002 nm^2) while for $W(CO)_6$ at incident electron energies between 2 keV-20 keV, the cross-section is lower and in the order of 0.5-$1.5x10^{-18}$ cm^2 [6]. Rosenberg et al reported that at a primary electron beam of 500 eV, the cross section for $W(CO)_6$ can be as high as $6.50x10^{-16}$ cm^2 [7]. Values obtained from experimental measurements of FIB deposition speed by Rudenauer et al [8] for cross-sections are $3.85x10^{-16}$ and $3.25x10^{-17}$ cm^2 for Pt and W, respectively. Similarly, van Dorp et al [6] reports that for $MeC_pPt(IV)Me_3$ from 20 to 20 keV, the deposition yield increases up to 150 eV, but then decreases for energies beyond 150 eV (as shown in figure 1.3). It can be inferred from this finding that the largest cross-section corresponds to a primary beam energy of ~150 eV. This decomposition mechanism will result in volatile fragments that can be extracted via the pumping system and fragments containing the metal or element one wishes to deposit remaining on the irradiated surface. The expected results would be for the metal to be deposited alone and not bonded to any other carbon hydrogen and/or oxygen atoms. In reality this has been difficult to achieve, and deposits remain relatively rich in carbonaceous, organic and oxide residues, that typically form an amorphous matrix where the metal particles, in many instances, grains or crystals, remain embedded. The deposition rate, or speed, needs to be a compromise between shorter process times and the quality of the deposit. The optimum beam voltage and current depends on the type and flux of precursor molecule and its cross-section. For example, one ion-beam study revealed an optimum growth efficiency possible with a 300 pA beam current [8]. Any lower will reduce the efficiency and be electron-limited, while any higher will result in material removal or erosion via sputtering (figure 1.4). This peak can be tuned and shifted with other accelerating voltages or beam energies. Generally, lower beam currents are good for ion deposition processes while larger currents will do a superior job at etching a substrate. It is noteworthy mentioning that we do not want for precursor-limited conditions where too many electrons or ions in the principal beam can end up eroding or sputtering away part of the deposited material. Even though counterintuitive, in

the case of helium or neon ion beams, it may be favorable to have some erosion take place, because the carbon in the deposit may be ejected preferentially, which may lead to a higher metal concentration.

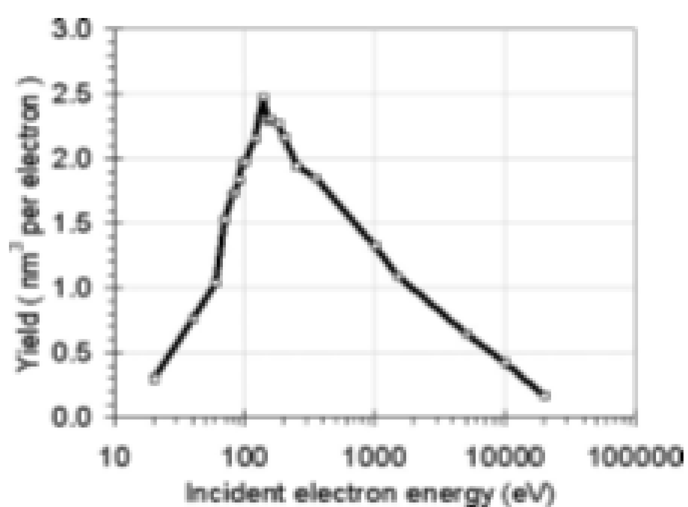

Figure 1.3. Deposition yield as a function of beam energy for the $MeC_pPt(IV)Me_3$ molecule [6].

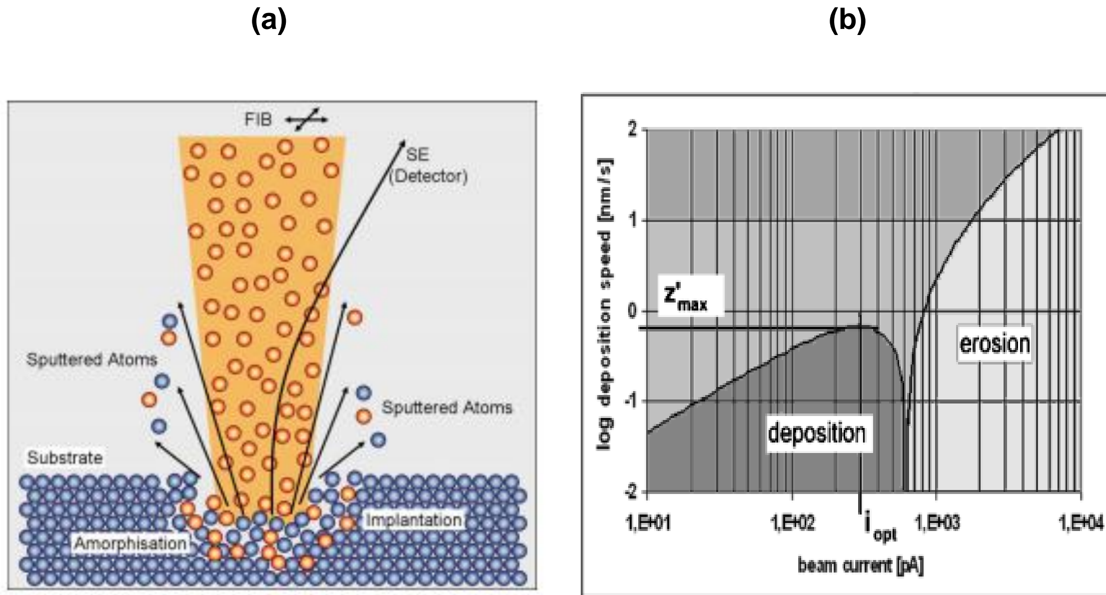

Figure 1.4. Principle of FIB milling or etching in a) [4], and the dependence of deposition rate on the beam current at constant spot size in b) [8].

The amount of generated secondary electrons that reaches the surface plays a major role in the deposition rate. De Teresa et al [9] has determined that the volume per dose is a function of beam energy. In Pt FEBID it has been found that at 30 kV the volume per dose is four times lower than at 1 kV. The vertical deposition rate can be expressed as per the formula below:

$$\mathbf{R} = \int_{0}^{\mathbf{E0}} \mathbf{f(r,E)}\,\boldsymbol{\sigma}\mathbf{(E)}\,\mathbf{N}\,\mathbf{dE}$$

where E_0 is the energy of the primary electrons, f(r,E) is the electron flux, σ is the electron-impact dissociation cross-section, and N is the molecular density on the surface. The cross-section shows a maximum at a particular energy which is typically well-below 1 keV. For example, the molecule C_2H_5 used to deposit graphene has a maximum cross-section at 18 eV [9]. Quite

interestingly, for FIBID of Pt using Ga^+, the reverse of FEBID is true. De Teresa et al also found that the volume of secondary electrons per dose increases with increasing beam energy. This can be rationalized by a larger amount of secondaries generated that reach the surface as a result of 30 keV gallium ions which are stopped just 50 nm below the surface. 30 keV electrons penetrate deeper into the substrate leading to lower SE density at the top surface. On the other hand, the volume per dose decreases with current. At 10 kV, a 50% higher volume per dose is obtained at 50 pA compared to 2.6 nA. This can be explained by a lack of full replenishment of the precursor molecules adsorbed on the surface at high beam currents [9].

Ubiquitous deposits to date are in the form of nanowires (NW) and made of most commonly W, Pt, Au, Cr, Co, etc. The NW configuration is favored in order to allow for 4-pt probe dc electrical testing of the structure. There is undeniably a direct correlation between resistivity and composition (or purity) of the device. While metal conductors are vital to the continuation of this technology, other compositions have also been deposited by these methods, especially silicon oxide (via the tetraethylorthosilicate or TEOS precursor). While nanostructures with very high insulation resistances have been achieved for SiO_2, NWs with bulk value resistivities still remain to be seen. Most commonly, and to date, composite structures represented by metallic crystallites embedded in an amorphous carbonaceous matrix, have been the results of EBID and IBID processes. Many in-situ and ex-situ annealing processes have been attempted, but the resulting purities, while better, do not match the bulk resistivity for the metal conductor. Recently, several promising attempts have been made in improving the purity of Pt deposits by using O_2 as carrier and reactive gas. Oxygen is far more effective in removing carbon from the deposits as these grow, while in tandem, Pt has very good oxidation resistance. This cannot be said of most metals where oxygen treatment would need to be followed by a hydrogen anneal. For Pt, the deposit purity relates to two beam parameters; the beam current and the beam energy. A perilous balance is observed in order to improve carbon removal from the deposit, as demonstrated by especially higher beam currents. When current and voltage are converted into a beam power per

unit area, there appears to be a threshold where the Pt content in at. % appears to level or saturate at a purity of only ~16 at. % because of the presence of stable carbon by-products [10].

Variation of beam parameters and deposition conditions along with several in-situ and ex-situ post treatments have been studied in order to attain nanostructures with higher purity. These can be found in a review publication by Botman et al [11]. Among the deposition parameters that can be varied are: higher beam current, slow speed scan, multiple high speed scans, vary dwell time, vary beam defocus, vary beam energy, vary gas injection nozzle position and do post-irradiation with e-beam of different durations. The results varied from “no effect” to in some cases lower resistivity, higher metallic at. % and larger metal crystallites. Most ex-situ treatments involved annealing up to 500°C in O_2 or hydrogen. Consistently, Pt improves its purity after treatments in oxygen. A technique worth mentioning is the exposure of the structure to a high voltage beam (~80 kV), as in a TEM, in order to increase crystallization and reduce resistivity as it was observed also for Pt. In-situ processing is more attractive since the sample does not have to leave the vacuum chamber. Unwanted exposure to air and other contaminants is thus prevented. These include when a dual beam system is available, exposure to low dose gallium beam resulting in one order of magnitude lower resistivity. However this could be due to gallium implantation ($\rho \sim 27\ \mu\Omega$-cm), but more likely to heating caused by the ion beam, or possibly the preferential sputtering of carbon atoms by gallium. Current-induced purification is another attractive concept. Joule, self-heating induced by sufficiently high currents could improve the conductivity of the deposit. Post-irradiation with electrons has in some cases improved the crystallinity of deposits that were initially amorphous. Once again, this is observed in platinum deposits. In an ESEM, where water vapor can be injected in the presence of an electron beam, the carbon content can be reduced by forming CO and possibly CH_4 molecules. The ultimate way of reducing carbon contents is by using carbon-free precursors. However, some of these can greatly affect the normal operation of the chamber.

Beam induced processing at high temperatures is an intriguing option, but involves limitations. Common sense suggests that higher temperatures during deposition would lead to purer deposits. However, this is precursor-dependent. Diffusion on the substrate surface is of course strongly dependent on temperature. In beam-induced depositions due to the proximity of the irradiated area and the gas flow, the distances are not too long thus leading us to believe that infrequent short hops may be sufficient to land a complex molecule in the right place for dissociation and desorption. More importantly, the residence time of fresh arrivals on an available site on the surface is a vital parameter that needs to be kept relatively long (in μs to ms). Higher temperatures will have a tendency to reduce these adsorption times and allow for a higher number of unfragmented molecules to leave the surface therefore reducing the growth rate. It is also true that as a deposit builds up diffusion of precursor molecules to the region of interest contributes to the precursor coverage. It is not desirable to have these molecules adhere on deposit sidewalls and compromise the lateral resolution.

Below, table 1.1 lists several important parameters corresponding to a pure, bulk sample of the materials of interest in this investigation.

Table 1.1. Several properties of interest for materials involved in the dc electrical study.

Material	**A (g/mol)**	**Density (g/cm3)**	**T_m (K)**	**ρ @20°C ($\mu\Omega$-cm)**	**α (K^{-1})**	**κ (W/m-K)**	**CTE (μm/m-K)**	**C_p (J/mol-K)**
W	183.84	19.25	3695	5.28	0.0045	173	4.5	24.27
Pt	195.08	21.45	2041	10.5	0.0039	71.6	8.8	25.86
Co	58.93	8.90	1768	6.24	0.0066	100	13.0	24.81
Au	196.97	19.5	1337	2.21	0.0034	318	14.2	25.42
Cr	52.00	7.19	2180	12.5	0.0030	93.9	4.9	23.35
a-C	12.01	2.2	3800	3500	-0.0005	0.3-10	1.5	6.0

Experimental Methods

LA-EBID NWs were received from CNMS and from Zeiss Microscopy (He-BID Pt and Co, Ne-BID Pt) for electrical analysis. These were deposited on photo-lithographically patterned electrodes of Cr(10 nm)/Au(100 nm) on SiO_2(100 nm)/Si substrate with four narrow interdigitated gold strips (500 nm wide) and 500 nm apart leading to larger probing pads (200μm x 200μm) for micro-probing. The NWs were usually 1.5 μm long with a cross section of around 300nm x 300nm. These had been deposited by LA-EBID for W-C-O, and by using He- and Ne-IBID for Pt-C and He-BID for Co. The precursors used in the GIS were $W(CO)_6$ for W, $MeCpPtIVMe_3$ for Pt, and $Co_2(CO)_8$ for Co. Simplified drawings of these molecules are shown below in figure 1.5. Two- and four-point DC electrical tests were made on all the samples in order to determine the sample resistivities. A Keithley SGS-4200 Analyzer was the instrument of choice. A vacuum chuck equipped micro-probing station mounted on a granite table was utilized for the study. The setup was also enclosed in a dark cabinet to eliminate any possible effects from room light or surroundings. The probing tips used were Signatone's SE-TB (tungsten, 25 μm). Sweeps of initially low voltages up to 1 mV, and when appropriate to 1 V and then 20 V were made in order to generate I-V curves, from which to determine the resistance, and then the resistivity by knowing the geometry of the nanowire. For the 4-point probing tests, the force current sweeps were started at low currents: typically up to 100 nA, 1 μA, and then lastly 10 μA when appropriate. The objective was to find relatively smooth and monotonically increasing responses representative of Ohm's law. However, not all ranges behave the same for the nanowires and various sweeps were undertaken to record the best data set possible before inducing any catastrophic failure. In many cases, the nanowires were destroyed or as in others, the test structures underneath the nanowires showed static discharge related failure. Relevant properties such as hysteresis, repeatability

(back-to-back sweeps), contact resistance, 2- versus 4-point probing were evaluated to ascertain the best procedures or protocols to measure the nanowires.

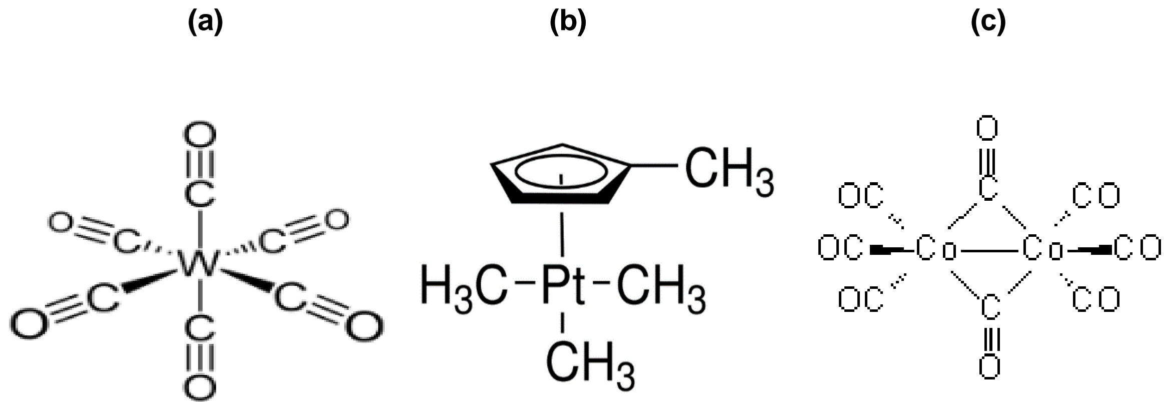

Figure 1.5. Depiction of molecular structures with ligands for $W(CO)_6$ in a), for $MeCpPtIVMe_3$ in b), and for $Co_2(CO)_8$ in c).

Results and Discussion

NW DC Electrical Measurements Review.

Using small test structures with narrow lines involves dimensional measurement accuracy challenges, which result in lower accuracy in the data (we will also have to elucidate scaling effects on resistivity as surface/interface scattering at the nanoscale is known to increase intrinsic resistance). Conversely, larger test structures (and deposits) improve the accuracy of the dimensional measurements and thus lead to more accurate resistivity values, however at the cost of longer depositions times. Thus, for coarse IBID parameter determination, smaller test

structures are convenient as deposition times are shorter. When optimum deposition parameters are determined, larger deposits using test structures with larger electrode spacing will improve the accuracy of the measurements.

In general, 2-point probe testing is much more convenient and less time-consuming than 4-point probe testing. Undeniably, the main advantage of the 4-point probe test is that it eliminates contact resistance, thus directly measures the deposited structure resistance. In figure 1.6, the 2-pt and the 4-pt testing of nanowires is compared on the test carrier. At this point we need to determine the order of magnitude of the contact resistance so we can determine what resistance values we need to be concerned with for the contribution of the contact resistance (importantly this may also vary depending on the deposition process). We used the contact resistance structures that were fabricated to compare for instance the contact resistance for Ga^+ deposited W and Ne^+ deposited Pt. After the general order of magnitude of the contact resistance is determined, we can discern when 4-point probe testing is important to determine the absolute value of the deposited resistance. A protocol for 2-pt probe testing involved the following steps:

a. Determining resistivity range by doing an initial voltage sweep from 0-1mV in 10μV increments with an initial 1μA compliance.
b. If current is not greater than $\sim 10^{-11}$-10^{-12} A range then re-test with higher voltage sweep (increasing in decade magnitude increments) until measureable current value and resistance can be obtained.
c. Determine saturation behavior and obtain saturated resistance
    i. For high resistance samples – as-possible increase voltage until the voltage versus resistance value saturates
    ii. For low resistance samples – increase current compliance one order of magnitude at a time (and if necessary the voltage range) to obtain a constant voltage versus resistance.

d. If low resistance is obtained and on the order of the contact resistance perform 4-point probe tests with comparable current value forces as those obtained with the saturated 2-point test.

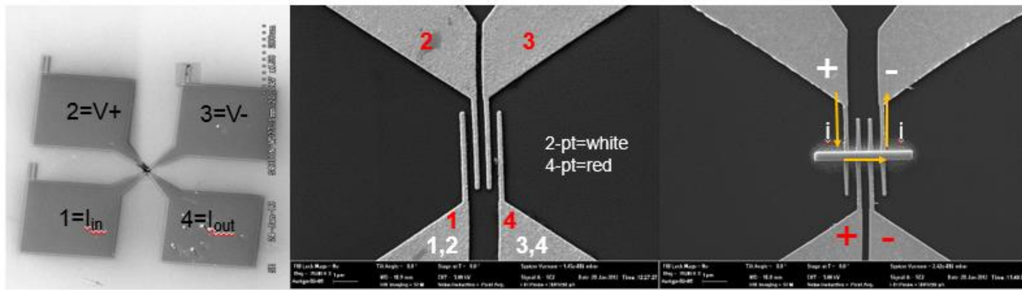

Figure 1.6. 2-pt and 4-pt testing of nanowires on one representative test structure. Probing pads and connections show flow of current and voltage sensing.

Dimensionality issues may arise as devices become even smaller introducing new effects by already well-understood stimuli which may impact conductivities (electrical or thermal) in new ways. Novel deposition and annealing methods inherently carry several limitations; one of which being the content of carbonaceous residues originating from the gas precursors. No metallic nanowire deposited via EBID or IBID is 100% pure. Therefore, as indicated by data collected in these experiments, the electrical conductivity within the nanowire is not optimal. It has been observed that during a test run, the I-V response is rarely smooth, thereby containing transitions and typically more than one region of significant interest. Some sporadic data points in a study may show much larger resistance than the rest, which may themselves form a relatively tight distribution. Ultimately, from within each group, the best sample was selected to represent the real viability and feasibility of high purity deposits in future studies.

Several distinguishable modes have been unveiled. Typically, for NWs with relatively low resistance, the I-V curves are smoother and noise free. Others, typically those with larger resistances, show fluctuations and some instability. In this case, the resistances have been observed to initially drop for larger electrical forces, as sweep voltages increase for a 2-pt probe test, or similarly where sweep currents increase for a 4-pt probe test. However, in these high-R NWs, further testing is often impossible after the first test, since they fail and then show responses indicative of an open-circuit condition.

In a consistency or repeatability test, one NW was subjected to five (5) consecutive sweeps without removing any of the probing tips, then after a ten (10) minute wait, the experiment was repeated. The findings indicate that the results remain fairly steady for the first set, but after the ten minutes, the resistances had dropped notably by two-orders of magnitude, before returning to the original range in the last three (3) sweeps. This raises questions about the consistency and repeatability of the results. At this moment, it can be assured that, in general, the results are going to be consistent for a sweep at lower voltages (for 2-pt probing) and at lower currents (for 4-pt probing) as long as the nanowire is not cycled multiple times.

This leads to an inherent weakness still present in NWs made as part of this study, and it all can be traced back to these being composites of two mismatched materials; namely, metal and amorphous-carbon coexisting in a fragile balance within the structure. As we will find out later, the test carrier also could have a strong effect on the reliability and survivability of the nanowires. It has been observed that the NWs exhibit an ability to undergo self-annealing, or current-induced annealing. This is supported by changing slopes in some I-V curves. These slopes (the resistance) show a tendency to decrease as the applied voltage rises. This effect can be clearly observed in the R-V plots since the response may not be flat or horizontal, and linked to a Joule-heating effect.

For one set of samples, a 2-pt and 4-pt probing comparison, was undertaken to elucidate how big a difference contact resistances may introduce in the measurements. In a comparison for eight (8) NWs, in general (most cases, except one), a drop of ~100-200 Ω is observed when switching from 2-pt to 4-pt. It was concluded that for high resistance NWs, 2-pt probe measurements (simpler setup) would suffice. The 100-200 Ω added resistance will not matter when measuring a sample of high resistance two or more orders of magnitude greater. However in the case, where the NWs would be of relatively low resistance, more specifically below 20 kΩ, then the 4-pt probing was the method of choice. Moreover, in order to improve the contact area between the micro-probing tips and the test pads, the larger Signatone SE-TB (width=25 μm) probes were selected.

LA-EBID Overview.

Laser-assisted EBID, or LA-EBID, is an in-situ method developed by our group to anneal EBID nanostructures as they are deposited. The diode laser used is infrared with a wavelength of 915 nm (1.36 eV) with up to 20 W optical power output. The control unit employed is DEI's PCX-7410 laser diode driver/current source (rated at 10A). The laser pulses are transmitted from the laser diode outside the chamber through an optical fiber into the Opto-probe assembly (mounted on a chamber port) that is a conduit for the optic fiber to the microlens inside the vacuum chamber. The microlens is ~ 6 mm in diameter with a ~ 9 mm working distance above the sample surface and is mounted at a 52° inclination (relative to the substrate). When focused on the sample, the irradiated area is slightly elliptical with an average radius of 50 μm (±20%). The pulse width can be varied from around a microsecond to seconds in duration. This corresponds to a maximum irradiance of ~186 kW/cm^2. The in-situ annealing in this case is likely going to be by pyrolysis, due primarily to heating. However, it must be kept in mind that many metallic surfaces are up to

70% reflective at this wavelength and a fraction of the laser intensity will not necessarily be absorbed in the sample. Carbon, on the contrary, reflects about 26% of the incident intensity. Refer to figure 1.7 below for diagrams showing the microlens and the pulsing of the laser with respect to the precursor gas pulses in the vicinity of the sample surface. The laser irradiation was applied during the refresh part of the cycle (beam spot parked away from region of interest) and was controlled by a Raith patterning software.

(a) **(b)**

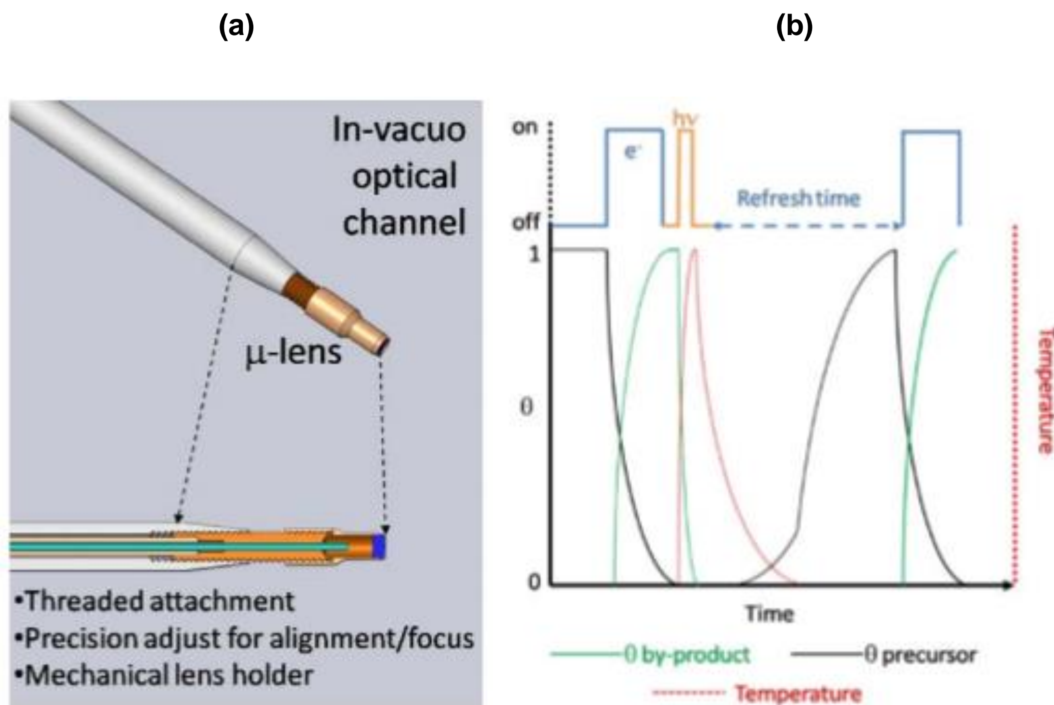

Figure 1.7. (a) Microlens positioned at the end of the fiber optic mounted on the Opto-probe assembly. (b) Idealized schematic depicting deposition process via EBID where precursor gas pulses are followed by a short laser pulse after each pass.

W NWs Made Via LA-EBID.

Recently, it has been documented that CVD decomposition of $W(CO)_6$ at 375 °C yields ~80 at.% purity for W. This can be attributed to the outgassing of deposition by-products, other than stable carbon, that were embedded in the structure. More specifically, unfragmented W(CO)y molecules that became part of the final deposit prior to an anneal step. In spite of higher purity, their corresponding resistivity was measured at above 1000 $\mu\Omega$-cm. On the other hand, annealing at 900 °C (0.25T_m for W) in vacuum produced a deposit with ρ~10-19 $\mu\Omega$-cm. Nevertheless, it must be mentioned that the above are not highly-localized depositions. Highly-localized EBID alone typically produces deposits with high resistivity. Therefore, it is imperative that appropriate annealing schemes, especially in-situ, are developed and integrated in order to realize high electrical conductivity metallic nanowires.

In this study, WC_xO_y NWs were processed using electron doses ranging from $3.13x10^{15}$ to $6.88x10^{17}$ e-/cm^2. A maximum power density by infrared irradiation delivery of ~186 kW/cm^2 was implemented. The laser pulse widths ranged from 0.1 to 25 μs in duration. These correspond to delivered energies per pulse (or per loop) of ~1.5 μJ up to 375 μJ. These pulses are synchronized with the electron beam pulses so that the laser delivers as soon as each electron loop has been completed. The laser is expected to raise the local temperatures significantly higher, especially owing to the low thermal conductances of the composite, the SiO_2/Si substrate and the vacuum conditions present.

As a result of the depositions, it has been found that the concentration of W decreases with e- dose per cycle due to increments in the growth rate per loop. When the thickness is higher, the effectiveness of the laser pulse appears to be reduced. At higher doses, on the other hand, enhanced purification can be observed where further decomposition of CO ligands in $W(CO)_6$ or its fragments such as $W(CO)_y$ (where y=1-5) proceeds unabated. A decreasing LA-EBID W purity

has been found for longer dwell times, which can also be linked to the disadvantage of faster per loop growth rates. The optimized growth rate for W has been approximated to be at 0.1-0.2 nm (or ½ to 1 monolayer).

Tungsten nanowires were characterized via 4-pt probing. DC electrical measurements up to 10 μA were performed in a region where the resistance data remains nearly constant and flat. The voltage drops across the tungsten nanowires were found to be present within a small range for those structures treated with the laser and at a much higher values for those untreated (EBID only). The resulting resistances were calculated at 4-1347Ω for the same geometry, but also dependent on the bias current (0.1-10 μA). At 10 μA, it is clearly inferred that the longer the laser beam stayed on for each deposited layer, the lower the resistance, and consequently the resistivity. However, the 0.1 μs long pulse appears to be too short. In all cases, there is a substantial difference when comparing with untreated nanowires. The tungsten deposits approach a lower limit in resistivity for the longer laser pulses (10, 25 μs). However reaching as low as the bulk resistivity for W, may be limited by: the formation of WC, with has nearly 10x the resistivity of pure W; WO_x (x=2,3) with high resistivity, and a-C, with a resistivity of at least ~1000 $\mu\Omega$-cm (graphite).

A set of six (6) deposits was measured and found to have some common and outstanding trends. First, as shown in figure 1.8, the laser-treated nanowires exhibit lower resistances than the untreated, or the as-deposited, nanowire. The difference is significant by at least two orders of magnitude. For the 10 and 25 μs laser-pulsed NWs, the resistances, and thus the resistivities [using ρ = [(A/L) R] are the lowest. It was determined that 0.1 and 1 μs may be too short of an exposure, which may not raise the temperature high enough to maximize the expected in-situ annealing effects by outgassing the previously condensed and incorporated by-products. Figure 1.9 shows the Log R vs. I responses for EBID and LA-EBID NWs between 10-100 nA. Here, a

current-induced annealing effect via Joule heating can help explain the changes observed in annealed vs. un-annealed samples. It was Reguer et al [12] that previously reported on Ga^+ W NW electrical modification by the Joule effect. In the next figure (#1.10), the W EBID and LA-EBID (at 10μs) samples are plotted together and compared with the target resistivity for pure W at 5.28 μΩ-cm. At 100 nA, the laser-treated NW exhibits resistivities less than two orders of magnitude above that of the target bulk value for tungsten. This constitutes a substantial improvement in the quality of the structure. Generally speaking, this study demonstrates the advantages of in-situ annealing and purification of NWs via the infrared laser pyrolysis.

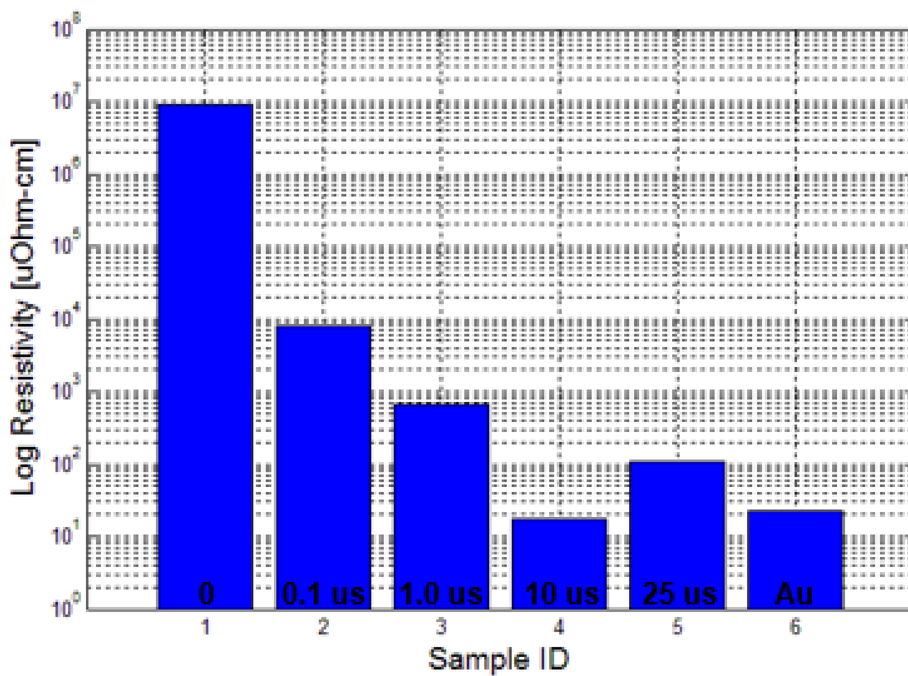

Figure 1.8. Bar plot showing the relative resistivity calculations for the six (6) samples measured at 10 μA.

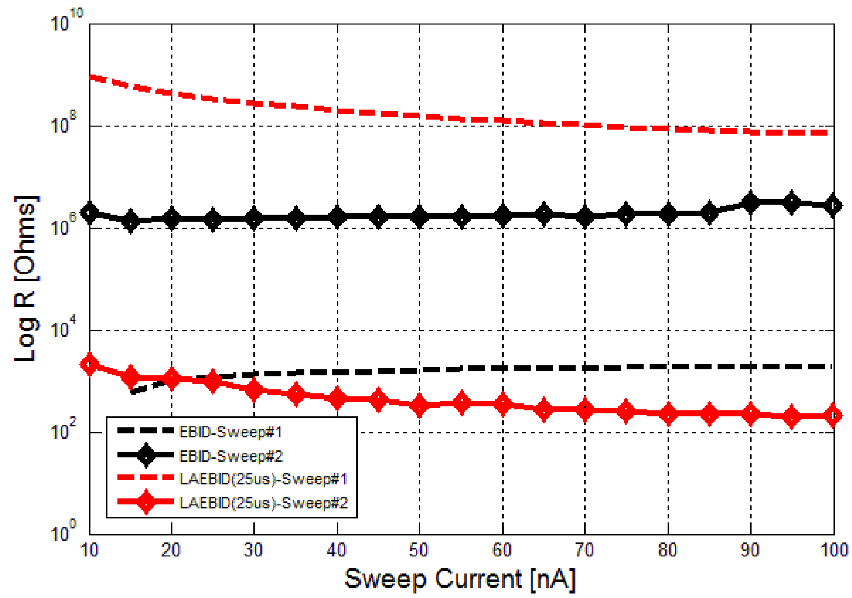

Figure 1.9. Resistance data comparing a non-irradiated W NW versus a laser-treated W NW on two consecutive sweeps. Note that the EBID NW has the tendency of moving to a high-R mode, while the LA-EBID NW appears to be healing, possibly via Joule heating.

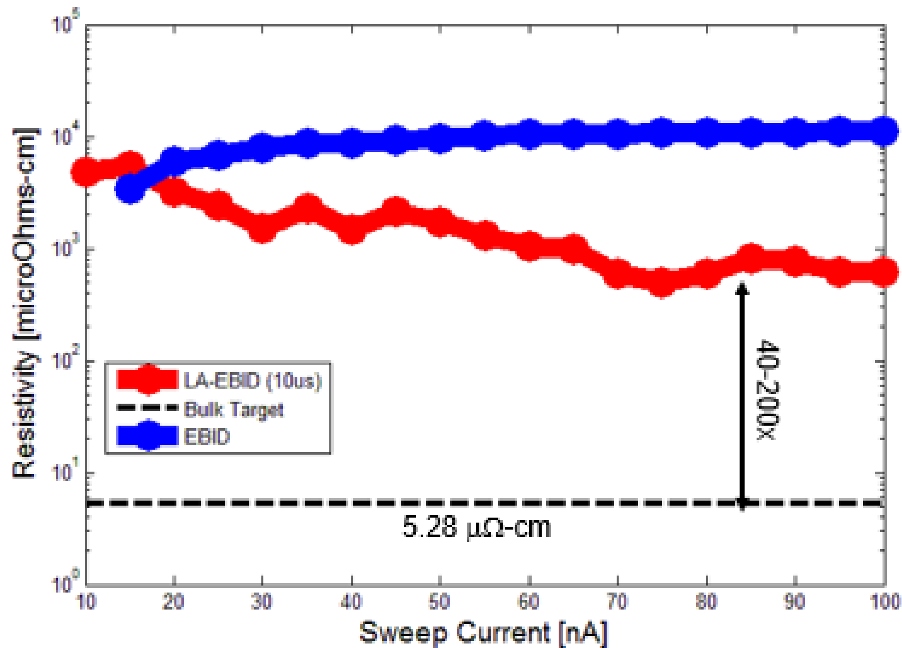

Figure 1.10. Plot showing the resistivity of an EBID and LA-EBID W NW from 10-100 nA and compared with the target bulk resistivity for tungsten.

In order to assess the uniformity and homogeneity of the tungsten nanostructure each adjacent segment of the nanowire, with equal lengths, was measured by 2-pt probes contacting the appropriate test pads. The results show a very consistent response, indicating that the NW was electrically, and indirectly geometrically and compositionally, homogeneous, all across its 1.5 μm length (refer to figure 1.11a). Another 2-pt test was performed in order to understand the effect of the contact resistance between the narrow gold electrodes, connected to the square test pads, and directly underneath the nanowire resting atop this test carrier. The results indicate that as the NW length increases, from 0.5-1.5 μm, a clear trend upwards, as expected, but with a near-constant series term between them, attributed to the contact resistance (see figure 1.11b). This total contact resistance has been estimated at 9.87 Ω, from a straight line fit extrapolation to zero NW length, as shown in figure 1.12. Since this R_C represents two contacts with the NW during the

2-pt probing test, the resistance per contact is half, 4.94 Ω. What this demonstrates is that the connectivity and condition of the interface between the NW and the Cr/Au electrodes is physically continuous and smooth, henceforth introducing into the measurements an undesired, yet not-so-significant, series parasitic resistance. As long as the resistance of the nanowire itself is much higher than this contact resistance the effect of the contact resistance in a 2-pt test will be minimal. Moreover, a specific contact resistivity can be determined by multiplying by the contact area. This results in 0.0074 $\mu\Omega$-cm^2, which is characteristic of a metal-on-metal contact (<0.01 $\mu\Omega$-cm^2). A current of 10 μA was inferred to be a testing upper limit before destroying the device. Most failures of LA-EBID are observed at higher current ranges at ~10 μA. This leads us to believe that laser pulsed tungsten deposits can withstand current densities up to 1.1x10^4 A/cm^2. This is considering the active cross-sectional area for conduction is the entire 300 nm x 300 nm of the nanowire. We know this is not true; first, because from EDXS data it appears that the NW is ~55 at.% W, thus not the entire cross-section may be a conductive path, and second, even if W is near 55 vol. %, the conductive path may consist of a narrower track of well-connected W nanograins; while the rest of the W may be part of less conductive phases such as WC, WC_2, WO_2 or WO_3. This leads to the possibility that the current density 'ratings' for the W NW could be higher, if not for the impending failure arising from the inability to cool the metallic path of least resistance that is surrounded by a thermally relatively-insulating jacket, or matrix. For the LA-EBID NW with the lowest resistance, again at 10 μA, the Joule heating arising from power dissipation ($P=V*I$) was at 4x10^{-9} W, or 2.67x10^{-4} nW/nm. In stark contrast, the untreated sample, EBID NW, failed at 10 μA, since in this case the linear energy dissipation was much larger at 100 nW/nm (40,000x higher).

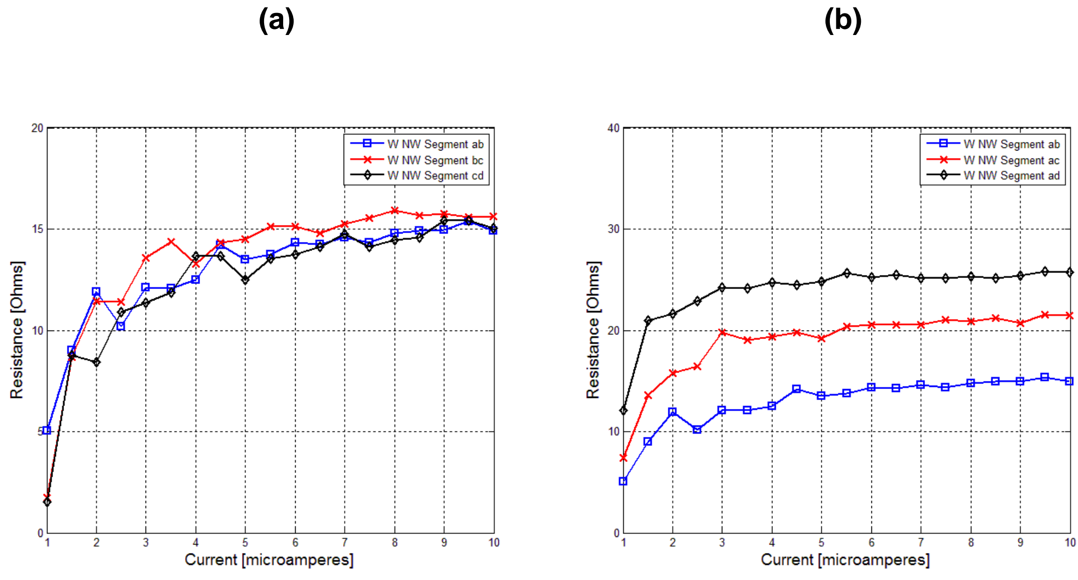

Figure 1.11. On left (a), resistances measured for equal length segments of W NW via 4-pt probing and between each test pad at 10 μs. On right (b), resistances measured for increasing length segments of W NW via 4-pt probing also at 10 μA.

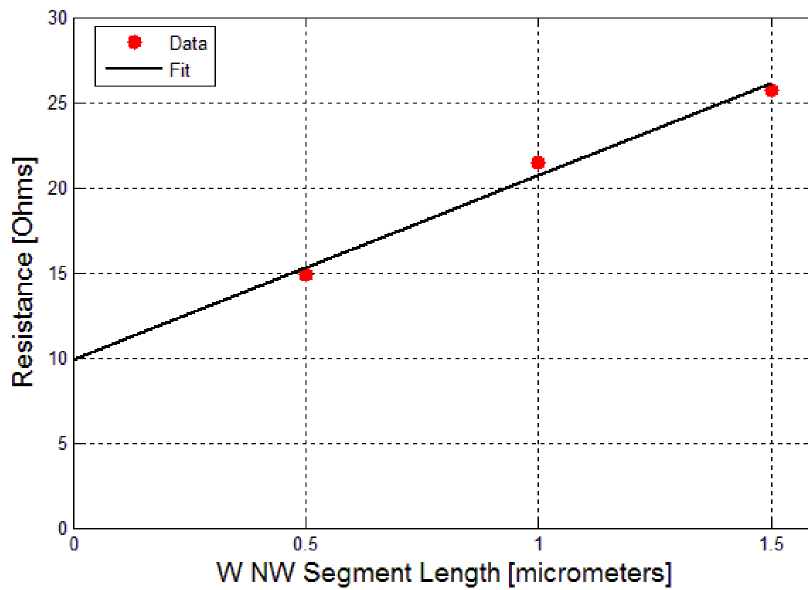

Figure 1.12. Data from Figure 1.11b plotted to determine the contact resistance for the W NW. This corresponds to two series contact surfaces with the nanowire, each contributing 4.94 Ω.

Pt NWs Made Via He- and Ne-IBID.

Ga^+ FIB Pt has produced deposits of ~46 at. % Pt, 24 at. % C, 28 at. % Ga and 2 at. % O, using $MeCpPtIVMe_3$. Here, implanted gallium may have a defining role in lowering the resistivity, and not the rest of the method itself. However, gallium is reactive and it does have higher ρ than most pure metals considered for EBID and IBID processes. In EBID, typically 15-25 at. % Pt is feasible, but with high ρ ~ 10^7 $\mu\Omega$-cm. Helium ion beam deposited material typically has yielded to date smaller size nanograins and larger resistivity (typ. 30,000 $\mu\Omega$-cm), relative to the gallium ion beam.

Platinum nanowires were deposited using a helium and a neon ion beam under different process conditions at Carl Zeiss Corporation. Samples were prepared with beam energies from 10-30 keV, beam currents from 1-20 pA, a total dose of 1 nC/μm^2, pixel spacing of 1 nm and a dwell time of 1 μs. The injected gas precursor was heated to 30 ^{o}C, while the N_2 carrier gas was heated to 45 ^{o}C. The nozzle was situated only 70 μm above the sample surface and at a 30° angle with respect to the same horizontal surface. A sample was prepared also on a 50 nm thick Si_3N_4 membrane for TEM analysis. The beam energy and current for He^+ and Ne^+ were the same for both at 20 keV and 10 pA, in order to compare the beams at the same variables or conditions. Beam currents were adjusted by changing the inert gas pressure at the gas field ion source. The dose range was from 0.25 to 1 nC/μm^2. The dwell times were also increased to 10 μs.

It has been found that helium induced depositions resemble EBID. Both yield very small Pt nanograins embedded in the carbonaceous matrix. Using helium to form Pt NWs typically yields a 16 at. % Pt purity and with resistivities in the 10^4-10^5 $\mu\Omega$-cm range. It is typical to find, as in e-beam deposits, an electrical behavior representative of weak intergranular coupling. On the other hand, when using neon, even though the purity is more less the same at 17%, the resistivity is markedly lower at about 600-3000 $\mu\Omega$-cm. The drop seems to be closely related to stronger

intergranular coupling characterized by larger nanograins. Neon decreases resistivity values to ~600 μΩ-cm, which can be explained by neon having smaller ion ranges and greater nuclear stopping losses, while in helium it is the electronic stopping that dominates the ion-solid interactions in the material. Since the nuclear stopping contribution is higher for neon, this may lead according to A. Dubner's thermal spike prediction (using a binary collision model) to localized heating [13]. This effect may enhance Pt nanocluster coalescence and coarsening. Since Pt and a-C are mutually immiscible, the inter-grain tunnel coupling improves, thus leading to higher electrical conduction.

In general, these results show lower resistivity NWs made possible by helium, and even lower values by neon. The resistivities at 1 μA are near 1200 and 500 μΩ-cm, for helium and for neon, respectively. Admittedly, this is still 50-120x higher than the target value at ~10.5 μΩ-cm, but a monumental milestone forward towards the realization of 100% metallic NWs. Refer to figure 1.13 for a comparison between helium and neon, in a 10 nA-1 μA range.

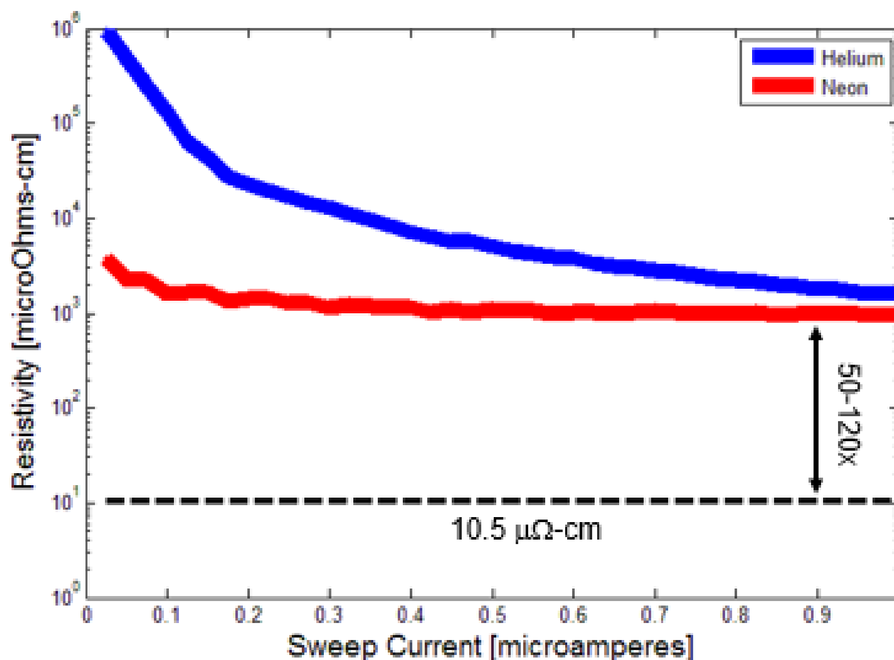

Figure 1.13. For Pt NW deposited using He and Ne, resistivity data for the range between 10 nA to 1 μA, and compared with the target bulk value for platinum.

A larger current density was found to induce slower growth rate and lower resistivity. For 2 pA He^+, the resistivity of the Pt NW was 1.8×10^5 μΩ-cm, while at 20 pA He^+ it was 4.7×10^4. This corresponds to a 74% drop. At 20 pA also, the deposition rate was found to be ~0.055 μm^3/nC, which is also one-fourth the value at 2 pA. This result is indicative of a mass transport limited regime, where apparent depletion of the precursor may be taking place. The beam energy was found to have a smaller effect on the deposition rates. However when changing from 10 to 30 keV, the resistivity increased by 40%. This is likely due to the reduced nuclear stopping power at higher beam energy and thus less knock-on events to coarsen the Pt grains and improve the tunneling coupling strength.

The Ne^+ induced Pt NWs were found to contain some implanted neon. This may have been as high as 4 vol. %. Since the highest dose in the study was ~ $4x10^{22}$ Ne^+/cm^2, it should not be surprising to find bubbles present once the solubility limit of neon in the deposited material has been exceeded. Based on TEM images, neon yields larger nanograins. In the case of helium, these are ~3.2 nm with a corresponding Pt purity of ~16.2%. On the other hand, for neon, the nanograins are slightly larger at 4.5 nm with a 17.4% Pt purity. Refer to TEM images in figure 1.14. In the Pt/C system, electron conduction by intergranular tunnel coupling is observed. In Ne-BID Pt, the electrical behavior shows a characteristic insulator-to-metal transition between the Pt nanograins as a function of temperature.

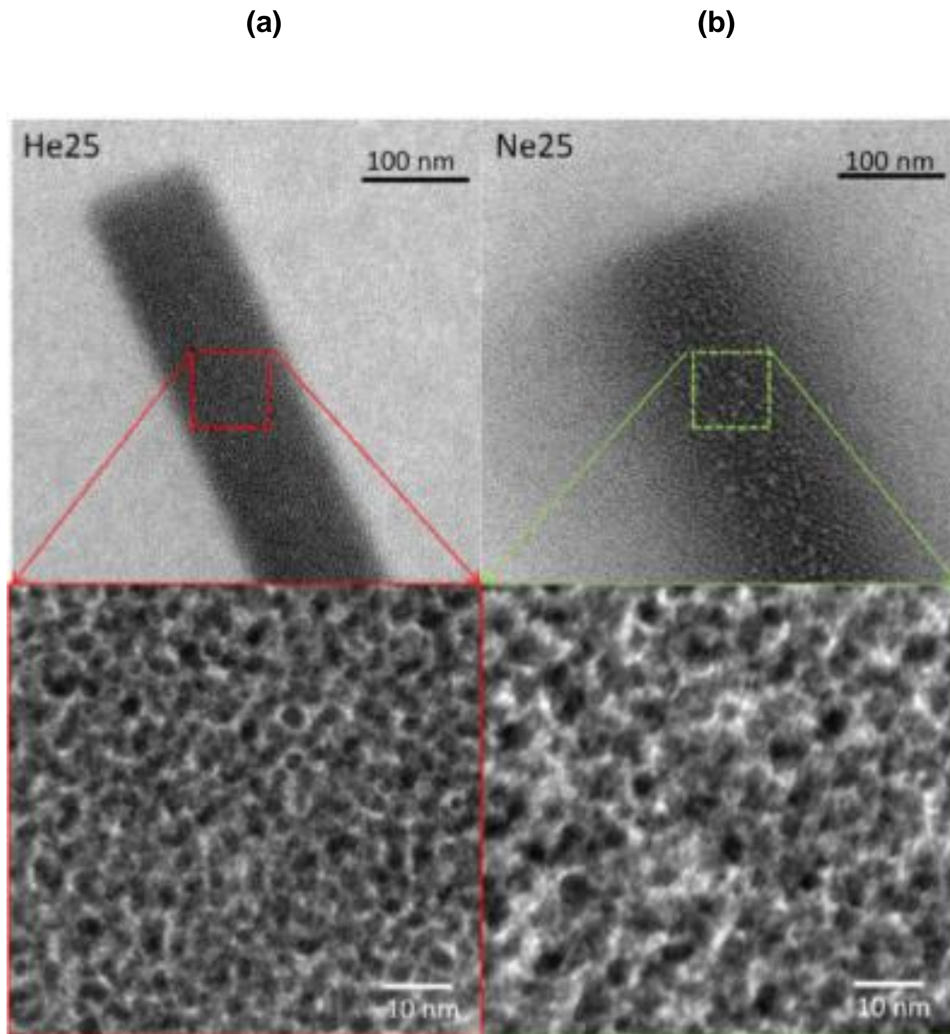

Figure 1.14. Comparison of nanostructures between He^+ (in a) and Ne^+ (in b) induced deposition of Pt. The grain sizes are clearly larger on the Ne-BID Pt NW.

Pt/C Considerations.

The discussion in this section very easily applies to any nanowire grown via IBID where a composite results in metallic grains embedded within an amorphous carbonaceous matrix. SRIM/TRIM [14] simulations are useful for visualizing the depth of the interaction by helium and neon ions impinging on the growing three-dimensional structure. As shown in figure 1.15 below,

for neon on Pt/C (17 at.% Pt, or Pt:C=1:5) a smaller interaction volume arises and very near the top incidence surface. This is rationalized to be quite benign for the growing process where more secondary electrons generated from the target are able to escape the material and reach the interaction zone on the surface to dissociate complex molecules, especially those diffusing on the surface under the primary beam. On the same figure, it can be seen that for helium ions the interaction volume within the NW is much larger and especially deeper. SEs in this case need to travel or cross longer distances across the deposit in order to reach the surface. The escape depth will not be large enough for many electrons generated deep within. Another factor that may impact the purity of NWs is the preferential sputtering of carbon, rather than the heavier platinum metal atoms. This while not confirmed experimentally, could be one reason making higher purities possible in the Ne-BID NWs. The diagram in figure 1.16 shows, at 20 keV, a higher sputter yield for carbon of near 0.5 atoms/ion while for platinum it is negligible. By the way, it is expected that most energy losses due to interactions of lighter neon and heavier platinum atoms will be of electronic nature at higher beam energies such as 30 keV. This should result in minimal sputtering and in more secondary electron generation, both beneficial to the goals of the process.

(a) (b)

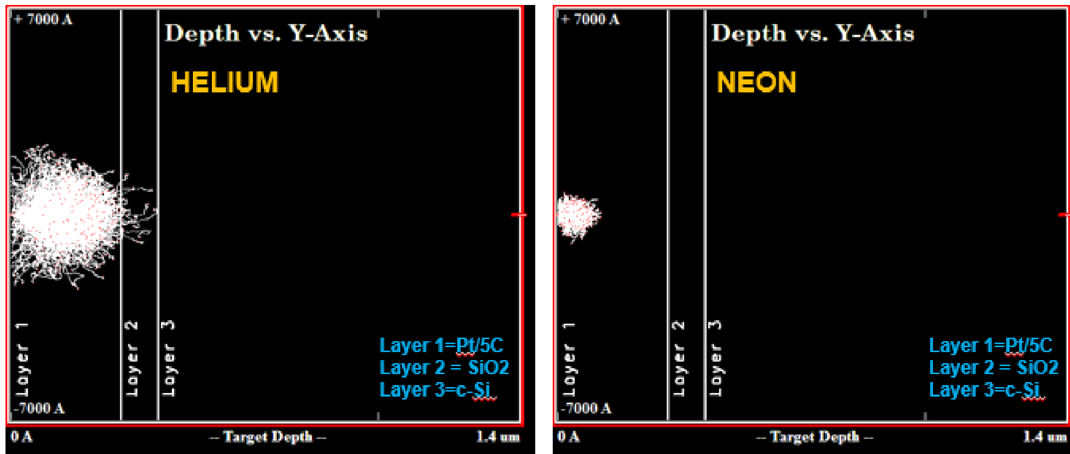

Figure 1.15. Interaction volumes for 1,000 ions of 30 keV helium (in a) and for neon (in b) in the Pt/C structure (300 nm). Layers 2 and 3 are SiO_2 (100 nm) and Si, respectively.

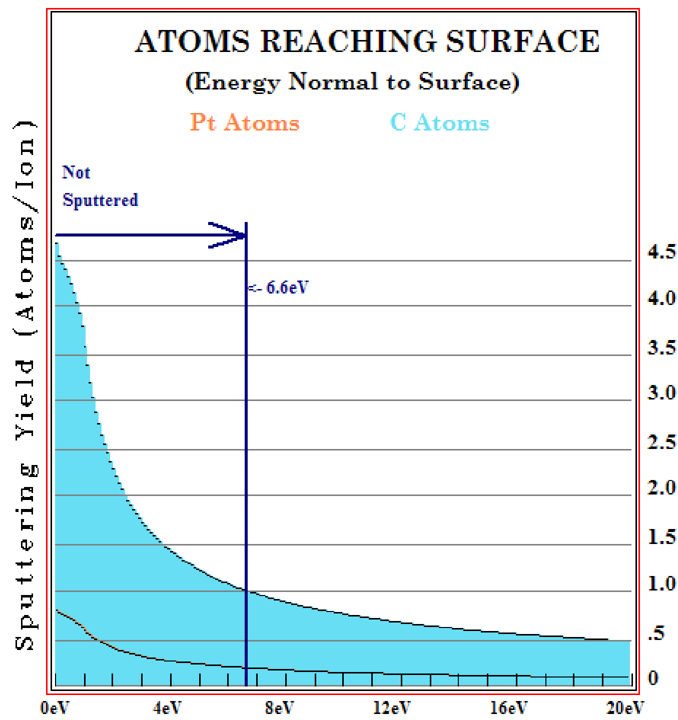

Figure 1.16. Sputtering yields of Pt and C by Ne^+ at 20 keV from SRIM/TRIM simulations.

Temperatures may also play a key factor in the deposition of high purity NWs. At the beginning of the process since there is no Pt/C deposit yet, the ion beam is depositing its energy directly in the substrate material. In this case, it is SiO_2 which has poor thermal conductivity (κ=1.5 W/m-K). Using independent heat sources with the energy transferred by the travelling ion into individual pixels, the temperature spikes can be estimated as in figure 1.17. For helium, the temperatures do not climb too high, thus remaining at near 330 K at the start of the process and dropping to almost room temperature at 298 K for a 300 nm thick deposit. On the contrary, neon produces a whole new set of possibilities. SRIM/TRIM derived temperature values at 1 ps (assuming 100% phonon energy converted into heat), can reach as high as 900 K initially and then drop to near 500 K. These conditions may be ideal for composite purification without the need of a heated stage. The heat is provided by the beam itself. The thermal diffusivities of SiO_2 and a-C are relatively low, and thus it is expected that even when a localized quench zone only nm in size is present as this heat is transmitted away by lattice vibrations and between ion strikes, the effective impacted region may be greater than just a 1-2 nm. In vacuum, there is going to be serious limitations to heat transport away from the structure. This may prove again to be beneficial in allowing the freshly deposited Pt atoms in the deposit, with high heat capacity, to nucleate and grow by combining with nearest neighbors in the immediate surroundings thus resulting in coarser rather than fine metallic crystallites. As the beam raster moves over the pattern, these temperatures will undergo a cycling process, that admittedly for the typical dwell times of 1 μs, would allow the irradiated volume to roll back to room temperature, before the beam returns to above the same spot several times. It is important not to ignore the possibility that there will be interaction volume overlapping. As the beam advances to the adjacent position or spot by typically 1 nm, heat may still be diffusing away from the previous thermal spike, probably resulting in slightly higher background temperatures than room temperature at the new position.

Figure 1.17. Temperatures computed from SRIM/TRIM's phonon energy at 0 nm (a, c) and 300 nm (b,d) thickness for He (a,b) and for Ne (c,d) ion beams on SiO_2/Si (0 nm Pt/C) and on 300 nm thick Pt/C on SiO_2/Si. Ion count was 1000.

(a)

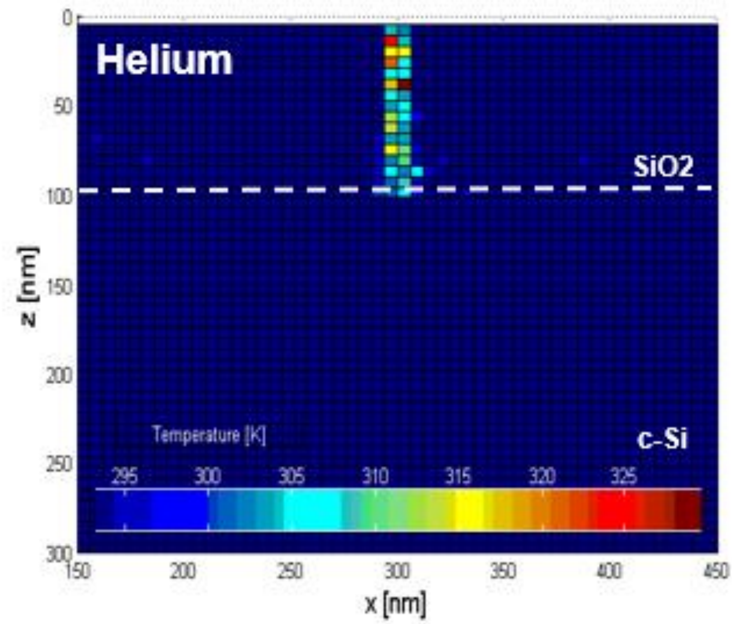

(b)

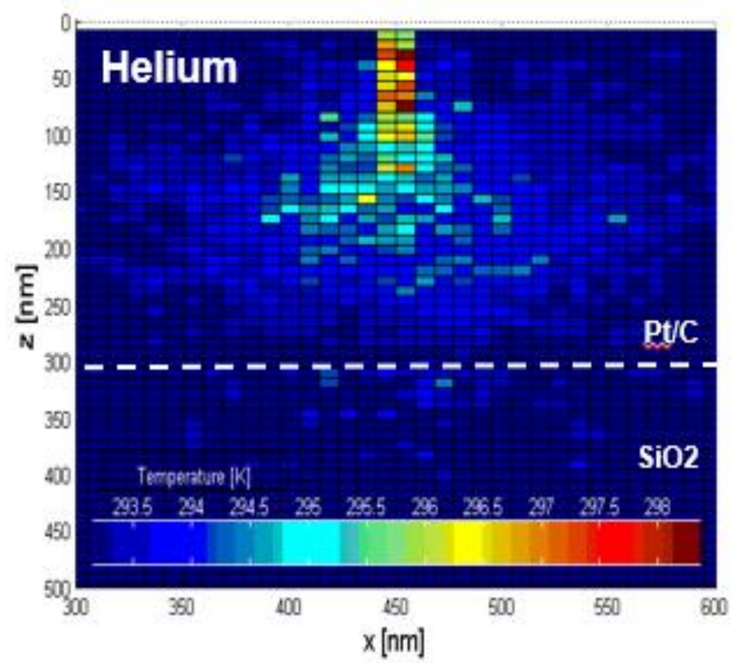

Figure 1.17. Continued.

(c)

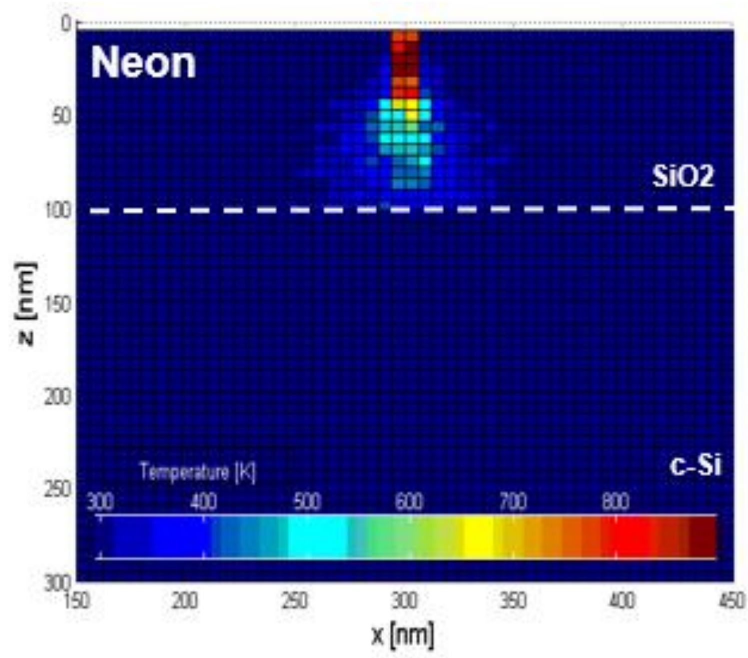

(d)

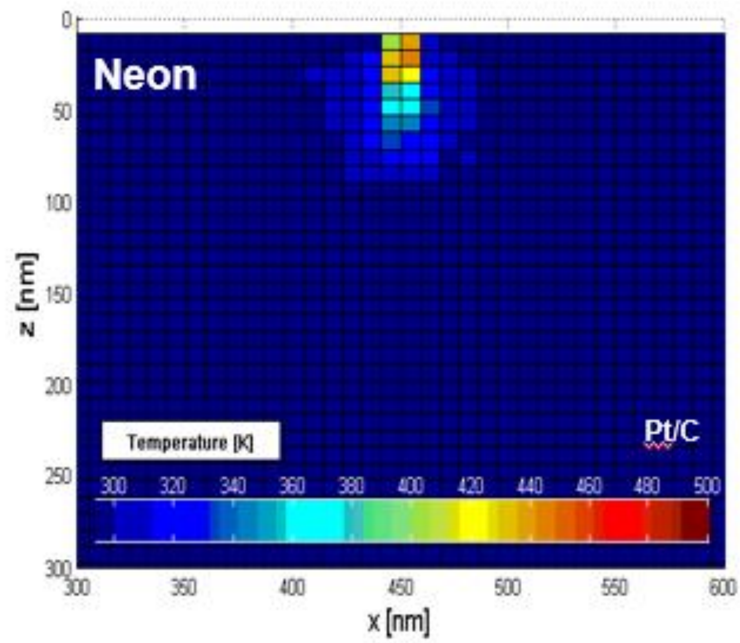

Figure 1.17. Continued.

Co NWs Made Via He-BID.

In the case of electron-beam induced cobalt deposition, the final resistivities can be as low as 159 $\mu\Omega$-cm and with 80 at. % Co content. High e-beam currents lead to high metal content deposits. However, high e-beam currents lead to poorer beam profiles thus hindering the ability to produce smaller features below 50 nm in size. The helium ion beam was utilized to produce cobalt deposits with no post anneal step involved. The beam energy was 35 keV, with a current of 1.5 pA, pixel spacing 1-5 nm, dwell time of 0.5 μs, in serpentine mode and with 100 μs refreshes. A 20 μm aperture was used initially, but for narrower Co NWs, a 5 μm aperture with only 0.8 pA was used instead. The cobalt three-dimensional structures were: 140 nm x 500 nm x 7500 nm. The narrow lines were however only 30 nm x 30 nm x 9000 nm in single line scan mode. At 35 keV, there is a larger interaction volume for helium in insulating SiO_2 which has a larger escape depth for secondary electrons.

Low magnification bright field TEM images of the cobalt deposits show nanoscale cobalt grains with a size of ~ 6 +/- 2 nm. For e-beam deposited cobalt, the nanograins have been before found to be 1-2 nm only. Using EELS, no measurable carbon peak was found at 284 eV (C, K edge), while a large absorption peak is present at 60 eV for the Co $M_{2,3}$ edge. The Co NWs by He^+ show high Co purity, larger nanograin sizes and low resistivity.

Cobalt NWs were tested via 4-pt probing. V-I and R-I curves are shown below in figures 1.18. The responses are quite smooth and fluctuations-free. Noise typically observed in other NWs at low biases, up to 100 nA, are absent here. As shown in figure 1.19, the calculated resistivities for the best cobalt deposit rests just 2x above the target value for a pure, bulk piece of cobalt (6.24 $\mu\Omega$-cm). Images obtained via TEM from Zeiss indicate quite obviously that for these the matrix consists of cobalt with no carbon or any remnants from more complex molecule fragmentations (figure 1.20). Helium makes here a strong case, by successfully yielding NWs of

low resistivity and therefore high purity. What Co and Pt do not have in common is the gas precursor utilized. This leads to a strong argument in favor of gas precursors that are simpler molecules, with fewer ligands and ideal enthalpies of formation. Unfortunately, for Pt, there is no carbonyl. Precursors such as PtF_3 and $PtCl_2$ would possibly yield purer deposits for Pt, but in non-dedicated chambers this would create other complications. Helium, as mentioned before, may provide a sufficiently large amount of secondary electrons to, in combination with higher cross-section for dissociation for cobalt-containing molecules, enhance cobalt's affinity to stick and precipitate in the solid state under the beam irradiated area.

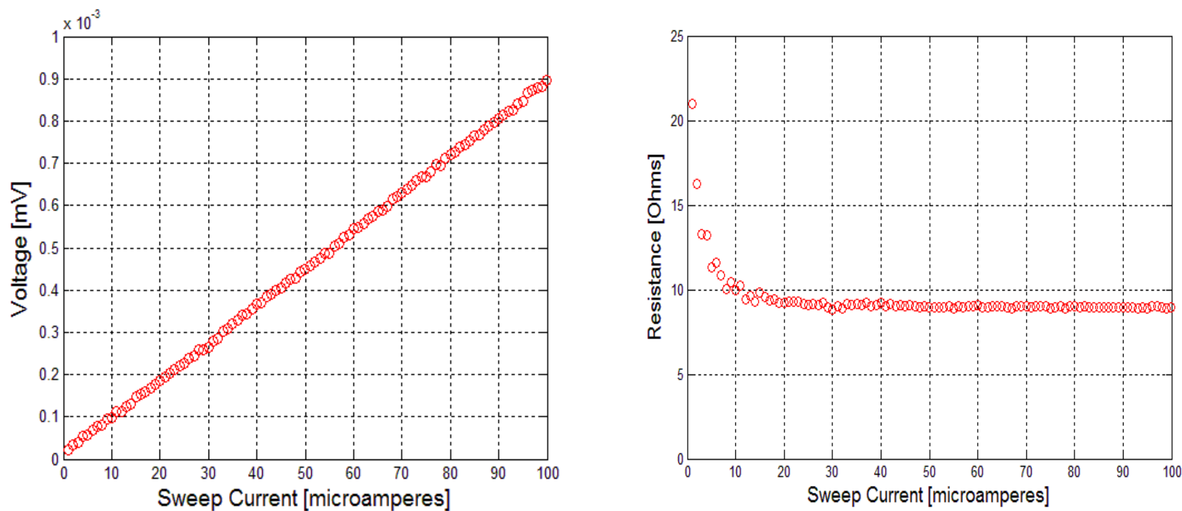

Figure 1.18. V-I sweep and calculated R-I curve for a Co NW made with a He ion beam.

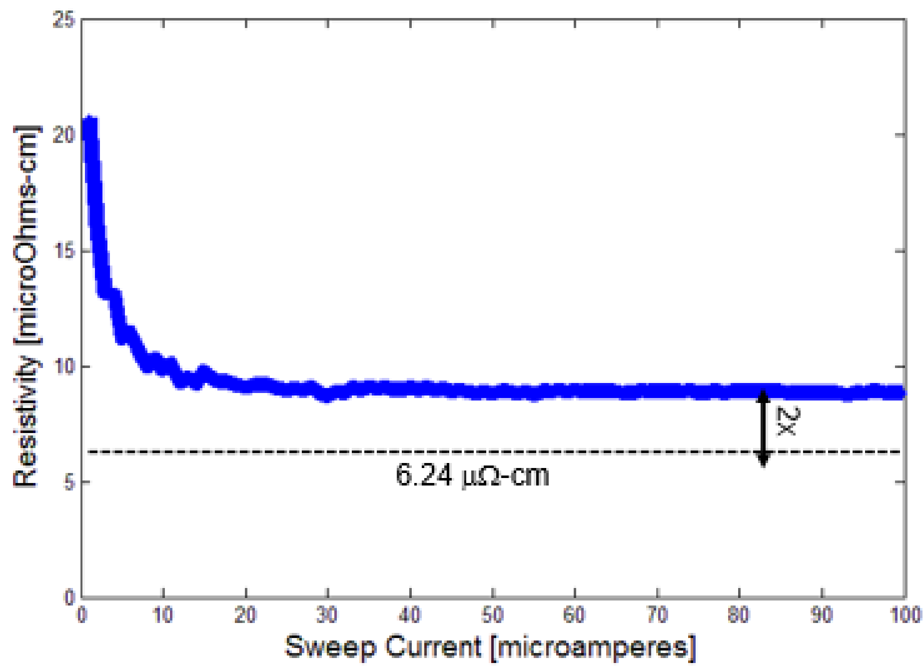

Figure 1.19. Calculated resistivity from the R-I curve for a Co NW made with a He ion beam. Dashed lines shows the target bulk resistivity for cobalt.

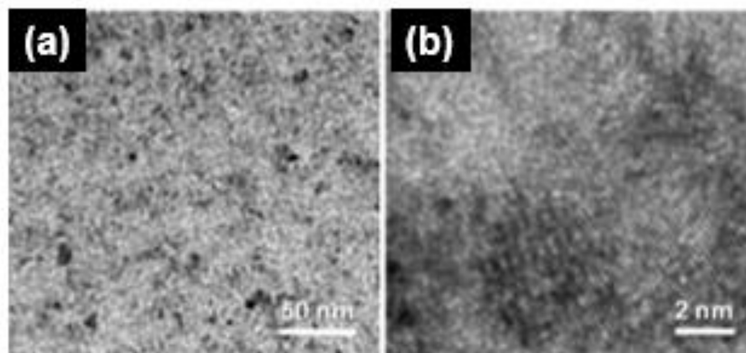

Figure 1.20. TEM images for a Co NW at two different magnifications. On the left (at lower mag), it is evident the higher purity of the deposits. Significantly larger amount of brightness, corresponding to Co grains. On the right, a closer look, showing granular crystallinity developing in cobalt, that shows larger nanograins at ~10 nm in width.

NW Microstructure and Failure Mechanisms.

One simple thermodynamic expression can help elucidate the extent of the heating effects in the nanowires. The following expression

$$\mathbf{Q = m\ c_p\ \Delta T},$$

relates the heat added to a temperature rise in the conductor (ignores thermal convection or radiation). In the equation, Q is heat or energy (in Joules), m is the mass (in grams), c_p, the heat capacity (in J/g-K) and finally the change in temperature (in K). The amount of energy added into the nanowire will be the power delivered ($P=VI=V^2/R=I^2R$) times the elapsed time ($Q=Pt$). The bias time has been taken as 1 s based on observations while the test was run. A quick few preliminary computations lead to the following general findings: for a 100% a-C NW (say R~1 MΩ), the temperature rise would be $6x10^6$ K; for a 100% W NW (say R~1 Ω), it would be only 3 K; and for a ~100 Ω NW consisting of the two phases (W:C=50:50), the ΔT would be ~450 K . This shows that a high-R NW made up mostly by a-C would heat tremendously for a simple electrical test at only 1 μA and a bias time near 1 s. Obviously, it would fail before heating any further. In reality, due to percolation effects even when the NW may be near 50:50 in composition, the metallic part will likely be poorly interconnected causing the NW to appear as if it is 100% carbonaceous and consequently fail.

The volume of the entire nanowire can be reasonably approximated by using a width of 300 nm, height of 300 nm and a length of 500 nm (distance between the adjacent sensing electrodes: V+ and V-). However, the volume required in order to calculate the mass in grams is going to be only that of the conductive tungsten path between the voltage sensing (middle two) terminals. The resulting current-carrying mass can be lower than the total mass of the W NW. The heat capacity in J/g-K and the density in g/cm^3 for an insulating jacket (the a-C matrix) around a path of least resistance can be obtained from literature for a-C and for W, for example. This will

have to be weighted, since the a-C matrix will contain a dispersion (below percolation) of W nanograins.

Amorphous carbon is ~20x less thermally conductive than tungsten which represents a major thermal management limitation in the structure. To further complicate matters, the heating caused by the insulating matrix may allow for temperatures to climb steadily causing some thermal expansion and contraction issues. W expands, and in a greater extent than other carbon- or oxygen-containing components in the matrix. While apparently beneficial for electrical connectivity, upon relaxation, this could lead to the formation of gaps or micro-cracks between the metallic grains and the carbon-rich walls that separate these. This can lead to intergranular disconnection and in the worst case scenario an open circuit, as observed many times after a first sweep up to 1 or 10 μA.

Similar to the case found in yttria-stabilized-zirconia (YSZ), the total resistivity of a W NW can consist mainly of two dominant factors: a grain interior and a grain boundary. In the NWs, the grain interior is analogous with the metal crystallites (or phase one), and the grain boundary with the carbonaceous matrix (or second phase). A useful expression for total resistivity becomes:

$$\rho = \rho_g + \frac{\delta_{gb}}{d} \rho_{gb},$$

where the ρ_g is the resistivity of the grain interior (low for W), the δ_{gb} is the grain boundary or wall thickness, the d corresponds to the grain size and finally the ρ_{gb} refers to the grain boundary resistivity (higher for a-C, WO_x and WC). Obviously, and not surprisingly, $\rho \propto d^{-1}$. Here it is predicted that for smaller metal grains and for larger carbonaceous walls (higher vol. % C), the total resistivity will be dominated by the less conductive phase in the system, or composite in our case. Refer to figure 1.21 for a depiction of the W NW microstructure.

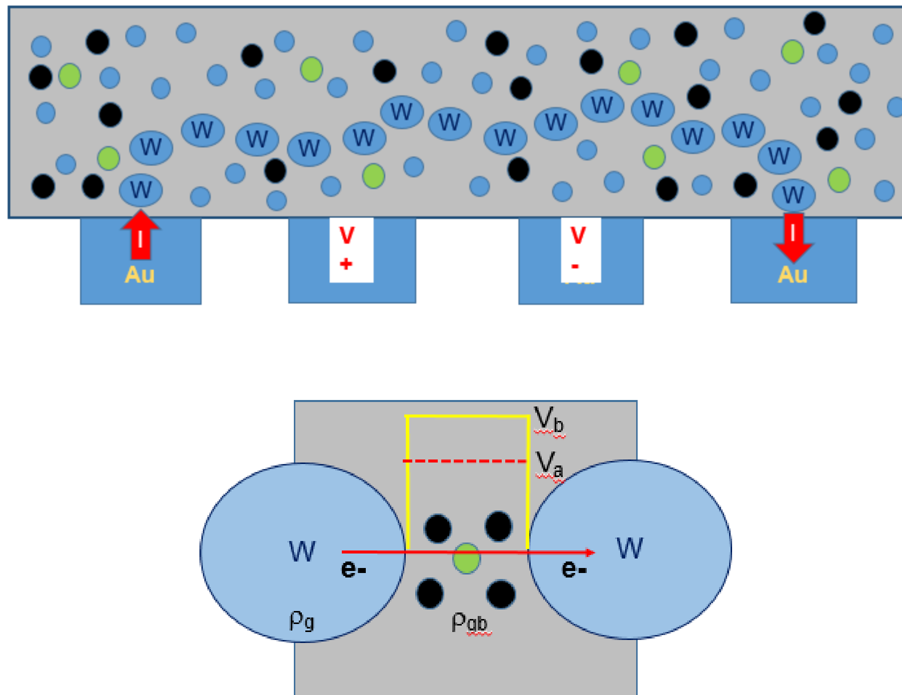

Figure 1.21. Diagrams showing the microstructure in a tungsten nanowire: a path of least resistance from one terminal to another, and a closer look at the region between two adjacent nanograins. In the later, the barrier (V_b) and applied voltages (V_a) are shown.

The instability of the EBID NW undergoing electrical test has been obvious. This is a result that is repeated with many NWs of larger resistance values. In the case of the EBID NW, as the current increases in a sweep, the resistance typically increases slightly, but upon measuring again the resistance had increased sharply by orders of magnitude. Further testing results in catastrophic failure when the NW shows a response indicative of an open-circuit. In the case of the LA-EBID samples, these exhibit resistances that slightly drop as the current sweep progresses. In the following sweeps in the same range, the resistance of the nanowires drops. Nevertheless, when tested at a new range at higher current levels (typically 10 μA) these also undergo in most cases a catastrophic failure. This arises very interesting clues about the intrinsic

nature of the nanowires and how these are behaving under dc electrical force fields. It can be argued that the EBID NW contains more complex organic remnants which upon heating by increasing current flow outgas and/or expand and then contract within the structure, resulting in the degradation of intergranular connectivity which in turn leads to higher resistances. This evolution basically results in the generation of micro-cracks due to thermal expansion coefficient mismatches present within the two (or more)-phase device that lead to the open circuit conditions detected in many instances. In LA-EBID NWs, the complex organic content has been minimized possibly to predominantly a-C forming the medium of the nanowire. Discrete and semi-isolated metallic grains are embedded in this amorphous carbon matrix. In this case, the Joule heating does not result in as dramatic expansions and contractions in the bulk, but, by the contrary, it may improve connectivity.

Inarguably, the tungsten nanowire consists of a complex structure. However, the electrical measurements provide clarity about the condition of the sample. Heat and temperature rise from laser beam exposure is expected to assist the desorption of most W-C-O molecules remaining within an EBID structure and also allow for coarsening of the metallic crystallites or nanograins resulting in improved contact area between this conductive phase inside the stable carbonaceous matrix. It must be noted that there is a probability that slightly higher resistivity WC_x (x=1,2) and high resistivity WO_x (x=2,3) may be present in the laser treated matrix (a-C still being the most stable solid by-product after gas precursor decarbonylization), while complex metastable molecules of $W(CO)_y$ may remain a constituent part in the untreated EBID NW. This is important in justifying the failures of the EBID samples in which it is suspected that the disintegration of the remnant molecules will lead to micro-cracking and opens in the NW. W NWs made by Reguer et al [12], were found to contain tungsten carbide crystals, in their case, as result of up to 2.5 V electrical treatment; in our case, resulting from the in-situ pulsed laser anneal.

From the experimental data of V and I, calculated P, R and ρ are obtained. Refer to figures 1.22 and 1.23. There are two characteristic regions discernible from the experimental results. Region I (for low currents) can be represented as a semiconductor, where the resistance drops with current (and temperature), while region II (for higher currents) by a Steinhart-Hart equation. These two equations are as follows:

$$\rho\ (T) = S\ \alpha^{B/T}\ ,\ \text{for a semiconductor}$$

$$\frac{1}{T} = A + B\ \ln(\rho)\ ,\ \text{or}\ \rho\ (T) = \exp\left[\left(\frac{1}{T} - A\right) / B\right]\ ,\ \text{for a metal.}$$

In the LA-EBID NW, and at low currents, it is evident that the behavior is semiconductor-like where the resistance is decreasing. This is an indication that the metallic content in the nanowire is still below its percolation threshold. This range will be dominated by either electron transport via hopping into localized states (low metal content) or into extended states (high metal content) [15]. In this range, the electronic transport is controlled by the intergranular material. This is consistent with NTCR behavior, or a negative temperature coefficient of resistance. This region can be fit reasonably well with a power law function which is characteristic in varistor materials. The microstructure can be viewed as a mixture of arbitrary pure W nanograins embedded in a matrix that is less conductive and consists of mainly other compounds in lesser concentrations such as carbides (introduced by the laser pulse anneals), oxides and amorphous carbon. These constitute the higher resistivity material between adjacent pure W nanograins. Thus, the total resistivity measured will be the sum of these two resistivities; $\boldsymbol{\rho_T = \rho_g + \rho_{gb}}$, where $\rho_g < \rho_{gb}$. It is known that the resistivity of the grain interior is going to correspond to pure tungsten, the lowest value at ~5.28 $\mu\Omega$-cm. Since ρ_g and ρ_{gb} are in series, the calculated resistivity is going to be greater, or ρ_T between the voltage sensing terminals.

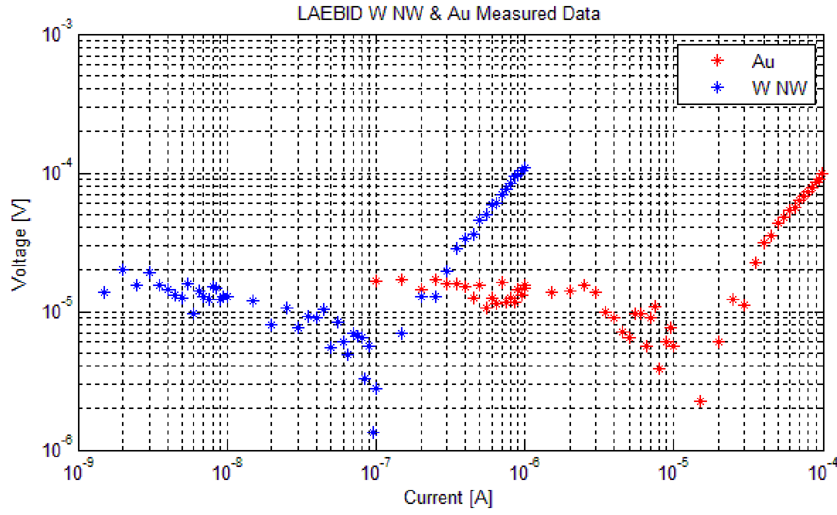

Figure 1.22. I-V measured data for the W NW (in blue) from 1 nA to 1 μA and for the Au reference (in red) from 100 nA to 100 μA.

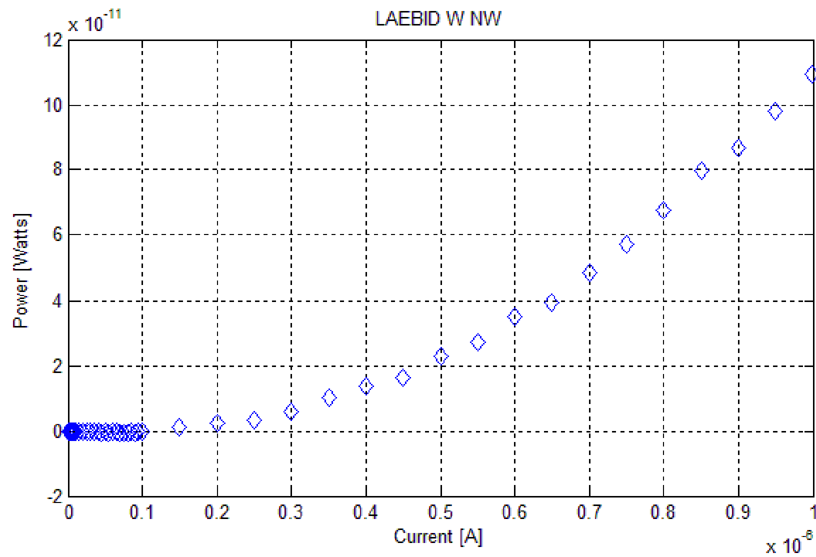

Figure 1.23. Calculated Power (=VI) from measured data versus current for the W NW.

Based on the results, the minimum resistivity is ~250 $\mu\Omega$-cm, and it increases from thereon as expected for metallic behavior. However, when accounting for 100% of the nanowire cross-sectional area, the resistivity appears to be twice as high as what would be predicted by a NW consisting of 50%W and 50% C. Since EDX data confirms the W at. % content is near 50%, then this observation has merit. In order to match closely the measured data with predicted data for the resistivity of a W/C NW, the effective cross sectional area will have to be ~50% of the total deposit. Refer to figure 1.24 for the expected ρ vs. T for bulk metals involved in this study, for a comparison between the ρ vs. T of pure W and the W NW and for the ρ vs. T for W NW accounting for an effective cross sectional area for electrical conduction of 100% and of 50%. At high currents, and thus high temperatures, expected to be below Au T_m (no damage observed to W NW or to test carrier), the resistivities are around 1000 K in both cases. Reguer et al [12] found grains to be 5 to 20 nm in dimensions for a Ga^+ FIB W NW. In this case, since the pulsed laser anneals were applied, the nanograins are expected to be higher than the range for unannealed Ga^+ FIB W NW. Admittedly, with a higher WC reacted content.

Figure 1.24. Several ρ versus T plots for bulk metals and for W NWs.

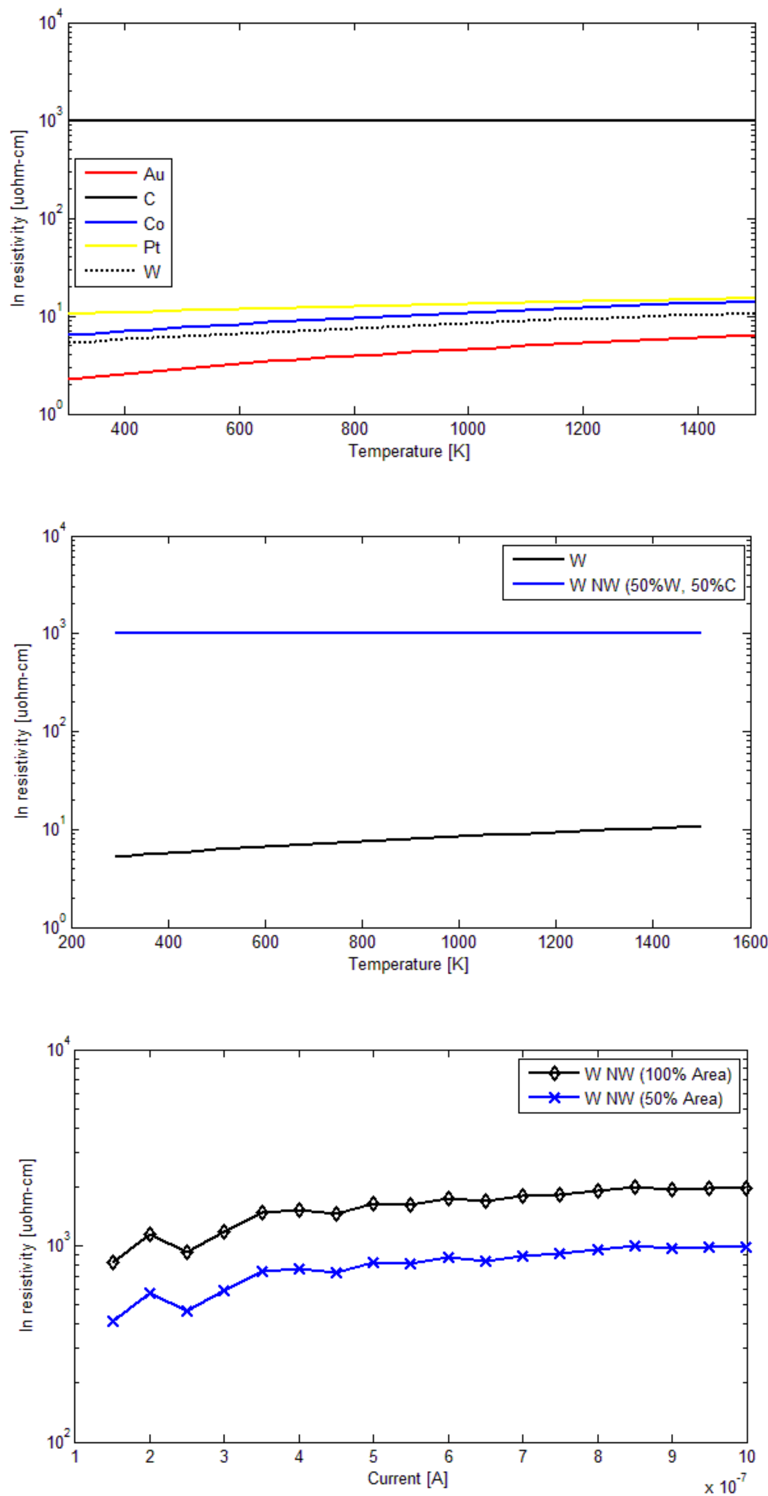

Figure 1.24. Continued.

It is well understood that for smaller grained materials a larger number of interfaces will diminish the mean free path lengths of the electrons. However, and effectively, the electron tunneling effect is responsible for current transport to increase. In the I-V curves, the slowly decreasing voltages indicate that the resistance of the intergranular wall is dropping as well. Thermal expansion (therefore wall thickness contraction) is not believed to be a dominant factor here, reason for which barrier potential lowering rather than barrier or wall width contraction is considered the prime driver for increasing conduction. This is due to the electrons being able to use accessible sites such as defects or energy states across the wall width to hop from one atom to another until they reach the next metal grain and thereon. Eventually, this transport process reaches a minimum voltage and therefore resistance, from which the NW starts behaving in a metallic manner. This new range will now become dominated by the intragranular material. The slope becomes positive showing a PTCR this time. This is characteristic of a thermistor material. In this region, and using the Steinhart-Hart expression for resistance, a good fit with the experimental data is obtained. Refer to fits of R vs. I for regions I and II in figure 1.25. The fits for ρ vs I for Au and the W NW are shown below in figure 1.26. At this point, the grains are thought to be interconnected with a minimum resistivity between them (still higher than bulk W because of the wall contribution). As the current and voltages increase, more power is dissipated on the narrow conductive path within the nanowire inducing some other effects such as Joule heating. The PTC is expected to be that of tungsten at the higher currents (and temperatures). Amorphous carbon contributes just a very small negative TCR of ~ 0.0005, while tungsten is ~0.0045. Thus, yielding a net increase for α of ~0.4 %/K. The most common carbide, WC, has relatively low electrical resistivity, typically ~42 $\mu\Omega$-cm. Transition metal carbides are also known to have low temperature coefficients of resistance. The resistor temperature dependence is usually expressed as: $R = R_0 [1 + \alpha(T-T_0)]$, which in turn leads to a similar linear equation for resistivity:

$$\rho (T) = \rho_0 [1 + \alpha (T-T_0)] .$$

Most transition metals have αs in the range of 3-5x10^{-3} K^{-1} that are relatively low, but positive. On the other hand Si, and, of more relevance in our case, a-C, have negative temperature coefficients of resistance (NTCR). This makes for an interesting competition between W and mainly a-C which still results in a net positive slope. In the sputtered Au reference, in a plot of ρ vs. I, the rate of change in region II (linear fit) was calculated to be ~0.0028 ($\Delta\rho/\Delta I$). This corresponds very closely to the 0.0034/K ($\Delta\rho/\Delta T$) expected in ρ vs. T for Au. What this indicates is that in gold, the current and the temperature are both increasing at comparable rates. When the same analysis is done using the W NW experimental V and I data, the rate of $\Delta\rho/\Delta I$ is much higher than for Au; actually by four orders of magnitude. This indicates an anomalous behavior for the PTCR in the W NW, where the temperature increases at a much faster rate than the current. This is not surprising since heat dissipation from the NW interior is controlled by the insulating carbonaceous matrix. Refer to figure 1.26 for estimates of the temperature-dependence of the W NW resistivity. Furthermore, when comparing the Au reference with the W NW, the transition to metallic behavior is observed at lower currents for the NW. This can be explained by the extent of heating occurring earlier for the W NW since the conductive path is surrounded by a thermally insulating matrix. In Au, there is a much gradual and slow temperature effect, thus it remains for a wider range of currents immersed in the intergranular regime. Based on the rough estimations for Au, at 100 μA, the Au strip should be at ~364 K, while the W NW at 1 μA, would have reached ~1265 K (not enough to induce further WC formation, or melt the gold electrodes).

The metallic region in the W NW is not smoothly and monotonically increasing with current, and thus temperature. Closer inspection demonstrates that there may be subregions within this region. At first, and when the PTCR dominates, the slope is steeper. This may have to do with a diminishing, but still present contribution from region I. However, as the current increases further,

the slope or rate at which the resistivity changes shows a transition to smaller values. It has been deducted that at the high temperatures present and introduced by currents up to 1 μA, the thermal conduction is showing transitions itself. At the low temperatures, since there are fewer electrons available for conduction, the thermal conductivity will be dominated by lattice vibrations, that all by themselves are incapable of conducting heat away as effectively. In the metallic range and at high temperatures, eventually there is an abundant supply of electrons in conduction bands that can move more freely therefore making it possible to transport heat away more effectively. This is supported by the smaller $\Delta\rho/\Delta I$ observed at high currents where the rate of change flattens and is not as steep. Undoubtedly, at this range where temperatures in the nanowire composite can reach up to below the melting point of gold, thermal expansion can become a principal factor by enhancing the connectedness between metallic grains (shorter wall thickness) which can lead to an improvement in thermal and electrical conductivities. Refer to figure 1.28.

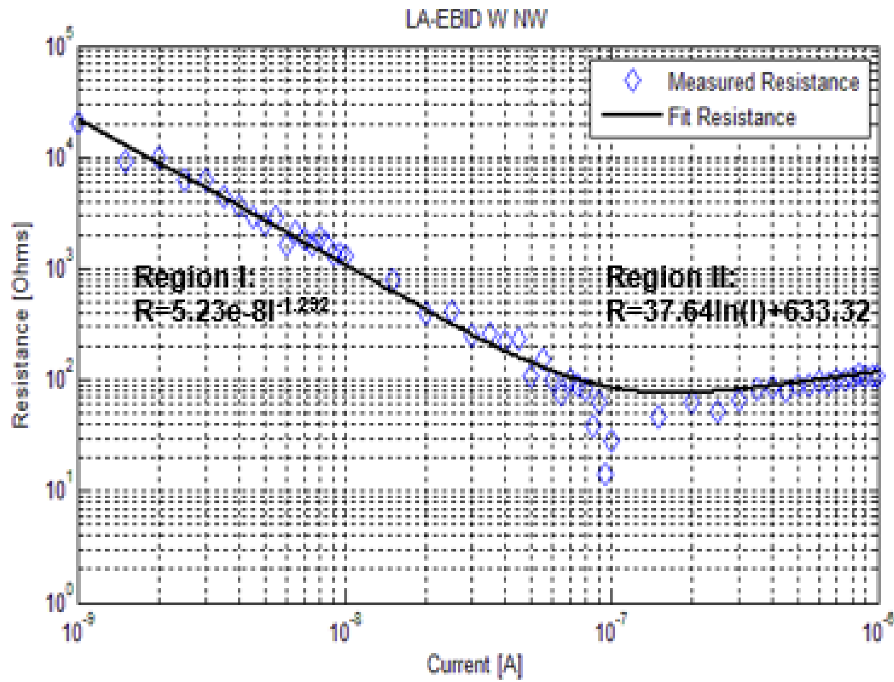

Figure 1.25. Calculated R (=V/I) from measured data versus current and fit using the power law (region I) and logarithmic functions (region II).

(a) **(b)**

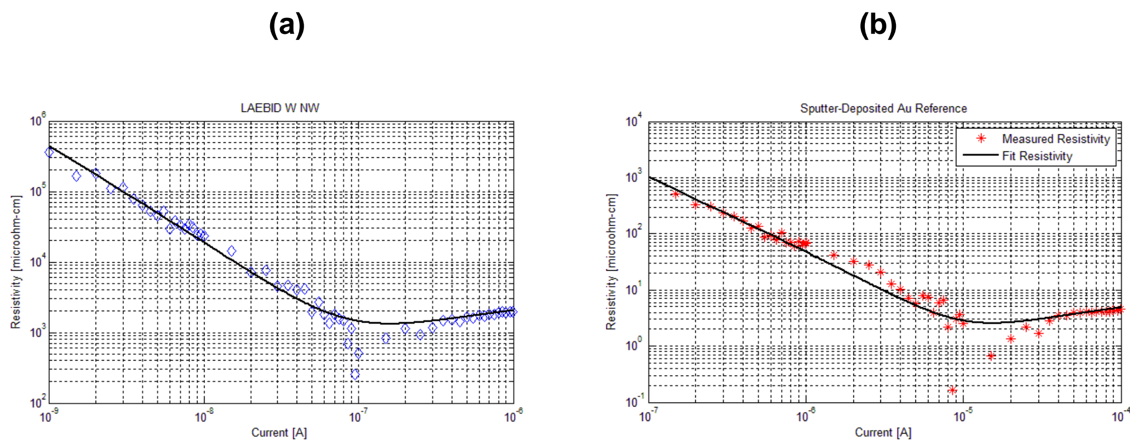

Figure 1.26. Calculated ρ (=AR/L) from measured data versus current and fit using the power law (region I) and logarithmic functions (region II) for the W NW (on a), and the Au reference (on b).

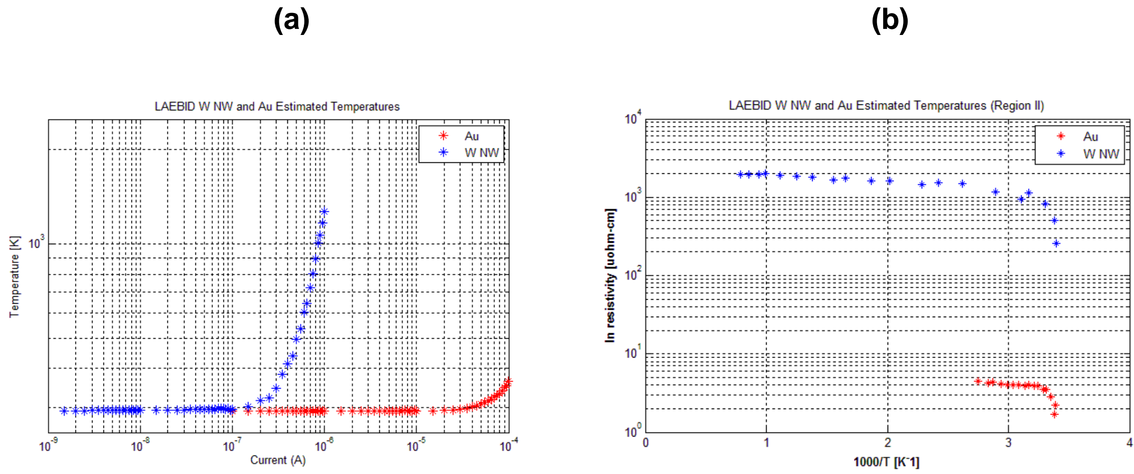

Figure 1.27. On left (a), the estimated temperature as a function of the applied current, and on the right (b), the estimated resistivity dependence on temperature. Both, the W NW (in blue) and Au reference (in red) shown.

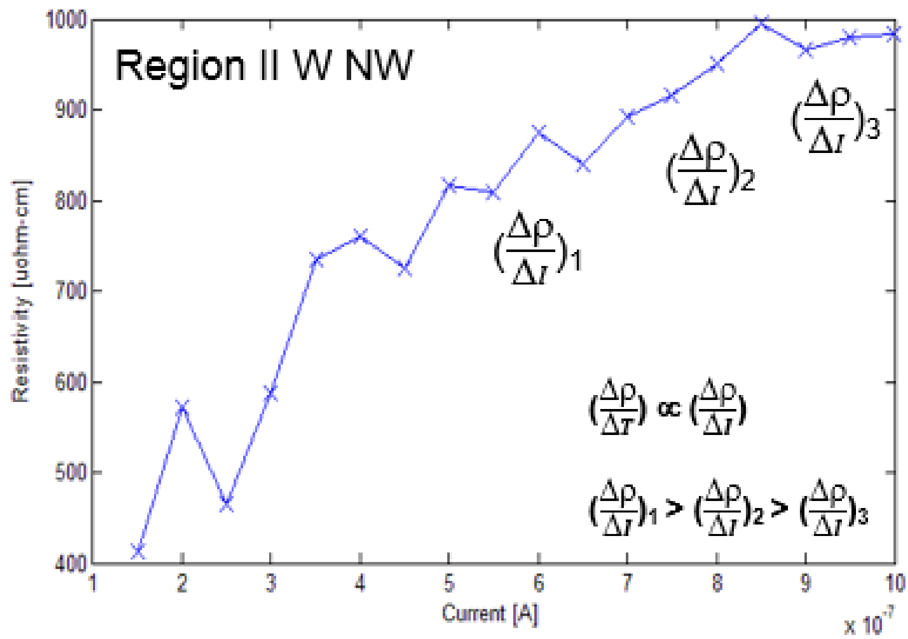

Figure 1.28. Metallic region in the W NW.

Other Perspectives on Failure Modes.

Pre-test and post-testing SEM images show several types of failures in the nanowires. While not the main scope of the investigation, some of these confirm and support the discussion presented in the preceding section. For the most part, NWs fail between the Au test electrodes. The logical argument will be that upon power dissipation and heating from increasing sweep currents, heat transfer is hindered and barely possible in an evacuated chamber (at near $1x10^6$ T) and especially for the portions of the NW laying directly on the SiO_2/Si substrate. The same 'continuous' structure rests directly on top four Cr/Au ~100 nm raised electrodes and on three (3) depressions on SiO_2/Si in between. The Au when heated expands substantially, the Cr not as much. On the other hand, SiO_2/Si will not exhibit as much strain. The displacement on the NW is expected to be larger on the Cr/Au because of the Au. Therefore, upon cooling, when the sweep is completed, the specimen tries to relax back to the original state, but is constricted by the mismatch. This mismatch is amplified at the steps (or near right angles) the NW has along its track. This failure mode (refer to figure 1.29a) has been observed often and results in the destruction of the NW especially between the interdigitated electrodes. This has posed one limitation to further testing of the NWs.

Also, clear from failed test carriers is that it affirmative that the temperatures could ascend high enough to cause melting. Notice in figure 1.29b, the appearance of the nanowire remnants that look rounded, bright (metallic-like) and smooth. This is an indication that melting and re-solidification may have taken place. The only remaining factor that could have an effect is the 'cleanliness' of the surroundings near the NW. The deposition process while highly localized can result in halos or staining of the surrounding surface because of gas precursor molecule breakdown outside the beam irradiated region where these stick and by the end of the deposition have no real time to diffuse properly to the active fragmentation area under the electron beam. These deposits could make up to a few monolayers, yet thick enough to insulate at first, but for

higher currents rapid breakdown could follow. This fact was observed especially during the deposition of cobalt nanowires. A large halo was detected which may have to do with the large (and laterally wide) interaction volume from which the electrons are escaping from the substrate. This collateral deposition needs to be reduced to avoid possible stray leakage currents or failure of the test structure. Reducing the accelerating voltage, increasing carrier gas (N_2) amount to dilute the precursor and optimizing the alignment via smaller aperture areas can help minimize this effect and its potential repercussions.

In some cases, and for larger voltages, the failure may appear to be caused by spark discharge. While a minimal capacitance exists between adjacent fingers separated by a mere 500 nm gap and ~100 nm thick electrode, there is the possibility that for higher resistance NWs, internal capacitances may be present between metallic grains separated by a thick amorphous carbon layer. Charge accumulation may be possible between conducting grains acting as electrodes with a quasi-dielectric medium separating them. At some point, this voltage will be sufficient to allow for a quick static discharge across the carbonaceous matrix, resulting also in failure. Since the testing is done in ambient temperature and conditions, between adjacent electrodes only about $5x10^{-19}$ Farads, can be expected. This admittedly is quite small. In the event of 1 V present between the terminals (as it would be the case for high-R NWs) the number of electrons accumulated on each side would be a mere three (3) electrons, hardly an amount near what would be expected to cause a devastating spark. It can be argued then that internal capacitances and charging between metallic crystallites can lead to a breakdown by static discharge across the matrix, especially true for the most insulating deposits. Based on SEM micrographs, it has been observed that one of the test carriers may have been faulty in that the Au/Cr metallization of the contact pads for the microprobes and the fingers over which the nanowire rests, may have been too thin (<100 nm), and not thick enough to withstand the current densities in the electrical tests (figure 1.29c and 1.29d). Some ensuing temperatures may have

reached beyond the melting temperature for Au with T_m=1337 K (figure 1.26d). There is another possible source of capacitance in this structure for NW electrical testing. Between the Au/Cr fingers and the silicon substrate below a capacitance may be present where SiO_2 is the dielectric. In this case one may expect near the NW a capacitance of near $2.2x10^{-16}$ F, which again is admittedly minute. In this case, the number of electrons that could accumulate at the electrodes would be near 1380 e^-.

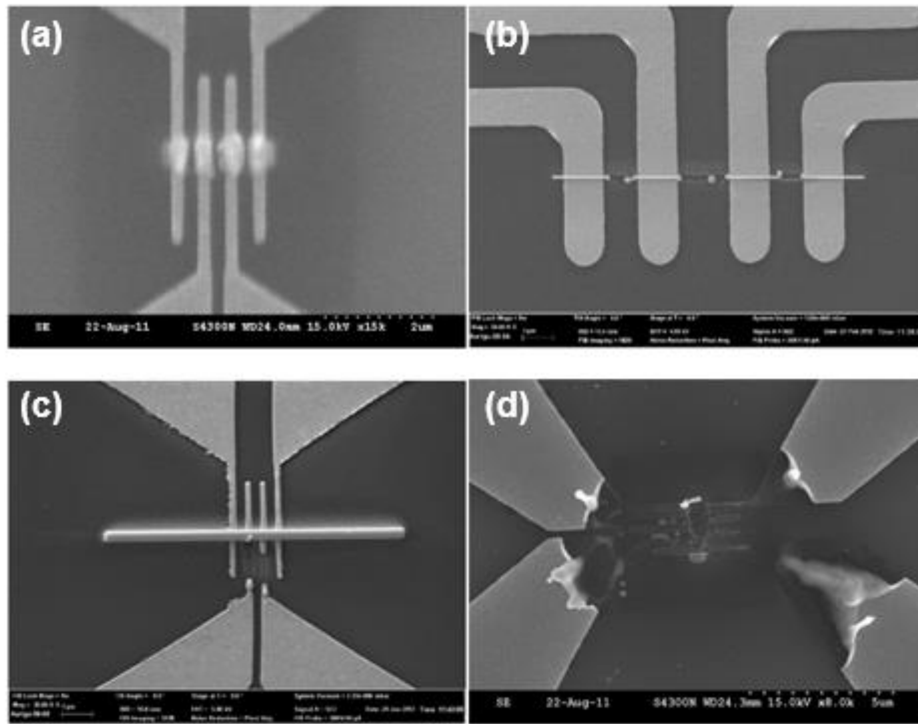

Figure 1.29. Failure modes observed in nanowires during dc electrical characterization.

Conclusions

LA-EBID and IBID built NWs of W, Co and Pt all show marked improvements in their conductivities and purities when compared with Ga-FIB. While still less than one (Co) to two orders of magnitude above the target bulk values, these new approaches involving laser irradiation and inert gas ion beams show the potential of manufacturing high-quality and reliable integrated nanostructures with attractive electrical or magnetic properties. The convergence of these two techniques (LA-EBID and He/Ne BID) could be a tractable solution for high-quality nanoscale materials synthesis.

Chapter 2:

Helium and Neon Focused Ion Beam Etching of the Mo/Si Extreme Ultra-Violet Mirror Mask Structure

Summary

The gas field ion microscope was used to investigate helium and neon ion beam induced etching (IBIE) of nickel as a candidate technique for extreme ultraviolet (EUV) lithography mask editing. No discernible nickel etching was observed for room temperature helium exposures at 16 and 30 keV in the dose range of $1x10^{15}$-$1x10^{18}$ He^+/cm^2, however transmission electron microscopy (TEM) revealed subsurface damage to the underlying Mo/Si multilayer EUV mirror. Subsequently, neon beam induced etching at 30 keV was investigated over a similar dose range and successfully removed the entire 50 nm nickel top absorber film at a dose of ~$3x10^{17}$ Ne^+/cm^2. Similarly, TEM revealed subsurface damage in the underlying Mo/Si multilayer. To further understand the helium and neon damage, we simulated the ion-solid interactions with our EnvizION Monte-Carlo model which reasonably correlated the observed damage and bubble formation to the nuclear energy loss and the implanted inert gas concentration, respectively. A critical nuclear energy density loss of ~80 eV/nm^3 and critical implant concentration of ~$3x10^{20}$ $atoms/cm^3$ have been estimated for damage generation in the multilayer structure.

Literature Review

General Background.

Extreme-UV lithography (EUVL) is a next generation lithographic technique proposed to continue the trend of miniaturization in the nanoelectronics industry towards the 10 nm node [16-20]. However this high energy source (~13.5 nm wavelength) requires reflective masks and thus a new paradigm for the mask geometry which consists of a multilayer dielectric mirror of two different materials with alternating refractive indices and thicknesses (2-5 nm), tuned to reflect a very narrow bandwidth. To protect the multilayer stack from oxidation and damage during mask processing, a thin protective layer (~2 nm), and a top EUV absorbing layer (~50 nm) is used to produce the pattern. Currently, ion-beam or magnetron sputter deposited Mo and Si multilayer stacks are most commonly used and studied for EUV lithography which is capped by a thin ruthenium protective layer [21-25]. The Mo/Si multilayer system is chosen due to its ability to act as a mirror in the 13.5 nm wavelength region with measured reflectivity as high as ~70% (shown in figure 2.1). However, this peak reflectance occurs in a narrow spectral range where the reflectivity is only 10% at 13.0 nm and 13.7 nm wavelengths [26]. Hence, subtle variations in construction and in the material properties, such as the formation of sillicides, can be deleterious to the mask fidelity. In another similar structure, the Mo/Be system outperforms slightly the Mo/Si, but Be is less desirable due to its toxicity [27]. Thin Ru barrier layers located in between the Mo and the Si layers have resulted in substantially less silicide formation at the interfaces [28, 29]. Other barrier materials such as a-C, and B_4C have also been characterized [30]. Au, W, Ge, Cr, Ta and TaN, Ta_2O_5 have also been investigated for absorber films. As an example, Cr will exhibit an n~0.93 and a k ~0.04. The top absorber thickness is required to be ~50 nm thick for R% to be ~0%. At 0 nm thick, the R% is obviously ~70%, while for only 5 nm of thickness, the R% drops slightly (but not sufficiently low) to a reflectivity ~50%.

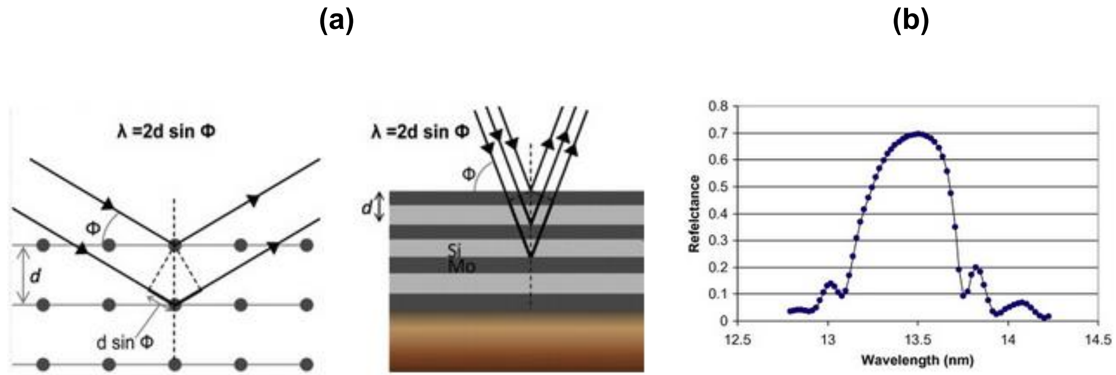

Figure 2.1. (a) Bragg's law showing constructive interference in a Mo/Si multilayer stack mirror, and (b) the reflectance from a Mo/Si mirror at near normal incidence [22].

Tantalum nitride (TaN) is the most commonly studied absorber layer, however TaN spontaneously etches when exposed to XeF_2 during mask repair, thus requiring advanced passivation schemes [31]. Nickel has superior EUV absorption over TaN, and thus is being explored here as a candidate EUV absorber layer. To be a candidate material, there must be appropriate mask repair solutions. In 1985, Vietzke and Philipps [32] investigated the high temperature erosion of nickel under 5 keV neon irradiation. They found no enhanced release of Ni atoms exceeding physical sputtering and normal thermal sublimation. One of the leading mask repair solutions is electron beam induced etching, however the low volatility of nickel halides has made it challenging to etch via focused electron beam induced etching. Hence, we have explored the new gas field ion microscope as a possible strategy for repairing opaque nickel EUV defects.

Focused electron beam (FEB) and focused ion beam (FIB) induced processing (IP) are well documented techniques [33, 34]. While gallium focused ion beam induced processing (Ga-FIBIP) has been used historically in many applications [12, 35], the resolution and gallium staining have made it obsolete as a mask repair tool [36, 37] for current and future state-of-the-art lithography masks. The enhanced resolution of the new gas field ion source (GFIS) microscope [38-40] compared to liquid gallium ion sources and the fact that the species are inert gases makes

it an intriguing option to study for mask repair. Focused helium or neon ions [40-42] seem a logical choice for mask-repair applications because their low atomic mass will dissipate less of the ion energy through nuclear loss - most of it being lost to electronic interactions [43]. Recently, helium and neon focused ion beams have been shown to be capable of high-resolution additive deposition and subtractive etching [44, 45] that is superior to the gallium focused ion beam and in some cases with enhanced material's properties relative to electron beam induced deposition [45, 46]**.** Hydrogen ions (H^+, H_2^+) generated via GFIS have also been characterized for EUVL mask repair. In this case, the authors concluded that, on actinic images, there was no difference between the repaired area and the non-repaired one [18]. Livengood et al [44, 47-52] have performed a dose-dependent study of He-beam induced damage in crystalline Si and Cu. Results demonstrated that no damage was observed up to a dose of ~$1x10^{15}$ ions/cm^2. However, at a critical dose between $1x10^{15}$ - $5x10^{16}$ He^+/cm^2 the defect density is sufficient to cause dislocations and amorphization. For doses higher than ~$5x10^{16}$ He^+/cm^2, helium is no longer soluble and the formation of subsurface nanobubbles is visible in TEM [47, 53]. These subsurface processes induce a measurable swelling in Si and Cu.

In order to optimize the optical properties during growth [54, 55] and to reduce stress in the multilayers [56-58] the thermal stability of the Mo/Si stacks for EUV applications has previously been explored [59]. Interdiffusion between the layers and the formation of molybdenum silicide intermetallics deteriorates the optical properties of the mirror. Because industrial applications require high mirror quality and lifetime, the kinetics of interdiffusion have been extensively characterized. Bozorg-Grayeli et al [60], concluded that in a multilayer system such as Mo/Si, heat transfer and dissipation between layers is substantially degraded due to a thermal conductivity 100x lower than for bulk values. This may be responsible for enhanced silicidation at the interfaces.

According to the phase diagram, molybdenum silicides (especially: Mo_5Si_3, and hexagonal and tetragonal $MoSi_2$) form at temperatures at and above 700 K and result in a net densification. The volume of one $MoSi_2$ unit cell is smaller than the summed volumes of one Mo and two Si atoms (Mo + 2Si → $MoSi_2$) by 27%. In the case of the widely investigated $MoSi_2$, its structure is hexagonal (h) and transforms to tetragonal (t) with a = 0.321 nm and c = 0.785 nm. Thus, thermal treatments have been demonstrated to result in an anomalous contraction of the multilayers [21, 59, 61, 62]. Interestingly, it has been proposed that contraction due to electron-beam induced heating may be used to locally correct phase defects in mirrors [59]. Montcalm [57] reported a measurable change in reflectivity for a 30 second anneal at 100ºC and a 2% reduction in reflectivity after 30 s at ~300 ºC. At increased temperatures, reflectance diminishes rapidly as volumetric contraction alters the optical properties of the mirror [63, 64]. TEM analysis revealed interlayer diffusion after a 1-hour anneal at 316 ºC [21]. As previously mentioned, to counteract interdiffusion several different types of diffusion barriers have been proposed [65-67].

In this chapter the He and Ne ions are explored as a method for etching a 50 nm thick nickel absorber layer on a Mo/Si multilayer EUV mask. Atomic force microscopy (AFM) and transmission electron microscopy (TEM) analysis have been performed to investigate the induced changes as a function of dose in the Mo/Si multilayer stack. The experimental results are subsequently simulated with the EnvizION Monte-Carlo modeling program [68, 69] in which we simulate the nickel sputtering process as well as the damage caused by the nuclear energy loss and implanted inert gas species.

Defect Generation and Interactions.

An invaluable topic closely related to irradiation effects in solids by a vast array of ion types is the introduction of distinguishable defect categories and their interactions which then produce the visual information we collect via TEM analysis especially. Numerous publications deal with the subject: many with mid-sized, reactive ions (more commonly those introduced in semiconductors such as B and P); others with very energetic ions (usually helium and alpha particles) in the MeV range and into relatively 'thick' targets (typically in the μm-scale); there are those reporting on the effects of heavier and reactive Ga^+ and, finally; light, inert (especially helium) ions implanted in elemental materials such as, and of special interest here, Si (c-, m-, and a-), Mo and Ni. Also of paramount technological interest are the irradiation effects on the compound SiO_2, or silica. Nevertheless, often the evaluations are done with single crystal materials. These will behave, not surprisingly, differently from our target material in this study: a multilayer structure of relatively thick nickel on bilayers of amorphous silicon and polycrystalline molybdenum.

Heavy implanted atoms tend to amorphize a target. Lighter ions with energies in the MeV range will amorphize a material, at substantially greater depths from the top impingement surface, when their nuclear energy losses become more pervasive. The effects by especially helium have been investigated in detail in single targets containing typically one element and no interfaces (or merely a single interface with a substrate material). In the case where the material exposed to the helium ions is crystalline, the extent of solubility of helium atoms in the target will be quite consequential. In general, helium and neon are have limited solubility in most materials (having positive heat of solution) which leads to a negative entropy (typically ~ -8 K) because the gas goes from a free standing state of high entropy to a locked interstitial state. For a perspective, the entropy of helium inside a bubble is larger than in a void [70]. The ion energy, dose and dose rate are parameters that also require close consideration. In many cases, a material can be bcc such

as Fe, Fe-C or Mo. In others, we may have an fcc structure like Al, Cu, Ni, and sometimes, Ni-Al alloys. These may show variations in damage effects.

Noble gases have very low solubility in crystalline materials. Nonetheless, when the target is poly-crystalline or amorphous, the inert gas species may be accommodated to higher extent. Inert gases exhibit no chemical reactivity or bonding, but can introduce extensive structural modifications in the target material. Depending on the energy and the size of the target atoms, the noble gas ion can displace host atoms, generally forward in the direction of the beam, which has been referred to as radiation biased-diffusion [71]. This scenario creates a large vacancy population near the top impingement surface. Host atoms, known as recoils move on to another spot, typically deeper within the structure and most likely coming to rest in interstitial positions. This means that within the stochastic and elastic collisional cascade, or interaction volume, from the top surface to the end of range ($R_p+2\Delta R_p$), there will be a number or density of Frenkel pair defects generated, where most vacancies reside near the top, self-interstitials closer to the end of range and most implanted atoms near the projected range. For larger doses, radiation enhanced diffusion will provide more effective vacancy-mediated diffusion paths because the bonding of lattice atoms is weakened by the earlier stages of bombardment. This makes easier the dislodging of host atoms since lower threshold energies are required. The distance or separation between the peak defect distributions depends on the ion used, its energy and the temperature of the target material. Larger ion energies generally will introduce a greater separation between vacancies and interstitial bands, therefore diminishing the chances of dynamic annealing via recombination or annihilation of defects ($V+I \rightarrow 0$). Prolonged irradiation leads to oversaturation. This oversaturation augments the effective diffusivity of solute gas atoms [72].

Most experiments are done under room temperature conditions, in which diffusion and migration is possible, however, certainly at relatively limited rates and shorter distances. In general, several migration mechanisms can be expected. These are basically: the interstitial type,

vacancy, dissociative and exchange [72]. The dissociative migration mechanism takes place when helium leaves a vacancy and enters an interstice from which it moves interstitially thereon. The exchange mechanism involves adjacent lattice atoms switching positions without the presence of vacancies [73]. The diffusion mechanism requiring the lowest activation energy will typically be the, practically athermal, interstitial type. Local heating or thermal spikes produced within a collision cascade can have a pronounced effect by enabling defect recombination. For increasing cascade energy, a larger fraction of defects may recombine. Figures 2.2 and 2.3 below show several possible migration mechanisms for an inert gas in a solid.

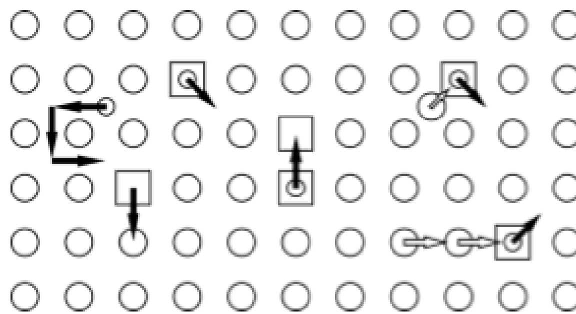

Figure 2.2. Shows possible migration mechanisms for helium. Large circles represent host atoms, smaller circles helium atoms and squares represent vacancies [74].

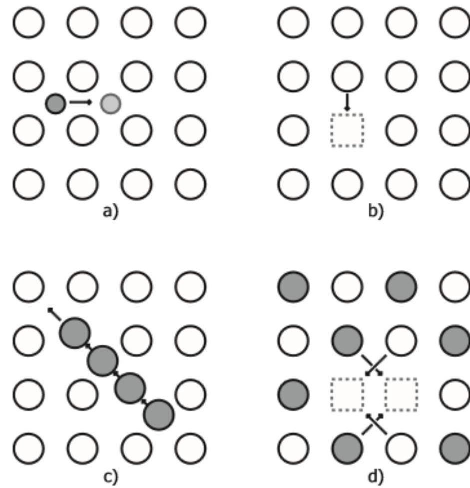

Figure 2.3. Depicted here, more specifically, are interstitial diffusion, vacancy-assisted self-diffusion, diffusion of interstitial clusters and divacancy-assisted self-diffusion [72].

In a semi-infinite target, the impinging energy dissipation is in a timescale of 10^{-12} s (~1 ps) and in a length scale of 10^{-7} to 10^{-8} m (nm-scale), within which the temperature rise along the ion track can be 10^3 to 10^4 K [$T \sim P/(\pi r \kappa)$] with subsequent quenching rates of ~10^{15} K/s [75, 76]. In the expression, P is for power (heat source, or ion beam), r is the beam spot radius and κ the thermal conductivity of the material. This can lead to the formation of a non-equilibrium amorphous phase. Generally, in metal systems, a thermal spike does not result in amorphization and resolidification of a local melt [77]. Metals typically absorb many of the Frenkel pairs produced in the earlier ballistic collisional stages. Thus the final number of defects after thermal spikes is reduced. Overlapping of collision cascades between consecutive pixels by the raster of a focused-ion beam can have an effect on the temperature profiles present within nanometer-sized bands of the exposed material. Here, the dose rate or flux (in ions/cm^2-s) can play a transformational role, but unquestionably, focused helium and neon ion beams operate at very low currents. It must be noted also that when a sample has high aspect ratio, the response may vary because of

thermal conductance constraints (geometry-limited heat transfer). For a perspective, the energy per atom required to melt material is much lower than the threshold energy to form a Frenkel pair [77].

As per A. Dubner [13], the temperature in a very small localized radius within a collision cascade region produced by a light ion in a heavier material (cylindrical rather than spherical model) can be derived by knowing several material parameters such as: mass density, heat capacity and thermal conductivity of the substrate. Of notable importance is the 'dE/dz, or ε' that represents the ion energy loss per unit length in the material. For very short durations of time, the temperature will peak and then relax back to the temperature of the substrate (typ. ~298 K), and until another ion strikes. Clearly, for larger beam currents one would expect more heating.

$$T(t) = T_0 + \frac{\varepsilon\sqrt{\rho\, c_p}}{(4\,\pi\,\kappa\, t)^{3/2}}$$

Intermixing is another factor that plays a key role in ion-solid interactions, and that has been documented as yet another side effect of ion beam irradiation. A direct relation does exist and has been documented for intermixing as a function of dose [78]. In general, intermixing increases with the square root of ion dose. Consequently, intermixing follows the same relation with time, as $t^{1/2}$ which has the same functionality as diffusion width, $w \sim (Dt)^{1/2}$. The following expression:

$$Q \sim \left[\phi\left(\frac{dE}{dz}\right)\right]^{1/2},$$

summarizes the relation between intermixing (Q) and dose (represented as ϕ here). "dE/dz" is also the energy loss per unit length. This mixed layer of Mo and Si will degrade the mirror's contrast $[(I_{max}-I_{min})/(I_{max}+I_{min})]$ that should typically be I_{max} ~70% and I_{min} ~5-10%, where I is the UV

radiation intensity. From Bozorg-Grayeli et al [60], the new width of an interdiffused region will change as a result of the diffusivity and the exposure time. The expression that summarizes this effect is shown below:

$$w^2(t) = 2Dt + w^2(0) ,$$

where w(0) is the initial layer thickness, at time=0.

At finite temperatures, all crystalline materials contain defects formed by thermally-activated processes. The quintessential expression for the concentration of defects at a given temperature is as follows, where C is the concentration of defects, C_0 the atomic density of the material, ΔF the free energy of formation for the defect. This free energy contains two terms; one for the enthalpy of formation and another for the entropy of formation.

$$C(T) = C_0 \exp(-\Delta F/k_B T), \text{ where } \Delta F = \Delta H + T\Delta S.$$

For the diffusion of a defect there is the universal expression: $D(T) = D_0 \exp(-E_A/KT)$, where E_A is the activation energy for migration. D also can be expressed in terms of other parameters such as f (a statistical factor), L (a jump length) and Γ (a jump rate): $D = \frac{1}{6} f\, L^2 \Gamma$. The 1/6 represents a probability factor that represents the chance an atomic jump may be completed in six (6) nearest neighbor directions in a crystalline environment [72].

A crystalline material always has a number of vacancies present at finite temperature. Even in the perfect crystal, vacancies can be occupied by implanted atoms which will then travel in the solid by a substitutional mechanism, or even a mixed one. Nevertheless, at room temperature, helium can diffuse rapidly interstitially in perfect fcc metals such as Ni [73, 79]. In another case, in Mo, a close to athermal diffusion takes place where helium migrates between

tetrahedral sites [73, 80]. As a result of migration, many defects agglomerate and form defect complexes. A bubble, or filled-cavity, is formed when these complexes cluster. Two growth mechanisms could be present: migration/coalescence, and Ostwald ripening [81]. Within crystalline materials, only one stable equilibrium condition for helium filled cavities is common: ~2 nm wide spherical or even discoidal bubbles. In c-Si, these can be spherical and 0.9-15 nm in size with helium concentrations up to ~1.7×10^{22} cm^{-3} [74]. This corresponds to an at. % ratio of ~3.4% He:Si. In some cases, there can be a heliophilic interfacial region, where two-dimensional platelet-filled vacancies form when it is thermodynamically favorable to wet a surface [82]. These larger entities are considered rather immobile, but under the right conditions gas atoms can be released, cross the wall energy barrier (bubble/matrix interface) and diffuse across the medium to join another cluster, or to an external surface for final desorption/exodiffusion. For emission of a single helium atom ($He_iV_j \rightarrow He + He_{i-1}V_j$) from a He_5V_1 cluster about 2.0 eV of energy is consumed [72].

Vacancy diffusion however could be enhanced by a supersaturation stage where the effective helium diffusivity rises several orders of magnitude compared to non-irradiated/non-damaged materials. This effect is commonly referred to as enhanced vacancy assisted migration. It can lead to a higher probability of precipitate nucleation. A side effect of too much irradiation reveals itself macroscopically as a dimensional instability, or swelling. This is the result of excess vacancy clustering growing to voids because they cannot recombine with interstitials that may be too far or even trapped by dislocations [82]. Peak nanobubble concentrations can be found at depths that are shallower than the helium projected range, in a region in which the radiation damage peak (maximum nuclear energy losses) is located. Gas filled nanobubbles will remain stable under irradiation as long as their volumes remain below a critical value. Above it, they will grow by capturing more vacancies. Bubbles formed by helium in c-Si have been reported at critical local concentrations of ~3.5×10^{20} cm^{-3} [81, 83, 84]. For neon, the first detectable bubbles in silicon have been found at doses at and below 5×10^{16} cm^{-2} [81, 85]. For neon also (at 60 keV), the

threshold concentration in molybdenum has been determined by Luukkainen et al to be around $3.6x10^{19}$ cm^{-3}. This corresponds to a fluence of $3x10^{17}$ neon ions/cm^2 in Mo [85].

In a crystal also, dislocations will be present, usually represented by a dislocation density in $cm^{-2.}$ Dislocations are also nucleation sites for bubbles [81, 84, 86]. Nanobubbles consist of an agglomeration of vacancies which helium uses to diffuse or binds with in order to form the defect complexes. Helium can assume several He-V configurations when embedded in the bulk of a material. Most helium (He) and vacancy (V) complexes are the following: He_5V, He_1V_2 (divacancy) and He_1V_1. Each has an enthalpy of formation associated with them (for He_1V_1 ~2.3 eV) and it is the HeV_2 that has the lowest formation energy at ~0.3 eV [74, 87]. The later will then be the most numerous defect complex generated at low temperatures. Vacancies and thus implanted helium atoms using a vacancy migration mechanism (or even a mixed migration mechanism), tend to agglomerate and coalesce at dislocation lines. Recall that helium typically can move in a solid interstitially, by vacancies and by a combination thereof (dissociative and exchange). Eventually, this effect has been found to harden materials, but sometimes to the extent of intergranular embrittlement. Hence, bubble formation tends to disrupt dislocation motion [88].

Another type of extended defect, indeed not present in single crystals, is a grain boundary and interfaces that have been described as excellent heterogeneous nucleation sites or defect sinks [84, 87]. In poly-crystalline materials, vacancy-rich structures tend to exist within a grain interior, while interstitials predominate in grain boundaries. Enhanced annihilation could be present where excess interstitials at grain boundaries cross the boundary (interstitial emission) into the grain interior and strongly react with vacancies there. However, the mobility of 'large' defects is hindered, and in order to diffuse further, single interstitial emission with higher mobilities takes place. These can cluster and grow relatively large. Accommodation is high at the free volume provided by grain boundaries and interfaces. In fact, there is a competition between stable interstitial clustering and trapping/absorption of interstitials at grain boundaries. At interfaces, it

has been documented that tensile strains will be induced by irradiation into initially latticed-matched layers [89].

Crystalline silicon forms an amorphous band and has been estimated that a critical value of energy deposition per unit volume in the order of 500 eV/nm^3 [90] is a reasonable criterion for the onset of amorphization in c-Si. Conversely, polycrystalline silicon shows no amorphous band, it shows little interstitial clustering, no denudation inside grains (as seen in metals), and exhibits preferential helium decoration on grain boundaries [84]. Typically, larger and more irregularly shaped bubbles are observed in poly-Si due to increased accommodation of vacancies. Unlike in c-Si, in poly-Si, defects such as the {311} rodlike defects and dislocation loops are not observed for room temperature implantation. Once again, the accommodation of interstitials within the free volume of grain boundaries plays a major role in eliminating these from the bulk. This results in improved radiation resistance in poly-Si when compared with c-Si [84]. On the other hand, in amorphous silicon (a-Si), the diffusivities of helium have been found to be substantially lower than in c-Si, which itself shows high permeability [71]. This may be the result of shorter mean free paths in a-Si. When helium is implanted in an amorphous alloy, where no clear crystallographic features are present, the bubble density does not saturate to a constant value as in poly-crystalline materials [84]. Therefore, no over-pressurized bubbles are expected in an amorphous material. Indeed, there should be a continuing accumulation of implanted gas here. Helium bubbles have not been observed in silica [83]. The migration in silica has been determined to be high enough leading to rapid helium diffusion out of this material.

In nickel, helium interstitial migration has been found to be quite large because of low activation energy (E_A), at only ~0.03 eV. Molybdenum also has a low interstitial activation energy of E_A ~0.05 eV [72]. In addition, another pathway known as pipe diffusion in nickel has been determined to have low activation energy of ~0.2 eV [73]. In nickel, it is thought that helium atoms migrate by a dissociative mechanism and that they are trapped by vacancies to become

substitutional helium atoms [91]. Typically, for vacancy migration around 1.3 eV in energy needs to be expended [72]. In poly-Ni, grain boundaries are strong trapping sites for interstitial helium. Helium implants interstitially in most cases in bcc as well as in fcc materials. As mentioned previously, in metals, the clustering of five helium atoms with one vacancy is not uncommon: He_5V_1. Ni, since it does not have a closed-shell electronic configuration [79], does not retain more helium than other fcc metals (such as Pd). In a Mo crystal, helium can be assumed to cluster in Mo vacancy positions. The interstitial helium can migrate to boundaries from where it will be released to the surroundings. Mo lattice atoms close to a cluster are significantly displaced from their equilibrium positions. The stress in the crystal results in an increase in stored elastic energy. This is common in bcc metals where the binding energy decreases when the number of helium atoms in a cluster increases [82].

Inert gases have very low solubility in crystalline metals which leads to over-pressurized bubbles (typically, 1-3 GPa). In this case, the vacancy supply is too low to relax a bubble to an equilibrium size. Pressures in a cavity at equilibrium (it neither expands nor contracts) can be expressed as: $P_{He} + P_V = P_C$, where P_{He} is the pressure from trapped He gas, P_V, pressure due to the osmotic effect, and P_C, the capillary pressure [82]. The pressure-radius relationship for stable bubbles is given by the equation below, where p is the pressure, γ the surface free energy, μ the shear modulus, b the Burger's vector and r_b is the bubble radius:

$$\boldsymbol{p = \frac{2\gamma}{rb} + \frac{\mu b}{rb}}$$

The concentration of atoms inside a bubble can be approximated by the equation below also relating it with the bubble radius [85]. In this case, concentration C is in at.%, n_0 is atomic density of host matrix in $Å^{-3}$, n_{Ne} is the gas density in the bubble also in $Å^{-3}$, V_b the bubble volume and r_b the bubble radius:

$$C_b(C) = \frac{n_0\, C}{V_b\,(100-C)n_{Ne}+C_{n0}}\ , where\ \ V_b = \frac{4}{3}\,\pi <r_b>^3 .$$

On a closely related note, EELS analysis of the plasmonic absorption (1s→2p transition) by individual nanobubbles containing helium gas has shown peak shifts from free helium at 21.218 eV to 22.6 eV (K-edge). The K-edge is not too close to the Si plasmon thus allowing for good signal extraction. The peak is a result of short range Pauli repulsion between electrons in neighboring atoms. This corresponds to an estimated helium density inside the bubble of ~28 atoms/nm^3. The gas density can be determined using the following equation: $\Delta E = C \times n_{He}$, where ΔE is the energy shift, C is a constant of proportionality determined theoretically for He bubbles in metals to be 0.016-0.044 eV/nm^3, and finally n_{He} is the helium density [74, 92].

For neon, it has been found that bubble sizes are smaller with higher pressures for metals with higher elasticity moduli [93]. In Mo, bubbles will have a tendency to be smaller and grow more slowly [85]. Molybdenum has one of the highest Young's modulus and bulk modulus known, at 329 and 261 GPa, respectively. Enhanced coarsening near the surface of nickel has also been reported. This has been attributed to Ostwald ripening effects. However, in general, intuition would suggest that the proximity of a surface would inhibit bubble growth. Neon typically produces about 5x more Frenkel pairs than helium [81]. Not surprisingly, a fraction of these survive the displacement cascade recombination. Individual neon atoms and Ne-V complexes are thought to have low mobility in Si. Values for neon interstitial formation and migration in silicon have been computed at as high as ~3.6-5.6 eV [94]. Nevertheless, some neon movement is inferred because experimental observations do not agree with TRIM predictions. Stable bubble nuclei in the form Ne_n-V_m are reached at the threshold neon concentrations. Thereon, these clusters tend to form isolated bubbles. Implanted neon atoms tend to move into large size voids created by the

implantation and transform these into bubbles. Proximity to a surface essentially inhibits bubble growth [93].

It is important also to recall that in pure metals amorphization is negligible [75]. This has been rationalized to be due to the lack of directional bonding as in covalent materials where amorphization is normally observed. Covalent systems such as c-Si, show marked orientational effects such as more diffusion along the closely-packed directions [95]. In covalent bonds and semiconductors, relaxations are not homogeneous, but are in a preferred direction (known also as coordination defects). The defects introduced by the collisional cascade can be electrically active therefore introducing deep level states in a semiconductor band gap [81]. The most stable arrangement for helium in c-Si is in a tetrahedral interstitial with formation energies of 0.77-1.28 eV [94]. Nevertheless, lattice distortions resulting from higher doses open easy pathways for gas diffusion. This is referred to as surface dimerization [94]. In many ceramic materials, especially in ionic solids, point defects can have an effective charge that results in traps for electrons or for holes [96]. The effect of this induced internal electric field in ceramics will impact diffusion behavior differently than in metals. Oxides may contain damaged boundaries that can lead to electrostatic interactions that are longer ranged and stronger than the elastic interactions dominating in metals [82]. In oxides, bubbles are in thermal equilibrium.

Helium bubbles can also form superlattices as seen in Cu and in Ni [97]. Ordering of bubbles normally coincides with the ion beam direction. Vacancies emerge in Mo and agglomerate into voids. Ordered nanopores can have diameters of ~5-7 nm, and lattice spacing ~20-30 nm [98]. Similar phenomena has been observed in W, Nb, Ni, and alloys. Voids grow and undergo ordering under continuing irradiation at about 0.3-0.4T_m. The ratio between separation distance and void radius is 3.1 for bcc and 2.2 for fcc crystals. This is a self-assembled void lattice relying upon a balance of repulsive and attractive forces within an asymmetric strain field. The elastic energy is minimized when the voids/bubbles organize in preferred directions by anisotropic

diffusion. These are close enough within each other's elastic fields, and can cause unaligned voids to shrink and disappear [98].

In a material, a variety of reactions between defects may take place. Of notice are those listed in table 2.1 below. In it, A stands for a dopant atom (He, Ne), and S for a surface. For a single interstitial (I) and a single vacancy (V), a reaction radius is defined as a constant r_0. Each defect has an inherent reaction radius. For a single vacancy and a single interstitial, r_0 will be about 0.4a, where a is the lattice constant. This means that when a vacancy and an interstitial are separated by 0.8a they can recombine. The capture radius is consistent with experimental data. It sets a limit of ~1 nm for vacancy-interstitial recombination while for a dopant like B and a vacancy (in c-Si) this capture radius drops to ~0.5 nm.

Table 2.1. Reactions between defects leading to clustering, complex interaction or annihilation [99].

Reactants	Products	Description
$V_n + V_m$	V_{n+m}	Vacancy clustering
$I_n + I_m$	I_{n+m}	Interstitial clustering
$V + V_nA$	$V_{n+1}A$	Complex interaction
$I + I_nA$	$I_{n+1}A$	Complex interaction
$V + I_nA$	$I_{n-1}A$	Vacancy annihilation
$I + V_nA$	$V_{n-1}A$	Interstitial annihilation
V + S	S	Vacancy annihilation
I + S	S	Interstitial annihilation
V + I	0	Total annihilation

Experimental Methods

The Ru-capped (2.5 nm) m-Mo/a-Si (40x7 nm) bilayer stacks were prepared on silicon wafers by Lawrence Livermore National Laboratory (LLNL) using an ion beam sputtering process. Two sets of samples were prepared, namely; one with a 50 nm nickel top absorbing layer and another without the nickel.

The room temperature helium exposures were performed with a Zeiss Orion microscope at the National Institute of Standards Technology (NIST). Rectangles of 0.5 μm x 5.0 μm were scanned with a 2 pA current and a 1 μs dwell time in a serpentine fashion at 16 and 30 kV. The doses ranged from $3\text{x}10^{14}$ to $1\text{x}10^{19}$ He^{+}/cm^{2}. Scanning electron microscopy (SEM) imaging of the helium and neon exposures were performed with a Zeiss Auriga Cross Beam and with an FEI Nova Lab 600 Dual Beam. TEM samples were prepared with the Auriga Cross Beam system and a Kleindiek micromanipulator. TEM analysis was done with a Zeiss Libra 200MC. Energy dispersive x-ray spectroscopy (EDXS) was performed with the Bruker Quantax system attached to the Libra 200. AFM measurements were performed in tapping mode with a Veeco Dimension 3100.

The neon exposures at room temperature were made at Carl Zeiss Microscopy in Peabody, MA using an Orion gas field ion microscope. Rectangles of 0.1 μm x 1.5 μm were scanned with a 30 kV beam, a current of 0.5 pA, a 0.3 μs dwell time, a 10 μs refresh time, 1 nm x 1 nm spacing (101x1501 dwell points) in a serpentine fashion and at 0° incidence. A set of eight rectangular exposures was patterned using a Fibics NPVE pattern generator. The doses ranged from 0.1 to 1.5 $nC/\mu m^{2}$ in increments of 0.2 $nC/\mu m^{2}$ ($6.25\text{x}10^{16}$ to $9.38\text{x}10^{17}$ Ne^{+}/cm^{2}). At the highest dose of 1.5 $nC/\mu m^{2}$, the total duration of the exposure run was recorded as 52 s (152 ms/frame). Increasing doses were realized by increasing the number of loops as follows: 23, 69,

115, 162, 208, 254, 300 & 346 loops for 0.1, 0.3, 0.5, 0.7, 0.9, 1.1, 1.3 & 1.5 nC/μm^2, respectively. The chamber base pressure without neon was ~$4x10^{-7}$ Torr and after the neon valve was opened the pressure stabilized at 2.5 x 10^{-6} Torr. The source trimer was stable during the entire test and did not require new tip formation. Milling was carried out at a working distance (WD) of 6.1 mm and with a 20 μm aperture.

SRIM/TRIM [14] simulations were initially performed in order to obtain predictive information for the experiment. Subsequently Monte-Carlo ion-solid simulations were performed using the EnvizION simulation. Exposures of 100k and 150k ions per run were simulated for helium and for neon, respectively. The raster grid was 10 nm x 10 nm, with 1 nm FWHM pixels, 2 nm pixel spacing and a dwell time of 0.5 μs. In order to simulate the multilayer, each scattering event is randomized to be either from Mo or Si in accordance with their volumetric ratio in the structure (taken as 60% Mo and 40% Si). The binding energy of nickel was assumed to be 4.46 eV, which corresponds to its heat of sublimation.

Results and Discussion

Predictions Based on SRIM/TRIM.

The sputtering yields (in atoms/ion) by Ne^+ calculated with SRIM/TRIM (using a 1000 ion run) for each component in the mask were: Ni (3.20), Ru (2.37), Mo (1.76) and Si (1.08). Predictions by SRIM/TRIM have been found generally to be overestimates, but good reference starting points for another simulation or experiment. In terms of vacancy generation (in vacancies/ion), the results for 30 keV Ne^+ are: Ni (0.136), Ru (0.116), Mo (0.080) and Si (0.146). According to the

diagrams below in figure 2.4, at 30 keV Ne^{+}, Ni shows the largest nuclear energy loss of all the mask components. It is actually, 2.3x its electronic energy loss (for helium, this same ratio is only 0.1x). When comparing helium with neon, the nuclear energy loss turns out to be 30x greater for neon in nickel. Importantly, the nuclear energy losses for neon in nickel at 30 and at 10 keV are about the same (only 1.04x difference).

Figure 2.4. Electronic and nuclear energy losses (in eV/nm) for helium (a,b) and for neon (c,d) in each of the components individually of the EUV mirror structure, as predicted by SRIM/TRIM. On e) and f), a comparison between neon and helium only on nickel. The nuclear energy loss in nickel is essential to bringing about sputtering of the top absorber layer in the mask.

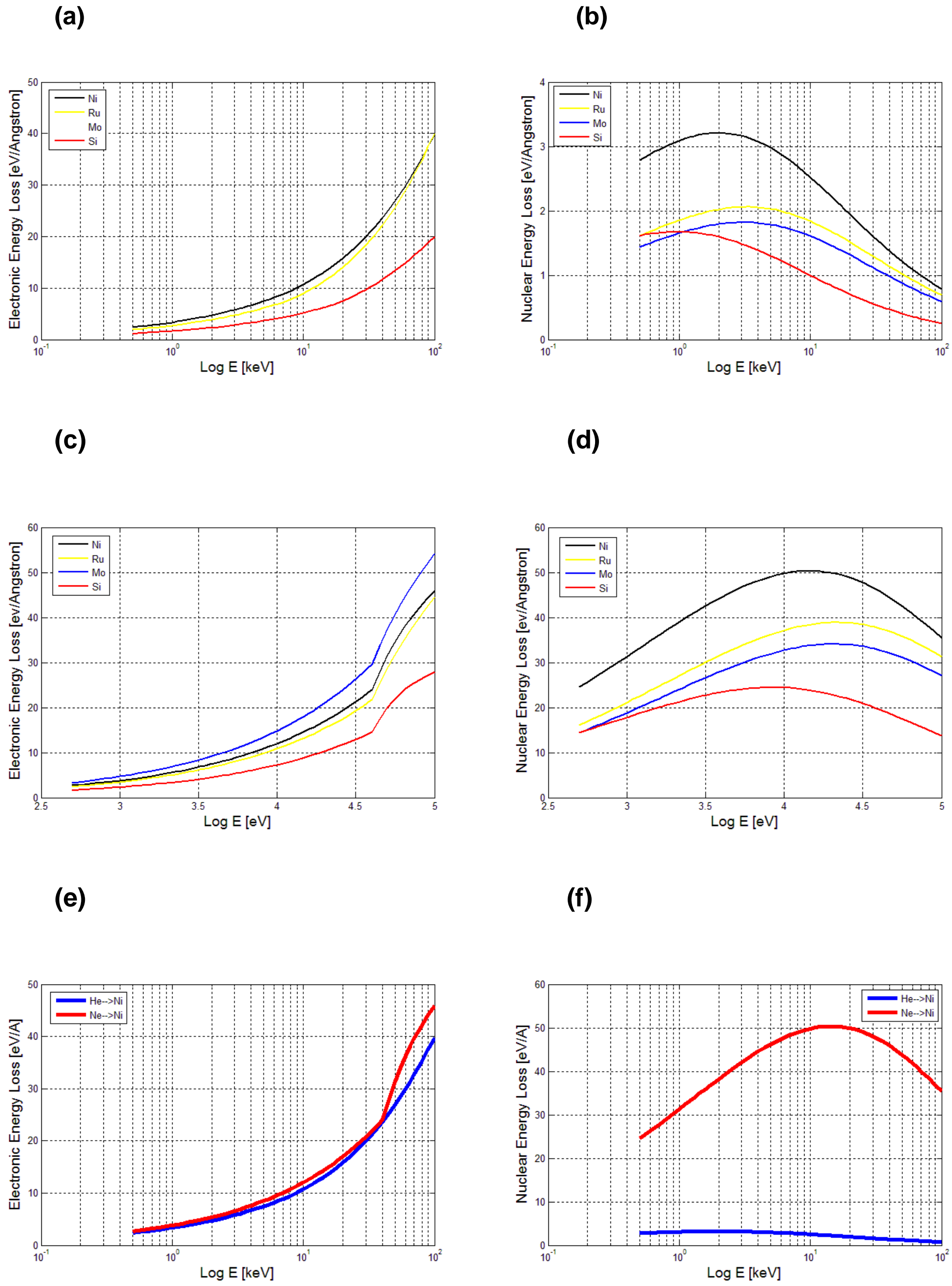

Figure 2.4. Continued.

Table 2.2. Summary of individual component's properties.

Element	A	Z (g/mol)	Tm (K)	Density (g/cc)	c_p (J/mol-K)	κ (W/m-K)	CTE (μm/m-K)	ρ (μΩ-cm)	E (GPa)	B (GPa)
He	2	4								
Ne	10	20								
Ni	28	59	1728	8.91	26.07	90.9	13.4	6.9	170	180
Ru	44	101	2607	10.65	24.06	117	6.4	7.1	447	220
Mo	42	96	2896	10.28	24.06	138	4.8	5.3	329	261
a-Si	14	28	1687	2.33	19.79	20	2.6	10^{11}	107	100

Focused Helium Beam Exposures.

TEM cross-sectional images were obtained for doses ranging from $1x10^{16}$ to $1x10^{18}$ He^+/cm^2 and for two beam energies, 16 and 30 keV. Figure 4 shows TEM micrographs of the exposed Ni-Mo/Si multilayer films as a function of increasing dose. The results demonstrate that the film stack contracts slightly with increasing dose, while there is no evidence of nickel etching. Also evident is a clear "beam interaction region" which emerges at the $5x10^{16}$ dose and is more obvious at the dose of ~$1x10^{17}$ ions/cm^2. Finally, Figure 2.5 e) & j) shows significant swelling at a higher dose of $1x10^{18}$ ions/cm^2 with noticeable bubble formation. Note that the bottom silicon substrates are aligned from a) to j) indicating the small changes in the thickness of the multilayer stack. Specifically, there is a series of contractions up to the $5x10^{16}$ dose, a smaller increase at $1x10^{17}$ (onset of swelling), followed finally by a dramatic ~180 nm expansion at $1x10^{18}$ He^+/cm^2. Figure 2.6 shows AFM data with measured heights as a function of helium ion doses. Aside from the contractions and swelling, we also observe (and measured via AFM) slight depressions, which

indicate subsurface contractions. The depressions are dose dependent and TEM analysis rules out ion-beam induced surface sputtering since there is no measurable reduction in the thickness of the Ni top layer. Shrinkage is consistent with silicidation as more energy is deposited with higher doses. This increases the probability that the required activation energy for Mo/Si interdiffusion is overcome and hence the stack densifies. These observations are consistent with the results of Livengood et al and can be explained by nuclear energy loss of the helium atoms causing beam induced mixing. At sufficiently high concentrations this leads to the formation of helium nanobubbles. Bubbling has been documented previously, especially in studies involving helium irradiation effects on silicon and silica substrates [53, 100]. It it clear from these micrographs that helium, under these conditions, is not viable for nickel etching.

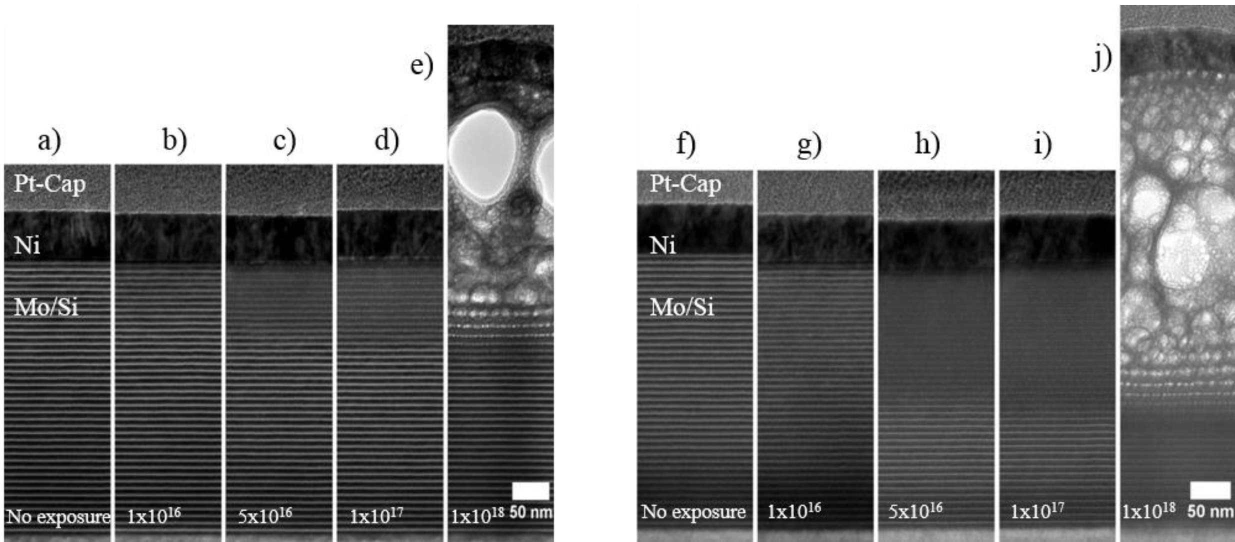

Figure 2.5. TEM cross-sectional micrographs of nickel on top of a Mo/Si multilayer stack that was exposed to 16 (a-e) and to 30 (f-j) keV helium ion energies in doses ranging from $1x10^{16}$ to $1x10^{18}$ ions/cm^2. The direction of the incident He^+ beam is normal to the top side of each panel from a) to j). Ions travel from top down across the image until they come to rest. The silicon substrate is seen on the bottom of each micrograph and aligned with the adjacent images.

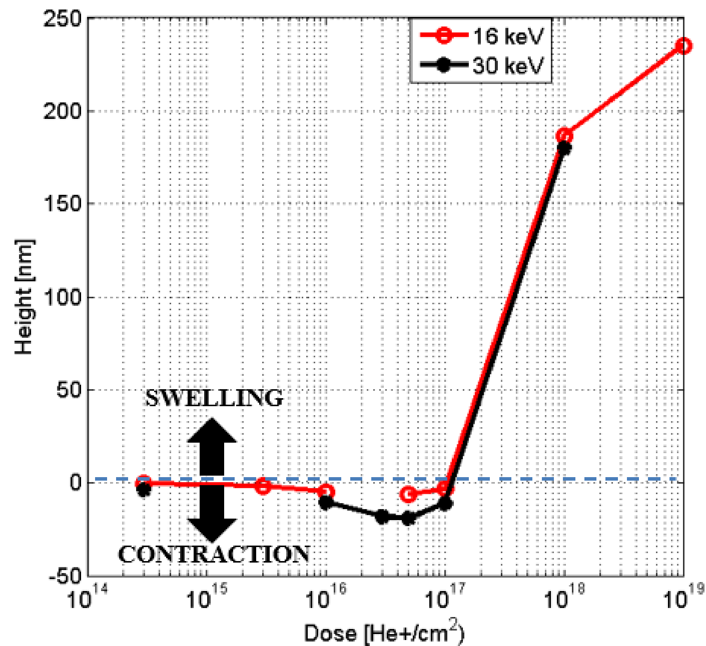

Figure 2.6. Plot of AFM data at 16 and 30 keV showing measured heights of exposed areas at different doses from $3x10^{14}$ to $1x10^{19}$ He^+/cm^2.

A closer inspection of the multilayer stack after exposure (figure 2.7a), reveals a thinning down of the silicon layer and intermixing of the Mo/Si layers which is also shown in the energy filtered TEM image (figure 2.7b). The intermixing is attributed to the nuclear energy loss via either thermal spike or knock-on processes. Heating is possible and exacerbated since inter-planar heat transfer is hindered by the many interfaces present in such multilayer systems. Moreover, bubbles are observed in the amorphous silicon layer (bright regions) within the stack (figure 2.7c). The observation that the bubble formation is preferential to the silicon layers (as seen in 2.7d) may be explained by a lower solubility limit for helium in silicon. Additionally, amorphous silicon (50-100 GPa, 0.13 GPa) [58] has significantly lower modulus of elasticity and yield strength, with respect to molybdenum (329 GPa, 0.45 GPa). Hence, we expect Si to elastically deform more under the

same internal stress and plastically deform at a lower dose than Mo due to strains introduced by the implanted helium atoms.

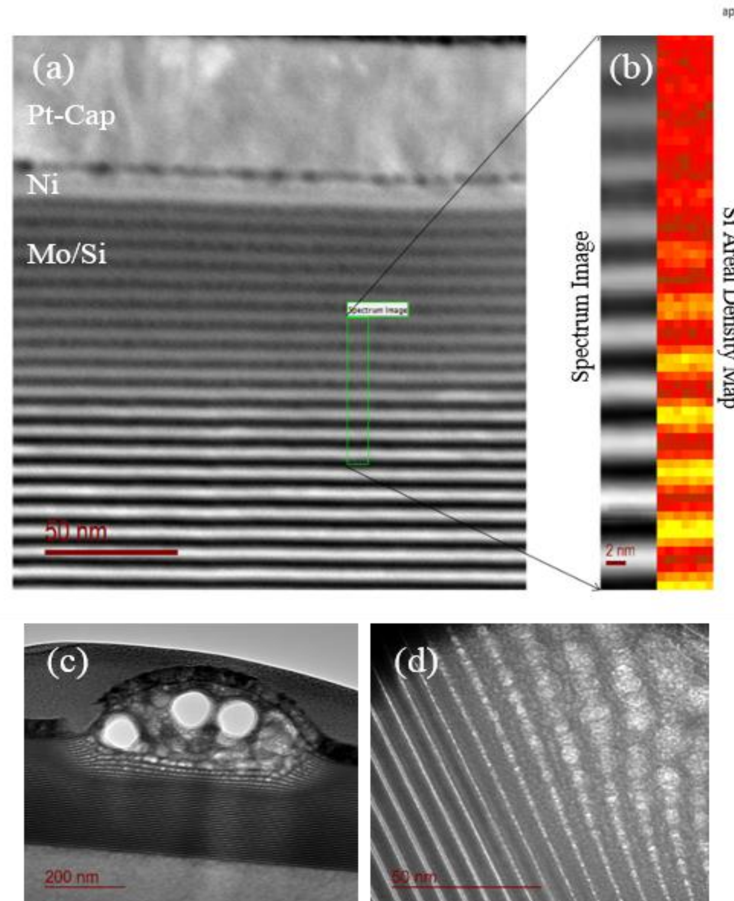

Figure 2.7. High magnification Z-contrast image of a 30 keV, $1x10^{17}$ He^{+}/cm^{2} exposure (a). Spectrum image and a silicon areal density map (b). At higher doses, such as $1x10^{18}$ He^{+}/cm^{2} severe bubbling is observed which originates preferentially in the silicon layer of the stack, as shown in c & d.

The micrograph in figure 2.8a makes it quite evident that the silicon layers nearest to the nickel top layer were consumed and thinned. The top multilayers (damaged) are more diffuse and less well-defined than those deeper in the structure (undamaged). EELS analysis (figure 2.8b) at two different locations in the multilayer stack indicate that the un-affected region are characteristic of a-Si and the damaged region is characteristic of reacted silicon which is suggestive of silicide formation. Energy transfer through direct knock-on is more probable for Si than Mo due to the relatively low atomic mass difference between silicon and helium. Additionally, the heat of sublimation for Si (359 kJ/mol) is much lower than Mo (617 kJ/mol), thus it requires less energy to dislodge Si from its lattice position than Mo. Hence, silicon is expected to preferentially be knocked out of its lattice relative to molybdenum and thus create vacancies for the helium atoms to occupy. The diffuse appearance of the silicon layers closest to the beam impingement surface indicates that many silicon atoms have been scattered, most likely forward as the momentum vector of the incident ions points downward deeper into the stack.

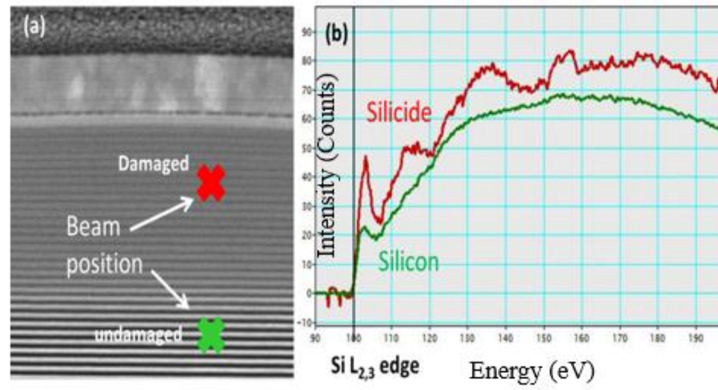

Figure 2.8. Z-contrast TEM image illustrating two comparable EELS spectra taken in the Mo/Si multilayers. The green mark in (a) represents an undamaged region, while the red mark represents a damaged region. The corresponding EELS spectra are shown in (b). The Si $L_{2,3}$ edge in the undamaged region corresponds to typical a-Si, while in the damaged region it shows characteristic silicide signatures.

Noteworthy, the a-Si layers closest to the top impingement surface of the ion beam have thinned down (fig 2.9). This in a low temperature regime can be the result of a collisional cascade diffusion mechanism. As atoms are knocked off their positions in the layer they acquire kinetic energy to move deeper inside the stack and come to rest in a new position. The mass transfer by collision cascade may account for part of the relocations. The periodicity from a line center to the next has decreased nearest to the top surface (6.12-6.43 nm). On the undamaged region, the periodicity is normally 6.9 nm. However, and as per Bozorg-Grayeli et al, in a multilayer structure made up by nanometric layers, which is the case of the Mo/Si EUV stack, there will be severe heat transport limitations. Boundaries, or barriers, exist at each interface, not too far away (a few nm) from where bursts of heat are engendered. This leads to a poor inter-planar, or out-of-plane, heat conductance. Most of the heat, in a semi-infinite target, will be expected to move laterally. Bozorg adds that the thermal conductivity of a good thermal conductor can become as low as

~1.5 W/m-K for layers of this kind. This creates the possibility of diffusivity via thermal excitation impacting the a-Si layer thicknesses. The denser material (Mo) should encounter little resistance to diffusing into the open structure of a-Si. The resulting intermixing increases with dose and thus with time, leading to the $(Dt)^{1/2}$ dependence. The initially pure a-Si layers (bright) have been replaced with a new interface (gray) made up by mixtures of Mo/Si (between dark and bright). Here the new layer density will be somewhere between the densities of pure Si and pure Mo.

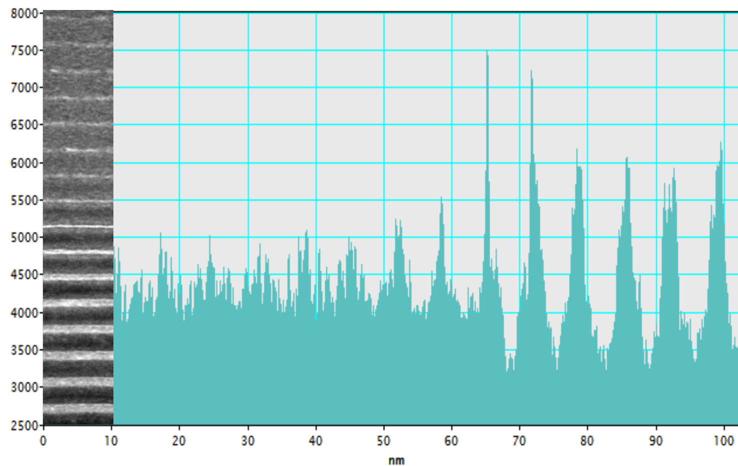

Figure 2.9. Closer look at condition of a-Si layers in the stack closest to the beam irradiated, or damaged, region by helium. On the right, in b), a line profile showing the line widths increasing as the scan moved away from the irradiated zone. Near the damaged area, the layers are so intermixed that each individual a-Si layer is almost indistinguishable.

Selected Area Diffraction (SAD) analysis, in figure 2.10, on the new intermixed region did not yield a crystalline pattern for $MoSi_2$. An amorphous ring is part of the image however, which may indicate an amorphous molybdenum silicide. Since the molybdenum layers are poly-crystalline, a plane signal was picked up by SAD and this was found to correspond to a [110]

direction for Mo grains. The line profiling does not provide a clearest result especially around the thinned layers since the contrast is not as sharp as for the layers deeper in the structure, as seen also in the figure below.

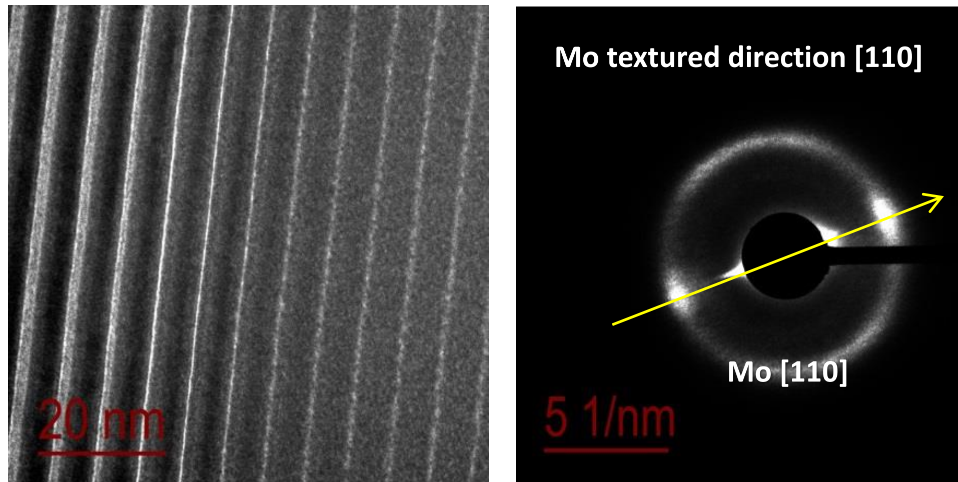

Figure 2.10. SAD analysis on the intermixed region in search of crystalline structure for Mo/Si, namely $MoSi_2$. Diffraction peaks for polycrystalline Mo were identified, while otherwise only an amorphous ring for Mo/Si was observed.

For a helium nanobubble, the low loss peak (figure 2.11) was identified at ~17.478 eV. Another peak is observed in the EELS low loss region at 34 eV. These can be linked to interband transitions of electrons in the trapped gas. For free helium, the peak is located at 21.218 eV, and a shift in its position can be directly related to a pressurized condition where a number of helium atoms are contained within a small volume, the bubble. A histogram was generated from the 30 keV, $1x10^{18}$ He^{+}/cm^{2} dose that produced the discernible irregularly-shaped bubble pattern in the structure (figure 2.12). The results show that while most of the nanobubbles are small and <5nm

(90% of them), there is an intermediate distribution of nanobubbles with sizes up to 33 nm. The number of nanobubbles (sample size) accounted for was quite large, at 386.

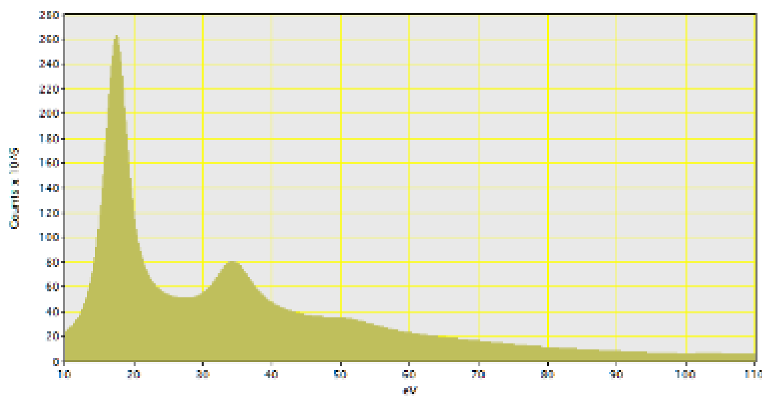

Figure 2.11. Low loss EELS plot showing a peak for helium valence electron energy transition when exposed to the 200 keV electron irradiation beam.

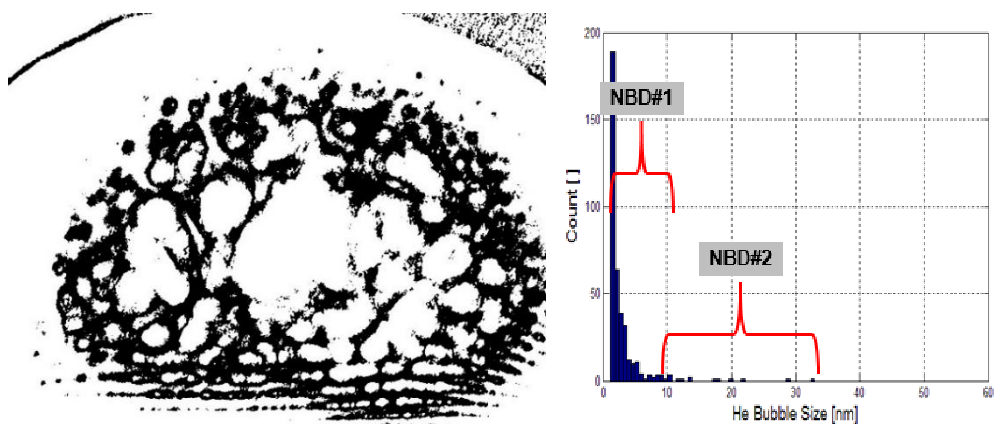

Figure 2.12. For 30 keV He^+ and $1x10^{18}$ ions/cm^2, showing in a) the TEM adjusted image with modified contrast limits (min, max) and brightness in order to carry out a particle size analysis as in the histogram on the right (b). Area was converted to diameter by assuming all were circular.

Helium Ion-Solid Modeling.

In order to better understand the observed damage induced by the helium irradiation, we simulated the energy loss associated with the 16 and 30 keV helium ion with our EnvizION simulation. From AFM and TEM imaging it is evident that the depth of the depression as well as the damaged region is greater for the 30 keV sample than 16 keV at the same dose. These observations are supported by the simulations. Silicide formation may be thermally induced or via knock-on collisions as described earlier. In both cases the nuclear energy loss is responsible, thus we can correlate the nuclear energy density loss to the observed damage profiles. In figure 2.13, the volumetric electronic and nuclear losses in eV/nm^3 for He^+ at 30 kV have been mapped. A simulation run of ~100k helium ions raster scanned over a 10nmx10nm area corresponds to an experimental dose of $1x10^{17}$ ions/cm^2. Near the surface of impingement, the ratio at the maximum energy loss between electronic and nuclear stopping is ~32, which is consistent with the lack of measurable sputtering of nickel by helium. Examining the simulated depth of the nuclear stopping energy density reveals good agreement with the observed damage profile in the TEM images and allows us to estimate an energy threshold for the observed damage. The 16 keV simulations were performed and, as shown also in figure 2.14a, the simulated nuclear energy threshold of ~80 eV/nm^3 correlates well with the damage threshold for the $1x10^{17}$ helium ions/cm^2 dose. Similarly, the simulated nuclear energy loss for 30 keV He^+ shows a clear range down to ~180 nm as can be seen also in figure 2.14b below. Beyond this depth, damage (halo) is not recognizable. At 30 keV the most significant nuclear loss remains close to the top surface and within the nickel layer. Based on these results, the nuclear energy loss near the top of the Mo/Si stack is still sufficient to induce some intermixing of Si and Mo. In this region, a critical energy density for silicidation has been estimated from the simulation to be ~80-100 eV/nm^3. As mentioned before, greater nuclear loss occurs within the nickel top layer, however the ductile metal film can apparently accommodate the energy loss in part by some observed grain growth. At $1x10^{17}$ He^+/cm^2, a critical

implant concentration for damage has been determined to be ~$2.5x10^{20}$ He/cm^3 (in close agreement with data for He in Si published by Nguyen et al [100]). This corresponds to ~0.5% He in Si, or a solubility of near 1 He: 200 Si. This agrees with Reutov and Sokhatski [53] where bubbles caused by a 17 keV He^+ beam in Si constituted ~1.6% of the volume. In our study, a 0.5% He content (1 He:62 Si) had not yet induced the formation of discernible nanobubbles in Mo/Si.

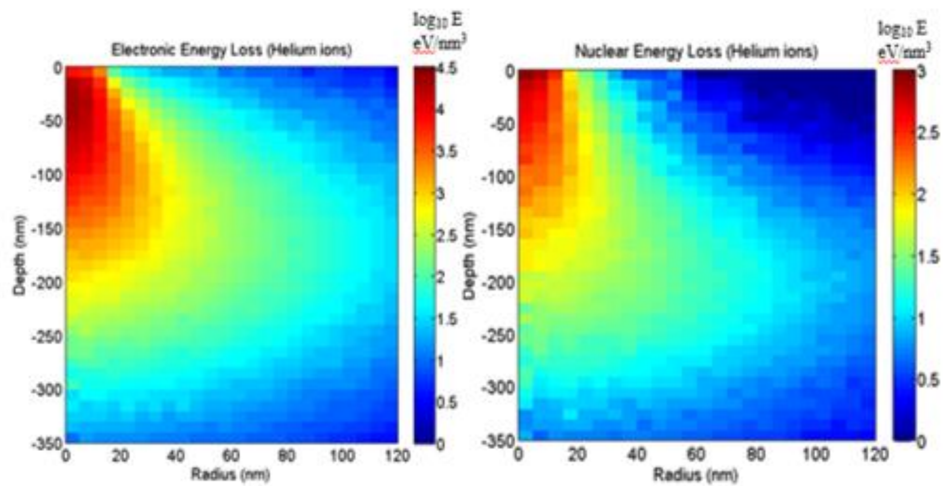

Figure 2.13. Simulated electronic and nuclear volumetric energy losses for helium ions at 30 keV at a dose of $1x10^{17}$ ions/cm^2.

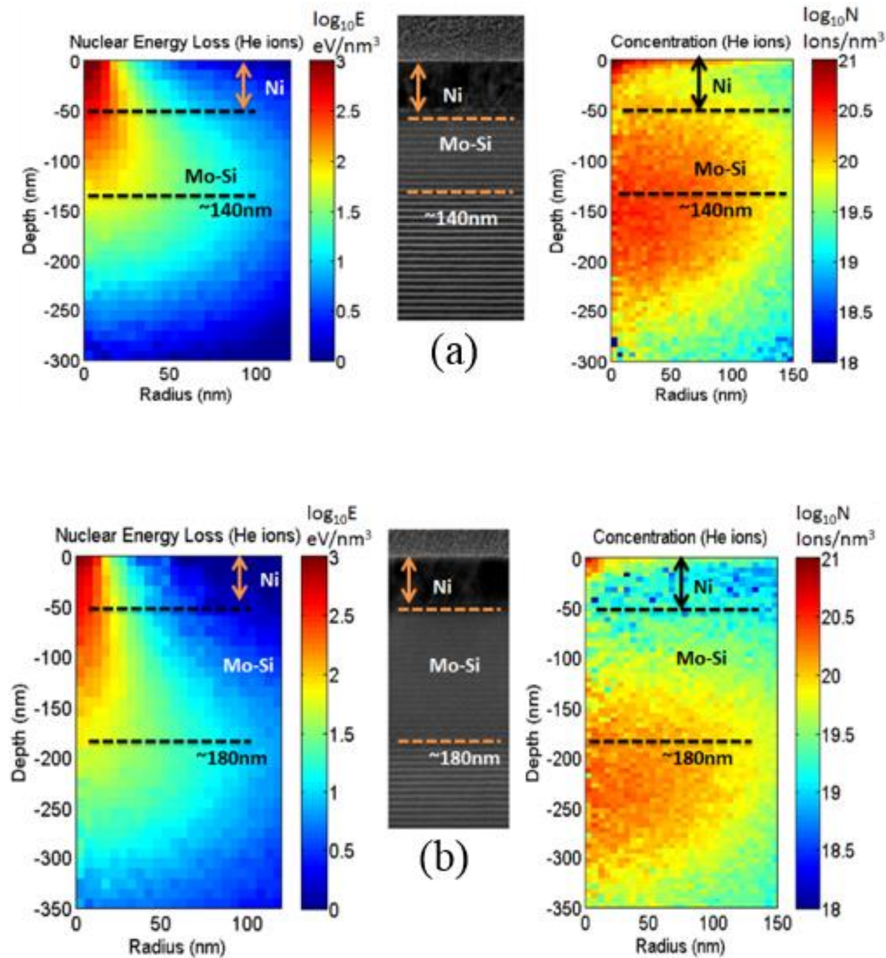

Figure 2.14. Simulated nuclear energy loss in eV/nm^3 (left) and the resultant helium implant concentrations in atoms/cm^3 (on right) are compared to the experimental TEM micrograph exposed to 16 keV at a dose of 2x10^{17} He$^+$/cm^2. In b), the same as in a), but for 30 keV He$^+$.

Preliminary Experiments with Nickel Etching.

Etching was accomplished on nickel by using a neon ion beam. Figure 2.15 shows a tilted view of a 1 mm x 1 mm box etched by neon. At this dose, it is discernible that the nickel has been etched away and the bottom of the box was somewhere within the oxide layer. In the same image, the darker and gray scale features can be explained by a milling process that is not absolutely homogeneous, thus generating some roughness on a non-uniform floor of the etch. The darker

areas are deeper etches, or valleys surrounded by taller regions, or hills. Next, an array (6x6) of 200nm x 200nm boxes was prepared to demonstrate the feasibility of preparing such nanostructures for some functionality in the future, or, as in our case, to study the effect of increasing ion dose from left to right on the grid. In figures c and d, an attempt to have a reactive etch of nickel by using neon ions did not produce the expected results. It shows damage on the nickel caused by milling, but the reactive gas, XeF_2, is apparently dissociated and reacts with the nickel, causing it to form NiF_2 (a solid not a gas). The NiF_x apparently retards the etch as it likely has a lower sputter yield relative to metallic nickel.

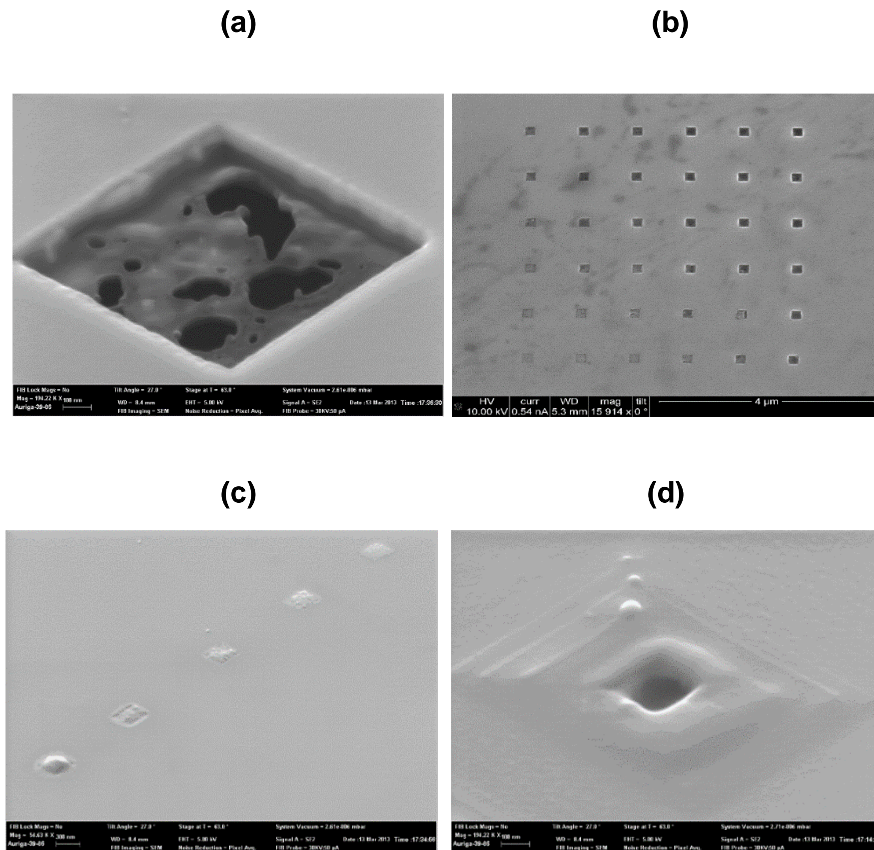

Figure 2.15. A 1μm^2 etch box by neon on Ni(50 nm)/SiO_2/Si (in a). In b), a 6x6 array of 200nm x 200nm etched nanoholes on the nickel top layer in the same sample as in a). Doses increased from left to right on each row. In c) and d), results of using the reactive gas, XeF_2, along with the Ne^+ beam, on the nickel surface.

Focused Neon Beam Exposures.

Figures 2.16 and 2.17 show a top view SEM (in #16) with its corresponding sequential TEM (in 17) cross-section images (a-h) for neon ion doses ranging from 0.1 to 1.5 nC/μm^2 (or 6.25x10^{16}-9.34x10^{17} Ne^+/cm^2). Clearly, nickel etching has progressively taken place. In our room temperature study, the nickel milling efficiency using a 0.5 pA beam was calculated to be 0.57 μm^3/nC, yielding an estimated sputter yield of 1.5 Ni/Ne^+. Sputtering yield is known to depend on

factors such as ion energy (here 30 keV), the mass ratio M_2/M_1 (here 2.8) and the incidence angle (here 0°). An expression [101] summing these relations up is:

$$Y(E_0) \cong \frac{1}{4}\ \Gamma_m\ \frac{\propto N\ Sn(E)\ \Delta x_0}{E_0}$$

where, α is dimensionless, Δx_0 is a depth interval for which atoms are set in motion with energy > E_0 (binding energy or sublimation enthalpy). The expression shows the important dependencies of sputter yield on nuclear stopping power as per $Y \propto S_n(E)$, and binding energy, $Y \propto E_0^{-1}$.

Aspect ratios (A.R.) follow a near-linear dependence on the neon dose, reaching 2.0 at the highest dose in these experiments. See figure 2.18, for a plot of A.R. versus Dose for Ne^+. Nickel sputtering already occurs at the lowest experimental dose of 6.25×10^{16} Ne^+/cm^2. Furthermore, the TEM images reveal similar subsurface damage as seen in the helium exposures. The dose at which bubbling occurs is lower, however ($<6.25 \times 10^{16}$ Ne^+/cm^2 versus 1×10^{18} He^+/cm^2). At low dose, very small nanobubbles become observable in the nickel layer. Figure 2.19 shows unexposed nickel (clearly granular) and exposed nickel with the precipitation of many small nanobubbles. The neon damage region is not as deep when compared with helium, but the damage appears more severe because neon has a smaller interaction volume. The formation of neon nanobubbles is evident and several regions are discernible; ranging first from: a) a narrow band with small, collapsing bubbles near the free surface, to b) a wider belt containing larger bubbles, followed by c) another band of smaller bubbles, and finally to d) a damage “halo” revealing Mo/Si intermixing. This is in agreement with patterns reported by Nguyen et al [100] for 50 keV He^+ in crystalline Si, and by Oliviero et al [81] for 50 keV Ne^+ also in c-Si.

(a) **(b)**

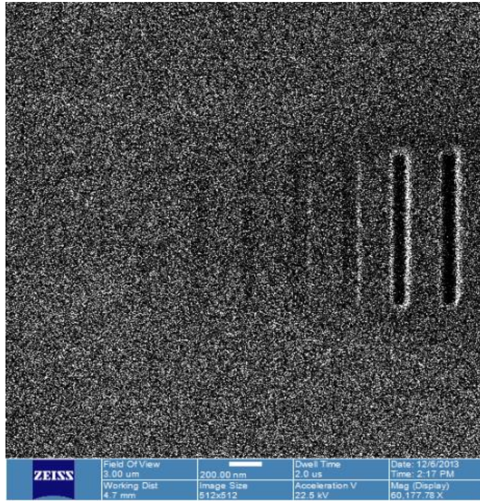

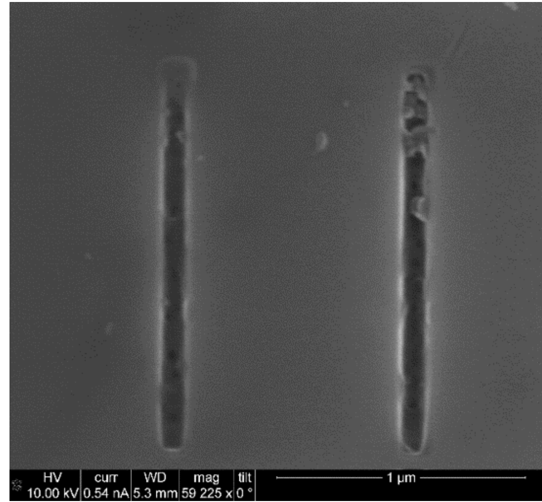

Figure 2.16. Top Ne-HIM view of etched lines (a), and top SEM view for two etched lines (b).

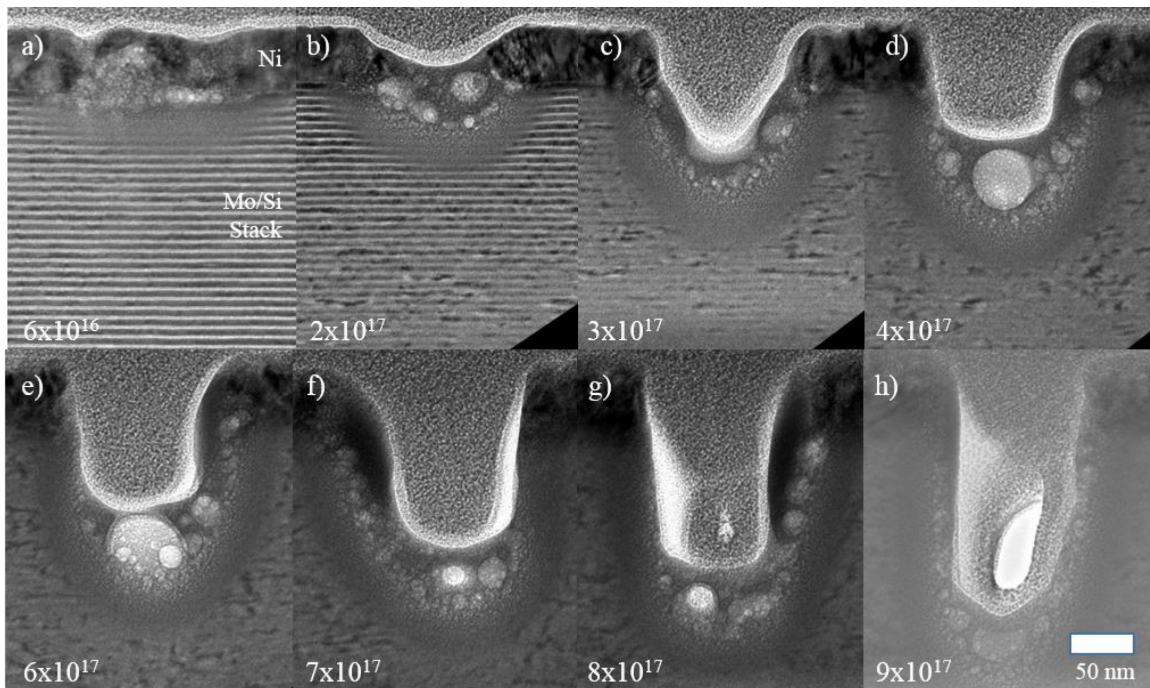

Figure 2.17. Sequential TEM cross-sections illustrating the progression in etch depth and the formation of cavities below the surface. The Ne^+ beam energy was 30 keV with doses ranging from 6.25×10^{16} (or 0.1 nC/μm^2) for a) to 9.38×10^{17} Ne^+/cm^2 (or 1.5 nC/μm^2) for h). The direction of the Ne^+ beam is normal to the top side of each panel from a) to h). Ions travel from top down across the image until they come to rest.

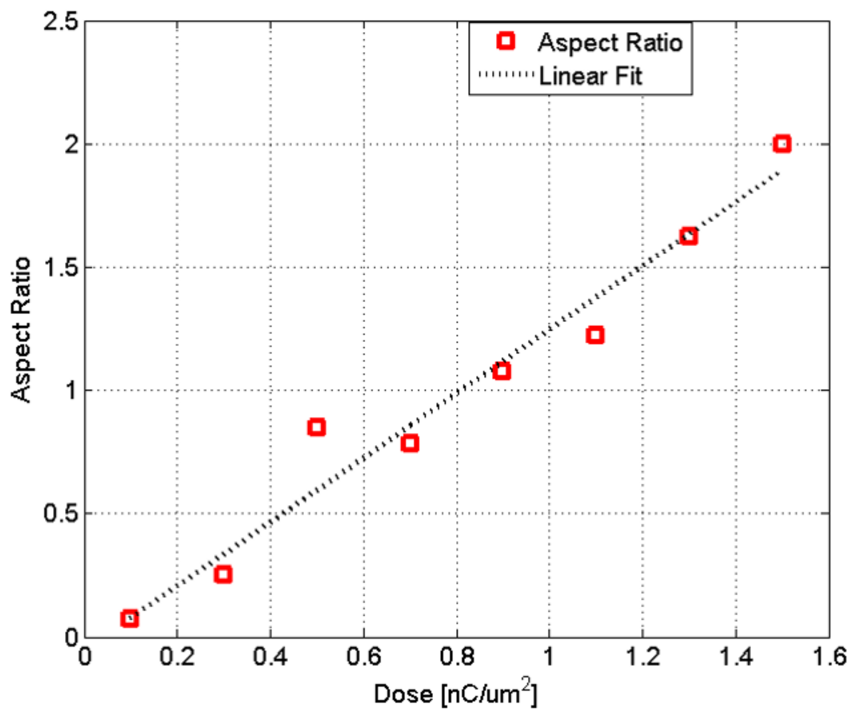

Figure 2.18. Via aspect ratios for 30 keV Ne^{+} exposures of doses ranging from 0.1 to 1.5 nC/μm^2.

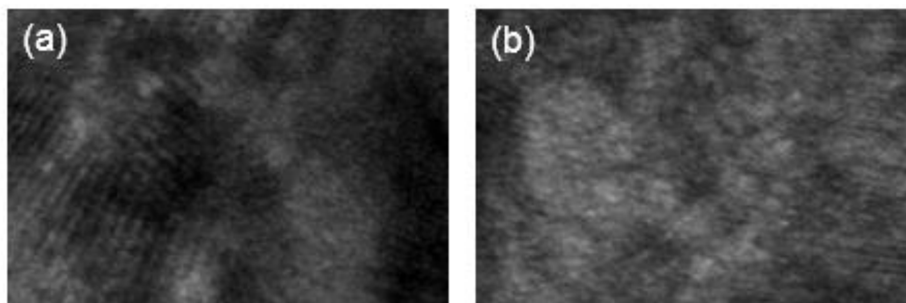

Figure 2.19. TEM images showing in a) the poly-crystalline condition of the nickel top layer without implantation or exposure to neon, and in b) the manifestation of small neon nanobubbles precipitating at grain boundaries. In b) some of the crystallinity is preserved within the grains, while the grain boundaries become decorated with nanobubbles.

EDXS analysis performed in the Libra 200MC instrument on the 0.7 nC/μm^2 sample (200 keV electron beam energy) detected the following elements: Ni, Mo, Si, Ru and Ne from the sample, and Pt and Cu from the protection layer on the sample and the mounting grid, respectively. At this dose, the nickel over-layer has already been removed and the etch front resides mostly within the now damaged Mo/Si stack volume. The analysis shows that higher counts for neon are present below the largest nanobubble, directly under the incident Ne^+ beam trajectory during ion irradiation. A slightly larger count at 850 eV may be due to embedded neon gas. This energy for Ne Kα is the same as for Ni Lα. However, at 7.47 keV, for Ni Kα, no significant counts and differences between three test points were detected. Thus it was concluded that appreciable nickel does not forward scatter deeper into the structure as the etching process mills across the top absorber layer. A summary of EDXS data is shown in figure 2.20 below. As a perspective, dense nanobubbles with high concentrations up to $1x10^{23}$ atoms/cm^3 (25 at. % He in Si) can have internal pressures in the low GPa range. This would remain below the elemental bulk moduli for Ni, Mo and Si. Already starting at room temperature in metals and at higher temperature in Si the first phase of helium/neon release is ascribed to dissociation of small noble gas/vacancy complexes, and in the second phase of release it is ascribed to noble gasses permeating from a bubble layer to the sample surface. The fact that bubbles are over-pressurized and that release does not occur from single bubbles, but from a bubble layer should be taken into account in a full physical description of the process [104].

Thinning of silicon layers is also observed for neon beam exposures (figure 2.21). In this case a clearer fidelity of each line is obtained. These quasi-linearly regain their original widths farther away from the top impingement surface. Closer to the top surface, these are thinner with centers displaced down closer to the next adjacent molybdenum layer. Nevertheless, this center recovers back to its expected position in the middle of a-Si layer with the expected thickness. As a result, the periodicity changed where it shows smaller values near the top. Since the binding

energy for silicon (4.7 eV) is lower than for Mo (6.8 eV), the result will be a greater number of Si atoms dislodged from their sites and relocated deeper into the structure. This may account principally for the blurring of the layers as a result of a radiation-enhanced diffusion process. For neon, the low loss EELS peak was found at 23.24 eV (figure 2.22). The transition for 3s—>3p for 1 atom Ne will involve an absorbed energy of 21.5 eV (1st ionization enthalpy). This indicates a pressurized cavity with a number of neon atoms present in it. Using the equation $\Delta E = C \times n_{Ne}$, the number of neon atoms in the large bubble will be ~108 Ne/nm^3, which is equivalent to [Ne]=1.08×10^{23} atoms/cm^3. Using the ideal gas law, PV = nRT, with n=1.788×10^{-22} mol Ne, T=298K and V for a 58 nm wide nanobubble, yields a pressure inside the bubble of 4.34 kPa. While significantly lower than 1-3 GPa for small nanobubbles of sizes <10 nm, it is possible that this large bubble, at equilibrium, is more stable and relaxed within the disturbed matrix. This is the best compromise, or lowest free Gibbs energy, between this lower surface area and larger volume of the quasi-sphere for neon embedded in this particular medium. Indeed, it is known for bubbles of small radius, the pressures are going to be much higher ($P \propto r_b^{-1}$). Another potential and simpler reason is that since the specimen was cut and thin down using the gallium ion beam as part of the TEM preparation, basically the bubble was able to depressurize.

Analysis of the bubble sizes reveals a few notable facts. Using the representative image at 3×10^{17} Ne^+/cm^2 dose, the histogram (in figure 2.23) shows a total population of 191 nanobubbles, out of which most are <5nm (90% of them), but no mid-range sizes (as in He) are present. In this case, the histogram is dominated by one large spherical formation at a size ~58 nm. A comparison with the helium results leads to the conclusion that for neon there may be an Ostwald ripening effect process present, where larger bubbles grow at the expense of smaller ones that shrink and eventually disappear.

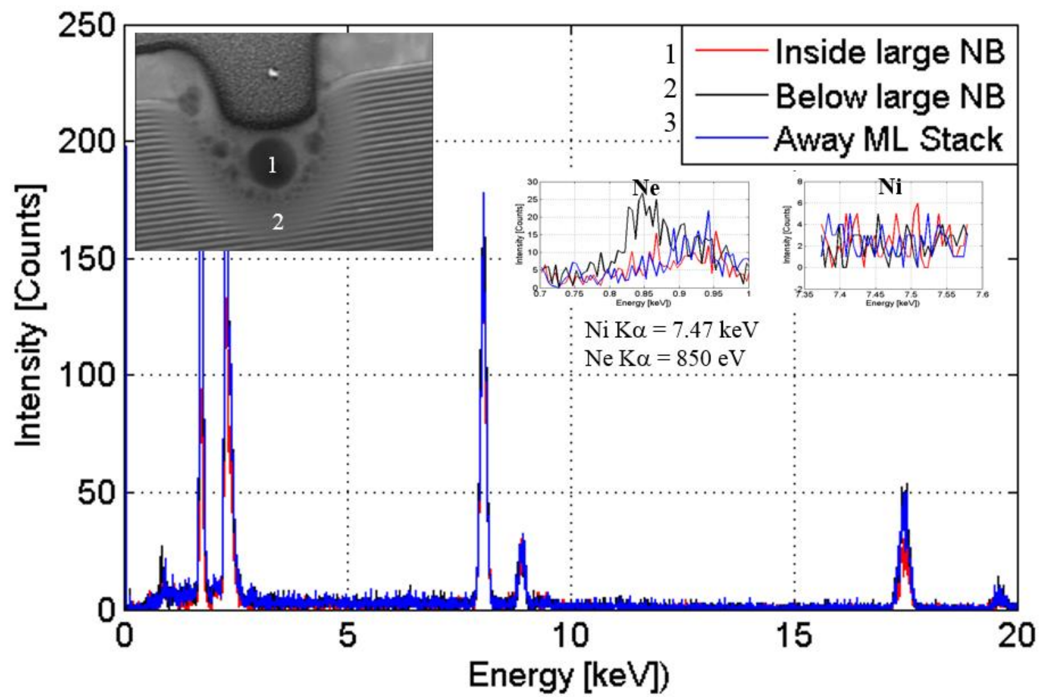

Figure 2.20. High magnification viewgraph while performing EDXS in the TEM around a large neon nanobubble located near the etch zone and directly under the beam trajectory for a dose of 0.7 nC/μm^2.

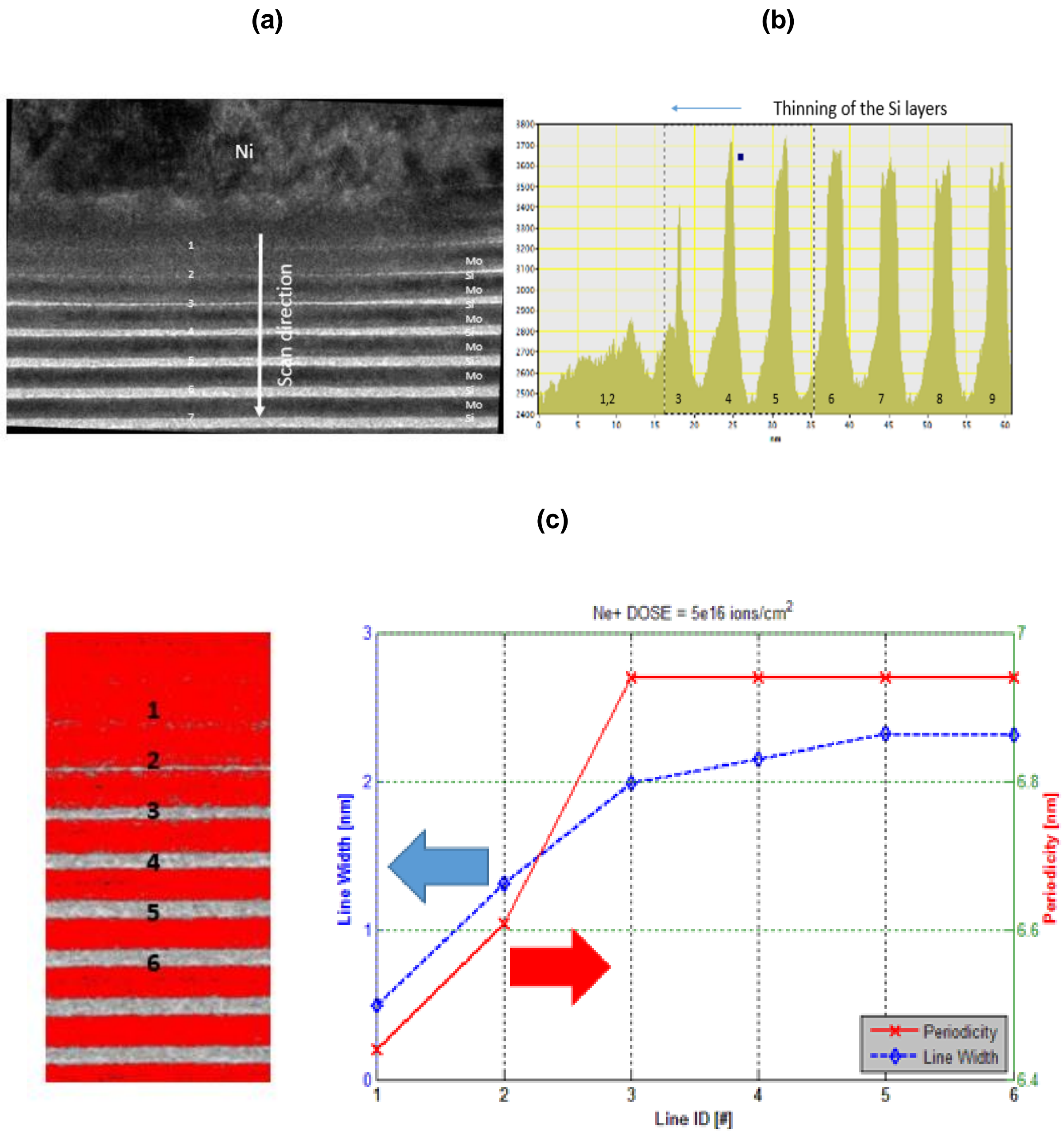

Figure 2.21. Closer look at the condition of a-Si layer in the stack closest to the beam irradiated, or damaged, region by neon. On the right, in b), a line profile showing the line widths increasing as the scan moved away from the irradiated zone. On c), a plot showing measurements for line width and for periodicity between the line centers for 24 keV Ne^+ and $5x10^{16}$ ions/cm^2.

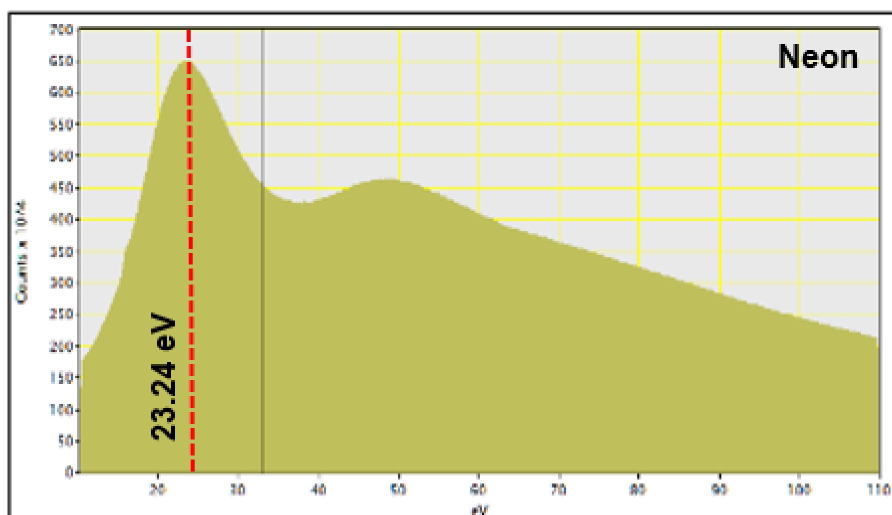

Figure 2.22. Low loss EELS plot showing a peak for neon valence electron energy transition when exposed to the 200 keV electron irradiation beam.

(a) **(b)**

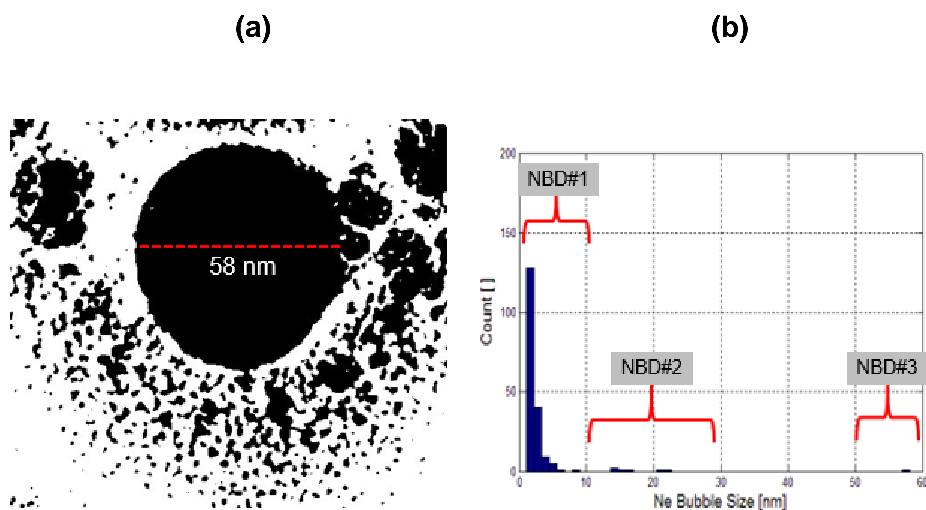

Figure 2.23. For 30 keV Ne^{+} and $4x10^{17}$ ions/cm^2, showing in a) the TEM adjusted image with different contrast limits (min, max) and brightness in order to do a particle size analysis as in the histogram on the right (b). Area was converted to diameter by assuming all were circular.

Neon Ion-Solid Modeling.

EnvizION neon simulations were also performed to better understand the experimental results. For the neon simulations we utilized a recent addition to the simulation which includes recoil and sputtering to reveal the evolving surface [68, 69]. To validate our EnvizION simulation for neon we performed energy dependent sputter yield curves for nickel. These show good agreement with experimental values. The calculated sputter yield at 30 keV is 2.0 Ni/Ne^+ which is a slight overestimation of the measured sputter yield of 1.5. Figure 2.24 shows experimental and simulated sputter yields. We attribute this discrepancy to factors that slow down the net removal of nickel such as the subsurface damage (effectively increasing the interaction volume and lowering the nuclear energy loss) and re-deposition on the via sidewalls.

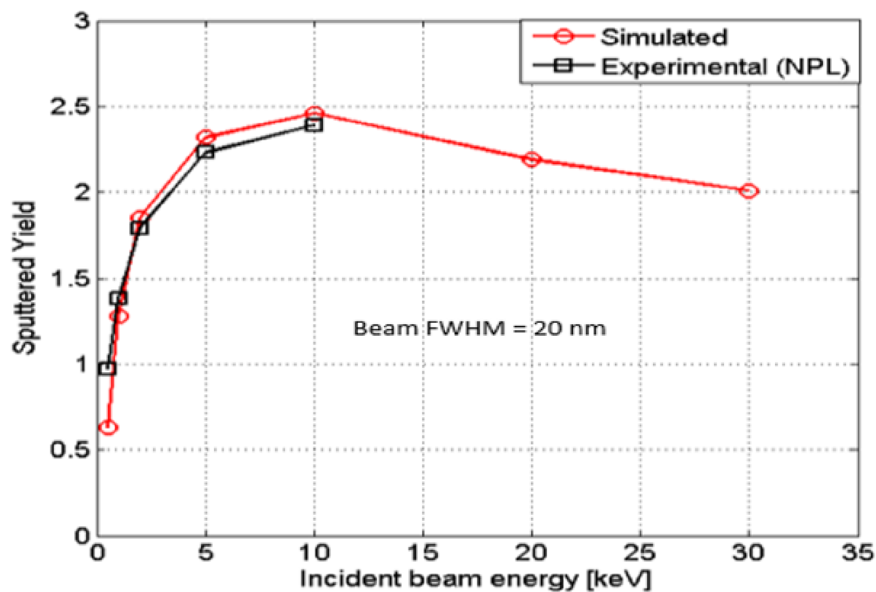

Figure 2.24. Experimental and simulated sputter yields of Ni under Ne^+ bombardment for energies up to 30 keV.

Figure 2.25 shows 3- and 2-D sputter profiles of the nickel top layer at a low dose. It must be noted that while in this case the neon peak concentration of implanted atoms remains within the nickel layer, a substantial amount of neon reaches the Mo/Si stack to about 100 nm deep, or 50 nm inside the Mo/Si stack. The etch cross section for an EnvizION run of 150,000 neon ions (in a 10nm x 10nm area) resembles the experimental data for a dose of ~$2x10^{17}$ Ne^{+}/cm^{2} at 30 keV. At this dose and energy, approximately 32 nm of the 50 nm nickel layer is removed. This etch depth agrees with the 33 nm measured experimentally in the TEM. Beneath the sputtered depth the implanted distribution tails down into the Mo/Si stack. Noticeably, the experimental via width is wider than the beam raster area. Experimentally, the 100 nm wide scan yielded ~136 nm opening in the nickel layer. The EnvizION simulation used a 10x10 nm^2 smaller exposed area (for shorter simulation times), which yielded a larger 15x15 nm^2 sputter etched via, demonstrating similar broadening due to the beam tails and interaction volume.

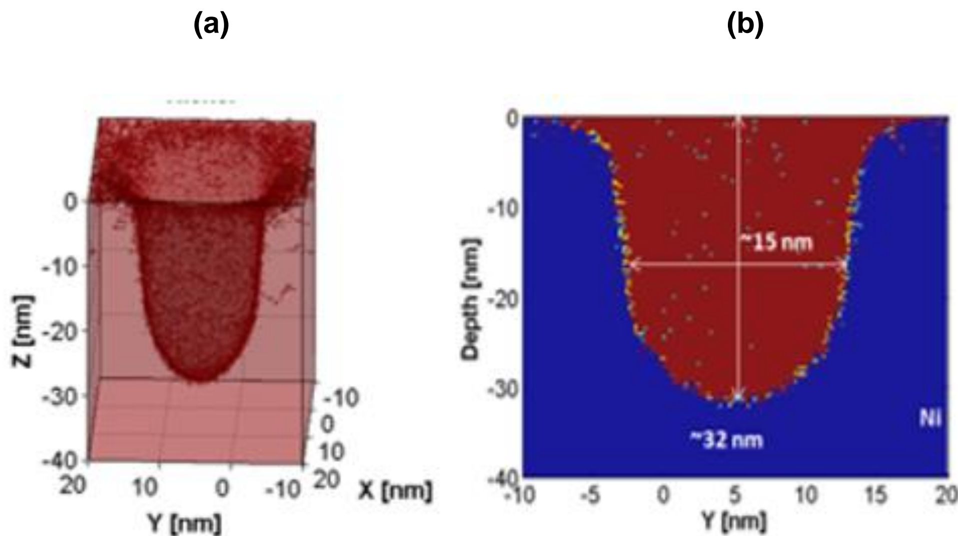

Figure 2.25. 3- (a) and 2-D (b) sputter profiles for Ne^{+} in Ni at 30 keV and ~$2x10^{17}$ $ions/cm^{2}$ (using a 10nm x 10nm exposure area).

In figure 2.26, the volumetric nuclear energy loss and final concentrations for neon at 30 keV are compared side by side with the actual TEM cross section micrograph at the same dose. In this case, it is notable that a high nuclear energy loss region extends beyond the nickel layer into the Mo/Si multilayer. The damaged region at ~2x10^{17} Ne^{+}/cm^{2} includes nanobubbles that are present a) in the nickel, but concentrated near the interface of the Mo/Si stack, and b) within the stack to a shallow depth of about 50 nm. Here it is clear that the peak energy loss is taking place within the Ni, where it causes physical sputtering, yet substantial nuclear energy loss also extends into the Mo/Si region down to ~100 nm from the original top surface of the nickel (experimentally, the halo extends to ~116 nm). For etching in nickel to take place, the simulation predicts a minimum nuclear energy density of ~30 keV/nm^3. Bubbling is observed and is attributed to the implanted neon at concentrations on the order of ~10^{21} Ne/cm^3; while conversely, no damage is again discernible below 80 eV/nm^3.

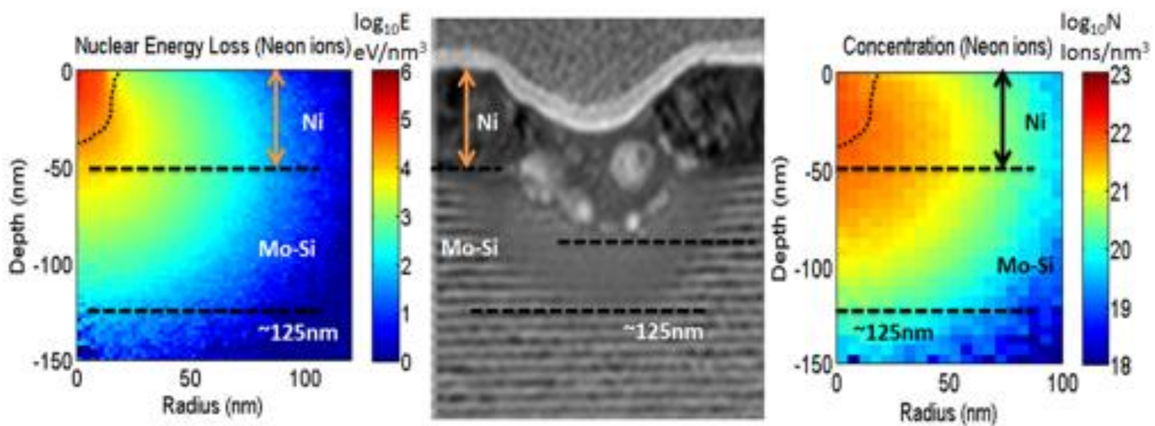

Figure 2.26. Simulated nuclear energy loss in eV/nm^3 (left) and the resultant neon implant concentrations in atoms/cm^3 (on right) are compared to the experimental TEM micrograph exposed to 30 keV at a dose of 2x10^{17} Ne^{+}/cm^{2}.

Figure 2.27 below shows a marked difference in nuclear energy losses between helium and neon at nearly the same dose (1-2x10^{17} ions/cm^2). Clearly, helium deposits its energy deeper and over a larger volume than neon. However, near the impingement top surface, the ratio between the peak nuclear losses of Ne:He at 30 keV is ~100, thus leading to the observed sputtering of nickel by neon.

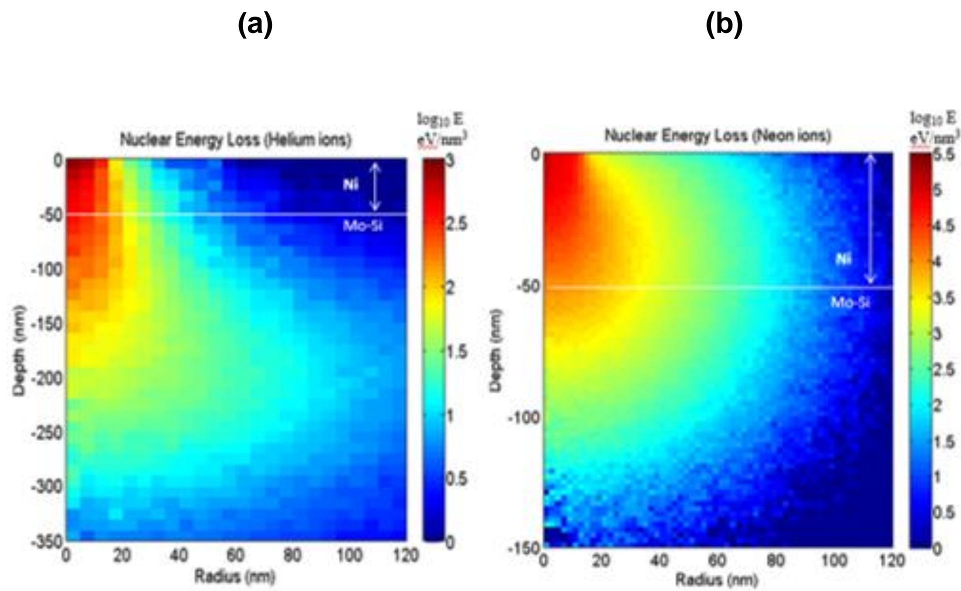

Figure 2.27. Comparison of the simulated volumetric nuclear energy losses of helium (a) and of neon (b) at 30 keV. EnvizION runs of 100k ions corresponded to a dose of ~1x10^{17} He^+/cm^2, and of 150k ions corresponded to a dose of ~2x10^{17} Ne^+/cm^2.

Ion Beam Energy Study.

The next stage in the study was to embark in an energy study for doses between 1×10^{15} and 1×10^{18} ions/cm^2. For helium, the only image of the study is an SEM obtained during the cutting and mounting process in the dual-beam microscope (figure 2.28). This sample was lost in transit to the TEM. However, the image provides a couple of useful observations. First, the discernible nanobubbling begins in the range of 1-5×10^{17} ions/cm^2. Secondly, the energy does not appear to have a marked effect on when this occurs. All energies between 28 down to 10 keV show discernible nanobubbling at 5×10^{17} ions/cm^2. By the way, no sputtering appears to occur for helium in nickel at the low energies when the nuclear interactions are known to increase. It appears that insufficient volumetric energy density is still delivered into the target especially near the surface where etching occurs. Furthermore, the swelling visible in 2.28b, appears to be lower at 10 keV. This, while somewhat unexpected, can be explained by a structure-dependent mechanism. Since the substrate is a single crystal, as the case of c-Si, at lower helium ion energies there will be less penetration deeper into the structure, particularly implantation at or near the a-Si ultra-thin layers, which have been shown to cause the swelling by deformation exceeding their elastic limits. Since at low energies more of the helium atoms will be implanted nearer to the top surface, or particularly in the nickel, this top poly-crystallline layer can accommodate the implants without showing the levels of deformation observed in the ultra-thin amorphous silicon below. Refer to figure 2.29.

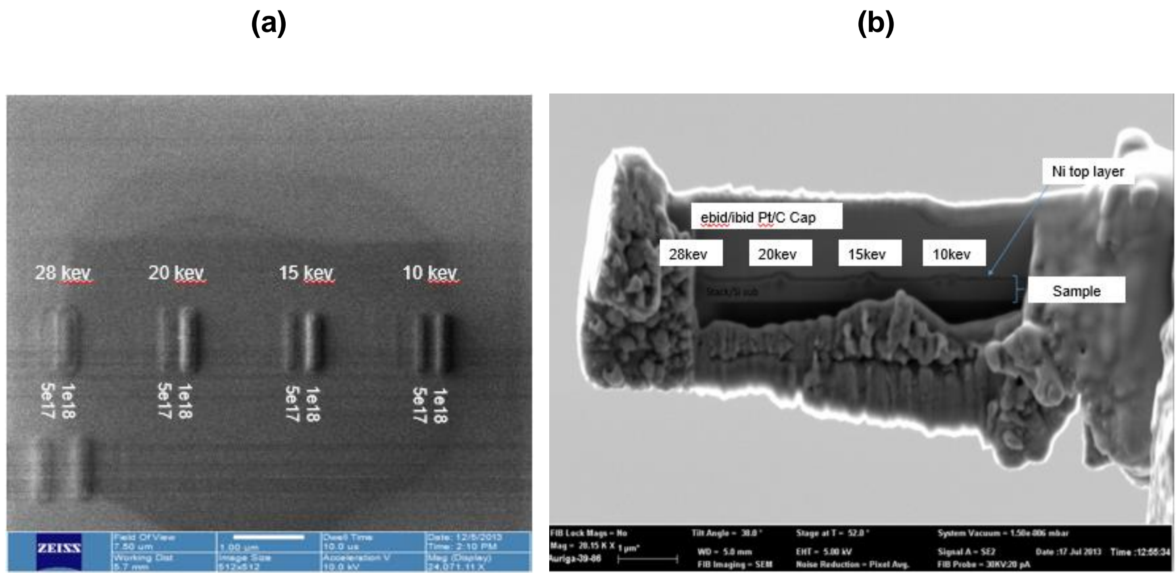

Figure 2.28. Helium energy study. Top HIM (in a) and lamellae side SEM (in b) views.

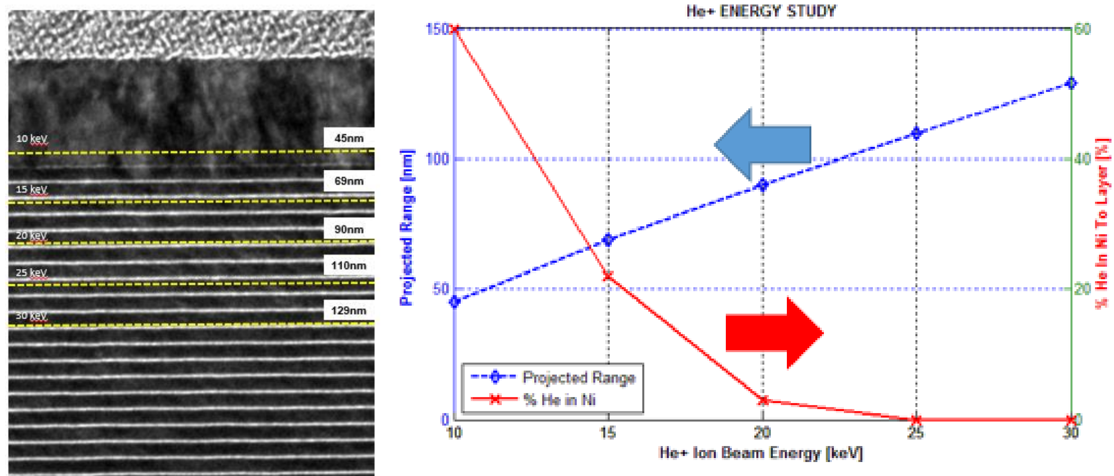

Figure 2.29. Projected ranges and straggles for helium ion beam energies from 10 to 30 keV as predicted by SRIM/TRIM.

TEMs images were obtained for a neon energy study from 22.5 down to 10 keV (figures 2.30, 2.31). It was challenging to maintain the same current and a focused image at this voltage range, therefore the doses are expected to have higher variation. Perhaps, not unexpectedly, the etch depth does not appear to have a strong dependence on the beam accelerating voltage for the range studied (simulations only suggest ~15% change in sputter yield). All the results are extremely similar, except one can observe that the extent of the damage below the etch front is lower for lower beam energy; which is consistent with the range of the neon ions increasing with increasing energy. In figure 2.31, however, the etch profile shows some distinguishable characteristics. For low doses, the etch looks more symmetric and rounded (A.R.<1). As the etch vacuum/solid interface progresses and moves deeper into the structure it quickly develops a more rectangular shape (A.R.~1.0), but for the deeper etches, the shape becomes more conical as the width narrows deeper inside the stack and approaches the silicon substrate (A.R.>>1). This can be explained by re-deposition effects more active for deeper etches into the material. From the TEM, it can be observed that the thick c-Si substrate has become amorphized by neon ion implantation (figure 2.31).

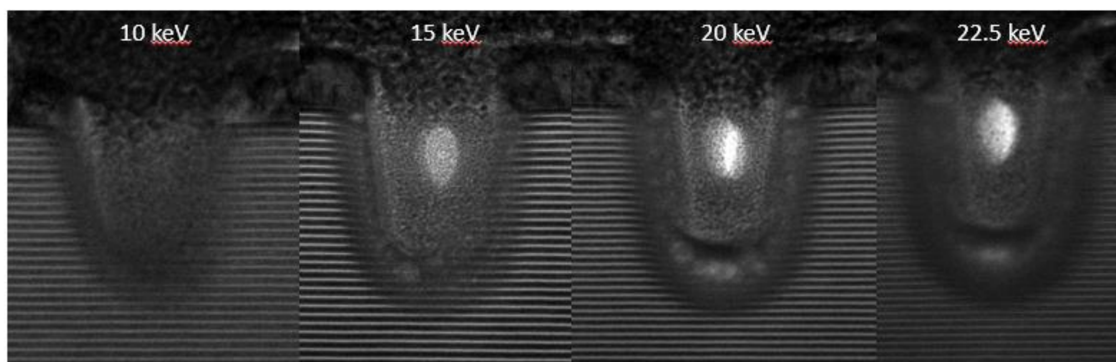

Figure 2.30. Energy study TEM images for neon ion beam etching at $5x10^{17}$ Ne^{+}/cm^{2} and energies between 10 and 22.5 keV.

(a)

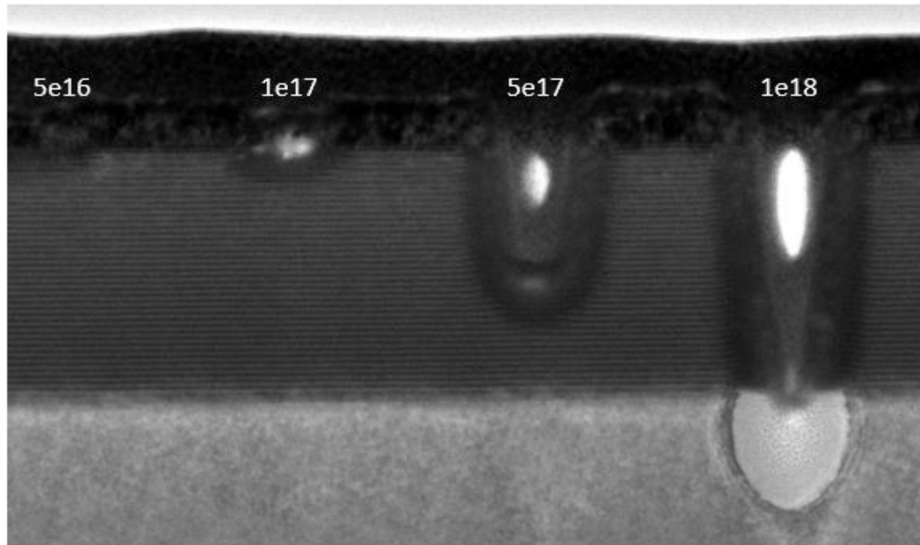

(b) **(c)**

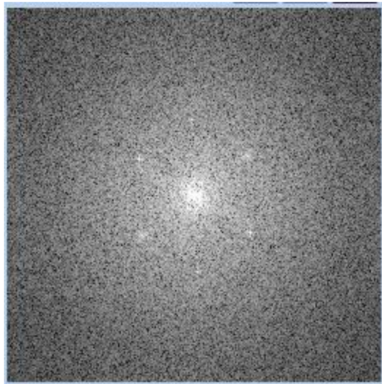

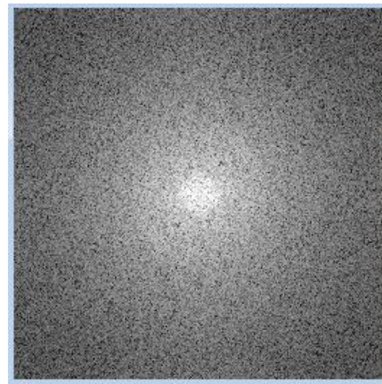

Figure 2.31. For a Ne^+ beam energy of 22.5 keV, the exposures from $5x10^{16}$ to $1x10^{18}$ Ne^+/cm^2. In b) below, the diffraction pattern for the silicon substrate, and in c) the same but within the region affected by the beam after a $1x10^{18}$ Ne^+/cm^2 on the structure.

Heating Considerations.

SRIM/TRIM provides useful information for estimating temperature rise due to ion-solid interactions, namely, the phonons which rely on the nuclear energy loss from the simulation. These results can be utilized to predict heating in our structure during ion milling. First, and foremost, is the time scale of these thermal spikes. Since nickel is a thick, good thermal conductor, the quench times expected are rather short. In a few ps, the temperature spike relaxes back to the initial background temperature. The thermal diffusivity ($\alpha=\kappa/\rho c_p$) of Ni is ~23 nm^2/ps (ρ stands for mass density in this case). Typical atomic hopping frequency when diffusing is 10^{13} Hz, which corresponds to 0.1 ps. Therefore the brief heating spikes may account for some short-range thermally activated diffusion. However, this does not take into account structural constraints in the system. Only target compositions, their densities, the beam species and their energies determine the results. At 1ps, after heating rapidly, the nickel will undergo locally (to a few nm in width quench volume) up to ~1200 K in temperature (figure 2.32). This is expected to introduce some localized changes in the material. As the beam scans, there will be a band of damage generated at certain depth, for neon closer to the top surface. This band will be continuous since overlapping will occur for adjacent beam dwells. We already know that for neon, since it etches, these localized regions will be eventually removed, unless the etch process stops (for a desired dose) and a band of damage remains buried at a certain depth beyond the etch surface, actually very near the bottom of the via, or box. When neon is compared with helium as in figure 2.32 below, the differences are quite notable. With respect to neon, helium does not produce significant heating, and in this regard it can be practically considered a pseudo-electron.

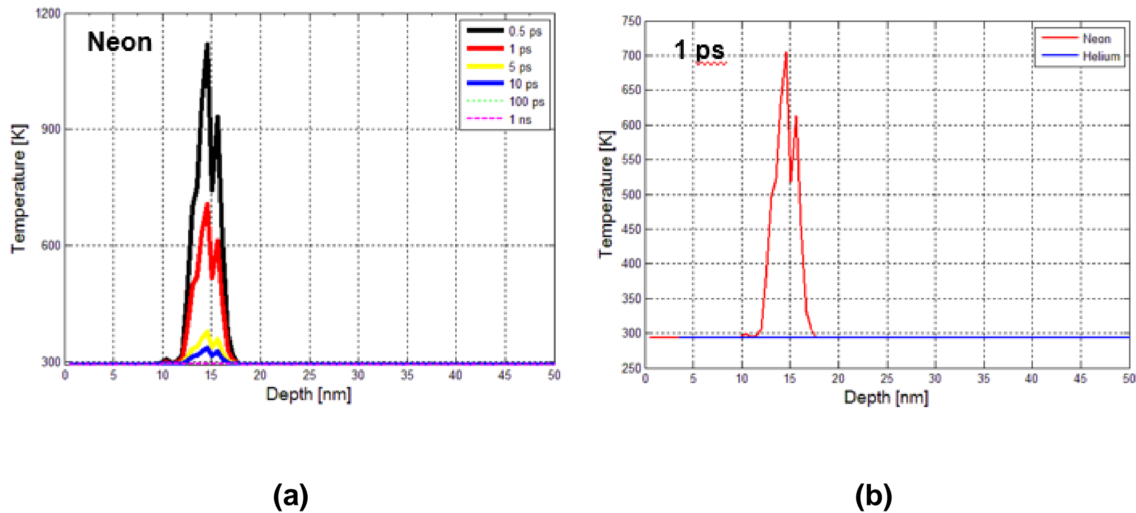

(a) **(b)**

Figure 2.32. On the left in a) the temperature profile versus time showing the rapid quench rate for thermal spike. On the right, in b) a comparison between a neon and a helium thermal spike 1 ps after the ion strike.

Most dwell times are 1μs or above. This length in time is sufficient for only six (6) ions (+0.25) at a typical 1 pA beam current to strike the material directly underneath. As shown in figure 2.33, the total 1μs dwell period contains six thermal spikes separated by an average 160 ns periods. This interval between strikes is long enough to allow the excited volume to recover to its initial temperature. This demonstrates how difficult it is for larger bulk volumes to reach higher temperatures during the etching process, unless there are other practical limitations to heat removal or sinking. While in the atomic scale a heat source temperature approximation can be obtained using, $T(t)=T_0 +1.6x10^{-9}$ x $(dE/dz)/(4\pi\kappa t)$; from equation $T=P/(\pi a\kappa)$, the resultant long-term temperature rise for nickel obtained for a 30 keV, 1 pA beam (P=VI) with 1 nm spot size is only 0.1 K. However, undoubtedly, sample geometry (including high aspect ratios) limits heat transfer. The color maps shown below in figure 2.34 are for helium and neon incident on the top of the Mo/Si EUV stack. According to SRIM/TRIM based simulations, the temperatures never

exceed 350 K during the etching process for either gas species. However, this changes when the via reaches the end of the nickel layer. This invokes a new set of constraints that need to be considered, and that find close agreement with the sequential images obtained from TEM for higher doses. In figure 2.35, a comparison between neon ion beams at 30 and 10 keV. In this case, clearly, heating effects take place much closer to the top impingement surface.

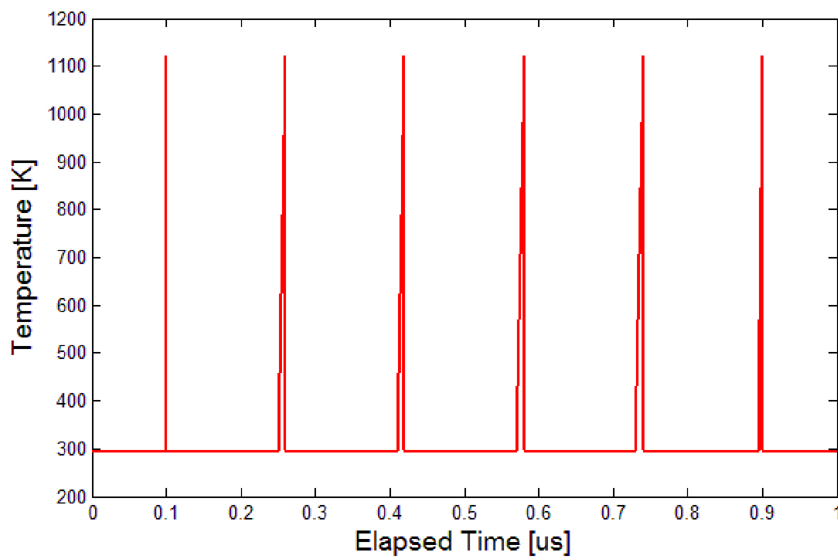

Figure 2.33. For a 1 μs dwell time by a 1 pA ion beam on a spot, a total of six (6) ion strikes will take place.

Figure 2.34. In a) the color map for a neon ion beam incident on the mask with nickel top layer (50 nm) and at the beginning of the etching process, showing the temperatures at different positions, including depth. In b) the same as in a) but now using lower thermal conductivities for the stack as per Bozorg-Grayeli's report ($\kappa=\kappa_{SiO2}$). The stack begins to show some minor heating at the interfaces within the stack. Now in c) and d), the same as in a) and b), but for the neon ion beam incident on the mask without the nickel top layer (0 nm). In this case, it shows substantial temperature rise because of the removal of the relatively thick nickel layer acting as an effective heat sink. Ion count=1000 and elapsed time=1ps.

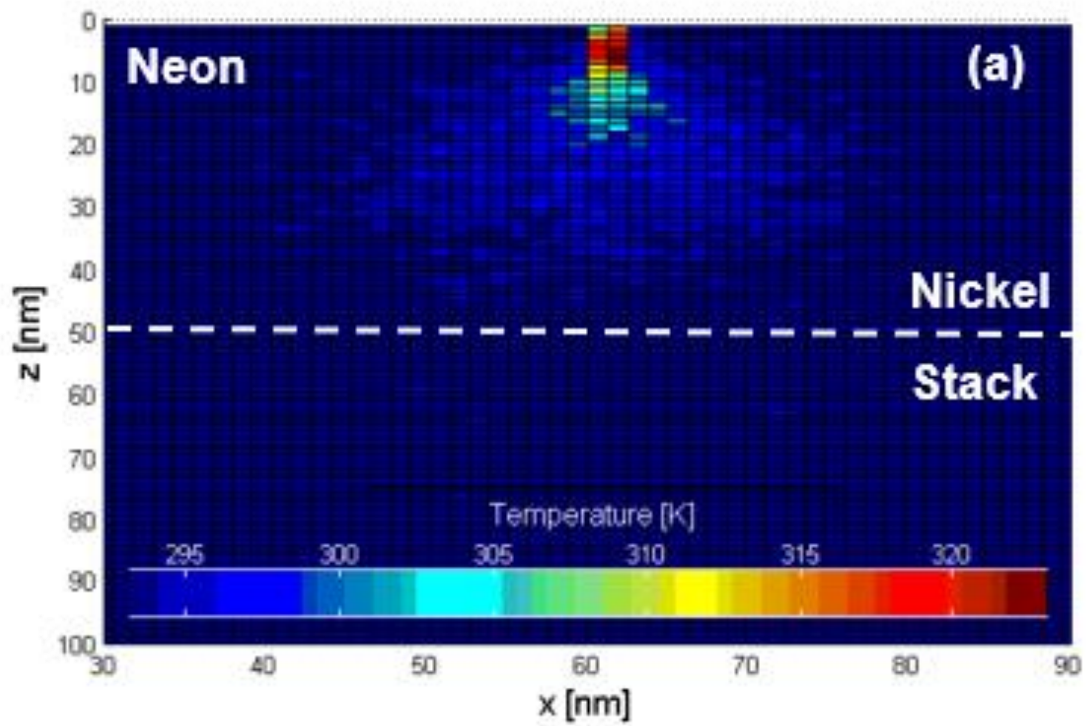

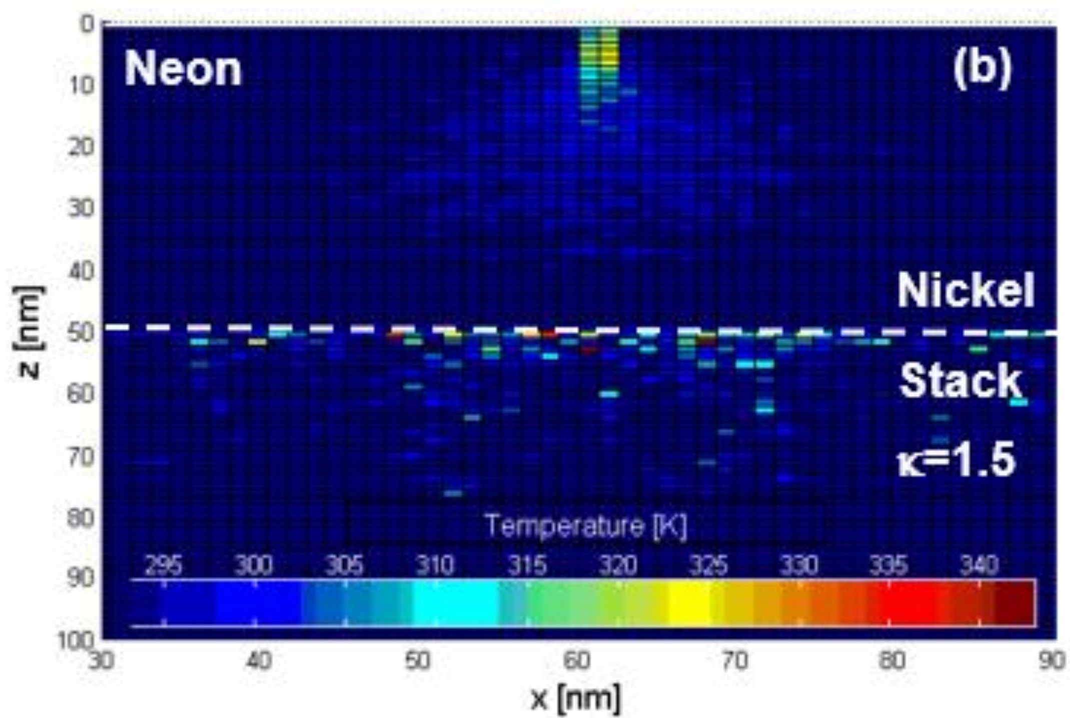

Figure 2.34. Continued.

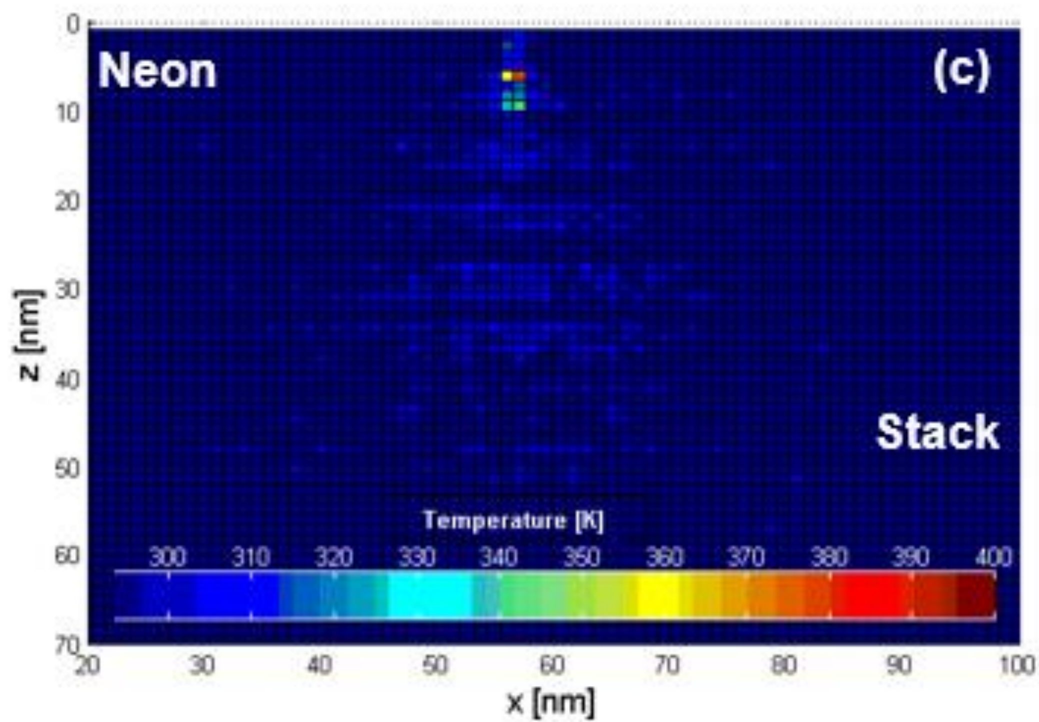

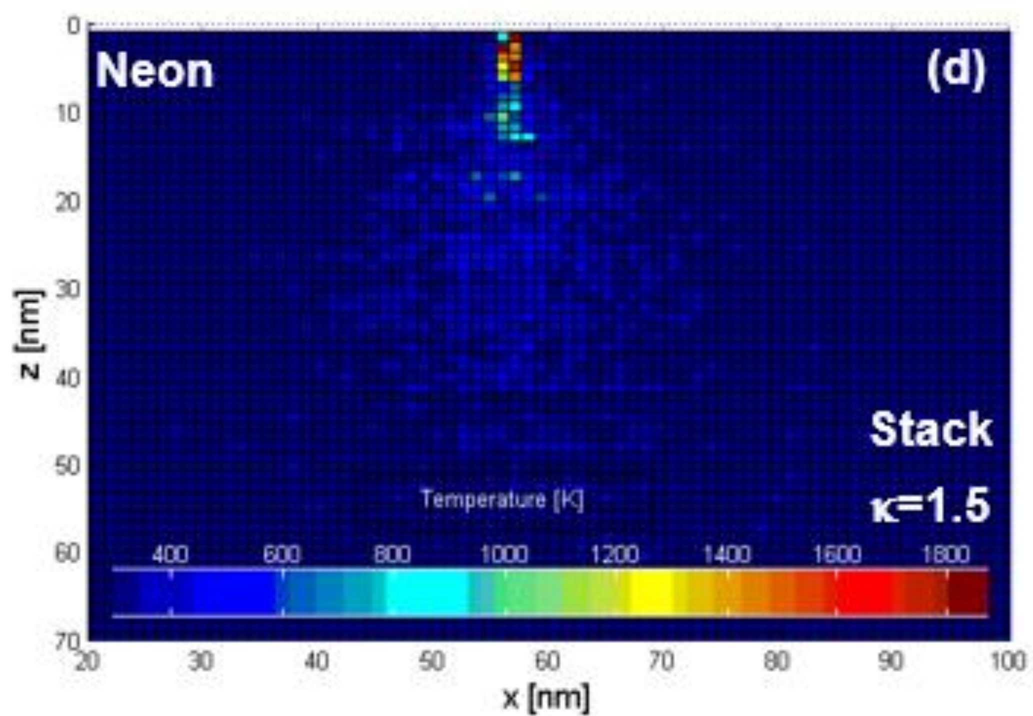

Figure 2.34. Continued.

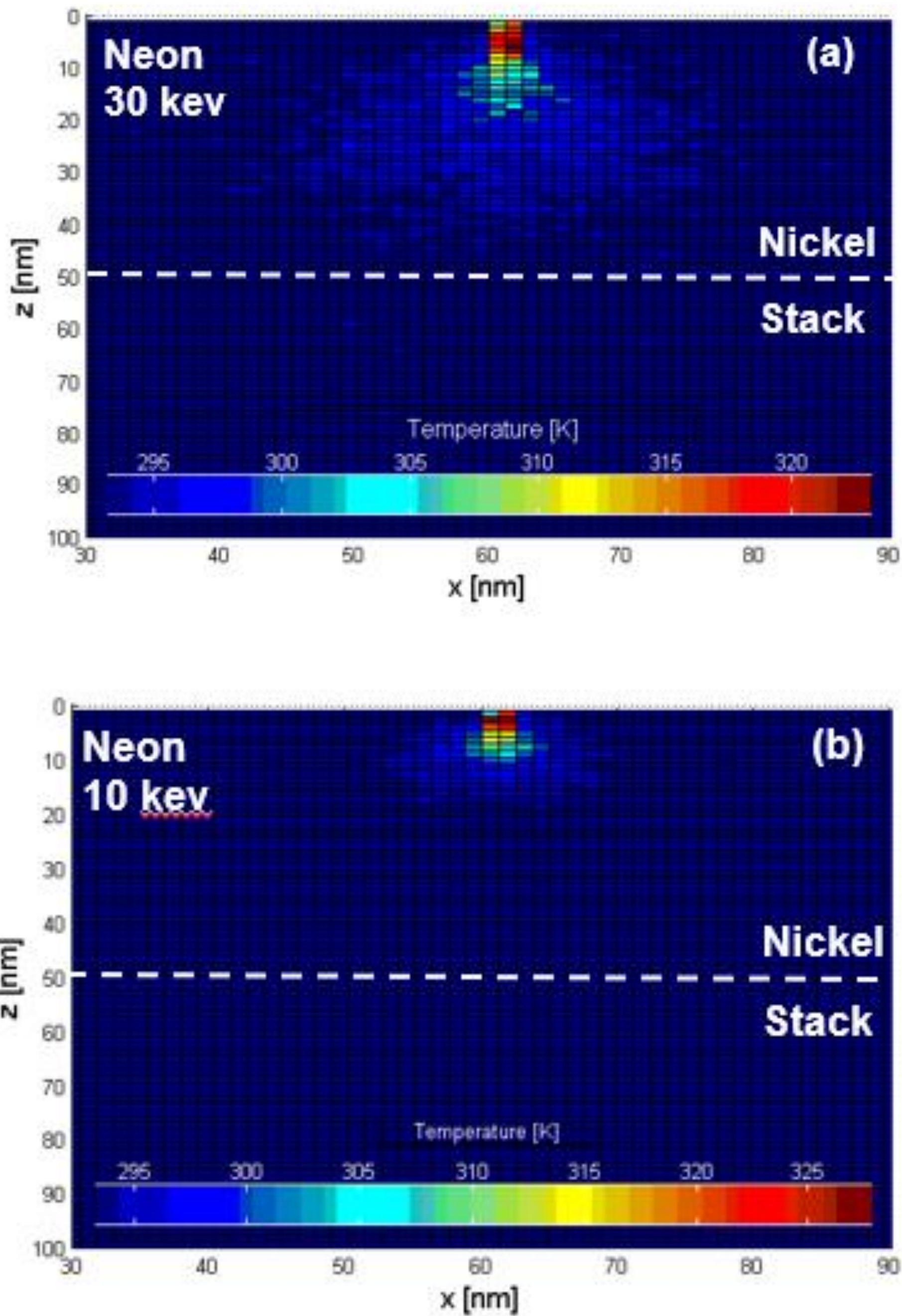

Figure 2.35. In this case, a comparison between 30 (in a) and 10 keV (in b) neon on the mirror structure. It shows how much more contained and closer to the top surface the temperature spikes are for the lower beam energy. Ion count=1000.

Implanted Atoms, Recoils and Vacancy Concentrations.

Complete awareness of entities such as vacancy, host recoil atom and implanted atom concentrations is vital to an understanding of the different mechanisms interplaying in the experiment. In a helium ion bombardment dose of $5x10^{17}$ He^{+}/cm^{2}, an implanted concentration profile shows a distribution that is quite broad over the structure from top to bottom, as well as laterally, both for about 400 nm. Most vacancy generation takes place in the multilayer stack. However, for helium, this generation rate is relatively low at ~0.0035 vacancies/nm-ion (or 1 vacancy per ~300 incident atoms/nm). It has been determined that by $5x10^{17}$ ions/cm^{2}, the onset of bubbling has been surpassed. At this point the concentration is already up to ~$3x10^{21}$ He/cm^{3}. More specifically, this critical dose lies somewhere between 1-$5x10^{17}$ where the peak concentrations will reach ~$3x10^{20}$ cm^{-3} for nanobubble formation. Host atoms such as Mo and Si will be relocate deeper into the structure, especially silicon since it has lower enthalpy of sublimation. This means that bands at different depths will be created during irradiation. In general, these will be a higher concentration of vacancies near the top surface, recoils causing intermixing between adjacent multilayers near the top of the stack and a peak implanted helium concentration deeper within the stack.

Figure 2.36 (a) shows as predicted by SRIM/TRIM, the concentration at $5x10^{16}$ Ne^{+}/cm^{2} (at which nanobubbling has been initiated already) of neon implants down to 50 nm deep in the mirror structure. In this case, concentrations of 10^{21} atoms/cm^{3} exist within nickel enough for small nanobubble precipitation in the bulk, whereas even at smaller concentrations, near the interface with the Ru/Stack, larger nanobubbles appear in the experiment (per TEM imaging) likely due to a heat transport hurdle on this plane. It has been determined that the critical concentration for nanobubble formation has been exceeded at this point. The threshold lies therefore somewhere between 1-$5x10^{16}$ cm^{-3}. In 2.37 (b), the vacancy concentrations are shown. These are mainly concentrated near the top and progress down to a shallow depth ~20 nm (~0.032 vac/ion-nm).

The generation rate is higher for neon, at 1 vacancy per ~30 neon ions/nm. For 30 keV Ne^+, this value is ~10x larger than for helium. Vacancies provide suitable empty sites for implanted atoms to migrate and fill in. Several (up to 5) noble gas atoms can be associated with one vacancy. However, while the quite accessible grain boundary volume is not saturated there is little incentive to diffusive and occupy a site perhaps a distance away, especially within a grain interior. Therefore, for more mobile helium some dispersed vacancies in a wider volume may contribute a small fraction of the total accommodation, while for less mobile neon, these vacancies that are mainly concentrated near the impingement surface may not be as accessible, unless heating is present. At low doses, but with low temperatures, helium clustering cannot be associated with vacancy absorption. There is a low concentration of these, very dispersed, atoms while there is a high volume of extended defects for accommodation. At the higher doses, since supersaturation ensues there is more damage in the structure and a relatively higher concentration of vacancies. This structural damage in the form of stored elastic energy or host atoms removed from their equilibrium lattice positions, provides additional routes for rapid helium diffusion. However, due to the suspected low temperatures, the main source of helium atoms for clustering will come from the extended defects where the high concentration of implanted atoms only require low activation energy for migration and then their coalescence into nanobubbles.

While TRIM simulates only a vertical streamline of ions (spot size=0) impinging atop a flat target surface, EnvizION makes possible realistic square patterning areas, typically 10 nm x 10 nm. Nevertheless, EnvizION is not set up to generate the vacancy distribution model at this time. Using the conventional TRIM modeling for 16 & 30 keV He^+ irradiation, predictions for the implanted helium and vacancy distributions can be easily obtained. The results for 10,000 ion runs are shown below in figure 2.37. It has been ascertained that, as expected, the vacancy peak distribution rests at a shallower depth in the stack with respect to the implanted helium. For 30 keV He^+, these positions correspond to ~125 nm and ~200 nm, respectively. EnvizION predicts

a slightly deeper helium implantation peak at ~225 nm. This fact may actually be a better approximation because the projected range is expected to be deeper from the top surface because of the accumulating damage with increasing dose. This structural damage to the stack results in lower mass densities (intermixing and low-density accumulating helium) which allow for energetic ions at higher doses to travel deeper into the structure before they eventually come to rest. Therefore, the projected range in a real material is a function of dose, where Rp is not static and is proportional to Dose. In the simulations, Rp (for EnvizION) > Rp (from TRIM). A closer inspection of the experimental results in figure 2.5 (i,j), and more specifically, for a dose equivalent to $1x10^{18}$ ions/cm^2, where the nanobubbling first arises with respect to the silicon substrate, matches (or aligns) closely with the end of the halo estimated from the $1x10^{17}$ dose. However, at $1x10^{18}$ it is discernable that the largest nanobubble formation appears closer to the top surface and at shallower depths that the projected range. This can be rationalized by invoking the high mobility (very low activation energies) of helium atoms expected within a highly damaged structure. The damage is larger at shallower depths where the vacancy concentration is highest (peaking at ~125 nm, or 75 nm below the Ni layer). Importantly, the vacancies generated by the incident beam have significantly lower mobility than the He, and thus they coalesce in the range of the highest vacancy concentration. As a result, the nanobubble field follows a Gaussian looking profile with depth, but displaced closer to the top impingement surface, due to the proclivity of helium to rapidly diffuse to fill /cavities where the damage is greatest, thus directing the structure into a more stable condition with lower Gibbs free energy.

Even though helium and neon atoms are known for their lack of reactivity, their tightly bound electrons in the shells (especially in neon) can interact with a lattice, for example nickel, where it has unpaired electrons, therefore effecting the net diffusivity in the solid. It can be expected that neon will diffuse at a slower rate in metals such as Ni and Mo. Weak van der Waals forces among the noble gas atoms are thought to exist within a pressurized bubble. It has already

been established that for many materials with defects such as vacancies and interstitials, an effective defect interaction distance is in the order of 0.5-1 nm. However, it appears that individual helium and neon atoms can interact and coalesce into an extended defect at slightly larger distances. Using the expected thresholds for helium ($3x10^{20}$ He/cm^3) and for neon ($4x10^{19}$ Ne/cm^3) for nanobubble formation, an average spacing or separation between each atom center can be calculated (assuming spherical shapes and using the atomic radii). The resulting average interatomic spacing between closest neighbors when coalescence or precipitation is initiated is ~3.2 and 5.7 nm, for helium and neon, respectively.

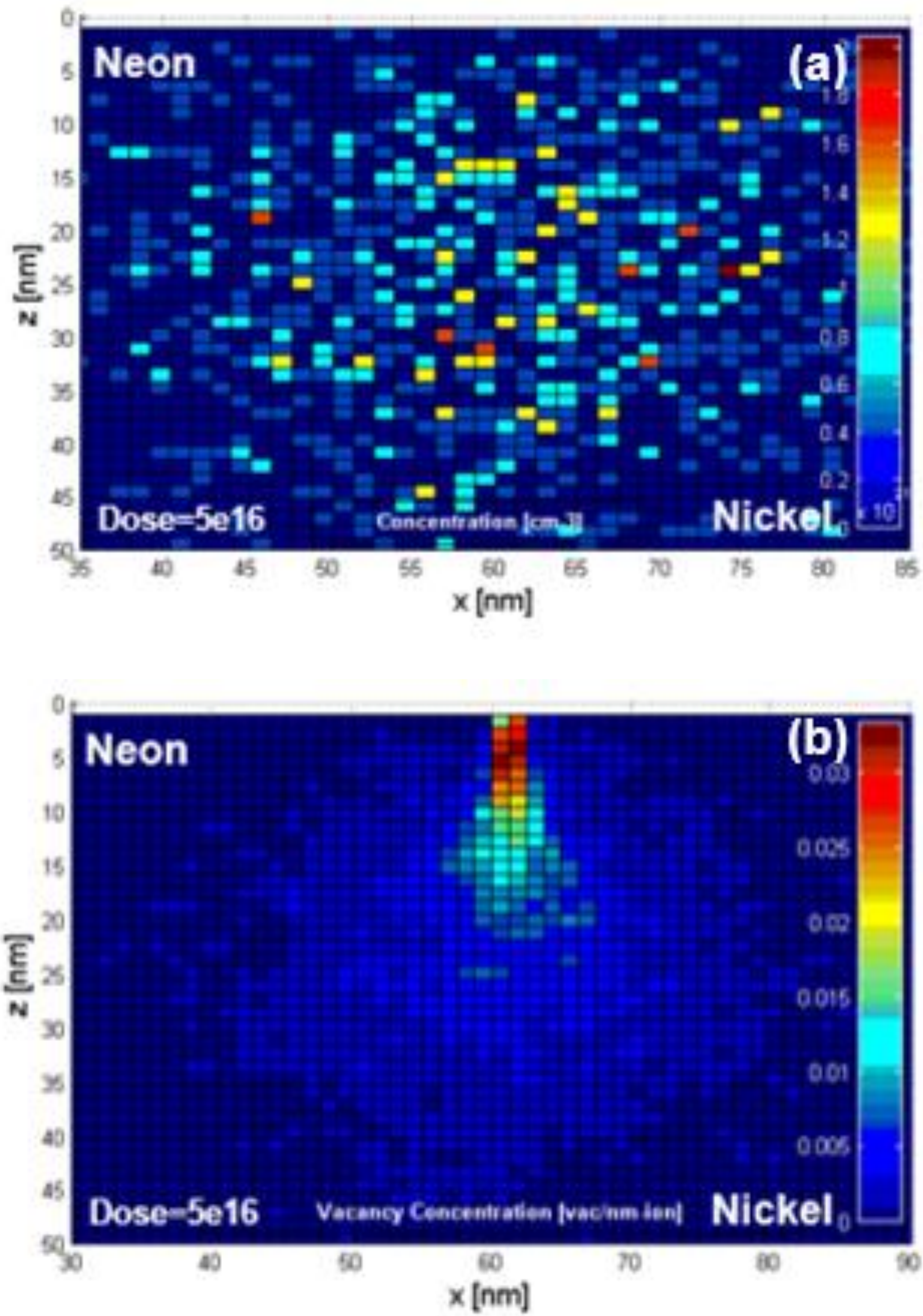

Figure 2.36. Implanted concentration (in a) and vacancy (in b) concentration profiles for neon ion bombardment at 5×10^{16} Ne^{+}/cm^{2}.

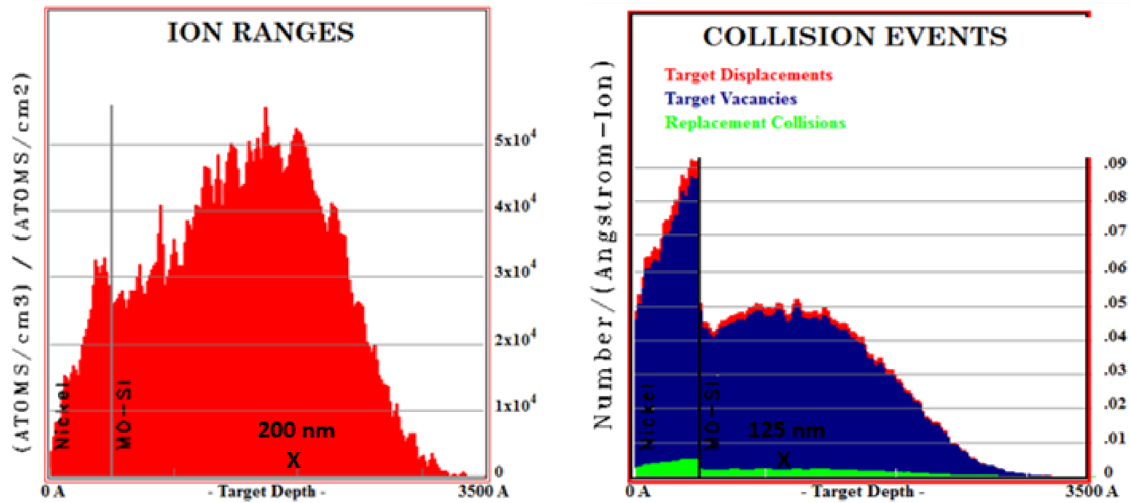

Figure 2.37. TRIM simulations showing the ion ranges for 30 keV He^+ and the number of vacancies created as functions of depth.

Defect Generation and Interactions in the Ni/Ru/40x(Mo/Si) Stack.

Starting with the helium exposures, it is evident that the mask structure has a relatively high solubility for this gas. It is not until a dose of ~$5x10^{17}$ He^+/cm^2, or a critical concentration of near $3x10^{20}$ helium atoms/cm^3, that the multilayer becomes decorated with discernible bubbles. The stack provides numerous pathways to accommodate the helium atoms. Since only the silicon substrate is a single crystal, the free volume in the amorphous silicon and the poly-crystalline molybdenum is relatively high. Each interface between the multiple layers, each grain boundary within multi-crystalline nickel (in addition to a large native concentration of vacancies at room temperature), poly-Ru and especially poly-Mo and, above all, the unoccupied free volume in amorphous silicon, all provide an abundance of heterogeneous nucleation sites, suitable for the energetic ions to come to rest. A crystalline, highly-directional structure like c-Si does not accommodate many atoms since grain boundaries are non-existent and the additives have to either replace a host atom by bumping it out (less likely) or fill interstitial positions (tetrahedral

sites are common) in typically preferred planes with lower atomic density. The small density of dislocations present in c-Si can also provide suitable sites for accommodation. At lower doses below $5x10^{17}$ He^{+}/cm^{2}, the accommodation occurs without severe damage. Basically, a widespread, seemingly passive or energetically complacent, number of point defects exists throughout the structure at this juncture. Staining of the affected areas is observable due to the evolving density of the region (lower now because of the vol.% helium added) and the intermixing of the Mo and Si layers. It is the critical dose and above it that visually (in the nm-scale) involves the greatest changes in morphology. In this range, swelling and nanobubbling occur in the multilayer structure.

At $1x10^{18}$ He^{+}/cm^{2}, the nickel layer contains no discernible bubbles. Discernible features are present deeper within the stack region (top 2/3 bilayers affected one way or another). The structure exhibits a marked curvature and the nickel (soft metal by itself) appears to store the elastic energy without cracking or exhibiting fracture. It can be deduced then that the stresses have to be below the ultimate tensile stress for nickel, possibly even below the yield strength. There is a range of nanobubbles, mostly below 5 nm in diameter or size with an intermediate distribution up to 33 nm. It is clear from the TEM image that within the 100 nm thickness of the lamellae, there is overlapping of some bubbles in the image. Thus, none of these exists above the thickness of the 100 nm slice. The number of nanobubbles present indicates a relatively static process. Once these nucleate and coalesce, there is hindered or no growth. The peak number of vacancies generated by helium strikes is relatively low (3/1000), which will result in a sparsely distributed field of vacancies in the bulk. This short supply of vacancies makes the nucleated nanobubbles have an irregular shape and does not allow these to relax to an equilibrium size (metastability condition). The abundance of trapping sites at grain boundaries and interfaces makes the role of vacancies less influential. Refer to figure 2.38 below for a depiction of the likely evolution leading to nanobubbling by helium.

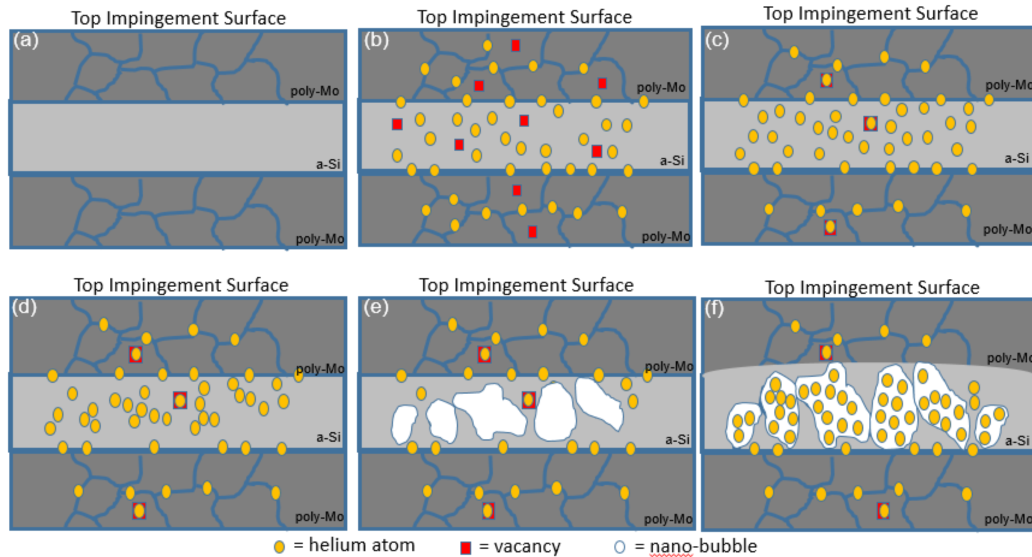

Figure 2.38. Diagram showing the evolution of individual implanted helium and defects leading to the formation of nanobubbles preferentially located in the amorphous silicon layer.

Knowing that the sample remains relatively cool, a bimodal distribution dominated by very small bubbles and just few of intermediate size is expected. Intuitively, bubble sizes are a maximum at or near where the simulated projected range for the helium ions is a maximum. At $1x10^{17}$ He^{+}/cm^{2}, the affected region by helium implantation (with discernible layer thinning) extends all the way down to 125 nm, which corresponds to a predicted 124 nm end of range (R_p+2ΔR_p). The larger bubbles correspond to where most ions have finally come to rest. In this region the density of helium atoms/nm^3 is greater and the distances between these implanted atoms are smaller. There should be a critical distance at which these implants will begin interacting with one another leading to an energy rearrangement where it will be energetic favorable to cluster. Limited vacancies would minimize the concentration of He-V_2, or divacancy complexes. At low temperatures helium will travel preferentially via interstices rather than by a vacancy-related mechanism. TRIM plots predict a small vacancy concentration peak present in the nickel top layer, close to the surface, and far removed from the stack. There is a significant

spatial separation between these distributions (the vacancy peak and the projected range). Thus, a vacancy diffusion mechanism is less likely, and neither is the possibility of helium atoms occupying these available sites. However, at the highest doses, and despite the low temperature during implantation, the gradually increasing damage in the target structure will lead to a diffusion rate enhancement where helium may make use of vacancies for migration. At these high doses, more divacancies are expected since these do not require high energy of formation. Since the temperature will not be a dominant factor, the proximity of gas atoms at the critical concentration will become crucial to coalescence. Helium has at its disposal several pathways requiring low activation energies in order to migrate and coalesce. It is already known that at room temperature interstitial diffusion will be possible, especially in Ni and in Mo (Mo more importantly). However, the interfaces and the grain boundaries provide easy access routes. Generally speaking, there is a network of capillaries capable of delivering highly mobile implanted atoms to a clustering destination. This destination appears to be preferentially in the a-Si layers. Helium in molybdenum travels fast (only <0.05 eV required for activation). This is characteristic of open-shelled, transition metals, including also nickel. That the Mo is poly-crystalline helps immensely in making mass transport easy. On the other hand, amorphous silicon acts as a sink because of its high free volume to store the excess implanted material. Because of this, a-Si provides a means for eliminating interstitial atoms from other materials in contact with it, like Mo. This translates to superior radiation resistance in a-Si > poly-Si > c-Si. However, c-Si has good permeability for helium atoms, while a-Si does not; $D_{He,a\text{-}Si} < D_{He,\ c\text{-}Si}$. Since there are no clear crystallographic features present in a-Si, the bubble density does not saturate to constant values as seen in polycrystalline and crystalline materials. The end result is a field of over-pressurized bubbles with a continuing accumulation of implanted, or diffused gas, in amorphous materials. In the a-Si layers, rapid diffusion from Mo followed by a slow diffusion in the amorphous silicon that can fit large concentrations of helium will lead to the observed preferential nanobubbling in these layers. That a-Si has a low yield strength allows for this 'sponge-like' layer to elastically stretch and later

plastically deform by exhibiting impressive elongations to fit the influx. The bubble size profile follows the implanted distribution, showing no bubbling in the nickel and then in the Mo/Si an increase in bubble size followed by a decrease deeper in the structure at $1x10^{18}$ He^+/cm^2. Laterally the same effect is observed where along the same a-Si layer starting away from the ion beam impingement axis on an undamaged section and moving normal to the beam axis, bubbles do not exist, then smaller ones appear until a peak size is reached below the beam axis, then decreasing until no radiation damage is once again detectable. These trends maintain a close relation with the Gaussian longitudinal and lateral range profiles of implanted helium ions in a material. At higher doses, because of oversaturation, the trend in expansion is expected to continue until the mechanical limits of the nickel are tested. Rupture and micro-cracking of the top layer then would yield a surface with high roughness and consequently many new pathways for the exodiffusion of helium that would result in empty voids.

In the case of neon, there are subtle differences that need to be addressed and can be reasonably explained. Since it has been demonstrated that temperature effects may be present, the morphology can be rationalized better. First, even though neon is a larger atom than helium, and it will exhibit lower diffusivities in the solid-state medium, the venues available (esp. grain boundaries and interfaces) for its migration in the multilayer stack are far more forgiving than in a closely-packed crystalline structure, where it would realize more resistance. Since neon etches the nickel, there is a dynamic, near-balanced (or near-compensated) mass transfer. Ions that are implanted into the structure, are removed shortly thereafter as the etch front progresses downward deeper into the structure. However, neon forms discernible nanobubbles at lower concentrations, at least by one order of magnitude lower doses than its counterpart helium. At the start of the experiment, these cavities begin forming at two main locations: a) where the highest vacancy concentration is found (~25 nm inside the nickel top layer) and directly under the beam axis (single nanobubble ~20 nm wide), and b) principally 50 nm down at the Ni/Stack interface

with several smaller, but definitely discernible, nanobubbles ~5-7 nm in width (where heating may be already playing a role). The range for neon is much smaller than for helium. In this case, it is 26 nm and the end of range is ~54 nm. This places neon ions at the interface from the start; admittedly at initially low concentrations. Vacancies are created near the impingement surface mainly, but their concentrations tail deeper into the nickel film. These are not expected to play a leading role in nanobubble formation because of the abundance of grain boundary sinks. Neon, however, will generate 10x more vacancies than helium, and in a narrower spatial distribution. Notably, neon offers a very unique characteristic at 30 keV. The peak temperature and the peak concentration of implanted atoms are very close to one another. Thus, there is going to be more thermal energy to enhance mobility in nickel where inert gases are known to be fast diffusers.

During the etch process, implanted neon is removed along with target atoms. This allows for a quasi-equilibrium state to be present. Neon has a steeper climb in order to reach high concentrations in the bulk since shortly thereafter it may be ejected, or simply outgassed, once the evolving free surface reaches a particular depth. At this point it is important to note that the threshold concentration for neon has been estimated at ~4×10^{19} Ne/cm^3. With this in mind, it is now obvious that nanobubbles form earlier with neon at lower concentrations. This may be a direct result of neon having almost 2x the atomic radius of helium. The atomic and the van der Waal radii of neon are 58 and 154 pm, which is roughly 1.87 and 1.1x that of helium. It is interesting that the atomic radius of Ne is ~2x that of He. Since the implanted neon is very tightly packed near the top surface and helium is distributed over greater distances and deeper into the structure, the implanted neon is expected to interact with one another much earlier, at lower doses, then coalesce or agglomerate. This is expected to lead to the early manifestation of neon nanobubbles.

At intermediate doses, particularly ranging from 4-6x10^{17} Ne^+/cm^2, other variables may have a more crucial role. As the etch progresses down, deeper into the stack, some heating can

begin contributing due to the interfacial thermal conduction issues discussed earlier. Heat is generated in the multilayer stack with low thermal conduction normal to the interfaces, thus inducing a preferential lateral flow. Interplanar heat disruption, lead to principally intraplanar conduction, or an anisotropic thermal conductivity. The many closely-spaced interfaces result in more phonon internal reflection, especially in a-Si with low phonon mean free paths, and less transmission across boundaries. As per Bozorg-Grayeli and his study of the Mo/Si multilayer stack, suggests the thermal conductivity drops to ~1.5 W/m-K for nanoscale layers [60]. Notice that this is roughly the conductivity of SiO_2. The effect of thermal spikes that is likely negligible in nickel could be a factor in the multilayers. Thus as the peak concentration of neon continues to be implanted ~26 nm below the bottom of a progressively deeper etch surface, there may be sufficient thermal energy available to grow the nanobubbles. When the beam is incident closer to the stack, a significant peak vacancy concentration exists within the stack as well as heat. This provides a way for bubbles to relax to an equilibrium size, while lowering its free energy and have a regular shape, namely more spherical. Not only can the nanobubble accommodate more implanted atoms in the extra sites or high-density of vacancies at shallow depths along the beam axis, but can also grow at the expense of its smaller neighbors. This Ostwald ripening effect leads to the coarsening of one or few nanobubbles that grow much larger in size than the surrounding neighbors. A large nanobubble can emerge with sufficient sphericity which means it has evolved to a low free energy configuration.

As the etch progresses, the oversized bubble will eventually meet the etch front and thus deflate by losing the accumulated neon. A partial void or empty cavity would then remain after this bursting process. Notable is the small range of the nanobubble field. Basically, from the freshly etched surface to the undamaged stack on the opposite side, one expects first a narrow width with small bubbles, then a large spherical bubble in a belt with others of similar size forming a radial band, then smaller nanobubbles once again, followed by a damaged region of intermixing

(no discernible nanobubbles involved here) before lastly reaching the undisturbed stack. Higher local temperatures enable the migration of neon to the band where they can be captured into evolving nanobubbles. Refer to figure 2.39 for a diagram showing neon nanobubble evolution.

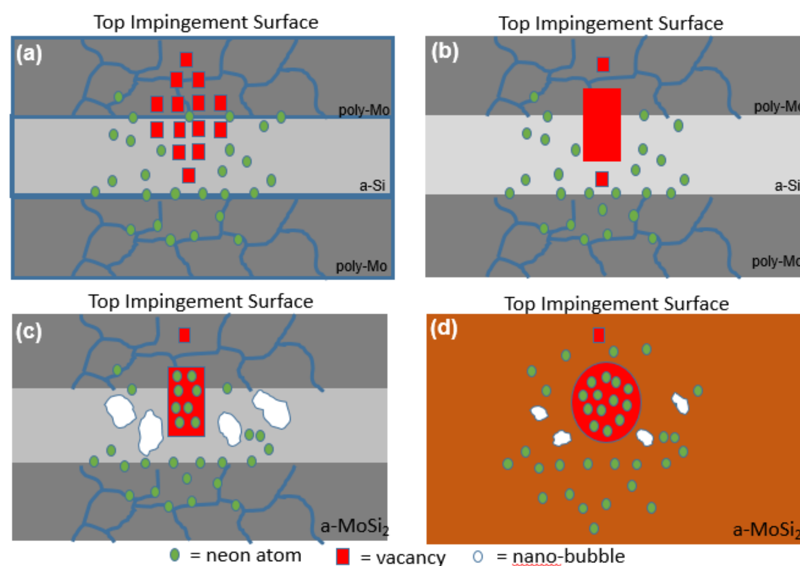

Figure 2.39. Diagram showing the evolution of individual implanted neon and defects leading to the formation of nanobubbles and ultimately Ostwald ripening.

Thinning of layers is detected and mirroring what was found with helium. The damage under neon irradiation is more severe and the intermixing fully mixes neighboring Mo/Si multilayers in close proximity to the nanobubble region. Nevertheless, no Mo/Si crystallinity is observed within this band thus apparently the $MoSi_2$ is amorphous – perhaps due to a room temperature process or thermal spikes too short to enhance longer-range ordering.

Below, figures 2.40 & 2.41, for two doses of neon in the EUV mask, the etch profiles are shown. This effect of overetching has been documented by Drezner et al [35] in Ga^+ FIB etching on Si <001>. From these images, plots were generated for the dependencies of via width with

depth, and for percentage of re-deposited material with aspect ratio. Clearly, the narrowing trend, or ‘V-shape’, can be observed and at an A.R. of 1.0, the re-deposited material (that is not sputtered out of the cavity) reaches 5% of the expected volume. By A.R. ~1.5, the sidewall coverage is up to ~10%. The trajectory and velocity of ejected particles can be altered via collisions with other particles within the trench and with the sidewalls. A finite sticking probability between 0-1 also exists for deep trenches with high aspect ratios. Within the hole with this confining geometry, the re-deposition rate rises and the removal rate falls. This can be rationalized by considering the large detrimental effect that localized pressures have on the mean free paths of the escaping atoms, a large fraction of which do not reach the top of the hole (where the vacuum pressures are much lower). The mean free path of a particle exhibits a $\lambda \propto p^{-1}$ relation, and both form part of the following expression [101], where d is a collision parameter:

$$\lambda = \frac{1}{\sqrt{2} d^2 \left(\frac{p}{kT}\right)}$$

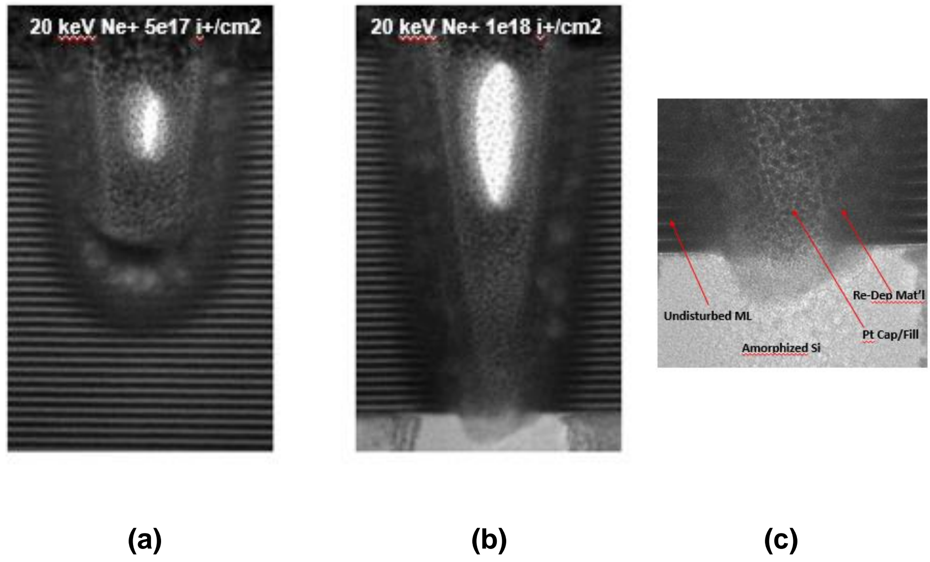

Figure 2.40. Etch profiles at 50 KX for $5x10^{17}$ (in a) and $1x10^{18}$ (in b) Ne^{+}/cm^{2}. A closer look (200 KX) near the bottom of the via in c).

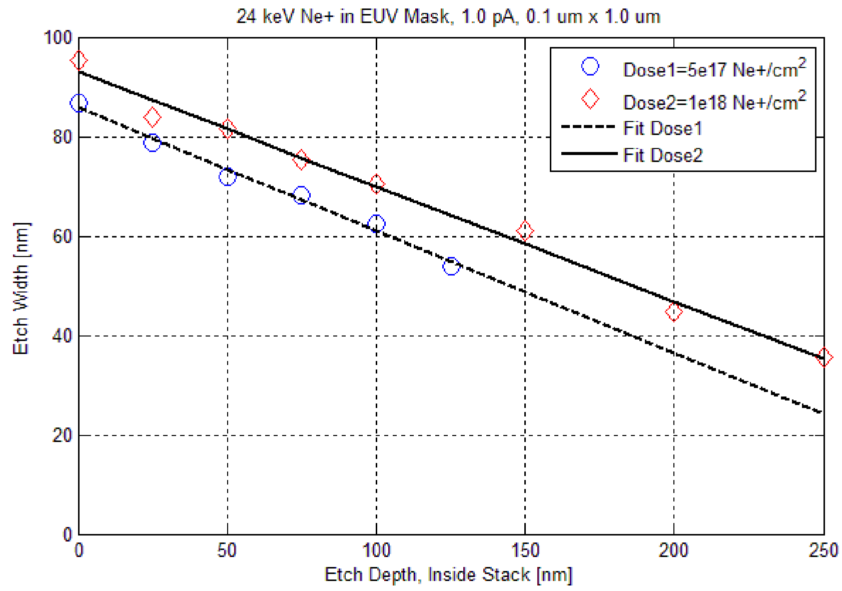

(a)

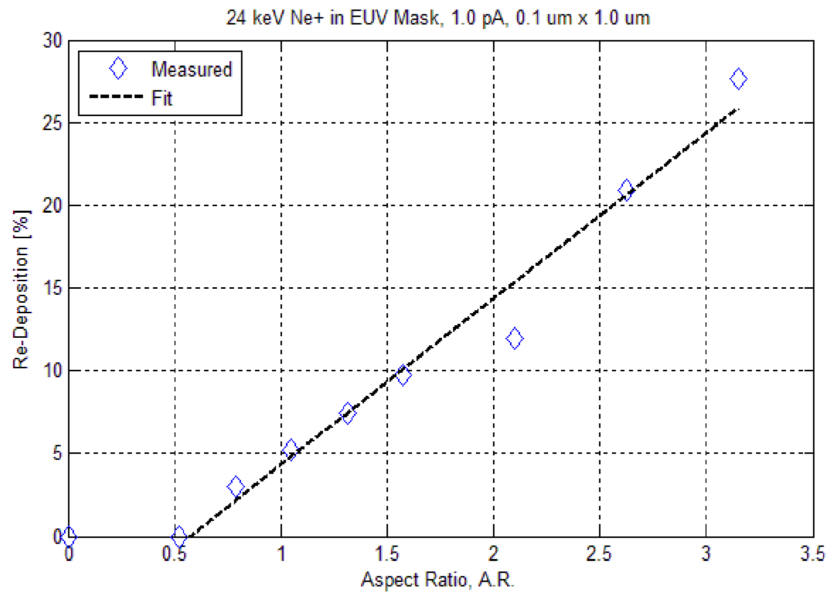

(b)

Figure 2.41. Plot (a) showing the change in width and its slope as a function of milling depth, for each case in figure 2.40, and another plot (b) with the re-deposition percentage as a function of aspect ratio (h/w).

Conclusions

We have studied the feasibility of etching nickel EUV absorber layers on Mo/Si multilayers via focused helium and neon ion beam processing. Helium ion beams at both 16 and 30 keV do not etch the nickel absorber layer and TEM imaging reveals unwanted intermixing of the underlying Mo/Si EUV reflector layers. At doses below $1x10^{17}$ He^{+}/cm^{2}, a progressive contraction consistent with molybdenum silicide formation is observed. At higher doses, nanobubble formation occurs and causes swelling that can be attributed to peak implant concentrations in excess of $3x10^{20}$ He/cm^{3}. Ion-solid Monte Carlo simulations at both 16 and 30 keV reveal that the damage can be correlated to the nuclear energy loss of the helium ion beam and that the Mo/Si intermixing is due to either knock-on collisions, a thermal spike or a combination thereof.

For neon ion beam induced exposures at 30 keV, the nickel absorber layer is effectively etched due to higher nuclear energy loss in the near surface region. TEM images reveal a subsurface damage profile consisting of nanobubbles and an extended region of apparent Mo/Si intermixing occurs. The measured sputtering rate of ~1.5 nickel atoms/neon ion is comparable to the simulated sputtering rate of 2.0 nickel atoms/neon ion (TRIM overestimates nickel sputtering at 3.2 Ni/Ne^{+}). Ion-solid Monte Carlo simulations reveal that nanobubbles form at much lower doses for neon due to the shorter range and thus higher neon implant concentrations. Nanobubble formation is correlated to concentrations exceeding $4x10^{19}$ Ne/cm^{3}. Furthermore, the observed damage region beneath the neon nanobubbles is attributed to knock-on or thermal spike induced intermixing of the Mo/Si layers due to the nuclear energy loss.

While helium was not found to be a viable ion for patterning nickel top absorber layers, neon resulted in acceptable etch rates. However, while inherently different, both introduced subsurface damage in the form of discernible extended defects that renders the EUV mask

structure useless. In a composite multilayer structure like this Mo/Si mirror stack many characteristic and relevant features have been identified and explained by using concepts of defect generation and interactions. Most of the noble gas retention and accumulation has been attributed to the existence of interfaces and grain boundaries (Ni & Mo), and to low permeability and high solubility in a-Si.

Chapter 3:

Helium and Neon Ion-Based Endpoint Detection

Summary

Currents in the pico-ammeter (pA) range have been detected from the stage in a Helium Ion Microscope (HIM) during ion irradiation. In tandem, the Everhart-Thornley detector video output has been used as a voltage signal source, typically in the tenths of volts range, to capture secondary electron (SE) signals and correlate these to the etch profile during helium or neon etching. Crystalline Si (c-Si) and SiO_2(100nm)/Si substrates, Ni(50nm) on top of the Mo/Si EUV mask, Au/Si and Au(100nm)/SiO_2/Si, Cu(9, 45 nm)/SiO_2/Si and gold in the middle of thin carbon layers (C/Au/C) for high-contrast measurements, have all been characterized. The onset of swelling in silicon has been detected electronically by this method. For larger etch areas, at and above 250nm x 250nm, the Mo/Si EUV mask shows poor, yet sufficient contrast between the nickel top layer and the subsequent Ru and Mo/Si bilayers stack, before reaching the silicon substrate. Higher primary currents correlated well with SE yields, and a weak, but detectable dependency on the ion beam energy has been recorded for helium and neon on silicon. A two-dimensional model using a Lambertian secondary electron angular distribution has provided a good fit with experimental data, and it predicts the observed sample or detector current that depends on the via width, or aspect ratios. Lastly, a binary endpoint detection method has been successfully implemented.

Tables from different sources were prepared by David C. Joy, PhD in his 'Database of Electron-Solid Interactions, 2008' [105]. From these, information about the SE yields using electron beams were used as a reference and predictor/guideline in our investigation using instead in this case helium and neon ion beams. Refer to table 3.1 below. Another useful reference is that when employing a Ga^+ FIB, it is known that 1-10 electrons with energies below 10 eV will be generated per incoming 5-50 keV ion [75]. For helium FIB, the SE yields are expected to be 3-9x per helium ion than those arising from a primary electron in an electron beam [106].

Utke et al [107] reported in 2006 on in-situ monitoring of gas-assisted and focused electron-beam induced processing. In it, the current balance can be expressed more simplistically as:

$$I_{stage} + I_{BSE} - I_p - I_{SE} = 0 \; .$$

In many cases, however, the backscattered electron (ion) contribution can be neglected. These currents strongly depend on sample topography and composition. A milling process can be stopped once it reaches an internal layer. An important note about the origin of the stage current is that when the number of emitted electrons (SEs) exceeds the number of primary beam electrons, there is a net flow of charge from the sample to vacuum. Since this imbalance needs to be replenished, the stage current with a vast reservoir of electrons (a metal plate) provides the source. By solving for I_{SE}, the simplified expression would be:

$$I_{SE} \sim I_{stage} - I_p \; ,$$

where now knowing I_{SE} as a function of the other two known parameters (I_{stage} and I_p in pA) allows for the determination of a secondary electron yield by helium or by neon as:

$$\delta \sim I_{SE}/I_p.$$

Randolph et al [34] reported on an empiric expression to describe the stage currents while depositing a pillar with a stationary electron beam. In it, another parameter is introduced, ε, which corresponds to a backscattered coefficient. Here, the sample current is related to the primary beam current (I_P) and the secondary (δ) and backscattered (ε) coefficients by: $\mathbf{I_s = I_P(1-(\delta+\varepsilon))}$. During etching, the sample current continuously increases, whereas during deposition it decreases. For nanoscale etching, the sample current increases due to the collection of secondary electrons by the sample as the aspect ratio of the etched spot increases. Secondary electrons leave the surface with a Lambertian distribution (i.e., cos(θ), where θ is the angle subtended from the primary beam axis). On a flat surface, all the secondary electrons leave the surface and effectively reduce the measured sample current. However, as the aspect ratio of an etched feature increases, a portion of the secondary electron distribution is recollected at the sidewalls. Converse to etching, Randolph claims, when depositing a nanoscale feature, the sample current systematically decreases as the feature grows. This is due to the enhanced secondary electron emission that results from the formation of a raised feature on the surface. Because the secondary electrons originate from the near surface region, the number of secondary electrons increases, which effectively lowers the observed sample current. Randolph et al adds that according to work done by Bret et al, by monitoring the current flow through the substrate during deposition (I_s), they showed that the current decreases during deposition due to electron scattering outside of a pillar ultimately reaches a material-dependent plateau value, $I_{plateau}$. The change in current as a function of time (or growth height) was empirically shown to follow a first order decay given by:

$$I(t) = (I_s - I_{plateau})[1-\exp(-t/\tau)],$$

where the decay constant, τ, was shown to be a strong indicator of defocus or precursor deficiency.

Three types of secondary electrons may be present at any given time. These are the SE(I), SE(II) and SE(III). SE(I)s are those produced by the primary beam electron collisions with the sample. SE(II)s are generated by high energy BSEs (from a primary electron beam) in collisions with the sample. Finally, the SE(III)s are created by high energy BSEs striking pole pieces and other surfaces near the specimen.

There are three (3) important steps necessary for the emission of secondary electrons from a target material: a) the production of these internal electrons from collisions or energy loss from primary beam electrons, b) the transport of these internal electrons from the bulk towards the surface, and c) their escape through the solid-vacuum interface. The energy loss of the primary electrons is usually depicted by using a power law relation: $dE/dz = -A/E^n$. Here the change in energy with depth is inversely proportional to the primary beam energy, elevated to an exponent (typically 1 or 2). This leads to a production of secondary electrons, represented by $N(z)dz=-dE/B$. The maximum penetration depth, R, can be expressed as $R=E_0^n+1/(n+1)A$, where $n\sim0.35$ [108].

It is well understood that the penetration depth of primary electrons increases with increasing energy. At high primary energies, the high velocity electrons have only a very short time where they interact with the lattice electrons. However, as the primary electrons slow down after many collisions, their interaction time with target electrons increases, thus resulting in higher yields. Hence, for high beam energies, high SE generation is expected deeper into the bulk. Most SEs will then originate from farther away from the surface of impingement.

As per Shih et al [108], the escape of internal SEs is usually described with an exponential decay function that contains a characteristic escape depth, L. For low primary beam energies

where R<<L (penetration depth<<escape depth), the internal SEs escape efficiently even though only few are created (due to low primary energy). On the other hand, at very high primary beam energies, where in this case R>>L, the exponential nature of the escape process limits the number of SEs that can escape despite an increase in SE generation deeper in the bulk. As a result, the yield drops with primary beam energy. Actually, the yield has a maximum value at a primary beam energy corresponding to R~L. This leads to a bell-shaped yield curve observed in most materials [108].

High SE yields are not always observed because of internal losses due to several types of interactions within the solid. The biggest difference occurs between metals and insulators. In the case of metals, internal SEs lose energy especially via interactions with conduction electrons. This translates into lower yields for metals that are typically between 0.5 (for Li) and 1.8 (for Pt). Clearly, the heavier atoms exhibit higher SE generation because of a higher number of electrons at greater distances (less strongly bound) from the atomic nucleus. In general, escape depths for metals are only between 1-5 nm. Conversely, in insulators, internal SEs do not interact with conduction band electrons, but rather with valence band electrons if their energy is large enough to excite electrons from the valence into conduction across a typically wide band gap. Basically, the wide band gap in insulators minimizes the energy loss because of the SEs. There are two other possibilities for energy transfer and loss; namely, the electron-phonon and the electron-defect/impurity interactions. Because of the absence of the predominant electron-electron loss mechanism, in insulators, the escape depth is larger and consequently, the SE yields. NaCl can have yields up to 6.8, while c-MgO an astounding 25 [108]. In general, most insulators exhibit escape depths typically between 10-20 nm, but can be as high as 50 nm. Kanaya-Okoyama came up with an expression for depth penetration, and Ono-Kanaya introduced a simplified formula for escape depth. These are as follows:

$$R = \frac{0.0276\, A\, E^{1.67}}{\rho\, Z^{0.89}}$$

$$L = \frac{2.67\, A\, V}{\rho\, Z^{0.667}}$$

where A is the atomic weight (g/mol), E the beam energy (eV), Z the atomic number , ρ the mass density (g/cm^3), and V the first ionization energy (eV).

The Everhart-Thornley (E-T) is the standard secondary electron detector. It can also be used to detect BSEs, if a negative voltage is applied to the grid in order to repel low energy SEs. The detector consists basically of a scintillator and photo-multiplier. The grid is typically biased between -50 and 300 V. In it, the number of cascade electrons produced by a photomultiplier tube (PMT) depends on the voltage applied between its electrodes (anode/cathode). This voltage is typically 10 kV. The scintillator fluoresces light in the UV range and this passes on to a light pipe for amplification. The scintillator signal is commonly amplified by $(\delta)^N$ or ~10^6. The total effective amplification of the PMT/scintillator combination is ~10^8 [109].

Experimental Methods

Box patterning was done using the pattern option on the Zeiss Nanofab apparatus. Measurements of stage currents were made using a Keithley 6485 picoammeter and of the ET detector output with an Extech 540 data-logger multimeter set to the VDC option. Before each pattern was initiated, the BNC output from the data acquisition terminal (video) was unplugged and connected to the voltmeter. The pA data from the stage was saved every two seconds in a text file via a

simple RS232 collection program. Data saved in the Extech memory was downloaded in another computer using Windows 2000 (version 1.0 software) and the data points were recorded at a 1 per second rate. Plots were then made with current and voltage simultaneously versus time (in sec) or dose. Other parameters were studied and their effects on the responses characterized. These were: ion type (He, Ne), ion beam energy (29 keV for He^+ and 24 down to 15 keV for Ne^+), primary ion beam currents (ranging from 0.6 to 4.0 pA), dwell times (1 μs to 1 loop) and pixel spacing (1nmx1nm to 10nmx10nm).

Samples used were: Ni(50nm)/Ru/Mo/Si (EUV mask), c-Si substrates, SiO_2(100nm)/Si, Au/Si, Au(100nm)/Cr/SiO_2/Si, Cu(9, 45 nm)/SiO_2/Si and finally structures of C/Au/C/Si that were prepared by sputtering and evaporation using the SPI Module Carbon Coater, the SPI Module Sputter Coater (with Argon gas) and the SPI Module Control. Here, the settings for Au deposition were ~2 Torr Ar, 20 mA plasma current, and 40 seconds total run time. For C evaporation: 0.1 T low vacuum pressure, 8V and 60 A_{AC}, for a total of 30 seconds.

Results and Discussion

Secondary Electron Yields by Helium and Neon Irradiation.

Table 3.1. Comparison of SE yields of several materials when using a primary beam of electrons, helium ions and neon ions. # includes BSI contribution. * ua (for unavailable), because the layers where too thin to ascertain individual yields.

Material	SE yield e- (@25keV)	SE Yield He+ (@29 keV)	SE Yield Ne+ (@24 keV)
Au	0.263	2.3#	3.0#
C	0.052	ua	ua
Cr	0.11 (@30keV)	ua	ua
Cu	0.161	2.2	1.2
Mo	0.214	ua	ua
Ni	0.117 (@30keV)	ua	1.5
Si	0.081	1.4	0.8
SiO_2	0.314 (@10keV)	1.7	1.5
Ru	ua	ua	ua

Table 3.2. Sputter yield and backscatter predictions by SRIM/TRIM, at 30 keV.

Material	Y by He (at/ion)	Y by Ne (at/ion)	BSI (%) He	BSI (%) Ne
Au	0.115	4.25	20.1	29.3
C	0.016	0.505	0.3	0
Cu	0.130	3.81	7.6	7.6
Mo	0.041	1.76	7.2	13.7
Ni	0.084	3.20	7.3	7.5
Si	0.039	1.08	1.6	0.8
SiO_2	Si (0.033) O (0.091)	Si (0.542) O (1.79)	0.5	0.7
Ru	0.067	2.37	12.4	14.1

Endpoint Testing Considerations.

While performing endpoint detection tests, a coordination must be observed between the beam raster conditions and the data collection rates by the meters. Since the equipment and the setup had the limitation of data capture every one second for the E-T detector (video output) voltage and 2 seconds for the stage current, the user had to be aware of how many monolayers of material were removed in each loop. As much as possible, the user attempted to collect data every second for each pass of 1 second, but the patterning times resulting were too long, typically in excess of 10 minutes. As much as possible, each experiment lasted in the vicinity of 2 minutes. Issues like those shown below in figures 3.1 and 3.2 were avoided. Figure 3.1 shows how for a w=250 nm, the dwell times can introduce undesired fluctuations. Consequently, in all experiments in the

following sections, a 1 μs dwell time was utilized. Clearly, the longer the beam dwells, the poorer the resolution in the measurements in order to detect the internal interface. In this case for 100 nm of Au on SiO_2/c-Si, up to 10 μs still provides reasonable quality data for discriminating where the top layer ends. In the next figure (3.2), the pixel spacing was varied from 1 nm x 1nm up to 10 nm x 10 nm. Again, the same effect is practically duplicated. At the largest pixel pitch, 10 nm x 10 nm, the endpoint cannot be resolved because of the wide fluctuations in the stage currents monitored at the picoammeter. This can be explained by the inability to etch a continuously homogeneous bottom surface where material may be left in between pixels. Thus, etch front irregularities or a non-uniform floor will introduce shadowing events in the data collection. For all the experiments in this section, a 1 nm x 1 nm pixel spacing was utilized.

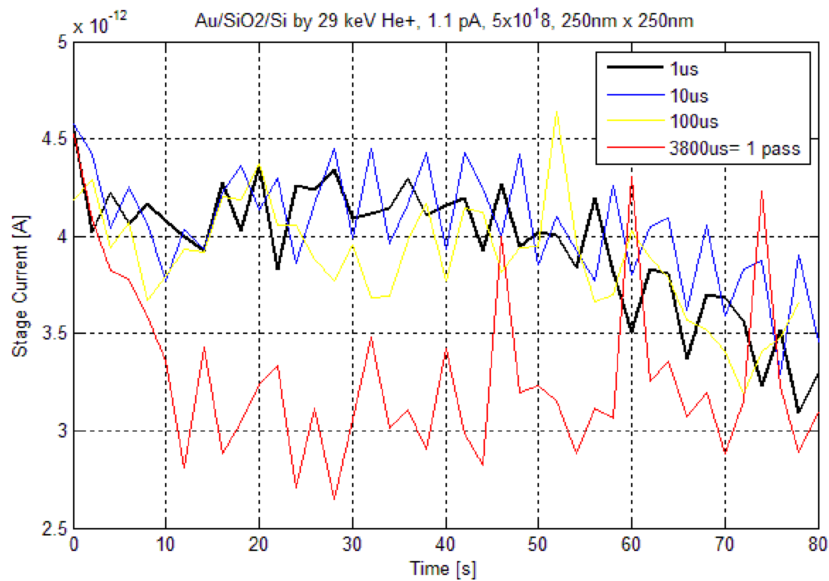

Figure 3.1. Effect of dwell times on the stage current signals.

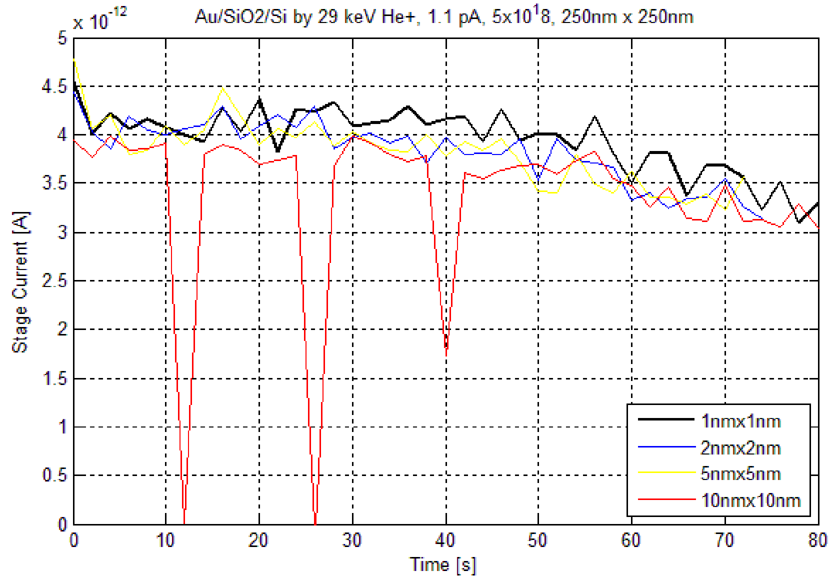

Figure 3.2. Effect of pixel spacing on the stage current signals.

Ni Endpoint Detection.

First, nickel endpoint characterization was undertaken with the Ni/EUV mask described in chapter 2. The plot below in figure 3.3 shows the E-T voltage and the stage current detected for a total dose of 1×10^{18} ions/cm^2 on the Ni-Mo/Si mask. These responses clearly show a greater sensitivity from the E-T detector to current fluctuations. The slower decay in stage currents is attributed to an increasing number of electrons captured at the sidewalls as the etch front moves deeper into the structure. It is important to point out that this difference is in stark contrast with what is reported by Randolph et al. In the case of a pillar growing atop the substrate surface, the stage current increases notably. This is attributed to the fact that the stage has to supply more electrons as the pillar grows since more of these leave the higher aspect ratio (AR) pillar and reach the detector near and above (I_{SE}' ↑). The growing pillar has a different composition (typically metal embedded in carbon) than the substrate where the mainly vertical deposit rests upon. Hence, the SE yields and SE escape depths are different at the beginning of the process (low AR) than later on (high

AR). In the case of this study, since the feature is now an etched via, as the mill progresses inward into the substrate material, an increasing number of generated electrons strike the sidewalls and never escape. Thus the number of electrons reaching the detector above decreases (I_{SE}' ↓), as well as the number of electrons that the stage has to supply (I_S ↓), since those captured at the sidewalls do not have to be compensated (I_{SE}'' ↑, I_S ↓). Refer to figure 3.4. A useful expression from charge neutrality or current balance, as for a node and Kirchhoff's current law (KCL) can be used to represent this effect: $I_S - I_{BS} - I_P - I_{SE}' + I_{SE}'' = 0$, from which $I_S \sim I_P + I_{SE}' \downarrow - I_{SE}'' \uparrow$. The net result is that I_S decreases with time. In this equation, the I_{SE}' is the current reaching the E-T detector, and I_{SE}'' is the current from electrons unable to escape the deepening etch. At time=0 (or flat surface), $I_{SE}''=0$ and thus, $I_{SE}=I_{SE}'$ and $I_S \sim I_P + I_{SE}$. Moreover, since the ions are positive, the backscattered ion is assumed to leave in a neutral state by capturing an electron from the specimen as in I_{BS}: $Ne^+ + 1e^- \rightarrow Ne^0$ (=BSA).

From this information it was possible to obtain the SE yield for nickel, since it is 50 nm thick, or thick enough to minimize contributions from the underlying stack. The BSI yield for nickel, according to SRIM/TRIM, is relatively low at only ~7.5% (refer to table 3.2). Because of the shallow escape depths (<5 nm), the initial SE yield results from the top nickel layer. The results have already been listed in table 3.1. Based on stage current data, the SE yield calculation for Ni is ~1.5 SE/Ne^+. Notably, the signal from the E-T detector provides clearer information by showing sharper transitions and reductions in the SE counts incident on the detector.

For the etching of a box 250nm x 250nm with 1.0 pA, 24 keV Ne^+ (figure 3.5), on the EUV mask with and another without the nickel top layer, the results were intriguing. It has been confirmed that because of the presence of nickel, the electron count is higher and drops as the etch progresses inward towards the multilayer interface. However, when starting the etch on the ruthenium layer (only ~2.5 nm thick) and moving on immediately into the bilayer stack, the counts start low, decreasing slowly and intersecting the response of the Ni-Mo/Si sample at ~40 seconds.

This time corresponds to a dose of ~$4x10^{17}$ Ne^{+}/cm^{2}, which is where in chapter 2, the 50 nm nickel top layer was completely etched according to TEM imaging (figure 2.17c). This test shows close agreement between endpoint detection and the visual information gathered from TEM analysis. The negative slope in the plot indicates the etching is taking place, but in the case of nickel, this slope is steeper which itself corresponds to a faster sputtering rate by neon on nickel. The signal strength is close to 2x higher at the start of the mill on the top surface (~0.5 V) with respect to the endpoint for the nickel layer (~0.275 V). This constitutes a signal intensity drop of 45% from the top to the bottom of the nickel top layer, which should be sufficiently large to provide good resolution, or distinction between Ni present and not present, on the multilayer structure.

(a)

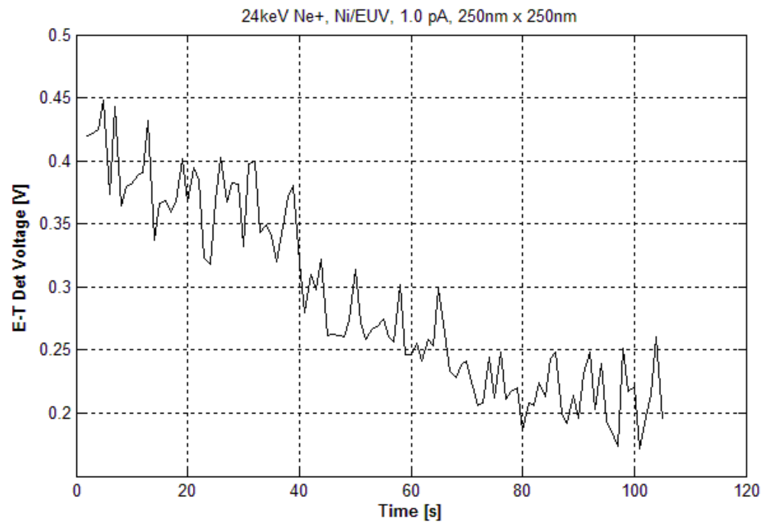

(b)

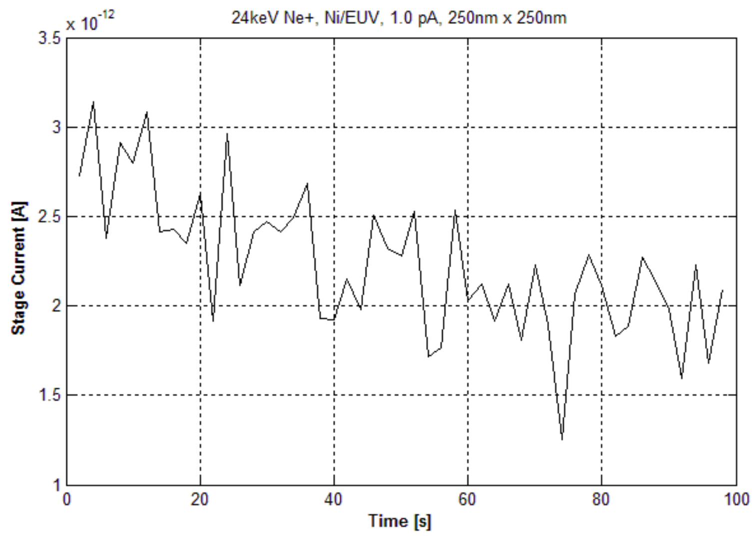

Figure 3.3. E-T detector voltage (a) and the stage current (b) for the electronic profiling of the EUV mask.

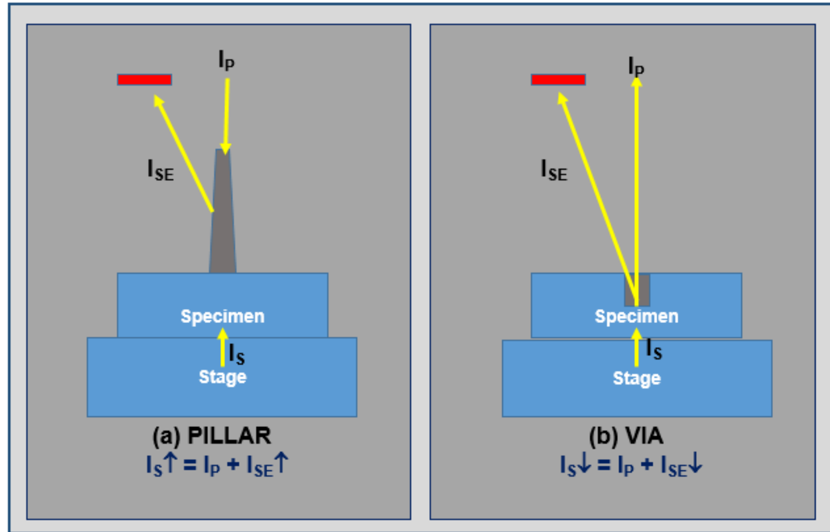

Figure 3.4. Comparison between growth of a pillar and etch of a via.

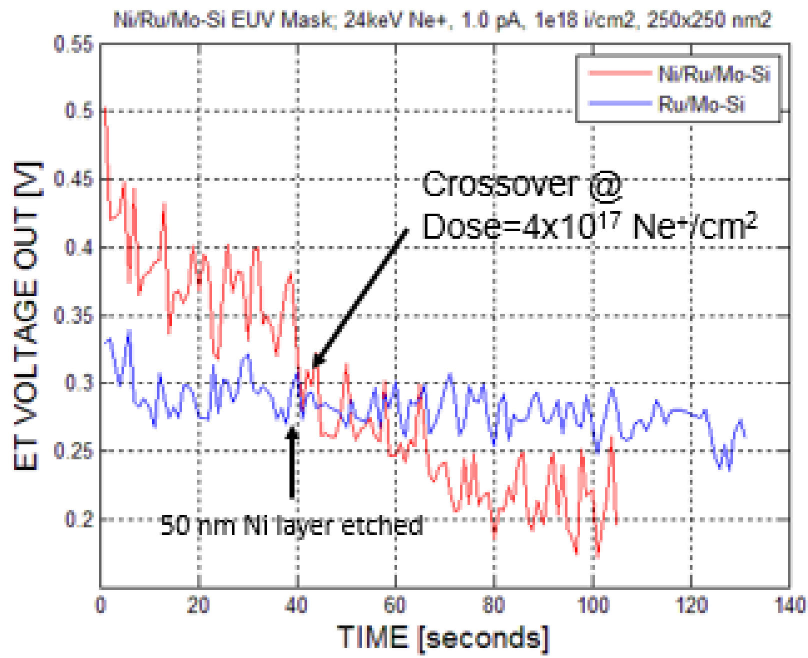

Figure 3.5. Voltage signals from the E-T detector for w=250 nm boxes etched on the EUV mask with (Ni-Ru-Mo/Si) and another without (Ru-Mo/Si) the nickel top layer.

In figure 3.6, a set of three (3) different size square boxes were etched on the EUV mask. Interestingly, it has been found that the narrower the etch width, the steeper the drop in SE collection at the detector above. This is an indication that geometrical and topographical dependencies are present during the etching process. More on this topic will be discussed in the crystalline Si section later on in chapter 3.

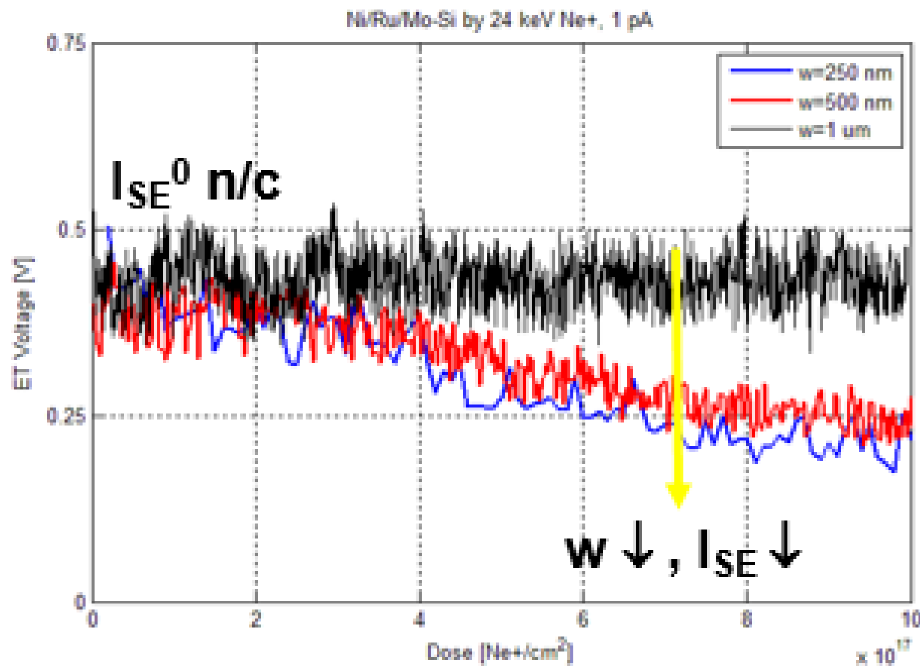

Figure 3.6. A dependence on box size, or width, found during etching of the EUV mask. Three (3) square box sizes, represented by their widths, are shown, where the smaller the width, the greater the slope, or reduction rate in SEs reaching the E-T detector.

The responses are admittedly noisy. This noise may be the result of small fluctuations in field ion source gas pressures and thus ion currents, the exact position within the etch front bottom surface at which the data is collected every 1 or 2 seconds and possibly instrumental noise. The

data represents only one instantaneous reading in time, therefore involving no averaging. After the data was collected and processed, a moving average smoothing method was implemented in order to filter the raw data. A comparison between raw data and smoothed data is shown below in figure 3.7. The smoothing was done using three (3)- and five (5)-point averaging. The figure shows clearly how smoothing sanitizes somewhat the information by eliminating many of the sharp data spikes. A 3-pt moving average will be used to find a suitable model/fit for the experimental data.

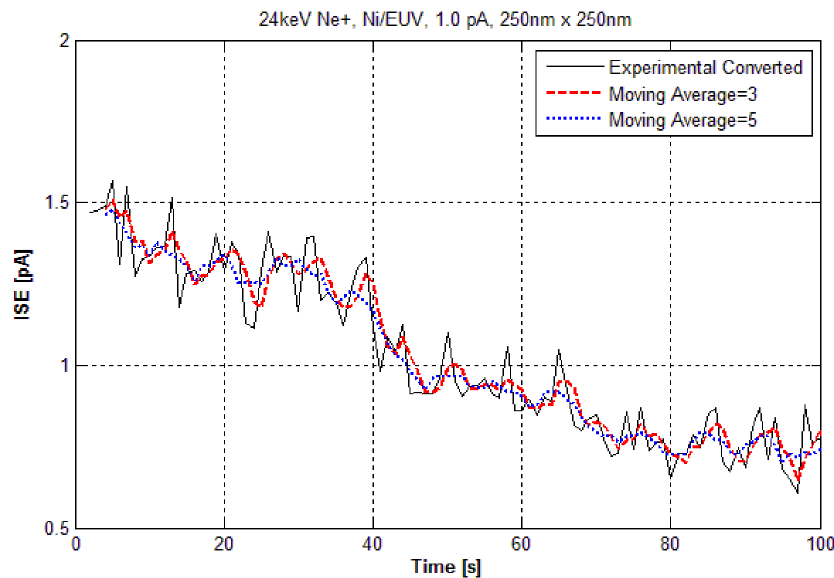

Figure 3.7. Experimental and smoothed data using a moving average filtering method.

Using Matlab R2013a, a 2-D model to predict the secondary electron and sample current was implemented. Refer to the algorithm in Appendix A. Using a Lambertian angular distribution for the secondary electron trajectories, $I_{SE} = \delta I_P \sin\theta$, an expression was obtained for the secondary electron intensity at the E-T detector (I_{SE}) as a function of time, dose or depth. At t=0,

h=0, or Dose=0; $I_{SE} = \delta I_P$ for a flat surface. This empirical expression for a single material is as shown below:

$$I_{SE} = \frac{w}{2\sqrt{h^2 + \frac{w^2}{4}}} \delta I_P$$

where w stands for box width, and h for the etch depth (here, h/w is the aspect ratio, A.R.). Note that h = v x t (where v is an effective etch velocity for the box and t is the etch time). Dose is Flux x time where Flux is basically I_P/w^2. In the case, where there are two different materials across a buried interface, the equation will have to take into account the difference in secondary electron yields (δ_1, δ_2) in addition to the geometry (w, h) of the milled box. The volume fraction factor inserted in the equation (vf_1) is based on the escape depth of the top material and accounts for the weighted contributions of electrons from the top and the bottom layers as the ion beam approaches the interface. In this case, the new expression will be:

$$I_{SE} = \frac{w\,[vf_1\,(\delta_1 - \delta_2) + \delta_2]}{2\sqrt{h^2 + \frac{w^2}{4}}} I_P$$

The analytical expression operates on the basis that the intensity of the secondary electron generated current at the E-T detector will depend on the sine function of an angle between the ion beam vertical axis and a straight line between the center at the bottom of the etch to the edge or corner of the box on the top surface. Refer to figure 3.8 for a sketch illustrating this condition.

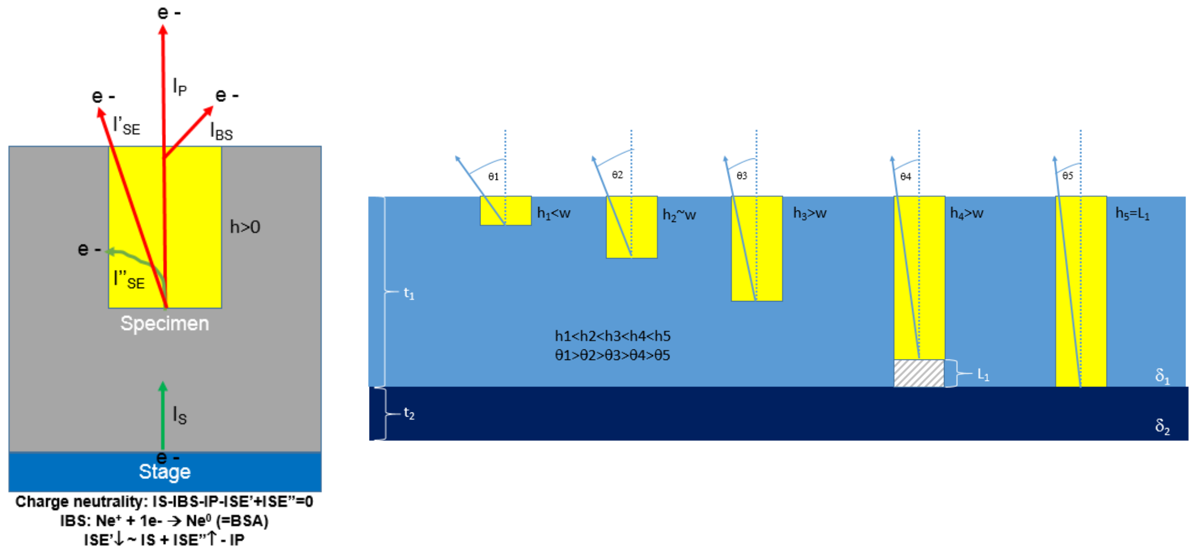

Figure 3.8. Sketches showing the currents present in a specimen during ion irradiation and the dependence of SE counts at the E-T detector on depth (h) and thus the angle θ, where $\tan\theta = w/2h$.

The simulation shows close agreement with the experimental data (figure 3.9). The multilayer stack was approximated to a single monolithic thick layer since the thicknesses are quite small (only between 2.5-4 nm) to be individually resolved at a 1 s data capture rate. Clearly, in this two-layer system with one interface, the higher SE yield from nickel when compared with the Ru-Mo/Si structure, provides a useful signature to monitor when the internal boundary has been reached. From it, the etch rate, or velocity in nm/s was obtained to be 0.4 nm/s, which when converted to sputter yield gives 1.45 Ni/Ne^+. This agrees closely with observations based on measurements of the etch profile (from TEM) and the EnvizION simulation results of 1.5 and 2.0, respectively. SRIM/TRIM predicts a 3.2 sputter yield. The etch depth at ~4×10^{17} Ne^+/cm^2, agrees with the nickel top absorber layer thickness. The expression [110] used to convert sputter yield (in atoms/ion) to etch rate (in nm/s), and vice versa is as follows:

$$\frac{z}{t} = \frac{M}{\rho\, N_A\, e}\; Y\, J_P$$

where M is the atomic weight (g/mol), ρ the mass density (g/cm^3), N_A is Avogadro's, e the charge of the electron, Y is the sputter yield (atoms/ion) and finally J_P is the primary current density (A/cm^2). When taking into account the dose required to etch the metal away completely, the sputter yield can be calculated by using the thickness of the layer (or etch depth). Hence, the yield in atoms/ion will be:

$$Y = \frac{Depth}{Dose}\; \frac{\rho\, N_A}{M}$$

Using the later equation, the dose for etching the entire 50 nm top later is 4×10^{17} Ne^+/cm^2, which yields a Y=1.14 Ni/Ne^+. Admittedly, not exactly 1.45, but within range. More precisely, the nickel endpoint may be between 3-4×10^{17} Ne^+/cm^2.

Figure 3.9. Experimental and fit data for the Ni EUV multilayer structure. First, showing ISE versus Dose, then versus Height (nm) and finally, the Etch Depth as a function of Dose.

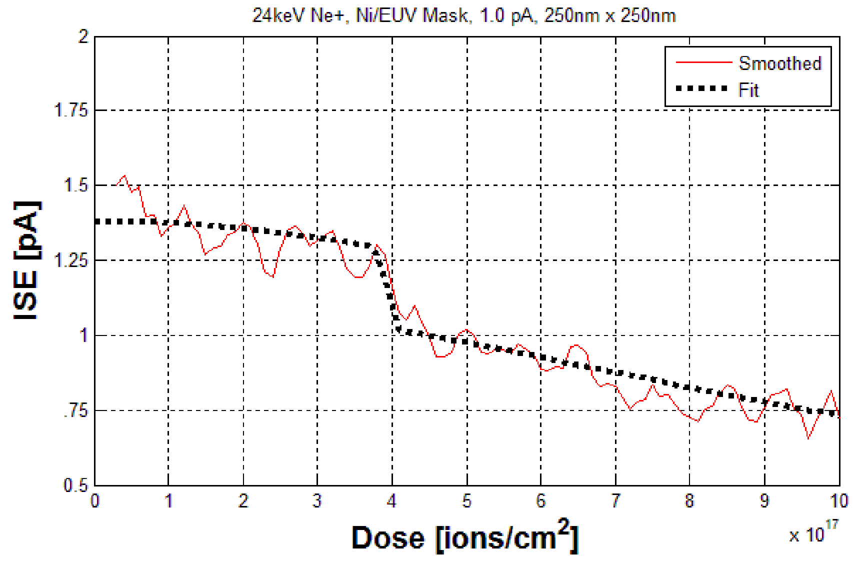

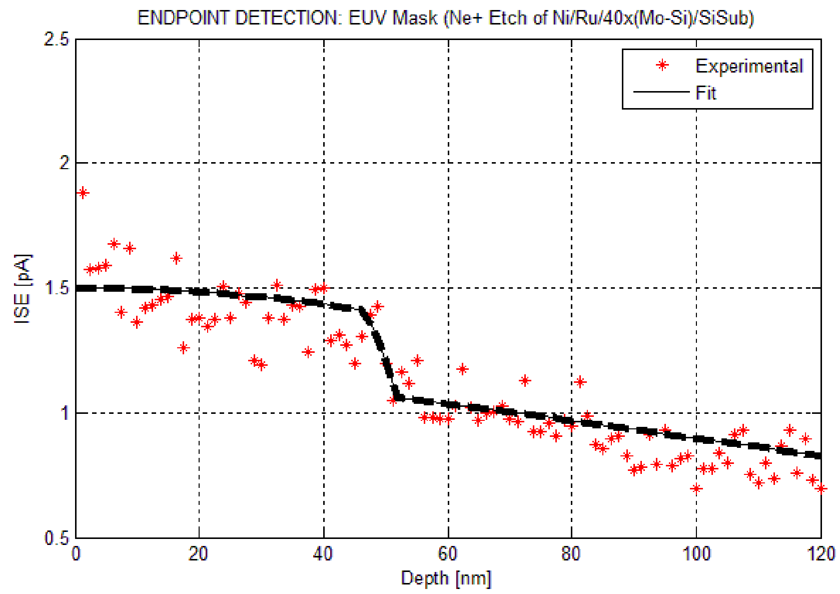

Figure 3.9. Continued.

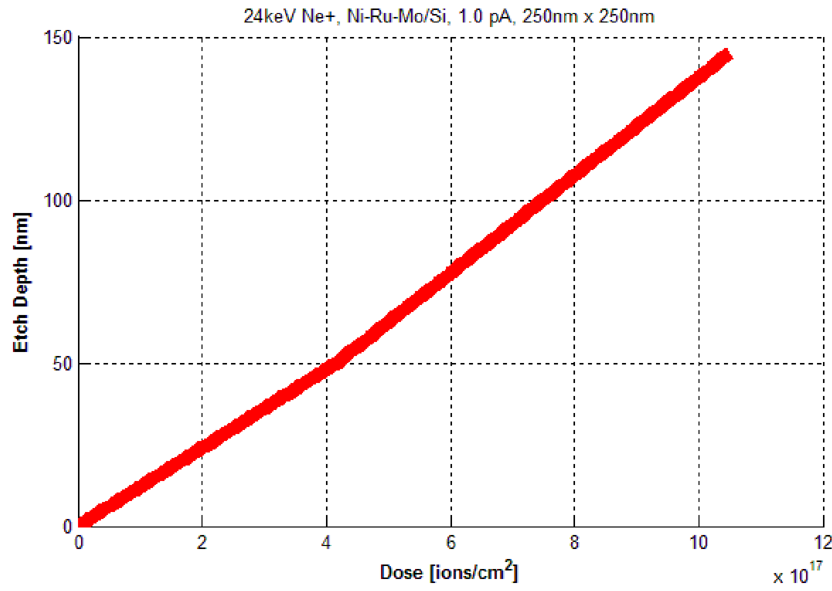

Figure 3.9 Continued.

The results and the fit in 3.9 show a characteristic sloping, or gradual, drop when moving from one material to near the next one below. If not for the finite escape depth (L>0), this drop would be expected to be a step function (for L=0). During the transition, and for thin residual layers (<5 nm for metals), the secondary electrons received at the detector will be arriving from the top layer and the next layer below. Since the Ru, Mo and a-Si films are so thin (2.5-4.1 nm), it is impossible at this time to resolve these interfaces and as shown in chapter 2, the beam induced damage causes intermixing which further blurs the transitions. Thus the fluctuations observed cannot be attributed to an unperturbed alternating nature of the stack since the noise level is relatively high.

c-Si Endpoint Detection.

Helium irradiation of crystalline silicon results in swelling caused by nanobubbling. However, for higher doses, once the blister has suffered a fissure the accumulated helium can escape, allowing the surface to recede. The oversaturation that precedes the swelling takes place rapidly at low doses for c-Si since in a crystal other than the intrinsic low point defect and dislocation concentrations present, only interstices typically within the tetrahedron in the each lattice can accommodate the host atoms. The supersaturation (or superlinear regime of implantation) results in extensive damage and weakening of bonds between silicon atoms. This eventually, and at relatively low doses of ~$4x10^{17}$ He^+/cm^2, leads to sputtering of silicon by helium since the binding energy has been reduced with the added elastic energies. Figure 3.10 shows this trend for box sizes w=250 and 500 nm, and for three (3) c-Si substrates with different doping levels. Note that while the E-T detector records the expansion of the top surface, this event is not conspicuous with stage current measurements.

(a)

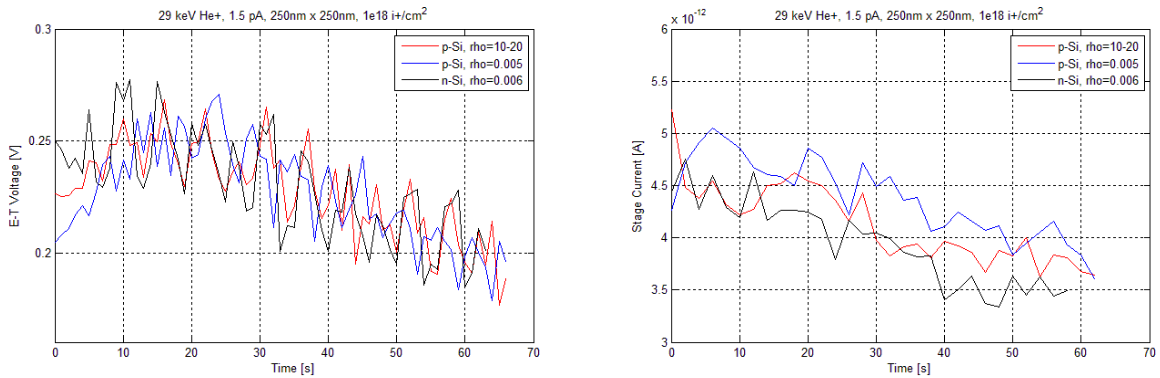

(b)

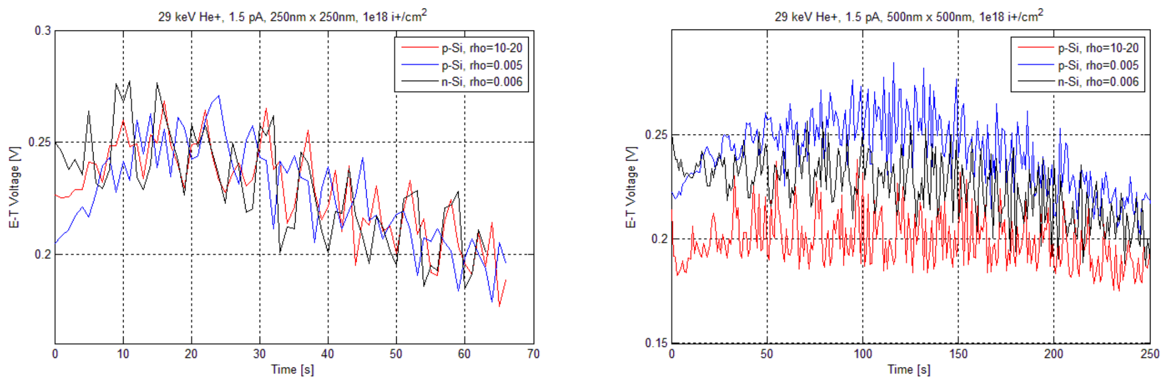

Figure 3.10. At w=250 nm (in a), and at w=500 nm (in b), the signals collected from the E-T detector for 29 keV He^+ in three (3) different c-Si substrates.

A crystalline silicon substrate was also irradiated with neon to pattern different box sizes, with widths of 100 nm up to 500 nm. The results for boxes with widths of 100, 250, 350 and 500 nm in silicon show a peculiar pattern as function of dose (figure 3.11). Each one of these has been plotted separately with a fit using the one-component 2-D Lambertian solution (figure 3.12). Each one of these responses required a different value for etch velocity (in nm/s) in order to fit the data. Values of v are shown on each subplot. When the etch depth is plotted against time and

dose, the effect is quite evident. Based on the experimental data and the electronic signatures recorded, the SE generation is extinguished more rapidly for the narrower patterns. This can be the direct result of the higher pressure present within the very confined well where the secondary electrons have a smaller mean free path and cannot readily escape the hole. Hence, the signal falls off rapidly. The etch rate can be affected significantly by this, leading ultimately to higher redeposition and lower net sputter rates. In figure 3.14, when the aspect ratio is plotted, the line distribution markedly tightens. This clearly shows that the electronic signature for different size etch patterns is the same and only dependent on the aspect ratio (h/w). The results have been reasonably fit with the simulation and yielded a set of characteristic curves for silicon etching (figure 3.15). First, it has been concluded that for smaller widths, the secondary electron current at the detector drops with a steeper slope; while, on the other end, at w=500 nm, the etch rate (effective velocity v for a box) is slower and has a smaller slope. All patterns were carried out at 1 μs dwell times and 10 μs refresh times. Evidently, for the larger boxes a larger number of passes has to be performed to reach the same depth. This response can be ascribed to a shadowing by the narrow holes where the now more confined secondary electrons cannot readily escape. This results in a greater slope as the count at the E-T detector falls more rapidly for the narrow etches with larger aspect ratios. Eventually, this re-collection of the generated secondaries is minimized by wider etched areas, unless the doses reach high enough when the aspect ratio becomes a germane factor.

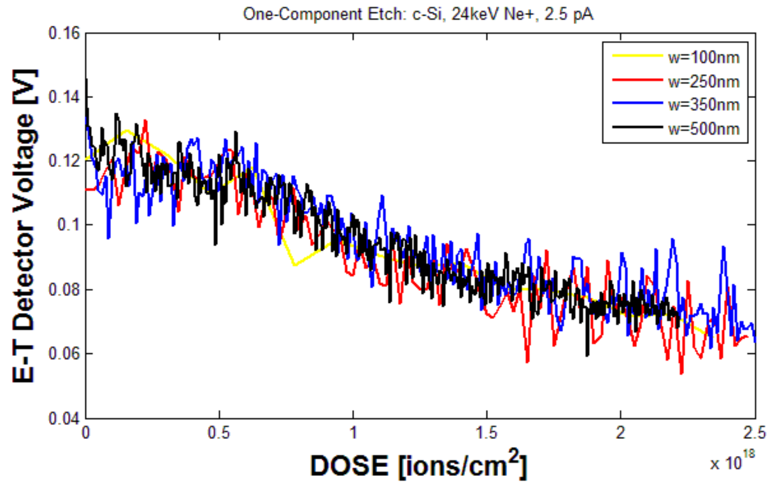

Figure 3.11. Actual measured data from the stage current for four (4) c-Si box widths profiled at the same voltage (24 keV Ne^+), current (2.5 pA) and final dose ($2.5x10^{18}$ ions/cm^2).

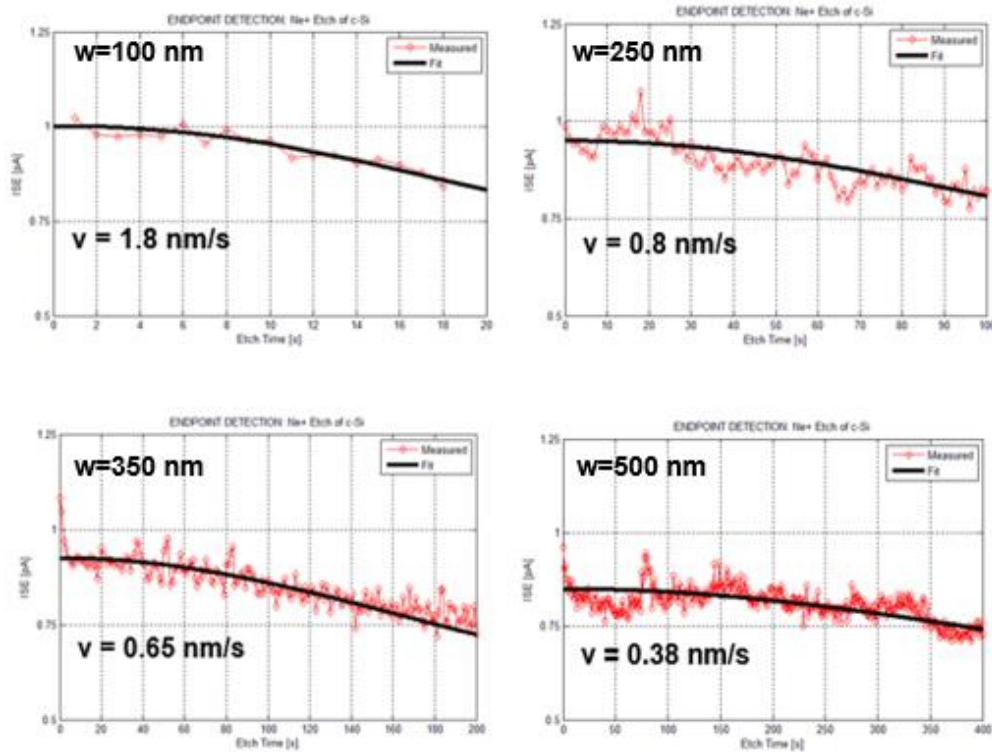

Figure 3.12. Actual measured data and fits for four (4) silicon box widths profiled at the same voltage (24 keV Ne^+), current (1.0 pA) and final dose ($1x10^{18}$ ions/cm^2).

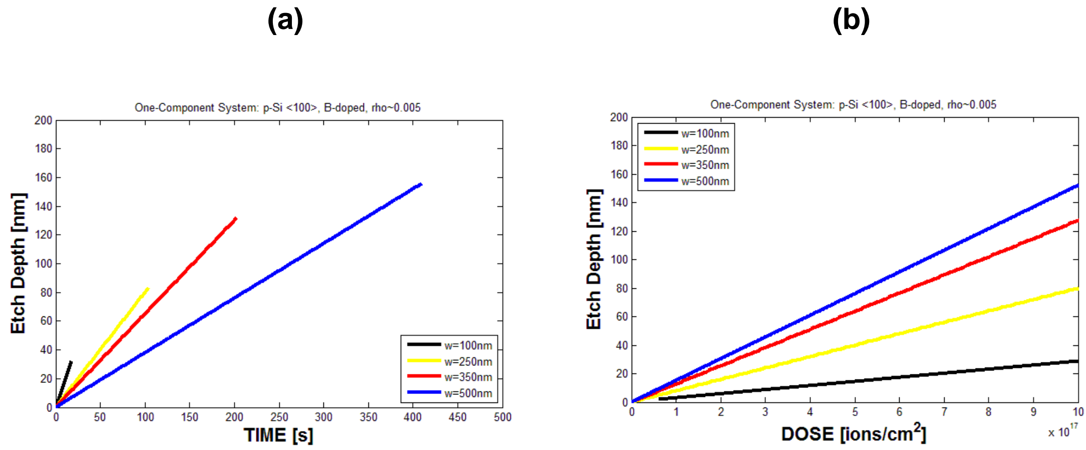

Figure 3.13. Etch depth dependencies on time (a) and dose (b) for a silicon substrate.

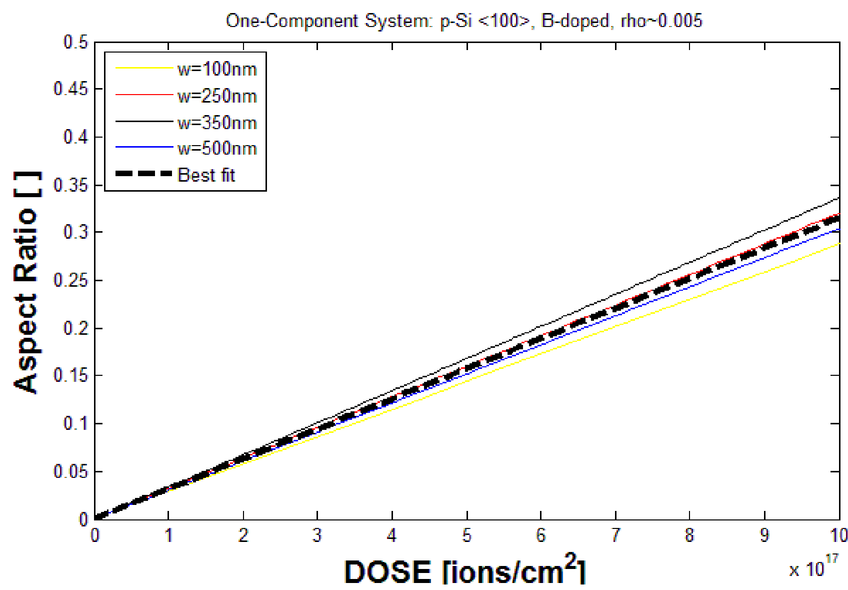

Figure 3.14. Aspect ratios plotted against the neon ion doses for silicon.

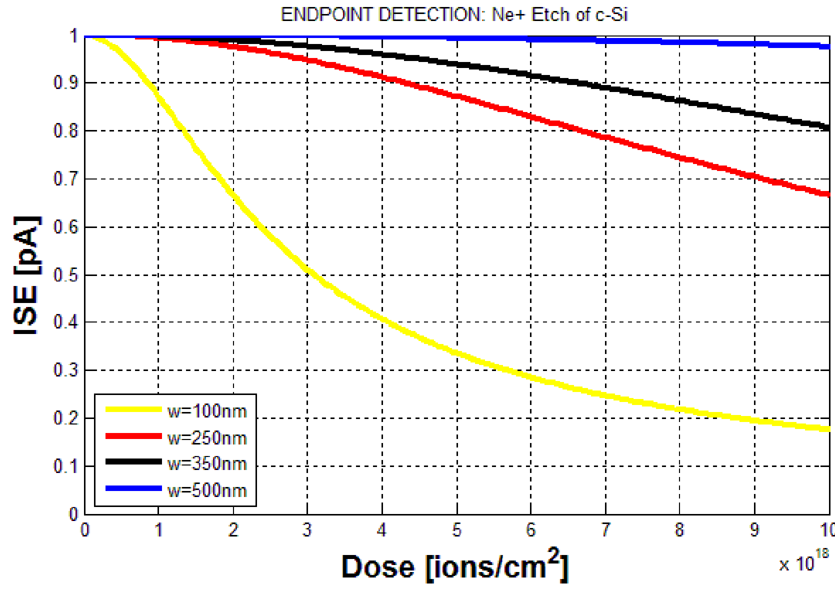

Figure 3.15. Fits from figure 3.12, all plotted together for widths from 100 to 500 nm.

Below, plots (figure 3.16 & 3.17) are shown for neon irradiation of c-Si at three (3) different beam currents with fixed energy (24 keV) and at three (3) different energies with fixed beam current (2.8 pA). All correspond to the same box size, 250nm x 250nm. A reasonable value for the yield of silicon by neon can be obtained from the stage currents and assuming the BSI is negligible. According to SRIM/TRIM simulations, the backscattering in this case should be as low as 0.8%. The SE yield is computed to be ~0.8 SE/Ne^+, from the initial values of I_s and using I_P. The expected rise in SE current was confirmed for higher currents into the silicon substrate. When the accelerating voltage is changed while maintaining the beam current constant, the data shows a tendency to higher SE yield at the E-T detector for lower voltages or energies. At lower voltages, while the electronic interactions drop by about 25%, the depth of penetration by the neon ions is less and closer to the top surface of impingement. Since the SEs reaching the E-T detector depend primarily on two factors; the amount generated by the material (near the surface at high ion energies and internally at lower ion energies) at certain energy and current, and the escape

depth; it can immediately be rationalized that the balance between generation and escape favors the escape under this range of energies. This finding is consistent with observations made before by De Teresa [9], where for lower e-beam energy the amount of SEs generated rose. He also claimed that for Ga-FIB, a larger amount of SEs reached the surface for increasing gallium ion beam energy. Clearly, gallium (70 a.m.u.) is 3.5x heavier than neon (20 a.m.u.). Furthermore, the slopes for these signals were closely fitted with a straight line and these show a slight appreciable increase with decreasing energies. This should be proof that etching enhancement has taken place also as a result one prior observation; the rise in nuclear energy stopping power. Refer to figure 3.18.

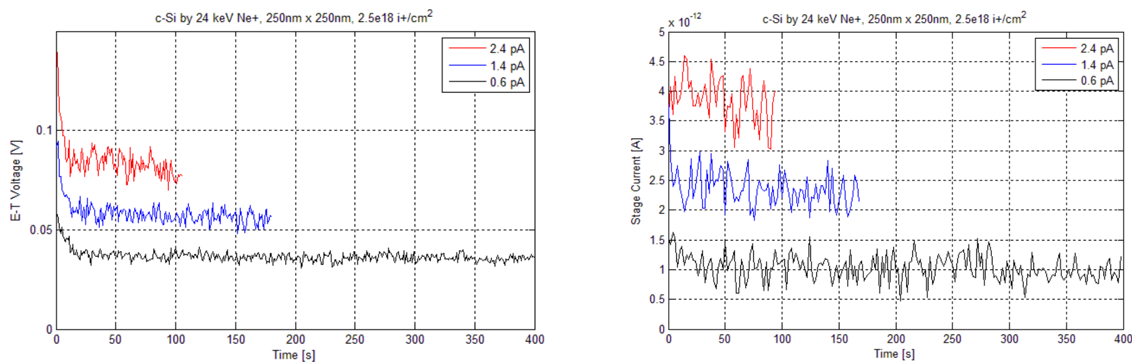

Figure 3.16. Data collected from the stage for 24 keV Ne^{+} in c-Si at three (3) different beam currents.

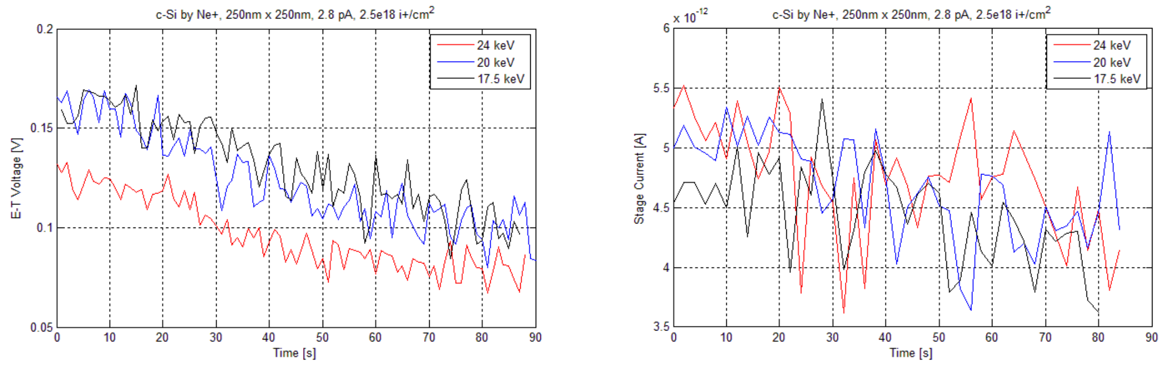

Figure 3.17. Data collected from the stage for neon in c-Si at three (3) different beam energies.

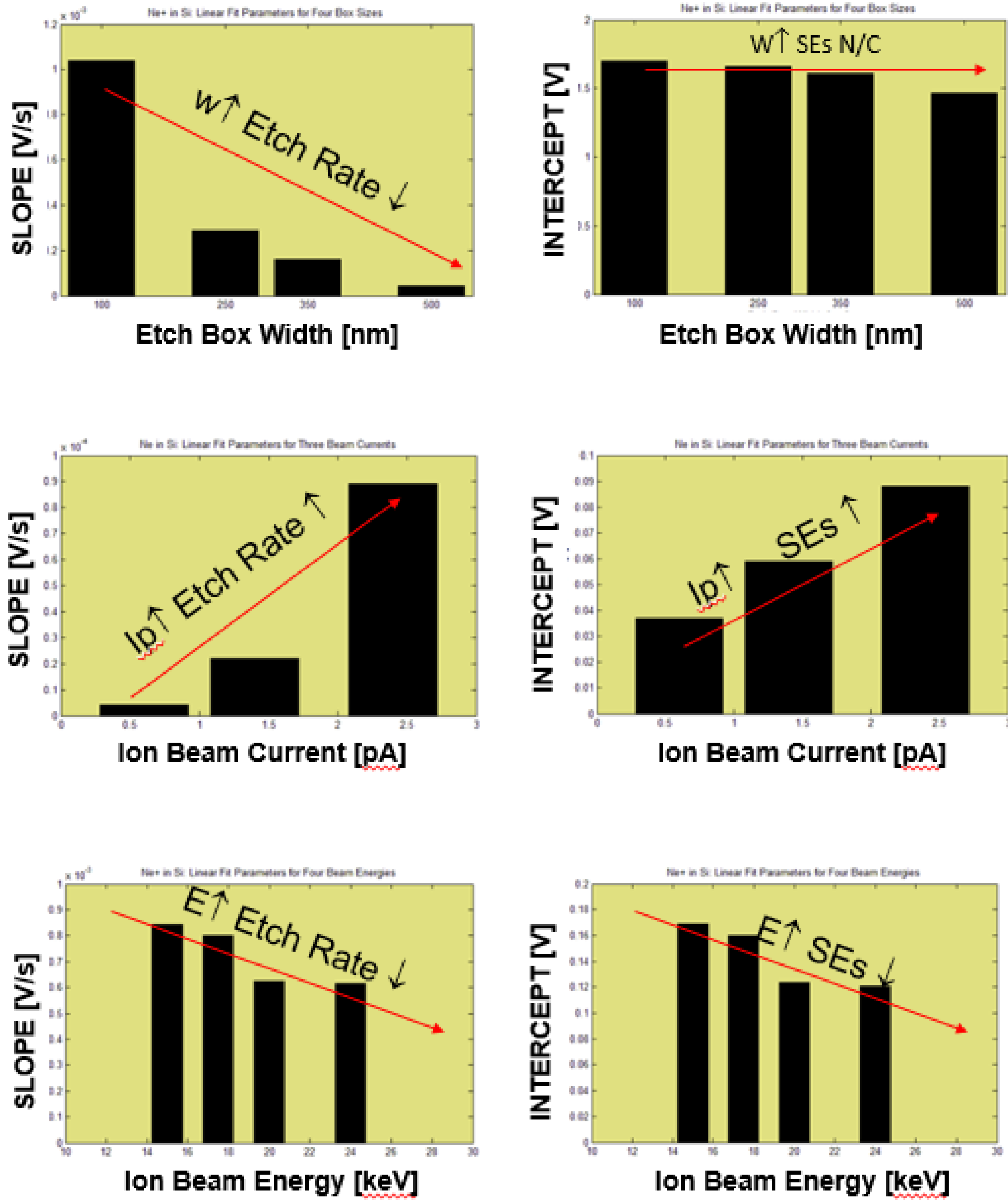

Figure 3.18. Summary of results for neon in silicon for different box sizes, beam currents and beam energies.

SiO_2/c-Si Endpoint Detection.

An oxidized c-Si substrate was also used to evaluate etching and endpoint detection. Oxidation for electrical insulation and passivation is a common practice in the micro- (nano-) electronics industry. At low doses, etching of SiO_2 is possible with helium ion beams. However, the presence of the c-Si substrate below presents the same challenges that have been discussed before. Even though the oxide layer acts as a mask, the critical concentration for nanobubble formation is reached at relatively low doses, since penetration of the ions occurs during irradiation. As shown in figure 3.19, when the primary beam current is varied from 2.0 to 4.0 pA using a helium ion beam, the output voltage at the E-T detector changes accordingly. Computing the SE yields for He in SiO_2, using the initial stage currents, shows that these are relatively close to one another, at ~2.0 SE/He^+. Nevertheless, the profiles show that as the etching progresses inward and downward, there is a point in time, or more importantly, a critical dose, where the slope changes from negative to positive. This is a clear electronic signature for the onset of swelling. The largest current induces swelling in the shortest exposure time, while the lowest current requires longer exposure times to reach this point. In all three cases, the threshold is the same dose at ~$4x10^{17}$ He^+/cm^2. As discussed before in chapter 2, swelling is the manifestation of nanobubbling in the crystalline silicon substrate. At $1x10^{18}$ He^+/cm^2 (the final dose), the magnitude of the swelling is greatest for the largest current since the electronic signal at the E-T registers the highest current, a direct result of greater expansion, or height, of the top surface from which now more unimpeded SEs can reach the detector. In this case, swelling has not been observed from the onset. It is evident that the oxide on top is acting as a mask and delaying the onset of swelling by accommodating some of the helium implants along the Gaussian projected range. This is in contrast to bare silicon where from the onset, the material is already expanding under the irradiated area.

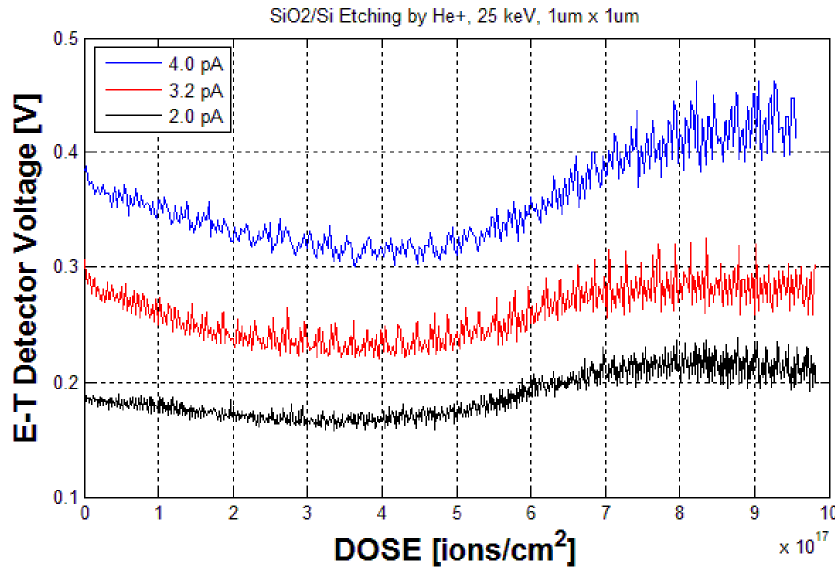

Figure 3.19. Data collected from the E-T detector for 29 keV He^+ in SiO_2/Si at three (3) different beam currents.

When, on the other hand, the beam energy is reduced from 25 to 20 keV He^+ (figure 3.20), the slope of the I_{SE} drop increases for the lower 20 keV energy helium ions. In addition to this, swelling is observed once again, yet for both energies the onset or turning point is at near the same dose, again ~$4x10^{17}$. However, as the dose continues to rise, the degree of swelling observed is higher for the lower ion beam energy, 20 keV. This can be explained relatively easily by the fact that for a monolithic structure such as c-Si, at lower energies, there will be less penetration by the helium ions which come to rest closer to the top impingement surface. This accumulation within a smaller volume and closer to the top surface allows for oversaturation and the superlinear regime of implantation to occur more dramatically, inducing a larger swelling height. This swelling behavior is inherently different from a multilayer system, as presented before in chapter 2, in that here at the lower energy more expansion is detected. The steeper slope corresponds to greater nuclear stopping at 20 keV relative to 25 keV, which then leads to a slightly faster etch rate of the top oxide layer on the c-Si. It must be noted that the SE current at the E-T

detector has dropped for the lower ion energy of 20 keV. In this instance, since the nuclear stopping power is augmented at lower energies, the electronic interactions and energy losses with the target material will decrease accordingly. One would expect that because of the lower penetration depths involved at lower energies, the SEs detected would rise. Nonetheless, the projected ranges at 25 and at 20 keV, remain much larger for helium than the escape depth. Hence, since at 20 keV the helium ions still penetrate deep into the sample, even though more SEs may be generated, a scarce amount of these reach vacuum at the top surface near the detector. Subsequently, at lower ion beam energies, the SE current levels drop. Figures 3.21a and 3.21b show the same results as in figures 3.19 and 3.20, but this time using the stage current rather than the E-T detector voltage.

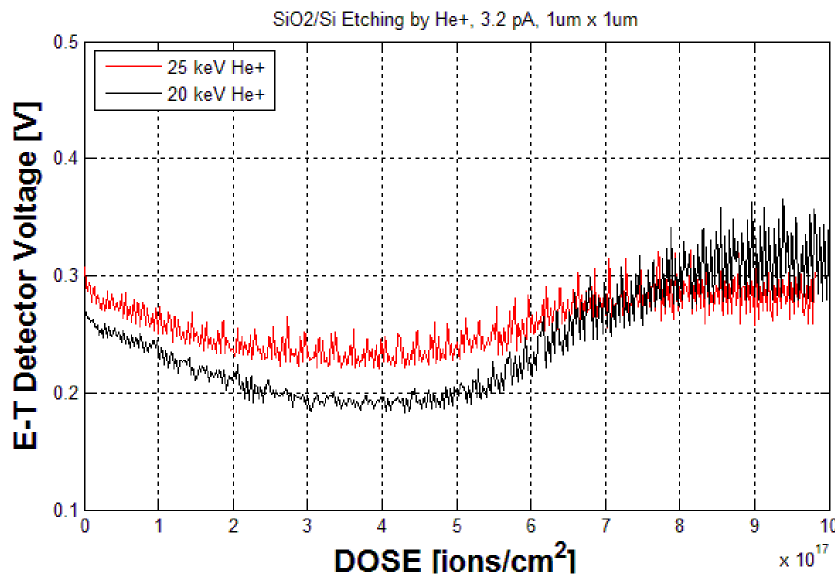

Figure 3.20. Data collected from the E-T detector for helium in SiO_2/Si at two (2) different beam energies (25 & 20 keV).

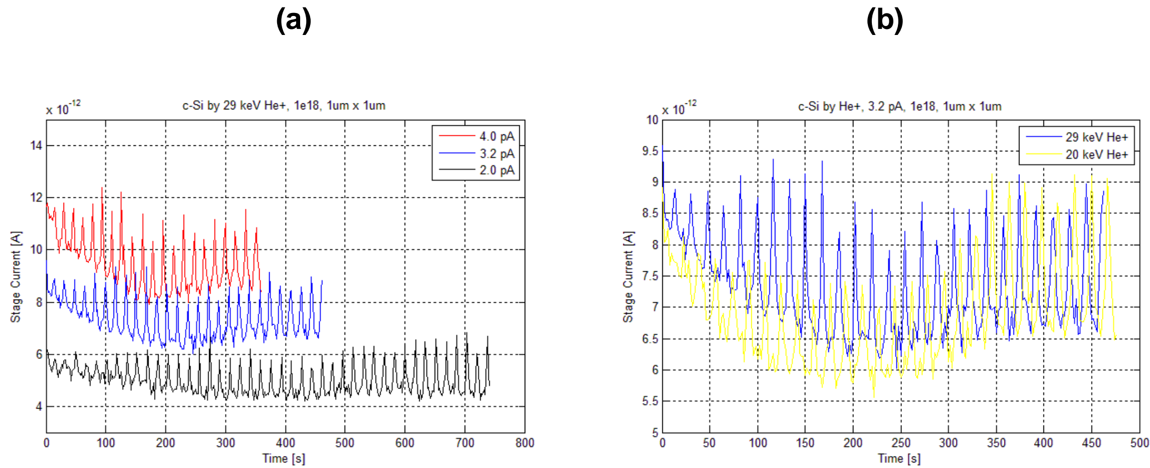

Figure 3.21. Data collected from the stage current for helium in SiO_2/Si at three (3) beam currents (in a) and two (2) different beam energies (in b).

Au & Cu Endpoint Detection.

Gold is a metal of significant technological important in electronics. Patterning it with helium or neon ion beams provides a reliable tool for machining nanoscale features. It has been demonstrated that both, helium and neon etch gold. Helium does it at a much slower rate, but given that in most cases the underlying structure will contain the c-Si substrate it will exhibit serious disadvantages because of swelling. Figure 3.22a below shows the results of a dose study for 29 keV He^+ in a 100 nm thick Au top layer. It has been determined that ~$2.5x10^{17}$ He^+/cm^2 is sufficient to etch the 100 nm of Au. For higher dose, as seen in 3.22b, the archetypical blistering emerges once again. In figure 3.23, another dose study but this time using 24 keV Ne^+ in Au. No blistering occurs under neon irradiation which in all cases produces a uniform and smooth square box of the desired depth on the c-Si substrate.

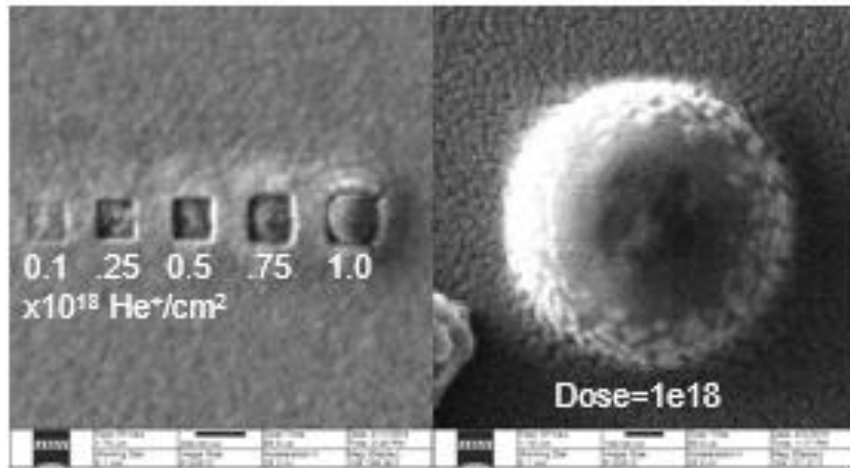

Figure 3.22. HIM image showing a dose study of Au etching by He^+ with a closer look (on the right) at archetypal high dose blistering.

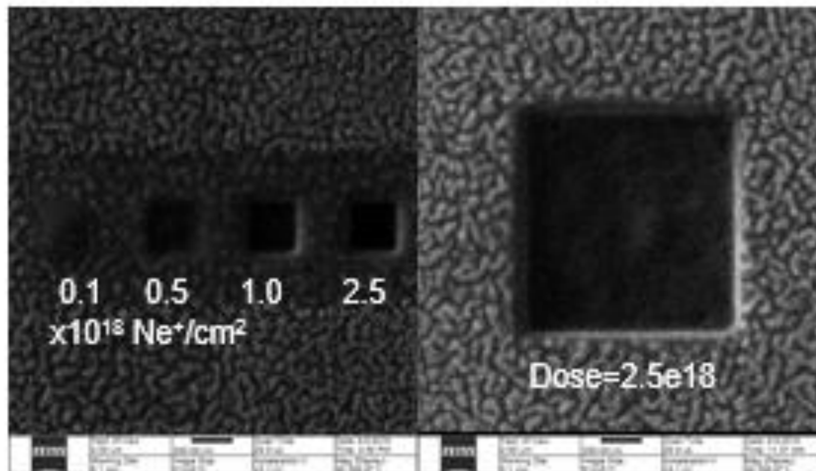

Figure 3.23. NIM image showing a dose study of Au etching by Ne^+ with a closer look (on the right) at the high dose etch.

Figure 3.24 shows that for decreasing gold box sizes under neon irradiation the slope increases. This, as seen before with bare silicon, can be attributed to re-collecting generated SEs that do not escape the hole. As seen for the 1μm x 1μm box, once the gold has been removed, the SE count reaches a steady slope corresponding to a single component, the silicon substrate. Figure 3.25 shows the estimated I_{SE} detector currents (converted from voltage to current using a gain factor when compared with I_s) arising from the Au/Si etch by Ne^+. From this sweep, the top surface or initial currents for each component (Au, Si), with two different secondary electron yields (I_{SE}^0), can be obtained with a straight line extrapolation (y-axis intercept). The two very discernible slopes ($\Delta I_{SE}/\Delta t$) indicate how much higher the gold etch rate (steeper) is compared with silicon under neon irradiation. In figure 3.26, the raw experimental data for Au/Si etch is shown, along with a 3-pt moving average implemented to smooth the response. Finally, in figure 3.27, a very reasonable fit using a two-component 2-D Lambertian model matches closely the experimental data collected from the E-T detector.

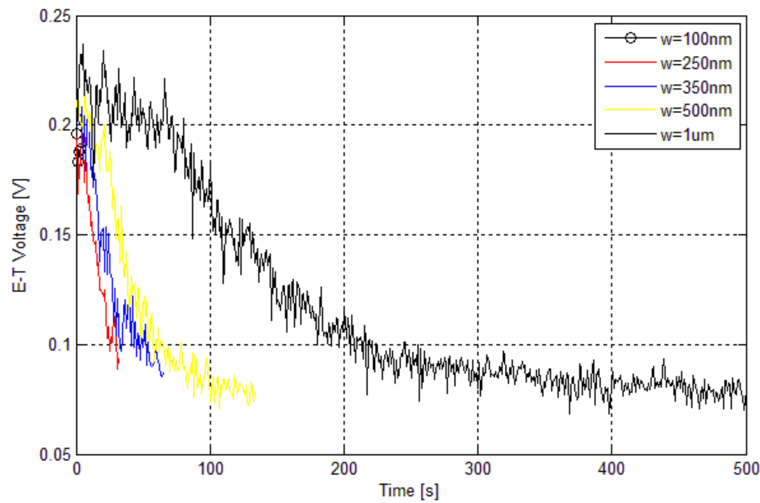

Figure 3.24. A dependence on box size, or width, found during Ne^+ etching of Au. Five (5) square box sizes, represented by their widths, are shown, where the smaller the width, the greater the slope, or reduction rate in SEs reaching the E-T detector.

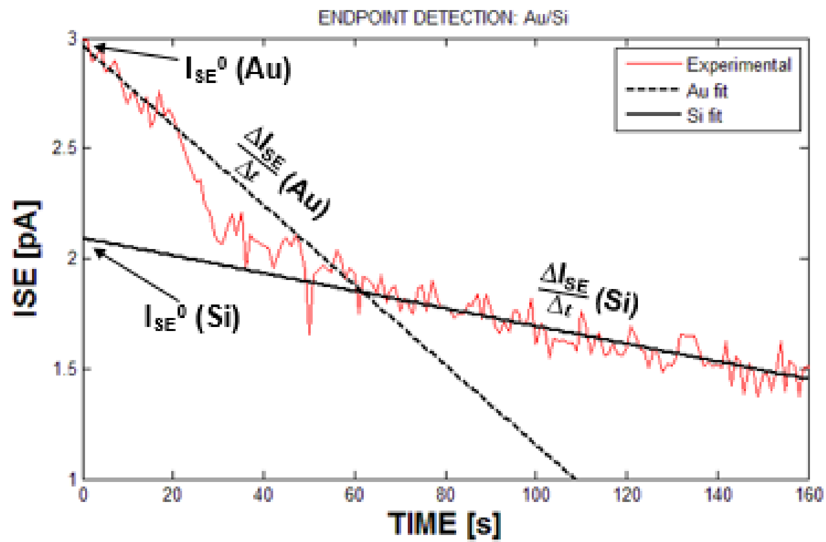

Figure 3.25. Extended line fits showing the voltage levels that the E-T detector would register at different times, and corresponding doses and depths, for each component: Au and Si.

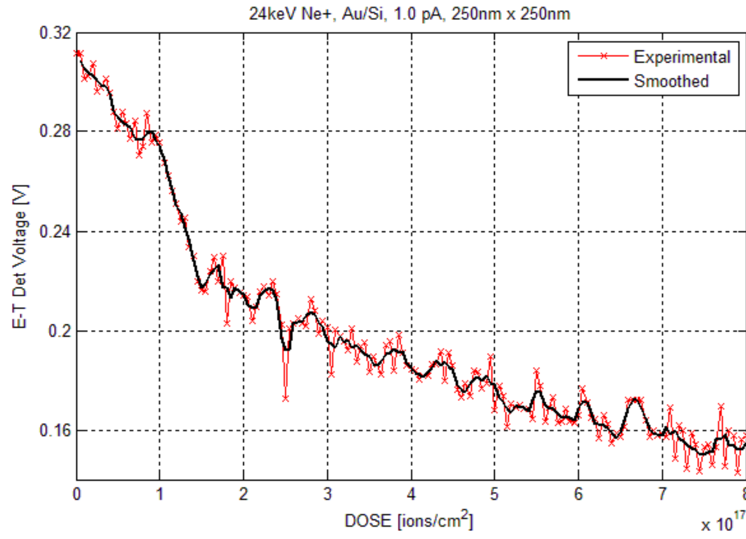

Figure 3.26. Experimental and smoothed data using a moving average filtering method.

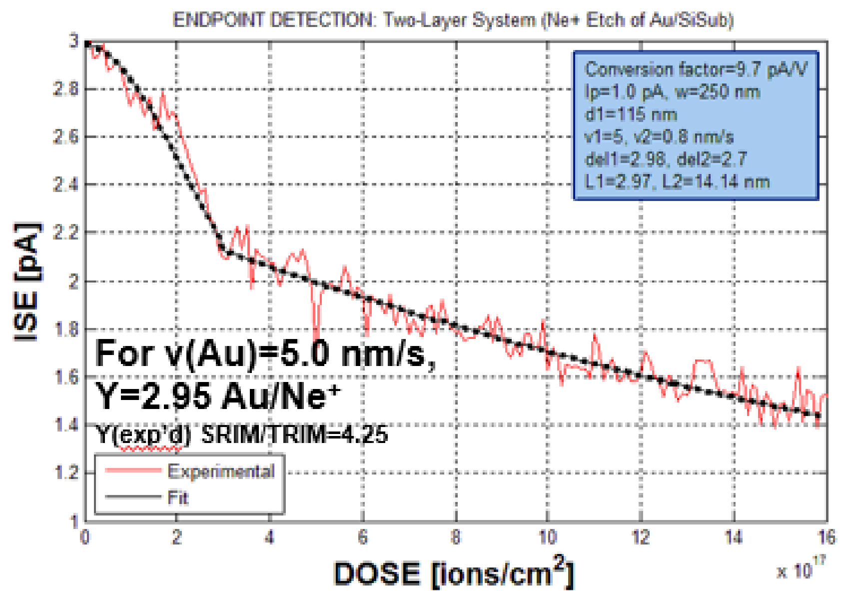

Figure 3.27. Experimental and fit ISE vs. Dose data for Ne^{+} on Au/Si.

When gold is instead deposited on SiO_2/Si rather than directly on Si, the helium ion etching endpoint response is as shown in figure 3.28 below. When the etching starts on the gold top layer, no swelling is detected up to at least 5×10^{18} He^+/cm^2. This shows how the top 100 nm of gold and 100 nm of silicon dioxide are masking and preventing silicon from reaching a critical dose for swelling. On the other hand, when gold is not present, immediately the current rises with positive slope, indicating that the silicon is already undergoing nanobubbling effects at the low helium irradiation doses. Once again, as reported earlier, the swelling does not increase indefinitely and at some point the surface breaks down allowing the implanted helium to escape. This will then allow for the etching to proceed, but with side effects such as mechanical damage to the adjacent perimeter. The pattern will be jagged and not square any longer.

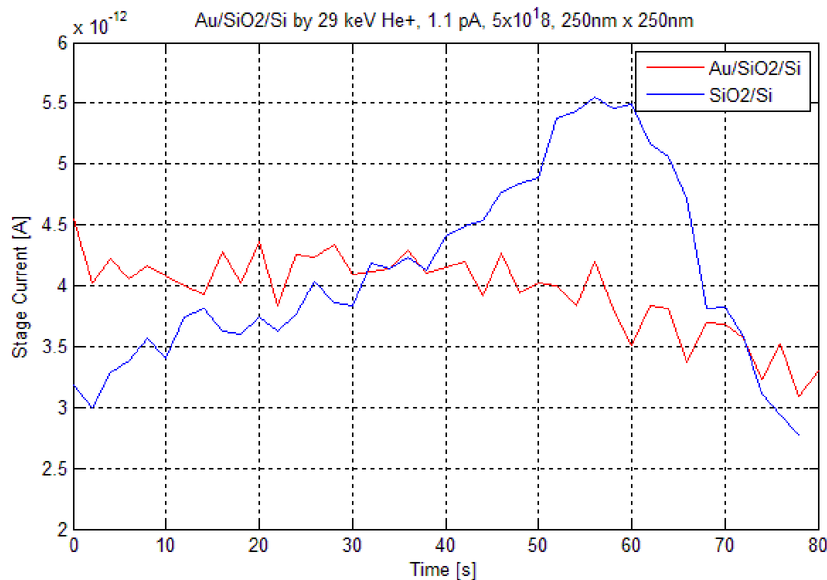

Figure 3.28. Signals for Au/SiO_2/c-Si undergoing helium etching. When Au (100 nm) is present, it acts as a mask, and swelling is not observed up to 5×10^{18} He^+/cm^2 (red trace). On the other hand, when the implantation begins on SiO_2/Si (no Au cap), swelling begins at low doses (blue trace).

A comparison was carried out between helium and neon etching of the Au/SiO_2/Si structure and plotted together in the same scale. Figure 3.29 shows how slow the etching of Au by He^+ proceeds compared with Ne^+. The Au is etched quickly, then there is a slower removal rate for the SiO_2 layer where the signal proceeds with a small slope across the oxide thickness. Since SiO_2 is an insulating material, the transition from SiO_2 into Si will not be as sharp as the one from Au into SiO_2. This is due to the effect of the longer escape depth. For Au, the escape depth for SEs originating in the SiO_2 is too small (~2.95 nm) and these basically are reabsorbed and do not reach the detector above. On the contrary, when the etch front approaches the SiO_2/Si interface, SEs originating in Si can overcome the remaining SiO_2 thickness and escape the sample. Therefore, the slope is more gradual for the transition from SiO_2 into another material. Once again, linear extrapolation, as shown in figure 3.30, is useful in providing the initial, top surface SE currents for each component individually, and also each slope shows the sputter rate of that particular material. It is evident that SiO_2 has higher SE yield and faster sputter rate than c-Si. In this case, $\delta_{Au} > \delta_{SiO2} > \delta_{Si}$ (t=0), and since $\Delta I_{SE}/\Delta t \propto$ Sputter Rate (z/t) and Sputter Yield (Y), $Y_{Au} > Y_{SiO2} > Y_{Si}$. In figure 3.31, etching of Au by He^+ is shown. The fit with the experimental data is very close, except for the initial response region where surface contamination reduced the electronic yield. Here, a good agreement for the sputter yield was obtained at 0.25 Au/He^+. Figure 3.32 shows a quite reasonable fit for the Au/SiO_2/Si structure using this time a three-component model with three effective box etch velocities (v_1, v_2, v_3) and three SE yields (δ_1, δ_2, δ_3). Notably, the escape depth for insulating SiO_2 needed for this fit is 45 nm and significantly greater than metallic Au (2.97) and for semiconducting Si (14.7 nm). Here, the resulting Y is 4.13 Au/Ne^+. The sputter yield ratio Ne/He in Au is ~17x.

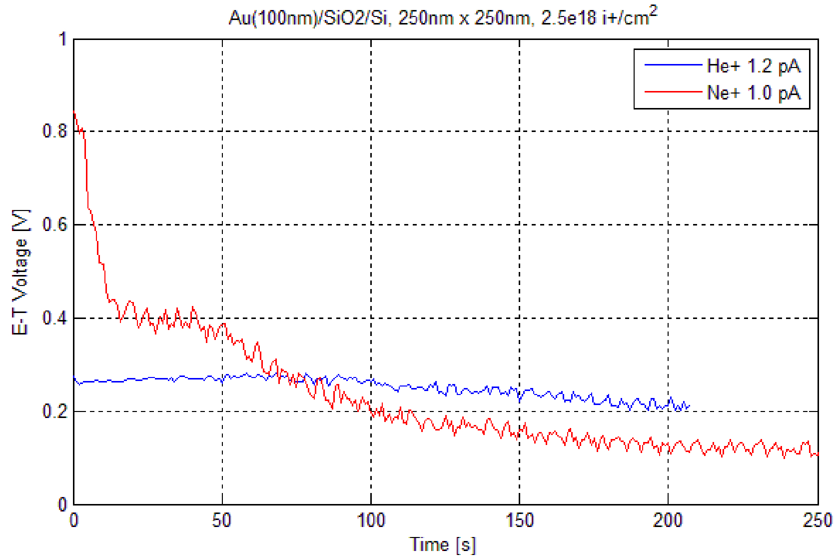

Figure 3.29. Comparison between helium and neon etching of Au/SiO_2/c-Si.

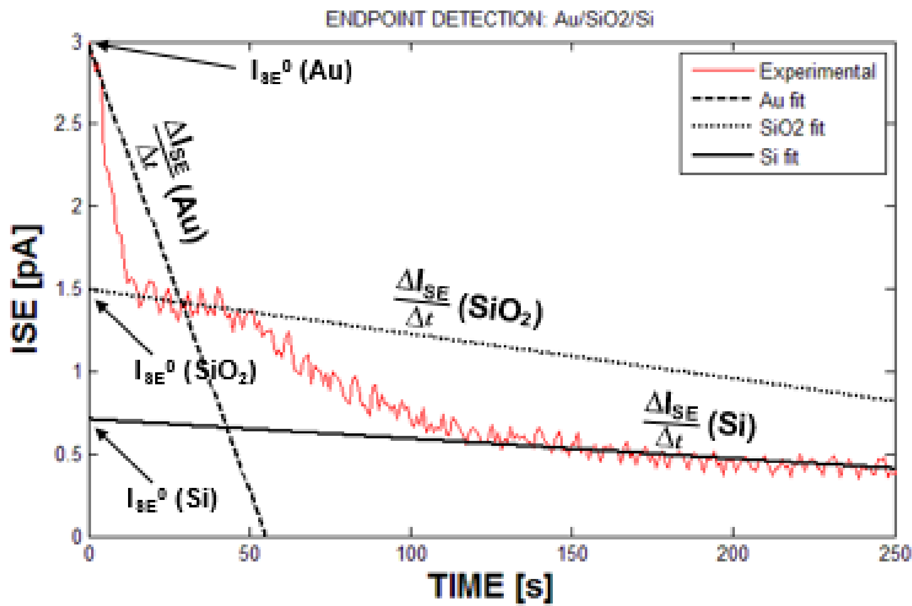

Figure 3.30. Extended line fits showing the voltage levels that the E-T detector would register at different times, and corresponding doses and depths, for each component: Au, SiO_2 and Si.

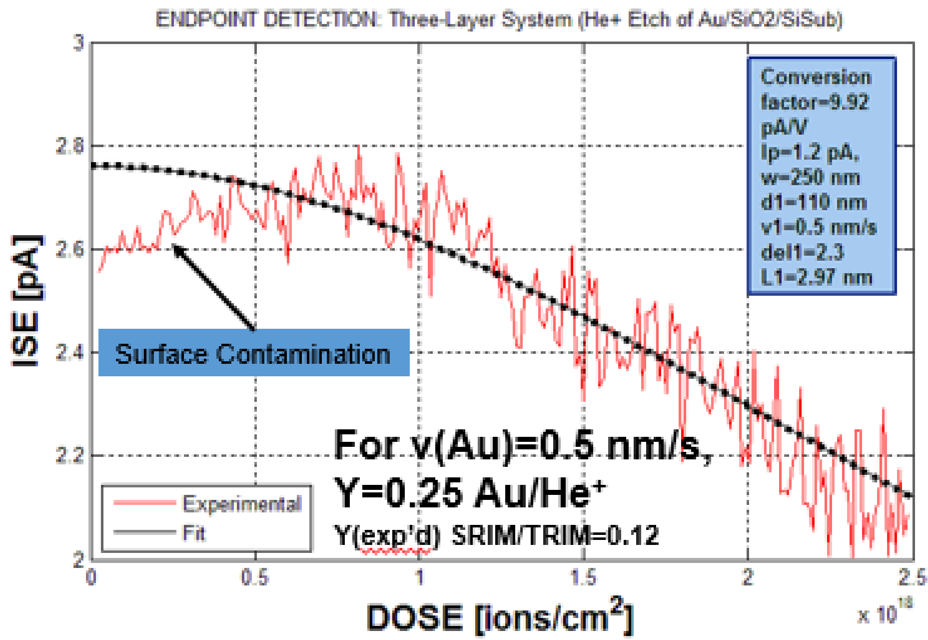

Figure 3.31. Experimental and fit ISE vs. Dose data for He^+ on $Au/SiO_2/Si$.

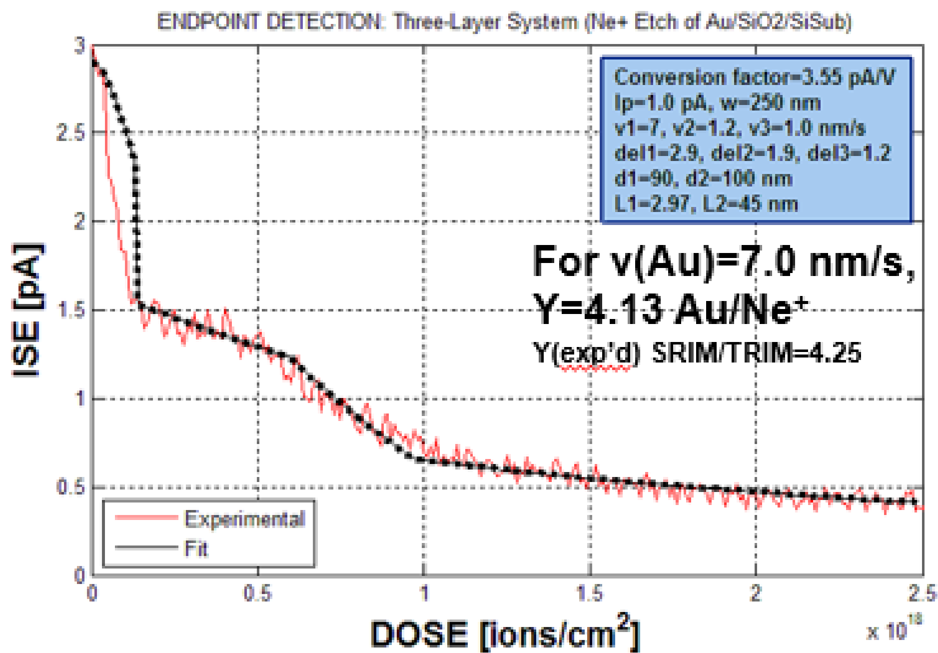

Figure 3.32. Experimental and fit ISE vs. Dose data for the neon etch of Au/SiO_2/c-Si.

Copper is another inviting material for many applications in integrated circuits and further miniaturization of devices. Its use has been on the rise mainly due to its high conductivity and because of its abundance and relatively low cost, especially when compared with gold. Patterns shown below in figures 3.33 and 3.34 demonstrate the feasibility of copper etch by both, helium and neon ion beams. Obviously, sputter etching is much faster with neon atoms. It must be reinforced once again that the substrate and structure beneath the copper is quite relevant to the final outcome and quality of any etch. In this case, since the copper is deposited on SiO_2 and c-Si, the saturation effects of helium in silicon will ultimately undermine the etch profile and fidelity. The applied dose needs to be monitored closely and it clearly has to be low, otherwise swelling artifacts can confuse the data and affect the underlying silicon. It has been discussed prior to this section that capped or masked silicon will begin showing signs of swelling at ~$4x10^{17}$ helium/cm^2. The copper etch by helium must be maintained below this level unless the underlying structure does not contain crystalline silicon. No swelling effects were observed under neon irradiation.

Figure 3.33. HIM image for a dose study of helium copper etching ($Cu/SiO_2/Si$). Swelling not observed since the copper top layer thickness is ~45 nm.

Figure 3.34. NIM image for a dose study of neon in a copper structure ($Cu/SiO_2/Si$).

Helium etching of two different thicknesses of copper (9 nm and 45 nm) on SiO_2/Si is shown in figure 3.35. Here, since the thinner copper top layer is 9 nm, the effect of swelling appears, not surprisingly, at ~$4x10^{17}$ He^+/cm^2. Interestingly, for the 45 nm thick copper, swelling does not appear by the end of the run at the final dose of $1x10^{18}$ He^+/cm^2. At low doses, it is evident when the top layer has been removed. Since the 45 nm Cu is thick enough and He^+ etches slowly, the signal remains nearly flat (with small negative slope) for longer times up to higher doses (to ~$2x10^{17}$ He^+/cm^2). In the thinner layer, swelling is occurring already by the expected threshold ~$4x10^{17}$ He^+/cm^2, whereas for the thicker sample it is clear that the copper etch is not complete and the residual concentration in the silicon is below the swelling threshold.

As seen in figure 3.36, the neon dose required to etch the 45 nm of Cu, is ~$1.25x10^{17}$ Ne^+/cm^2. By $5x10^{17}$ Ne^+/cm^2 and at 0.5 pA, the etch front has reached the underlying c-Si substrate. Again here, a slow decay in the SE yield is observed for the transition across the oxide layer into the silicon. SiO_2 generates almost 2x more secondaries than Si. In figure 3.37, both the helium and neon etching process of the 45 nm thick Cu top layer are shown together. Lastly, figure 3.38 shows another close fit between the experimental data and a 2-D Lambertian model for a three-component multilayer system. The escape depth for copper is ~4.74 nm, which is larger than for gold.

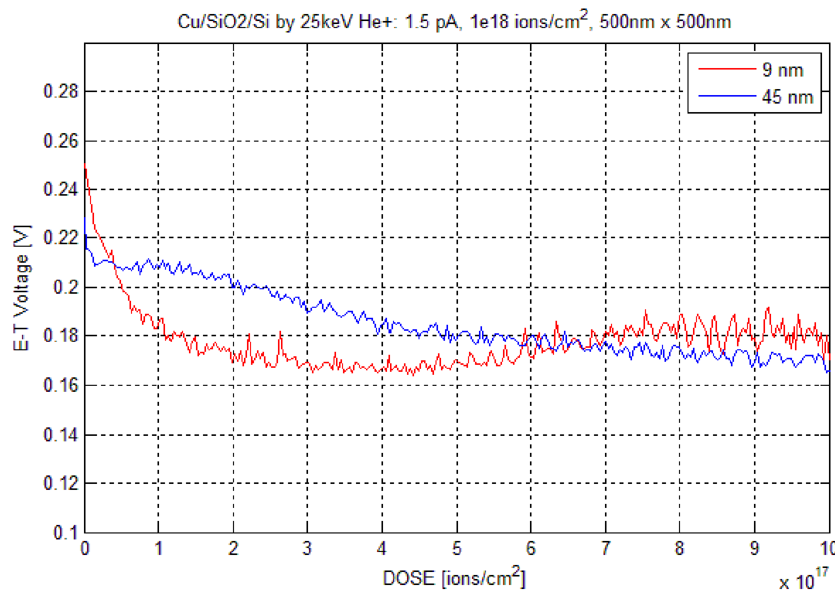

Figure 3.35. Responses collected for two (2) different copper top layer thicknesses when etched by helium.

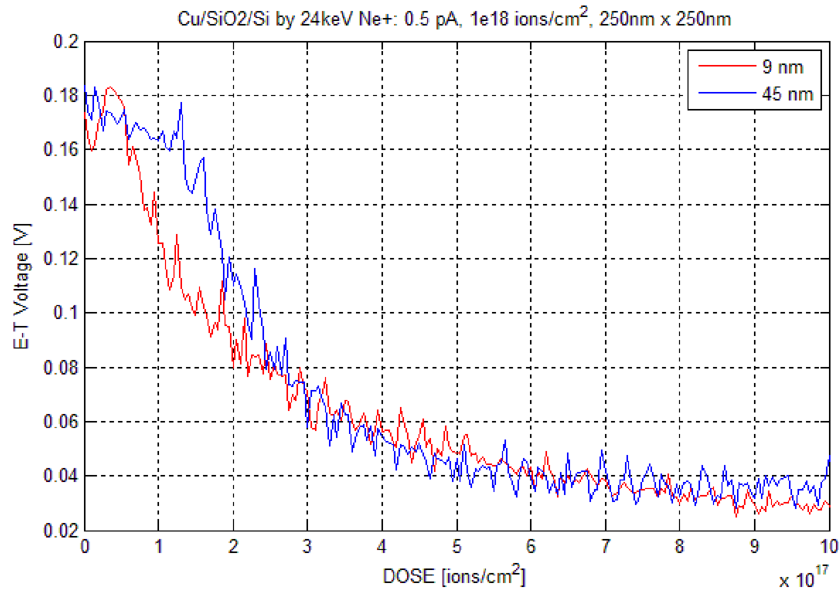

Figure 3.36. Responses collected for two (2) different copper top layer thicknesses when etched by neon.

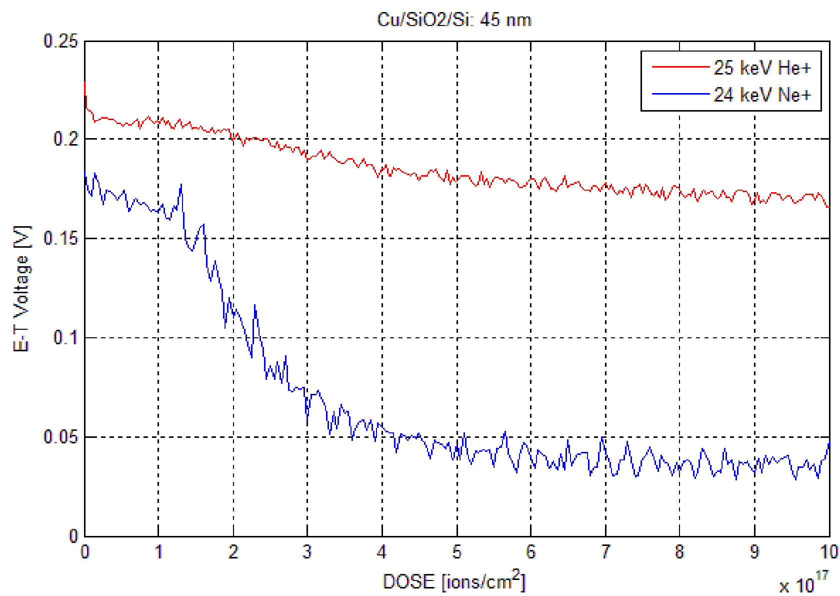

Figure 3.37. Comparison between helium and neon etching of Cu/SiO_2/c-Si.

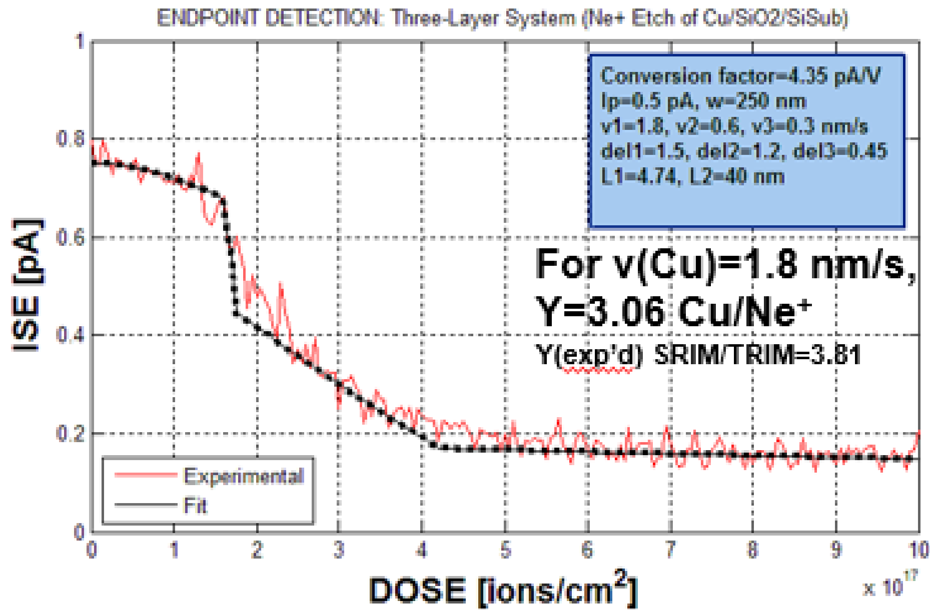

Figure 3.38. Experimental and fit ISE vs. Dose data for the neon etch of Cu/SiO_2/c-Si.

By using the doses at which the top layers of Au and of Cu are completely milled, the sputter yield can be calculated. In the case of gold, the dose is ~$1x10^{17}$ Ne^+/cm^2 for a layer 100 nm thick. This results in a Y=4.13 Au/Ne^+, which in this case is close to what SRIM/TRIM predicts, 4.25. For copper, since for the 45 nm film, since it was etched by both helium and neon, two yield estimates are possible. For helium, the dose is ~$4.5x10^{17}$ corresponding to a Y=0.103 Cu/He^+. SRIM/TRIM predicts 0.130. For neon, a Y=3.06 Cu/Ne+ is obtained, when SRIM/TRIM predicted 3.81. In the case of copper, it is clear that copper etches faster than nickel. The binding energy for copper is 3.52 eV (lower than Ni, at 4.46). Hence, sputtering of Cu by He^+ (unlike in Ni) may be a direct result of its lower binding energy. Copper is a softer, more ductile material than nickel, even though they have almost identical electronic configurations and mass densities. Their mechanical properties, particularly hardness (Vickers test), are quite different, with nickel (638 MPa) exceeding copper (369 MPa) by almost 2x.

High-Contrast (C/Au/C) Endpoint Detection.

Au and C were selected for this experiment since the primary electron beam SE yields are the highest for gold and the lowest for carbon. This significant difference based on SE yields from electron beams should be reproducible using ion beams. The difficulty that arose in this case is that the carbon films were deposited via evaporation and these did not produce thick enough films (slow deposition process). The carbon rod tends to heat and spark during the process and had to be allowed to cool down quite frequently. Etching by neon in figure 3.39 shows a response that unlike those presented before, starts low, increases to a peak and then decreases. This is expected for a C/Au/C where the initial rise corresponds to thin carbon rapidly etched away followed by an increasing SE yield from Au reaching the detector. At the peak, the etch front will be at the top of the internal gold layer, but since it not very thick gold etches quite rapidly, the response does not remain high, or nearly flat, for an extended period of time. Immediately a decline is recorded due to the rising weighted contributions by the underlying carbon and then c-Si substrate below. Since these films were very thin (<<50 nm), the endpoint detection becomes a significantly more challenging task. However, the collected signals demonstrate that for thicker films, when high contrast is present, a high count plateau can be obtained between two regions of low yield, such as carbon and even silicon ((C(or Si)/Metal/C(or Si)). In order to explore the possibility that with stage biases present the endpoint detection in a high-contrast structure may be improved, +50V were applied to the sample stage. This positive bias is expected to prevent SEs with energies up to 50 eV from escaping the sample and reaching the detector. The assumption here is that either Auger electrons or BS atoms could provide a signal with sharper transitions. Figure 3.40 shows that with a +50V bias, the difference between high and low counts is roughly ~78%, while with no bias, it is 20%. Therefore, it is affirmed that the contrast has in fact been enhanced.

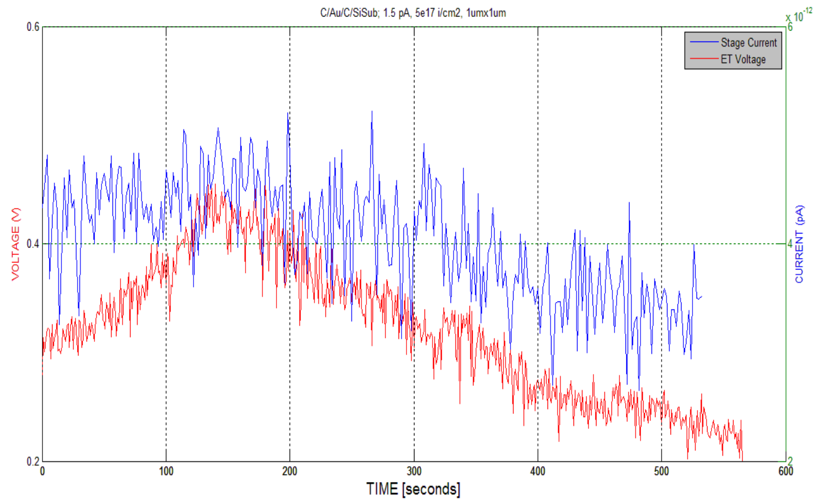

Figure 3.39. E-T detector voltage and stage current for neon etching of a C/Au/C high-contrast structure.

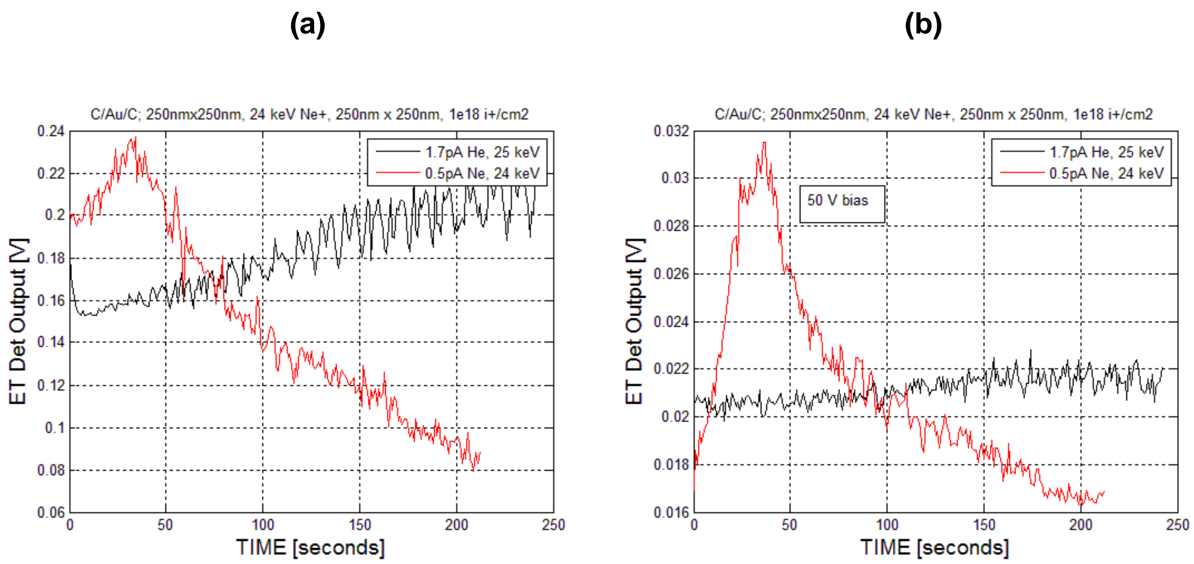

Figure 3.40. Comparison between helium and neon etching of C/Au/C and at two (2) stage biases: 0 V in a) and +50V in b).

Conclusions

Endpoint detection using helium and neon has shown both its advantages and its weaknesses. For helium, onsets of swelling due to nanobubbling have been electronically recorded. Au has been confirmed to have high SE yield while C, Si and SiO_2 lower, and therefore more difficult to discriminate or tell apart amongst themselves. The SE yields for Cu and for Ni are high enough to discern layers from one another and where the top layer ends internally within a structure. Interfaces and the end of an etched layer can be detected, but the transition is not sharp as in a step or heaviside function; but gradually decreasing. This is especially true when a silicon dioxide is present internally. In ultra-thin multilayer systems the interaction volume still encompasses more than a single layer leading to electrical signals that represent a combined, or weighed, secondary electron yield emanating from the interaction volume. In general, the ET detector produced data that is easier to interpret and correlate with the structure been tested. A 2-D model for one to three components in a multilayer, and that incorporates geometrical variables as well, has been implemented and resulted in fairly good fits of the experimental data. Consequently, another model producing a binary output has reasonably determined the end of the top metal layer at the internal boundary.

Conclusions

LA-EBID and IBID built NWs of W, Co and Pt all show significant improvements in their conductivities and purities when compared with Ga-FIB. These new approaches involving laser irradiation and inert gas ion beams show the potential of manufacturing high-quality and reliable integrated nanostructures with attractive electrical or magnetic properties.

We have studied the feasibility of etching nickel EUV absorber layers on Mo/Si multilayers via focused helium and neon ion beam etching. Helium ion beams do not etch the nickel top absorber layer and TEM imaging reveals unwanted nanobubbling and intermixing of the underlying Mo/Si EUV reflector layers. For neon ion beam induced exposures, the nickel absorber layer is effectively etched due to higher nuclear energy loss in the near surface region. Nevertheless, subsurface damage consisting of nanobubbles and an extended region of apparent Mo/Si intermixing also develops as with helium. Defect engineering, while realistically restricted in this mask design, could help mitigate the gravity of some of the deleterious effects resulting from ion beam irradiation, thus facilitating defect-free mask repair strategies.

Endpoint detection has demonstrated a new level of electronic (not visual) sensitivity and detectability to changes in samples undergoing a controlled etching process. This advantage has been validated by the accurate determination of the onsets of nanobubbling and the doses required for etching a top metal film in a multilayer structure. Experimental data has been closely matched to a 2-D Lambertian model that accounts for topographical changes on the specimen.

Future Work

In the near future, we may wish for a photolytic laser-assisted ebid process where bond energies are matched to incident photon wavelengths in the UV range. Data available from NIST and SWRI [111, 112] leads us to believe that a minimum of ~10 eV is needed to rupture most molecules involved in our electron-and ion-beam deposition processes. For example, charts show that below a peak near 10 eV, the cross-sections for dissociation by photons drop markedly. The company Hamamatsu Photonics sells the S2D2 VUV Light Source (L10706), with wavelengths of 115-400 nm (or 3.1-10.8 eV) from a compact deuterium lamp with MgF_2 window. It is equipped with vacuum flange and cooling mechanism capable of closely irradiating objects under depressurized conditions. In 1985 (Inorganic Chemistry Communications), a study about photofragmentation of $Ru_3(CO)_{12}$ to mononuclear products was documented [113]. For the reaction:

$$Ru_3(CO)_{12} + 1h\nu \rightarrow Ru_3(CO)_{11}S + CO \text{ (S=Solvent, like octane).}$$

In the presence of other ligands, then photo-substitution should occur readily. In our case, it is not desired to substitute the lost CO. The electronic absorption spectrum of $Ru_3(CO)_{12}$ shows a strong peak of quantum yields for fragmentation (and substitution) at ~375 nm (or only 3.3 eV), falling within the UV range of the light source proposed for further investigation. A logical follow-up beyond molecular dissociation via pyrolysis will be photo-dissociation.

A quite peculiar carbonyl molecule, $Ni(CO)_4$, has mainly been used as an intermediate in the Mond process for nickel refining, but it also is used for vapor-plating in the metallurgical and electronic industries, and as catalyst for synthesis of acrylic monomers in the plastic industry. Ni-halides and other compounds (NiF_2, NiCl, NiBr, NiO_2, etc) are all in solid form at near room temperature conditions. Nickel tetracarbonyl, with molecular mass of 170.73 g/mol and boiling

point of only +43 °C, is the only molecule identified that contains Ni and that is exists in gaseous form at near room temperature and ambient conditions. Its vapor pressure @25°C is high, at 390 mm Hg (or 390 Torr). This is much greater than Ga (MP=30°C, BP=2204°C), 0.0075 Torr @ 1310K. Its standard enthalpy of formation at 298 K = -632 kJ/mol (equivalent to 6.55 eV). A reaction [114] for this compound formation is shown below:

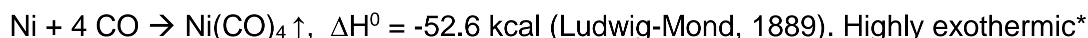

$$Ni + 4\,CO \rightarrow Ni(CO)_4\uparrow,\ \Delta H^0 = -52.6\ \text{kcal}$$ (Ludwig-Mond, 1889). Highly exothermic*

*A high conversion rate commercial nickel carbonyl process requires a large heat removal system.

Reflectivities from the EUV mask have been characterized at UV-VIS-NEAR IR from 200-900 nm wavelengths, and for Cu kα x-rays at 1.54 wavelength. It would be the next logical step to assess the reflectivity of a damaged Ru/Mo/Si mask at the soft x-ray wavelength of 13.5 nm, which corresponds to the tin and xenon plasma sources that can provide up to hundreds of watts in optical power.

Low energy ion irradiation may provide a suitable solution for nanomachining ultra-thin films and multilayers on silicon. If an application-specific apparatus using 0.5-5 keV neon ions in combination with an electron beam for imaging, it may be possible to initiate a more fruitful era of damage-free, high-accuracy milling materials for electronic, magnetic or optical applications.

List of References

[1] http://www4.nau.edu/microanalysis/Microprobe-SEM/Signals.html

[2] http://beam.acclab.helsinki.fi/~knordlun/thesis/node7.html

[3] M. Huth, F. Porrati, C. Schwalb, M. Winhold, R. Sachser, M. Dukic, J. Adams and G. Fantner; Beilstein J. Nanotechnol. 3, 597 (2012).

[4] I. Utke, P. Hoffmann, and J. Melngailis; J. Vac. Sci. Technol. B 26, 1197 (2008).

[5] I. Utke, V. Friedli, M. Purrucker, and J. Michler; J. Vac. Sci. Technol. B 25, 2219 (2007).

[6] W. F. van Dorp, J. D. Wnuk, J. M. Gorham, D. H. Fairbrother, T. E. Madey and C. W. Hagen; Journal of Applied Physics 106, 074903 (2009).

[7] S. G. Rosenberg, M. Barclay, D. H. Fairbrother; Phys. Chem. 15, 4002 (2013).

[8] F. Rüdenauer, G. Mozdzen, W. Costinand, E. Semerad; ADVANCED ENGINEERING MATERIALS 9, 8 (2007).

[9] J. M. De Teresa, R. Córdoba, A. Fernández-Pacheco, O. Montero, P. Strichovanec, and M. R. Ibarra; Journal of Nanomaterials 936863 (2009).

[10] J. J. L. Mulders and A. Botman; Functional Nanoscience, 179 (2010).

[11] A. Botman, J. J. L. Mulders and C. W. Hagen; Nanotechnology 20, 372001 (2009).

[12] A. Reguer, F. Bedu, D. Tonneau, H. Dallaporta, M. Prestigiacomo, A. Houel and P. Sudraud; J. Vac. Sci. Technol. B 26, 175 (2008).

[13] A. D. Dubner; MIT PhD Thesis, p. 95-107 (1990).

[14] *The Stopping Range of Ions in Solids*, edited by J. F. Ziegler, J. P. Biersack and U. Littmark (New York: Pergamon 1, 1985).

[15] A. Fernandez-Pacheco, J. M. De Teresa, R. Cordoba and M. R. Ibarra; Physical Review B 79, 174204 (2009).

[16] R. H. Stulen, and D. W. Sweeney; IEEE J. Quantum Elect. 35, 694 (1999).

[17] A. Lyons, R. Teki, and J. Hartley; Proc. SPIE 8322, 83221X (2012).

[18] H. J. Levinson, P. Mangat, T. Wallow, L. Sun, P. Aukmann, and S. Meyers; Proc. SPIE 8679, 867916 (2013).

[19] R. Peeters, S. Lok, E. van Alphen, N. Harned, P. Kuerz, M. Lowisch, H. Meijer, D. Ockwell, E. van Setten, G. Schiffelers, J. W. van der Horst, J. Stoeldraijer, R. Kazinczi, R. Droste, H. Meiling, and R. Kool; Proc. SPIE 8679, 86791F (2013).

[20] F. Aramaki, T. Ogawa, O. Matsuda, T. Kozakai, Y. Sugiyama, H. Oba, A. Yasaka, T. Amano, H. Shigemura, and O. Suga; Proc. SPIE 7969, 79691C (2011).

[21] T. W. Barbee, S. Mrowka, and M. C. Hettrick; Appl. Optics 24, 6 (1985).

[22] S. P. Vernon, D. G. Stearns, and R. S. Rosen; Opt. Lett. 18, 9 (1993).

[23] R. S. Rosen, D. G. Stearns, M. A. Viliardos, M. E. Kassner, S. P. Vernon, and Y. D. Cheng; Appl. Optics 32, 34 (1993).

[24] R. S. Rosen, M. A. Viliardos, M. E. Kassner, D. G. Stearns, and S. P. Vernon; Proc. SPIE 1547, 212 (1992).

[25] J. M. Slaughter, D. W. Schulze, C. R. Hills, A. Mirone, R. Stalio, R. N. Watts, C. Tarrio, T. B. Lucatorto, M. Krumrey, P. Mueller, and C. M. Falco; J. Appl. Phys. 76, 2144 (1994).

[26] T. Heil, and M. Lowisch, Manuf. Technol.; Photonik Intl. 2, 70 (2008).

[27] M. Singh, and J. J. M. Braat; Proc. SPIE 3997, 412 (2000).

[28] T.G. Kim, J. Ahn, S. Y. Lee and J. G. Park; J. Korean Phys. Soc. 45, 1229 (2004).

[29] S.Y. Lee, T.G. Kim, and J. Ahn; J. Korean Phys. Soc. 43, 826 (2003).

[30] S. Braun, H. Mai, M. Moss, R. Scholz, and A. Leson; Jpn. J. Appl. Phys. 41, 4074 (2002).

[31] M. G. Lassiter, T. Liang, and P. D. Rack; J. Vac. Sci. Technol. B 26, 963 (2008).

[32] E. Vietzke and V. Philipps; J. Nucl. Mater. 337, 1024 (2005).

[33] I. Utke, P. Hoffmann, and J. Melngailis; J. Vac. Sci. Technol. B 26, 1197 (2008).

[34] S. J. Randolph, J. D. Fowlkes, and P. D. Rack; Crit. Rev. Solid State 31, 55 (2006).

[35] Y. Drezner, D. Fishman, Y. Greenzweig, and A. Raveh; J. Vac. Sci. Technol. B 29, 011026 (2011).

[36] A. Reguer, F. Bedu, D. Tonneau, H. Dallaporta, M. Prestigiacomo, A. Houel, and P. Sudraud; J. Vac. Sci. Technol. B 26, 175 (2008).

[37] I. Utke, V. Friedli, M. Purrucker, and J. Michler; J. Vac. Sci. Technol. B 25, 2219 (2007).

[38] N. Yao, and A. K. Epstein; Microscopy: Science, Technology, Applications, and Education 3, 2190 (2010).

[39] W. B. Thompson, J. Notte, L. Scipioni, M. Ananth, L. Stern, C. Sanford, and S. Ogawa; Proc. ISTFA, 339 (2009).

[39] L. Scipioni, P. Alkemade, V. Sidorkin, P. Chen, D. Maas, and E. van Veldhoven; Am. Lab. 41, 26 (2009).

[40] B. Ward, J. A. Notte, and N. P. Economou; Photon. Spectra 41, 68 (2007).

[41] M. Ananth, L. Stern, J. Notte, L. Scipioni, C. Huynh, and D. Ferranti; Proc. SPIE 8036, 80360M (2011).

[42] J. Maas, E. van Veldhoven, and P.F.A. Alkemade; MRS Proc. 1354, mrss11-1354-ii03-03 (2011).

[43] D. C. Joy, R. Ramachandra, and B. Griffin; Microsc. Microanal. 15, 648 (2009).

[44] F. H. M. Rahman, S. McVey, L. Farkas, J. A. Notte, S. D. Tan, and R. H. Livengood; Scanning 34, 129 (2012).

[45] L. S. W. Thompson, H. Wu, D. Ferranti, D. Xia, F. Khanom, P. D. Rack, and C. Gonzalez; Proc. ISTFA, 455 (2012).

[46] H. M. Wu, L. A. Stern, J. H. Chen, M. Huth, C. H. Schwalb, M. Winhold, F. Porrati, C. M. Gonzalez, R. Timilsina, and P. D. Rack; Nanotechnology 24, 175302 (2013).

[47] R. Livengood, S. Tan, Y. Greenzweig, J. Notte, and S. McVey; J. Vac. Sci. Technol. B 27, 3244 (2009).

[48] S. D. Tan, R. H. Livengood, R. Hallstein, D. Shima, Y. Greenzweig, J. Notte, and S. McVey; Proc. ISTFA, 40 (2011).

[49] S. D. Tan, R. Livengood, P. Hack, R. Hallstein, D. Shima, J. Notte, and S. McVey; J. Vac. Sci. Technol. B 29, 06F604 (2011).

[50] R. H. Livengood, Y. Greenzweig, T. Liang, and M. Grumski; J. Vac. Sci. Technol. B 25, 2547 (2007).

[51] S. D. Tan, R. Livengood, D. Shima, J. Notte, and S. McVey; J. Vac. Sci. Technol. B 28, C6F15 (2010).

[52] Y. Drezner, Y. Greenzweig, D. Fishman, E. van Veldhoven, D. J. Maas, A. Raveh and R. H. Livengood; J. Vac. Sci. Technol. B 30, 041210 (2012).

[53] K. J. Abrams, J. A. Hinks, C. J. Pawley, G. Greaves, J. A. van den Berg, D. Eyidi, M. B. Ward, and S. E. Donnelly; J. Appl. Phys. 111, 083527 (2012).

[54] A. Kloidt, K. Nolting, U. Kleineberg, B. Schmiedeskamp, U. Heinzmann, P. Muller, and M. Kuhne; Appl. Phys. Lett. 58, 2601 (1991).

[55] H. J. Voorma, E. Louis, N. B. Koster, and F. Bijkerk; J. Appl. Phys. 83, 4700 (1998).

[56] R. R. Kola, D. L. Windt, W. K. Waskiewicz, B. E. Weir, R. Hull, G. K. Celler, and C. A. Volkert; Appl. Phys. Lett. 60, 3120 (1992).

[57] C. Montcalm; Opt. Eng. 40, 469 (2001).

[58] T. Leisegang, D. C. Meyer, A. A. Levin, S. Braun, and P. Paufler; Appl. Phys. a-Mater. 77, 965 (2003).

[59] P. B. Mirkarimi, D. G. Stearns, S. L. Baker, J. W. Elmer, D. W. Sweeney, and E. M. Gullikson; J. Appl. Phys. 91, 81 (2002).

[60] E. Bozorg-Grayeli, Z. J. Li, M. Asheghi, G. Delgado, A. Pokrovsky, M. Panzer, D. Wack, and K. E. Goodson; J. Appl. Phys. 112, 083504 (2012).

[61] H. Azuma, A. Takeichi, I. Konomi, Y. Watanabe, and S. Noda; Jpn. J. Appl. Phys. 32, 2078 (1993).

[62] D. L. Windt; J. Vac. Sci. Technol. A 18, 980 (2000).

[63] M. Wedowski, J. H. Underwood, E. M. Gullikson, S. Bajt, J. A. Folta, P. A. Kearney, C. Montcalm, and E. Spiller; Proc. SPIE 3997, 83 (2000).

[64] T. Feigl, H. Lauth, S. Yulin, and N. Kaiser; Microelectron. Eng. 57-8, 3 (2001).

[65] S. A. Bajt, and D. G. Stearns; Appl. Optics 44, 7735 (2005).

[66] H. Takenaka, H. Ito, T. Haga, and T. Kawamura; J. Synchrotron Radiat. 5, 708 (1998).

[67] T. Bottger, D. C. Meyer, P. Paufler, S. Braun, M. Moss, H. Mai, and E. Beyer; Thin Solid Films 444, 165 (2003).

[68] R. Timilsina, D. A. Smith, and P. D. Rack; Nanotechnology 24, 115302 (2013).

[69] R. Timilsina, and P. D. Rack; Nanotechnology 24, 495303 (2013).

[70] S.E. Donnelly and J. H. Evans; Fundamental Aspects of Inert Gases in Solids, Springer Science (1991).

[71] V. F. Reutov and A. S. Sokhatskii; Technical Physics 48, 68 (2003).

[72] O. Runevall; KTH Royal Institute of Technology, Doctoral Thesis (2012).

[73] A. J. Adams and W. G. Wolfer; J. Nucl. Matls. 158, 25 (1988).

[74] C. Dethloff; KIT Scientific Publishing (2012).

[75] C. A. Volkert and A. M. Minor; MRS Bulletin 32, 389 (2007).

[76] S. Dhara; Critical Reviews in Solid State and Material Sciences 32, 1 (2007).

[77] L. Pelaz, L. A. Marques and J. Barbolla; J. Appl. Phys. 96, 5947 (2004).

[78] M. Nastasi, J. W. Mayer and J. K. Hirvonen; “Ion-Solid Interactions, Fundamentals and Applications;” Cambridge Solid State Science Series, p. 295-99, 218-28, 180-7 (2004).

[79] J. Xia, W. Hu, J. Yang, B. Ao and X. Wang; physica status solidi b 243, 579 (2006).

[80] O. Runevall and N. Sandberg; Journal of Physics: Condense Matter 21, 335401 (2009).

[81] E. Oliviero; Journal of Applied Physics 100, 043505 (2006).

[82] I. J. Beyerlein, A. Caro, M. J. Demkowicz, N. A. Mara, A. Misra and B. P. Uberuaga; Materials Today 16, 443 (2013).

[83] K. J. Abrams, J. A. Hinks, C. J. Pawley and G. Greaves; Journal of Applied Physics 111, 083527 (2012).

[84] K. J. Abrams, S. E. Donnelly, M. –F. Beaufort, J. Terry, L. I. Haworth and D. Alquier; physica status solidi c 6, 1964 (2009).

[85] A. Luukkainen, J. Keinonen and M. Erola; Physical Review B 32, 4814 (1985).

[86] E. Chason, S. T. Picraux, J. M. Poate, J. O. Borland, M. I. Current, T. Diaz de la Rubia, D. J. Eaglesham, O. W. Holland, M. E. Law, C. W. Magee, J. W. Mayer, J. Melngailis and A. F. Tasch; J. Appl. Phys. 81, 6513 (1997).

[87] M. I. Baskes and V. Vitek; Metallurgical Transactions A 16, 1625 (1985).

[88] R. N. Wright and C. D. van Siclen; Journal of Nuclear Materials 206, 87 (1993).

[89] A. Pathak, P. Anand, R. Nageswara, D. K. Avasthi, A. M. Siddiqui, S. K. Srivastava, F. Eichhorn, R. Groetzschel, N. Schell, and A. Turos; AIP Conference Proceedings 680, 593 (2003).

[90] L. Pelaz, L. A. Marques and J. Barbolla; J. Appl. Phys. 96, 5947 (2004).

[91] T. Ezawa, M. Sugimoto, K. Niwase, S. Sasaki, A. Iwase, T. Iwata and F. E. Fujita; Journal of Nuclear Materials 179, 974 (1991).

[92] M. L. David, F. Pailloux, V. Mauchamp and L. Pizzagalli; Applied Physics Letters 98, 171903 (2011).

[93] E. Oliviero, S. Peripolli, P. F. P. Fichtner and L. Amaral; Materials Science and Engineering B 112, 111 (2004).

[94] A. C. Eddin and L. Pizzagalli; Journal of Physics: Condensed Matter 24, 175006 (2012).

[95] J. Nord, K. Nordlund and J. Keinonen; Physical Review B 65, 165329 (2002).

[96] A. I. Ryazanov, A. V. Klaptsov, A. Kohyama, V. Katoh and H. Kishimoto; Physica Scripta T111, 195 (2004).

[97] R, V. Nandedkar, K. Varatharajan, S. Panchapakesan and A. K. Tyagi; physica status solidi (a) 72, 89 (1982).

[98] H. –C. Yu and W. Lu; Acta Materialia 53, 1799 (2005).

[99] S. Tian, S. J. Morris, B. Obradovic, G. Wang, A. F. Tasch and C. M. Snell; IEEE Transactions on Electron Devices 45, 1226 (1998).

[100] M. A. Nguyen, M. -O. Ruault and F. Fortuna; Adv. Nat. Sci: Nanosci. Nanotechnol. 3, 015015 (2012).

[101] file:///C:/Users/unlgtutk/Downloads/9780387231167-c2%20(8).pdf

[102] H. R. Shanks and L. Ley; J. Appl. Phys. 52, 811 (1981).

[103] E. Oliviero, S. Peripolli, L. Amaral, P. F. P. Fichtner, M. F. Beaufort, J. F. Barbot and S. E. Donnelly; J. Appl. Phys. 100, 043505 (2006).

[104] W. B. A. Van Veen, T. R. Armstrong, K. T. Westerduin, L. M. Caspers and J.Th.M. De Hosson; Nucl. Instrum. Methods 209/210, 1055 (1983).

[105] D. C. Joy, Database of Electron-Solid Interactions (2008).

[106] B. W. Arey, V. Shutthanandan, W. Jiang; W.R. Wiley Environmental Molecular Sciences Laboratory, pacific Northwest National Laboratory.

[107] I. Utke, M. Gabureac, V. Friedli, L. Bernau and J. Michler; J. Physics: Conf. Ser. 241, 012072 (2010).

[108] A. Shih, J. Yater, C. Hor and R. Abrams; Applied Surface Science 111, 251 (1997).

[109]http://www.stehm.uvic.ca/using/training/workshops/CAMTEC/2010/secondary_electron_detectors.pdf

[110] http://www.specs.de/cms/upload/PDFs/IQE11-35/sputter-info.pdf

[111] http://www.nist.gov/data/nsrds/NSRDS-NBS31.pdf

[112] http://phidrates.space.swri.edu/#

[113] M. F. Desrosiers, D. A. Wink and P. C. Ford; Inorganic Chemistry Communications 24, 1 (1985).

[114] S. S. Naboychenko, I. B. Murashova and O. D. Neikov; Handbook of Non-Ferrous Metal Powders: Technologies and Applications; 1st Edition, Chapter 17 (2009).

APPENDICES

APPENDIX A:

Matlab Code End-Point Simulations

```
%Endpoint Detection Profile for Silicon Etched By Neon
%Materials: c-Si Sub;
clear all;
figure
%time_exp=xlsread('data_test11.xlsx','c5891:c5908');
%ETVolt=xlsread('data_test11.xlsx','d5891:d5908');
%ETCurr=ETVolt/0.17
%plot(time_exp,ETCurr,'r*');
%hold on;
v1=5.34 %etch velocity bttm layer, nm/s;
d1=1000 %top layer thickness, nm;
del1=1.5 %se yield top layer;
Ip=1.0 %primary current, pA;
w=20 %box width, nm;
runtime=100 %total etch/exposure time, s;
Flux=Ip*1e-12/(1.6e-19*w^2*1e-14) %instantaneous dose, ions/cm^2-s;
TotalDose=Flux*runtime %total dose, ions/cm2;
%L1=6;
v=v1;
t=0;
del=del1;
ti=d1/v1;
h=v*t;
hmax=50;
grid on;
%ylabel ('Etch Depth [nm]')
k=1;
for h=0:5:hmax
   w1=15;
   v=758.45;
   Dose=Flux*t
   %h=v1*t
   h1(k)=h;
   ISE=Ip*w1/2*del1*(h^2+w1^2/4)^-0.5
   Is=ISE-Ip;
   Is1(k)=Is;
   k=k+1;
   %plot(t,ISE,'r*-')
   %plot(Dose,ISE,'ro-')
   %plot(t,h,'r*-')
   %plot(h,ISE,'r*-')
   %title('Neon Etch of Copper');
   %legend('15x15 nm2', '20x20 nm2','30x30 nm2');
   %xlabel('Etch Time [s]')
```

```
    %ylabel('ISE [pA]');
    %xlabel('Dose [ions/cm^2]')
    %ylabel('Depth [nm]');
    %xlabel('Depth [nm]');
    %grid on
    %hold on
end
k=1;
for h=0:5:hmax
    w1=20;
    v=758.45;
    Dose=Flux*t
    %h=v1*t
    h2(k)=h;
    ISE=Ip*w1/2*del1*(h^2+w1^2/4)^-0.5
    Is=ISE-Ip;
    Is2(k)=Is;
    k=k+1;
    %plot(t,ISE,'r*-')
    %plot(Dose,ISE,'ro-')
    %plot(t,h,'r*-')
    %plot(h,ISE,'k*-')
    %title('Neon Etch of Copper');
    %legend('15x15 nm2', '20x20 nm2','30x30 nm2');
    %xlabel('Etch Time [s]')
    %ylabel('ISE [pA]');
    %xlabel('Dose [ions/cm^2]')
    %ylabel('Depth [nm]');
    %xlabel('Depth [nm]');
    %grid on
    %hold on
end
k=1;
for h=0:5:hmax
    w1=30;
    v=758.45;
    Dose=Flux*t
    %h=v1*t
    h3(k)=h;
    ISE=Ip*w1/2*del1*(h^2+w1^2/4)^-0.5
    Is=ISE-Ip;
    Is3(k)=Is;
    k=k+1;
    %plot(t,ISE,'r*-')
    %plot(Dose,ISE,'ro-')
    %plot(t,h,'r*-')
    %plot(h,ISE,'b*-')
    %title('Neon Etch of Copper');
    %legend('15x15 nm^2', '20x20 nm^2','30x30 nm^2');
    %xlabel('Etch Time [s]')
    %ylabel('ISE [pA]');
```

```
    %xlabel('Dose [ions/cm^2]')
    %ylabel('Depth [nm]');
    %xlabel('Depth [nm]');
    %grid on
    %hold on
    %disp(v)
    %disp(del1)
    %disp(Flux)
    %disp(Dose)
    %disp(ISE)
    %disp(h)
    %disp(t)
end
plot(h1,Is1,'bo-')
hold on
plot(h2,Is2,'k*-')
hold on
plot(h3,Is3,'r-')
grid on
title('Neon Etch of Copper');
legend('15x15 nm^2', '20x20 nm^2','30x30 nm^2');
xlabel('Depth [nm]');
ylabel('I Stage [pA]');
```

```
%Endpoint Detection Profile for a Two-Layer System Etched By Neon
%Materials: Au/SiO2/Si;
clear all;
Ip=1.0 %primary current, pA;
w=1000 %box width, nm;
time_exp=xlsread('ausi_3x.xlsx','a1:a162');
ETCurr=xlsread('ausi_3x.xlsx','e1:e162');
Flux=Ip*1e-12/(1.6e-19*w^2*1e-14)
Dose_exp=Flux*time_exp;
plot(Dose_exp,ETCurr,'r-')
hold on
%plot(time_exp,ETVolt,'-')
v1=14 %etch velocity bttm layer, nm/s;
v2=1.6 %etch velocity bttm layer, nm/s;
v3=2.65;
d1=340 %top layer thickness, nm;
d2=0 %bttm layer thickness,nm;
d3=300000;
del1=3.95 %se yield top layer;
del2=3.58 %se yield bottom layer;
del3=3.4;
Ip=1.0 %primary current, pA;
w=1000 %box width, nm;
runtime=162 %total etch/exposure time, s;
A1=79 %atomic number layer 1;
A2=30 %atomic number layer 2;
A3=14;
I1=9.2255 %first ionization energy, eV;
I2=16 %first ionization energy, eV;
I3=8.1517 %first ionization energy si sub, ev;
Den1=19.32 %density, g/cm^3;
Den2=2.65 %density, g/cm^3;
Den3=2.33;
Z1=196.9665 %atomic mass, g/mol;
Z2=60 %atomic mass, g/mol;
Z3=28.0855;
L1=2.67*A1*I1/(Den1*Z1^0.667)%Ono and Kanaya escape depth, nm;
L2=2.67*A2*I2/(Den2*Z2^0.667)%Ono and Kanaya escape depth, nm;
L3=2.67*A3*I3/(Den3*Z3^0.667)%Ono and Kanaya escape depth, nm;
Flux=Ip*1e-12/(1.6e-19*w^2*1e-14) %instantaneous dose, ions/cm^2-s;
TotalDose=Flux*runtime %total dose, ions/cm2;
%L1=1;
L2=32;
%L3=8;
v=v1;
t=0;
del=del1;
ti1=d1/v1;
ti2=d1/v1+d2/v2;
h=v*t;
k=1;
```

```
for t=0:runtime
    if ((d1-h)>L1)
        v=v1
        h=v*t;
        ISE=Ip*w/2*del1*(h^2+w^2/4)^-0.5
        ISE1(k)=ISE
        Dose1(k)=Flux*t
        h=v1*t
        k=k+1;
    elseif ((d1-h)<=L1 & (d1-h)>0)
        vf1=(d1-h)/L1
        v=v1
        h=v*t;
        ISE=Ip*w/2*(vf1*(del1-del2)+del2)*(h^2+w^2/4)^-0.5
        ISE1(k)=ISE
        Dose1(k)=Flux*t
        disp(['the value of t is',t])
        disp(['The value of h is',h])
        h=v1*t
        k=k+1;
    elseif (h>=d1 & h<(d1+d2-L2))
        v=v2
        del=del2;
        h=d1+v2*(t-ti1)
        ISE=Ip*w/2*del2*(h^2+w^2/4)^-0.5
        ISE1(k)=ISE
        Dose1(k)=Flux*t
        k=k+1;
        disp(['the value of t is',t])
        disp(['The value of h is',h])
     elseif (h>=(d1+d2-L2) & h<(d1+d2))
        vf2=(d1+d2-h)/L2
        v=v2
        h=d1+v2*(t-ti1)
        ISE=Ip*w/2*(vf2*(del2-del3)+del3)*(h^2+w^2/4)^-0.5
        ISE1(k)=ISE
        Dose1(k)=Flux*t
        disp(['the value of t is',t])
        disp(['The value of h is',h])
        h=d1+v2*(t-ti1)
        k=k+1;
    elseif (h>=(d1+d2))
        v=v3
        del=del3;
        h=d1+d2+v3*(t-ti2)
        ISE=Ip*w/2*del3*(h^2+w^2/4)^-0.5
        ISE1(k)=ISE
        Dose1(k)=Flux*t
        disp(['the value of t is',t])
        disp(['The value of h is',h])
        k=k+1
```

```
    else
    end
    disp(t)
    disp(h)
    disp(L1)
    disp(L2)
    disp(L3)
    grid on;
    title('ENDPOINT DETECTION: Three-Layer System (Ne+ Etch of Au/SiO2/SiSub)');
    %xlabel('Time [s]');
    xlabel('DOSE [ions/cm^2]')
    ylabel('ISE [pA]');
    %ylabel ('Etch Depth [nm]')
    %plot(t,ISE,'k-')
    plot(Dose1,ISE1,'k-')
    legend('Experimental', 'Fit');
    %plot(t,h,'r*')
    %t=t+1
end
 %[haxes,hline1,hline2]=plotyy(time_exp,ETVolt,tn,ISEn)
```

```
%Endpoint Detection Profile for Silicon Etched By Neon
%Materials: c-Si Sub;
clear all;
figure
%time_exp=xlsread('data_test11.xlsx','c5891:c5908');
%ETVolt=xlsread('data_test11.xlsx','d5891:d5908');
%ETCurr=ETVolt/0.17
%plot(time_exp,ETCurr,'r*');
%hold on;
v1=1.75 %etch velocity bttm layer, nm/s;
d1=100 %top layer thickness, nm;
del1=1.0 %se yield top layer;
Ip=1.0 %primary current, pA;
w=100 %box width, nm;
runtime=200 %total etch/exposure time, s;
Flux=Ip*1e-12/(1.6e-19*w^2*1e-14) %instantaneous dose, ions/cm^2-s;
TotalDose=Flux*runtime %total dose, ions/cm2;
%L1=6;
v=v1;
t=0;
del=del1;
ti=d1/v1;
h=v*t;
grid on;
%ylabel ('Etch Depth [nm]')
k=1;
for t=0:runtime
   w1=100;
   v1=1.75;
   Dose=Flux*t
   h=v1*t
   ISE=Ip*w1/2*del1*(h^2+w1^2/4)^-0.5
   t100(k)=t;
   dose100(k)=Dose;
   ISE100(k)=ISE;
   k=k+1;
end
k=1;
for t=0:runtime
   w2=250;
   v2=0.875;
   Dose=Flux*t
   h=v2*t
   ISE=Ip*w2/2*del1*(h^2+w2^2/4)^-0.5
   t250(k)=t;
   dose250(k)=Dose;
   ISE250(k)=ISE;
   k=k+1;
end
k=1;
for t=0:runtime
```

```
    w3=350;
    v3=0.8;
    Dose=Flux*t
    h=v3*t
    ISE=Ip*w3/2*del1*(h^2+w3^2/4)^-0.5
    t350(k)=t;
    dose350(k)=Dose;
    ISE350(k)=ISE;
    k=k+1;
end
k=1;
for t=0:runtime
    w4=500;
    v4=0.35;
    Dose=Flux*t
    h=v4*t
    ISE=Ip*w4/2*del1*(h^2+w4^2/4)^-0.5
    t500(k)=t;
    dose500(k)=Dose;
    ISE500(k)=ISE;
    k=k+1;
end
plot(dose100,ISE100,'ko',dose250,ISE250,'r*',dose350,ISE350,'bo',dose500,ISE500,'y*')
title('ENDPOINT DETECTION: Ne+ Etch of c-Si');
legend('w=100nm', 'w=250nm','w=350nm','w=500nm');
%xlabel('Etch Time [s]')
xlabel('Dose [ions/cm^2]')
ylabel('ISE [pA]');
grid on
```

APPENDIX B:

Matlab Code for Binary Endpoint Simulations

```
%Binary Endpoint;
clear all;
totalpts=410;
totalpts1=409;
%k=1;
[A,B]=xlsread('ni_euv.xlsx');
%d=xlsread('data_test13','d2871:d3083')
for k=1:1:totalpts
   t(k)=A(k,1)
   d(k)=A(k,2)
end
for k=1:1:totalpts1
   t1(k)=A(k,1)
end

aver=(d(1)+d(2)+d(3)+d(4)+d(5))/5
%aveslope=((d(2)-d(1))+(d(3)-d(2))+(d(4)-d(3))+(d(5)-d(4))+(d(6)-d(5)))/5
aveslope=0.0168;
aveinty=0.3795;
for k=1:1:totalpts1
   g=k+1
   slop(k)=abs(d(g)-d(k));
   avecon(k)=(d(g)+d(k))/2;
   valy(k)=aveslope*t(k)+aveinty;
   diff1(k)=100*abs(slop(k)-aveslope)/aveslope;
   diff2(k)=100*abs(valy(k)-d(k))/valy(k);
   diff3(k)=100*abs(valy(k)-avecon(k))/valy(k);
   if (diff2(k)<82 & diff3(k)<82)
      v(k)=1
   else
      v(k)=0
   end
end
[haxes,hline1,hline2]=plotyy(t1,v,t,d);
legend('Binary Data','Measured Data');
title('Au/Si Endpoint Binary Modeling');
xlabel('Time [s]');
ylabel('Binary Output [1=Au]');
grid on;
```

APPENDIX C:

Binary Endpoint Modeling

In order to establish a practical and visually simple cutoff value, where the top film, typically a metal conductor, ends internally within a structure, it is useful to have a binary depiction of the secondary electron detection analog profile that exhibits no noise. These fluctuations can be of instrumental (meters) origin, due to small variations in gas pressure and thus beam current and to the data collection method, more specifically if fetching only one point and how often versus several points in close succession and saving an average. The methods here were more rudimentary by collecting one data point every one or two seconds. It is crucial to have an understanding of where the beam raster is positioned at the instant the data is collected. In this study, an effort was made to have every data point taken at least after one or two passes within the selected irradiated zone (fewer monolayers etched per data point collected). Transforming the analog signals into binary form to represent when there is top layer thickness remaining with a '1' and when there is not with a '0' has the advantages of being visually simplistic and having the potential to be used in an automated nanomachining apparatus. The figures below, show the conversion of the analog measured data to binary form for Ni (50nm), Au (100nm) and Cu (45nm) as top layers.

The case of gold poses its challenges because gold sputters quite rapidly. Therefore, nanoscopic films will be practically consumed in very short process times. The case of Ni presents its particular set of challenges because the SE emission yields between the nickel top layer and the structure beneath (Ru/Mo/Si) have relatively similar magnitudes, thus making the signal levels before and after the nickel is milled comparable in magnitude (~45% difference). Despite the limitations, with a simple linear approximation and using the slope and intercept of the fit against each pair of consecutive averaged data points, reasonably good binary profiles have been

obtained in each of the three (3) cases mentioned above. Admittedly, this method will have its limitations when it comes to films thinner than ~50 nm and etch patterns smaller than ~250 nm. This because the mill times would be too short, and this is especially true for gold. Refer to figure C.1 below.

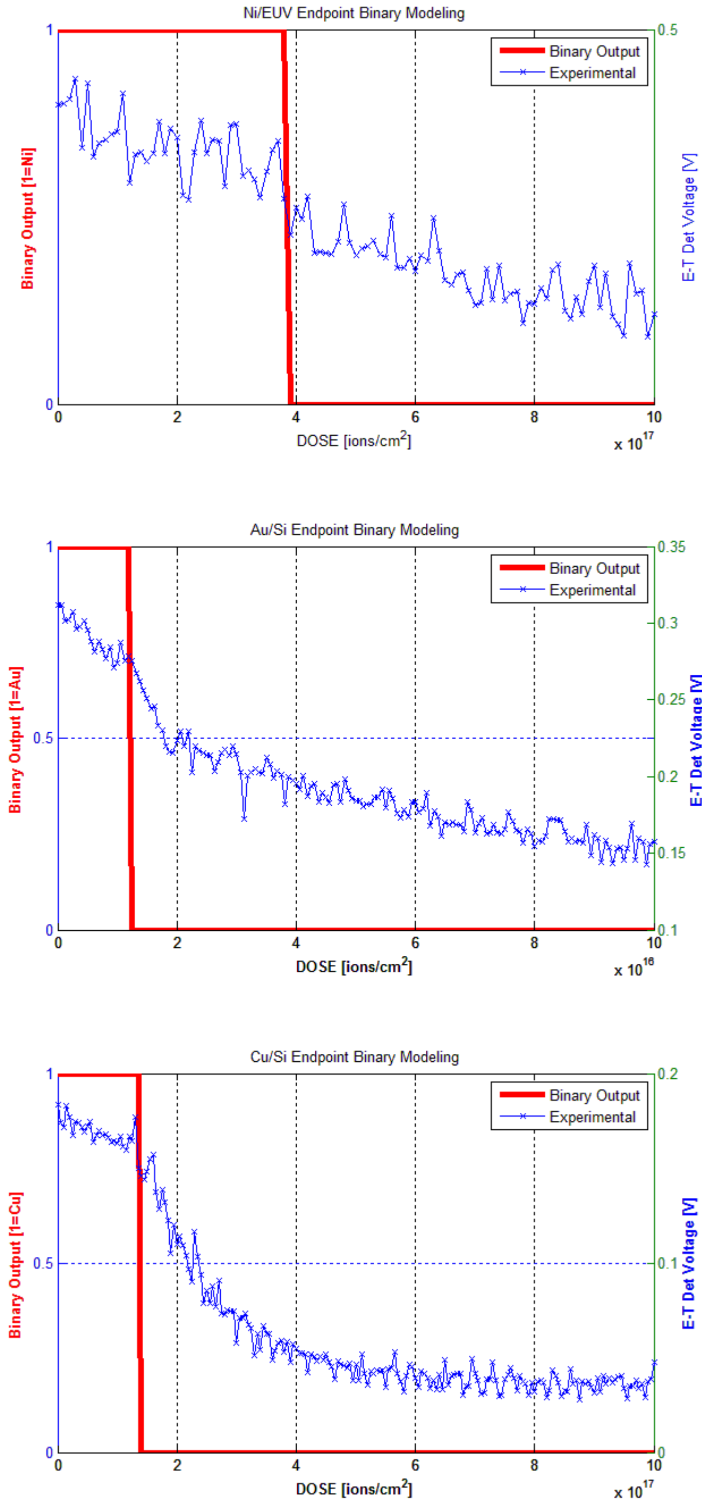

Figure C.1. Binary endpoint detection of the end of the layer for Ni, Au and Cu etched by Ne^{+}.

Vita

Carlos Manuel Gonzalez was born December 31, 1964 (New Year's Eve), at 11:06 pm in Lincoln, NE. He grew up in Ponce, Puerto Rico and Spanish is his first language. He earned BS degrees in Theoretical Physics at The University of Puerto Rico, Mayaguez Campus, and in Electrical Engineering at the University of Nebraska in Lincoln, Nebraska. He also completed a Master's degree in Ceramic Engineering at The Georgia Institute of Technology in Atlanta, GA. In Georgia Tech, Carlos was the President of the American Ceramic Society (ACerS). He then worked in the electronics manufacturing industry in Puerto Rico as a Process Engineer with DuPont Electronics and as a Components and New Product Introduction (NPI) Engineer with Hewlett-Packard Corporation. For one year, in a temporary basis, he was a Lecturer of Electric Circuits and of Electronics at the University of Puerto Rico in Mayaguez. He returned to the continental US to work as Senior Engineer, testing prototype passive devices for the Research Division of AVX Corporation in Myrtle Beach, SC. In January 2010, he joined the University of Tennessee in Knoxville as a Research Associate and started his PhD in the Materials Science & Engineering program the following fall term. In UTK, Carlos was the Founder and first President of the local Materials Research Society (UT-MRS) and later became the Vice-President of the Society of Hispanic Professional Engineers (UT-SHPE). He completed his Doctorate of Philosophy degree in December 2014.